universität
wien

DISSERTATION

Titel der Dissertation

“Quantum chemical studies on electronic structure and photodynamics of ruthenium complexes”

verfasst von
Dipl.-Chem. Leon Freitag

angestrebter akademischer Grad
Doktor der Naturwissenschaften (Dr. rer. nat.)

Wien, 2015

Studienkennzahl lt. Studienblatt:	A 796 605 419
Dissertationsgebiet lt. Studienblatt:	Chemie
Betreut von:	Univ.-Prof. Dr. Leticia González

ABSTRACT

Ruthenium complexes have found their way into many applications in the last decades. Among those, ruthenium polypyridyl compounds have been employed as light harvesting devices and photosensitisers in artificial photosynthesis and molecular photocatalysis. Ruthenium nitrosyl complexes are rapidly emerging as NO delivery agents to biological tissues with promising applications in anticancer photodynamic therapy, thanks to their ability to photorelease nitric oxide (NO). This thesis encompasses computational studies on reactivity, electronic structure, excited states and photodynamics of several ruthenium nitrosyl and polypyridyl complexes.

The first part of the thesis deals with ruthenium nitrosyls. The cis-trans isomerisation mechanism of RuHIndNO, a ruthenium nitrosyl derivate of the prominent anti-cancer drug candidate KP1019, is investigated with density functional theory calculations. Next, the electronic structure of the ground and the first excited triplet state of RuHIndNO is studied with multiconfigurational methods including the density-matrix renormalisation group (DMRG). The obtained multiconfigurational wavefunctions and DMRG-based orbital entanglement analysis provides theoretical insight into the non-innocence of the NO ligand in nitrosyl complexes by describing the electron correlation in the Ru–NO bond and assigning oxidation states to the metal and the NO ligand. Another study is performed on excited states of ruthenium nitrosyl complexes with quantum chemical calculations and surface-hopping dynamics to obtain insights into the photodissociation mechanism of NO.

The second part of this thesis is devoted to the excited states and photophysics of ruthenium polypyridyl complexes. Accurate excitation energies of tris(2,2-bipyridine)ruthenium (II), the prototype ruthenium polypyridyl are obtained with multiconfigurational calculations assisted by an orbital entanglement analysis. Subsequently, the effect of the ligand substitution on the photophysics of a series of ruthenium polypyridyl photosensitisers and a hydrogen-producing catalyst is investigated.

This thesis demonstrates the applicability of density functional and multiconfigurational methods to ruthenium complexes and provides examples of the ability of these methods to aid the rational design of functional molecules for solar light conversion, photocatalysis and photodynamic therapy.

ZUSAMMENFASSUNG

Rutheniumkomplexe haben in den letzten Jahrzehnten ihren Weg in ein breites Spektrum von Anwendungen gefunden. Darunter sind Ruthenium-polypyridylkomplexe bekannt, die als Lichtsammeleinheiten und Photosensibilisatoren in künstlichen Photosynthesesystemen und molekularen Photokatalysatoren ihre Anwendung finden. Ruthenium-Nitrosyle sind vielversprechende Träger für das Stickstoffmonoxid (NO) im biologischen Gewebe, die eine Anwendung, u. a. in photodynamischer Therapie finden können. Diese Dissertation umfasst theoretische Studien zu Reaktivität, elektronischer Struktur, angeregten Zuständen sowie Photodynamik von einigen Ruthenium-Nitrosyl- und Polypyridylkomplexen.

Der erste Teil der Arbeit beschäftigt sich mit Ruthenium-Nitrosylen. Der Mechanismus der cis-trans-Isomerisierung von RuHIndNO, einem Nitrosylderivat des potentiellen Antikrebsmedikaments KP1019 wird mit der Dichtefunktionaltheorie untersucht. Anschließend wird die elektronische Struktur des Grund- und des ersten Triplettzustands von RuHIndNO mithilfe von multikonfigurationellen Methoden untersucht, darunter auch mit Dichtematrixrenormalisierungsgruppe (DMRG). So erhaltenen multikonfigurationellen Wellenfunktionen sowie die auf DMRG aufgebaute Verschränkungsanalyse der Orbitale erlauben eine theoretische Einsicht in den “nicht-unschuldigen” Charakter des NO-Liganden, indem sie die Elektronenkorrelation in der Ru–NO-Bindung beschreiben sowie die physikalische Oxidationsstufe dem Metall und dem Liganden zuweisen. Eine weitere Studie betrachtet angeregte Zustände der Ruthenium-Nitrosylkomplexe mit quantenchemischen Rechnungen und Surface-Hopping-Dynamik, um Einsichten in den Photodissoziationsmechanismus von NO zu bekommen.

Der zweite Teil dieser Arbeit widmet sich den angeregten Zuständen und Photophysik der Ruthenium-Polypyridylverbindungen. Hochgenaue Anregungsenergien von Tris(2,2-bipyridyl)ruthenium (II), dem Prototyp der Ruthenium-Polypyridylkomplexe werden mithilfe von multikonfigurationellen Methoden mit Unterstützung der Orbitalverschränkungsanalyse. Anschließend wird der Einfluß der Ligandensubstitution auf die Photophysik bei einer Reihe von Ruthenium-Polypyridyl-basierten Photosensibilisatoren und einem Photokatalysator zur Wasserstoffherstellung untersucht.

Diese Arbeit veranschaulicht die Anwendbarkeit der Dichtefunktionaltheorie und multikonfigurationellen Methoden auf Rutheniumkomplexe und zeigt anhand von Beispielen wie diese Methoden das rationale Design von funktionellen Molekülen für künstliche Photosynthese, Photokatalyse sowie photodynamische Therapie unterstützen können.

FREQUENTLY USED ACRONYMS

ANO	Atomic natural orbitals
bpy	2,2-bipyridine
CASPT2	Complete Active Space Cecond Order Perturbation Theory
CAS	Complete Active Space
CASSCF	Complete Active Space Self-Consistent Field
CI	Configuration interaction
DKH	Douglas-Kroll-Hess
dqp	2,6-di(quinolin-8-yl)pyridine
DFT	Density functional theory
DMRG	Density matrix renormalisation group
DSSC	Dye-sensitised solar cell
ECP	Effective core potential
HF	Hartree-Fock
ISC	Intersystem crossing
KP1019	(IndH)[trans-RuCl$_4$(1H-Indazole)$_2$]
LLCT	Ligand to ligand charge transfer
MLCT	Metal to ligand charge transfer
MC	Metal-centered
MCSCF	Multiconfigurational self-consistent field
MPS	Matrix product state
NAC	Non-adiabatic coupling
NO	Nitric oxide
PaPy3	(N,N-bis(2-pyridylmethyl)amine-N-ethyl-2-pyridine-2-carboxamide
PDT	Photodynamic therapy
PES	Potential energy surface
RAS	Restricted Active Space
RASSCF	Restricted Active Space Self-Consistent Field
RASPT2	Restricted Active Space Cecond Order Perturbation Theory
RI	Resolution of identity
ROS	Reactive oxygen species

RuHIndNO	[trans-$RuCl_4$(NO)(1H-Indazole)$]^-$
SOC	Spin-orbit coupling
TD-DFT	Time-dependent density functional theory
TDSE	Time-dependent Schrödinger equation
TISE	Time-independent Schrödinger equation
TM	Transition metal
TON	Turnover number
tpy	2,2′:5′,2″-terpyridine
VDZP	Valence double-zeta polarised
VTZP	Valence triple-zeta polarised

CONTENTS

1 INTRODUCTION 1
- 1.1 Preface 1
- 1.2 Ruthenium nitrosyl complexes and nitric oxide 1
- 1.3 Ru polypyridyl complexes for light harvesting 4

2 THEORY 6
- 2.1 Schrödinger Equation and Born-Oppenheimer Approximation 6
- 2.2 Quantum Chemical Methods 8
  - 2.2.1 The Hartree-Fock Method 8
  - 2.2.2 Electron Correlation 9
  - 2.2.3 CI and MCSCF 9
  - 2.2.4 Density Matrix Renormalisation Group 11
  - 2.2.5 Orbital Entanglement Analysis 13
  - 2.2.6 Density Functional Theory 13
  - 2.2.7 Density Fitting and Cholesky Decomposition 16
- 2.3 Additional Corrections 17
  - 2.3.1 Relativistic effects 17
  - 2.3.2 Solvent Effects 17
- 2.4 Dynamics 18

3 RUTHENIUM NITROSYL COMPLEXES 20
- 3.1 Ground state studies on RuHIndNO 20
  - 3.1.1 Mechanism elucidation of the cis-trans isomerisation 21
  - 3.1.2 Electronic structure multiconfigurational studies 22
- 3.2 Excited states of photoreleasing nitrosyls 26
  - 3.2.1 Photodissociation mechanism in a NO photoreleasing complex 26
  - 3.2.2 Insights into dye-mediated NO photodissociation 28
- Appendix 3.A Attached Papers 32

4 RUTHENIUM POLYPYRIDYL COMPLEXES 79
- 4.1 Multiconfigurational calculations on $[Ru(bpy)_3]^{2+}$ 79
- 4.2 Computational study on Ru dqp complexes 86
- 4.3 Substitution effects in a Ru-based photocatalyst 88
- Appendix 4.A Attached Papers 90

5 SUMMARY AND CONCLUSION 115

1

INTRODUCTION

1.1 PREFACE

Ruthenium is an incredibly rare element, being only the 74th most abundant element in Earth's crust, exceeding even gold and platinum in its scarcity.[1(p. 29)] At the same time, it is the element with the largest available span of oxidation states, from −2 to 8,[2] with an accordingly rich coordination chemistry. Despite the scarcity of ruthenium, its complexes have found their way into a broad range of applications in the last decades. Ruthenium polypyridyl complexes, perhaps the most famous group of ruthenium complexes, are used in various photochemical and photoelectrochemical applications. Other ruthenium complexes have been used as catalysts for organic reactions, with the most prominent example being the series of *Schrock catalysts* – ruthenium complexes with N-heterocyclic carbenes employed in olefin metathesis.[3] Application as anticancer drugs is a new field for ruthenium compounds which is rapidly emerging: two ruthenium anticancer compounds, NAMI-A[4] and KP1019[5] (Fig. 1) reached phase I clinical trials, and a large number of other ruthenium compounds have been shown to have anticancer activity.[6] Ruthenium nitrosyl complexes deserve special attention because of their ability to deliver nitric oxide (NO) to biological tissues and as promising drug candidates for the photodynamic therapy against cancer.[7]

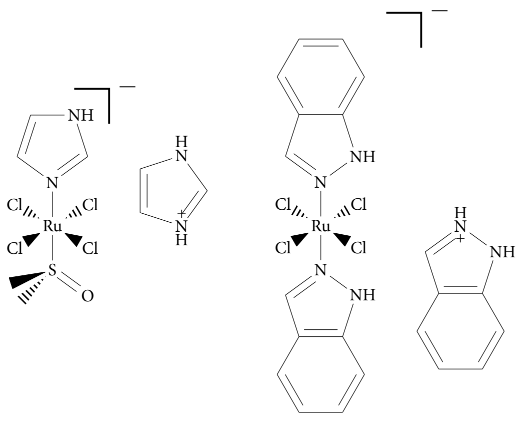

(a) NAMI-A **(b)** KP1019

Figure 1: NAMI-A and KP1019, the Ru anticancer drugs in clinical trials.

The broad (and growing) field of applications of Ru complexes demands both optimisation of properties of the complexes for their respective applications and understanding of fundamental processes behind their mechanisms of action. The main goal of this thesis is to show how theoretical and computational chemistry can aid both of these quests with a series of studies on reactivity, electronic structure and photochemical properties of selected ruthenium nitrosyl and polypyridyl complexes.

1.2 RUTHENIUM NITROSYL COMPLEXES AND NITRIC OXIDE

Nitric oxide (NO) is one of the most important physiological regulators in the human body, where it plays a role, among others, in neurotransmission, immune response and blood pressure control.[8] Additionally, NO shows several anticancer effects including control of tumour growth, inducing cancer cell death and tumour sensitisation to chemotherapy.[9] The versatility of the biological functions of NO stimulated research on molecules able to deliver NO to biological tissues. In this regard, transition metal (TM) nitrosyl complexes which are able to release NO upon exposure to light are particularly promising, as light-activated NO release allows its selective delivery to particular tissues and body areas.

The ability of many TM nitrosyl complexes to selectively photorelease NO open possibilities of their use in photodynamic therapy (PDT).[7] The working principle of PDT[7,10] is illustrated in Fig. 2: PDT involves administration of an inactive precursor, which is then accumulated in the tumour, followed by light irradiation of the cancer area. The precursor releases the cytotoxic species only upon light activation and destroys the cancer with limited damage to surrounding healthy tissues. Therefore, PDT shows less side effects associated with the lack of drug selectivity towards cancer cells than conventional chemotherapy. Traditionally, PDT treatment employs photosensitisers[7,10] which generate the highly cytotoxic singlet oxygen and other reactive oxygen species (ROS) on activation (cf. Fig. 3a). Photosensitiser-based PDT has flourished in the recent years, leading to the development of a wide variety of photosensitisers for PDT,[10] including ruthenium polypyridyl complexes (cf. Section 1.3).[6,11] However the anticancer effects of NO open an alternative mechanism of action for PDT involving NO (Fig. 3b), which potentially might have advantages over singlet oxygen and ROS generation due to hypoxia found in many tumours.[12]

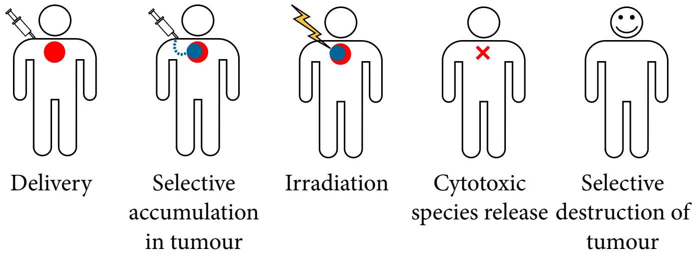
Delivery
Selective accumulation in tumour
Irradiation
Cytotoxic species release
Selective destruction of tumour

Figure 2: A schematic view of the working principle of photodynamic therapy.

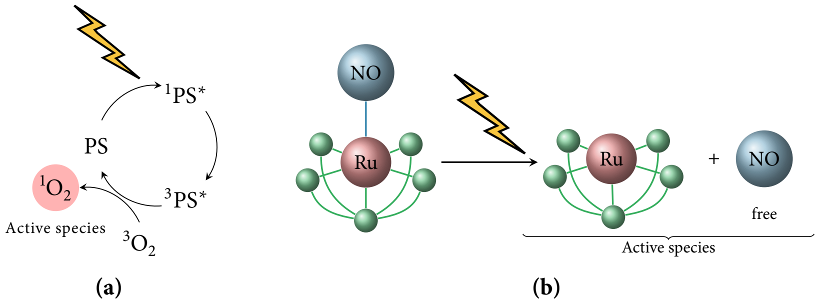

(a) (b)

Figure 3: Mechanisms of conventional (photosensitiser) (a) and ruthenium nitrosyl-based PDT (b).

Much effort has been devoted to search for the TM nitrosyls suitable for NO photorelease. Early studies focused on well known nitrosyls such as $Na_2[Fe(CN)_5(NO)]$, Roussin's salts, $(NH_4)[Fe_4S_3(NO)_7]$ and $Na_2[Fe_2S_2(NO)_4]$)[13] or metalloporphyrines derived from heme,[14] while more recent studies have led to the preparation of a number of iron,[15] manganese[16] and ruthenium[17–21] nitrosyl complexes with other auxiliary ligands. In this regard, ruthenium nitrosyls have been particularly promising: they are stable in the absence of light,[22] and the ruthenium complex formed after the NO dissociation may show anticancer activity independently from the NO ligand.[6] Additionally, ruthenium nitrosyls have been shown to play a role as intermediates in the mechanism of action of other ruthenium anti-cancer drug candidates.[23]

NO AS A NON-INNOCENT LIGAND. Potential applications as NO carriers is not the only reason for a broad academic interest in ruthenium and other transition metal nitrosyls. NO is a so-called "non-innocent ligand", i. e. it does not allow to unambiguously define the oxidation state of the central metal (and neither its own) upon coordination.[24] In particular, NO can coordinate to a metal as a neutral ligand, NO^+ or NO^-. Enemark and Feltham[25] proposed a general notation for metal nitrosyls which reflects the oxidation state ambiguity, $\{M(NO)\}^n$, with n being the total number of electrons in the metal d and NO π^* orbitals. For example, a $\{RuNO\}^6$ complex could be described as either $Ru^{II}{-}NO^+$, $Ru^{III}{-}NO^o$, or anything in between. The oxidation states of the metal and NO in metal nitrosyls has been subject of many theoretical, spectroscopic and electrochemical studies.[26–30]

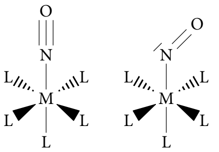

Figure 4: Linear and bent coordination of NO in transition metal nitrosyls.

Different structures of $\{M(NO)\}^n$ moiety go hand-in-hand with different coordination modes of NO to the metal, most prominently in a linear or bent configuration.[31,32] (Fig. 4) Other coordination modes of NO such as side-on coordination[33] or coordination with the oxygen atom[34] also exist, but examples of such coordination are rare. Many studies speak in favour of ascribing linear NO coordination to NO^+ and bent NO to NO^0 or NO^- coordination,[32,35] and that most linear $\{RuNO\}^6$ complexes[36] and many $\{FeNO\}^6$ complexes[37] are best described as $Ru^{II}{-}NO^+$, but this is not without controversy.[30] A correct assignment of metal and NO oxidation states in nitrosyl complexes would also aid in understanding reactivity and redox processes involving these complexes, for example metabolism steps of ruthenium anticancer compounds involving nitrosyl intermediates.[23]

NO PHOTODISSOCIATION MECHANISM. The Mascharak group[20,38,39] conducted several studies on tuning the wavelength for the NO photorelease in metal nitrosyls. In their studies only energies and characters of the lowest bright excited states have been considered. Based on the excited state character, different mechanisms have been postulated: a "direct" mechanism if the bright excited state has a NO dissociative character and an "indirect" mechanism otherwise. Such mechanism classification is helpful but limited, as the photophysical processes occurring after photoexcitation of metal nitrosyls and the involvement of other states (especially the triplet states) in the NO dissociation has not been studied so far. Yet, detailled insights into the NO photodissociation mechanism would greatly aid the rational design of NO photoreleasing metal nitrosyls for photodynamic therapy.

In this thesis three ruthenium nitrosyl complexes are investigated, putting the emphasis on their reactivity, NO non-innocence and the photorelease of NO. We begin with the elucidation of the mechanism of a *cis*↔*trans* isomerisation of a ruthenium nitrosyl, followed by a study of the electronic structure of the Ru–NO bond, aimed at resolving the ambiguity of the metal and NO oxidation state. We continue with other two Ru nitrosyls, which have been shown to release NO upon irradiation of the UV and visible light, by exploring their excited states and their NO photodissociation mechanism in detail. The NO photodissociation mechanism of one Ru nitrosyl is investigated in detail with a surface hopping dynamics study.

1.3 RU POLYPYRIDYL COMPLEXES FOR LIGHT HARVESTING

The photochemistry of ruthenium polypyridyl complexes has flourished ever since the discovery of the photosensitising ability of the ruthenium (II) tris(2,2-bipyridyl) ($[Ru(bpy)_3]^{2+}$, Fig. 5), the prototype ruthenium polypyridyl by Adamson and Demas[40] in 1971. Their unique excited state properties have led to a wide range of applications in photoredox catalysis,[41] electroluminescent devices,[42] as light harvesting complexes for artificial photosynthesis systems or photovoltaic devices such as dye-sensitised solar cells (DSSCs)[43–46] and in biological applications such as cellular imaging and, not least, PDT.[6,47] The feature-rich photochemistry of ruthenium polypyridyls has attracted the attention of many researchers, and the prototype $[Ru(bpy)_3]^{2+}$ has been often used as a model in studies aiming at understanding the fundamental photoprocesses in ruthenium polypyridyls.[43–45,48–51] Being a subject of many experimental photochemical studies, $[Ru(bpy)_3]^{2+}$ has also attracted computational and theoretical chemists, not least as a test-bed for novel theoretical developments in photochemistry.[52–54]

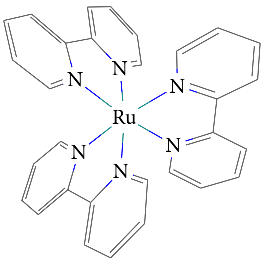

Figure 5: $[Ru(bpy)_3]^{2+}$

One of the primary reasons for the broad success of Ru polypyridyls in photochemical applications lies in their ability to efficiently induce charge separation upon photoexcitation. Another reason is the easy tunability of their photophysical properties: their excited state picture can be widely tailored by the choice of ligand sphere, and Ru may be complexated with a very broad range of ligands (see Appendix 4.A.1). This gives a synthetic chemist broad possibilities to accordingly tune the excited state properties of the complexes, and, more importantly, an opportunity for computational chemistry to predict the ligand influence on photophysical properties.

Fig. 6a shows a simplified diagram of the photophysical fate of a Ru polypyridyl complex. In the ground state, a typical Ru polypyridyl shows a Ru d^6 electronic configuration with the three doubly-occupied Ru d orbitals as frontier orbitals. Upon photoexcitation, one of the Ru d electrons is excited into a ligand π^* orbital, leading to a singlet metal-to-ligand charge transfer (^{1}MLCT) state. A follow-up ultrafast intersystem crossing (ISC) leads the system to a triplet MLCT (^{3}MLCT) state, which is usually long-lived (often with lifetimes of several μs[55]). The long lifetime of the ^{3}MLCT state allows the separated charge to be transferred onto an electron acceptor (A in Fig. 6b), which usually depends on the application of the complex: for example, the conducting band of a semiconductor for DSSCs or a hydrogen-generating catalytic site (or an oxygen molecule for a ROS generation reaction in PDT). The missing charge may then be replenished from an electron donor (D in Fig. 6b) to restart the process.

One of the grand challenges in the design of light harvesting complexes is to maximise the population transfer into the ^{3}MLCT state and to increase its lifetime to allow an efficient follow-up electron transfer. From the photophysical point of view, this strategy is equivalent to eliminating any competing photodeactivation pathways. Typical competing pathways which do not end

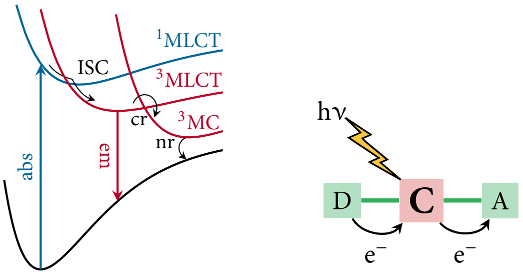

(a) (b)

Figure 6: (a) Schematic diagram of energies of the ground and important excited states in Ru polypyridyl complexes with important photophysical processes highlighted: absorption (abs), intersystem crossing (ISC), charge recombination via the ^{3}MC state (cr), emission (em) and nonradiative deactivation (nr). (b) Scheme of light-driven electron transport in a donor-complex-acceptor (D–C–A) setup, typical for many applications of Ru polypyridyl complexes.

up in electron transfer include deactivation via the metal-centered (^{3}MC) state, which implies charge recombination, or a nonradiative deactivation to the ground state (cf. Fig. 6a).

One design strategy to increase the ^{3}MLCT state lifetime is increasing the ^{3}MLCT–^{3}MC gap. Usually this is achieved by increasing the energy of the ^{3}MC state, e. g. by increasing the ligand field splitting of the *d* orbitals.[56] Lowering the ^{3}MLCT state has also successfully been employed,[57] although, as a side effect, it would also lower its energy difference to the ground state, increasing the probability for the fast radiationless ground state deactivation, potentially decreasing the ^{3}MLCT state lifetime. Another well-established strategy is the localisation of the separated charge close to the acceptor, which is optimally achieved already at the photoexcitation stage, thus avoiding additional charge transfer from another ligand: such design strategy has been termed *directional charge transfer* and has been successfully employed in increasing the efficiency of hydrogen-producing photocatalysts, as measured in terms of the *turnover number* (TON) i. e. the number of converted molecules per catalyst molecule.[58]

In this work, Ru polypyridyl complexes have been investigated with two purposes. First, $[\mathrm{Ru(bpy)_3}]^{2+}$ is used as a testbed for pushing ab-initio multiconfigurational calculations to their limits. Subsequently, we concentrate on the photochemical application of Ru polypyridyls: two computational studies illustrate the role of the ligand substituents in improving the photocatalytic and photosensing properties of complexes. The first study shows the role of the substituent in enabling directional charge transfer and avoiding charge recombination via the ^{3}MC state, while another study on a ruthenium polypyridyl hydrogen-producing photocatalyst demonstrates that the directional charge transfer paradigm need not be strictly followed to increase the turnover number (TON) of the catalyst.

2

THEORY

The present chapter will briefly cover the methods employed in this work to study the photophysics and photochemistry of transition metal complexes. Only an overview is provided here: for more details, the reader is referred to the books and reviews cited in the text. Section 2.1 introduces the Schrödinger equation and the Born-Oppenheimer approximation as the fundamental pillars in quantum chemistry. Quantum chemical methods, with an emphasis on describing electron correlation and methods for calculating the properties of excited electronic states, including multiconfigurational methods and time-dependent density functional theory, will be presented in Section 2.2. Transition metal complexes are typically large: thus, a special attention is paid to the recent approximations which overcome the steep scaling of the quantum chemical methods with the system size, such as the density matrix renormalisation group (DMRG, Section 2.2.4) and the density fitting and Cholesky decomposition techniques (Section 2.2.7). Section 2.3 covers relativistic effects, which are important for transition metals as heavy atoms, and an introduction into modelling of solvent effects, which are important for obtaining quantitative agreement with the experiment. Finally, Section 2.4 introduces approaches to model excited state dynamics, in particular a mixed quantum-classical molecular dynamics method – the surface-hopping.

2.1 SCHRÖDINGER EQUATION AND BORN-OPPENHEIMER APPROXIMATION

> *"Schrödinger's equation is the key to all*
> *Chemical systems, large or small."*
>
> —Michael Tschuggnall, "The Schrödinger's Equation Song"

In quantum mechanics, the time evolution of a system is described by the time-dependent Schrödinger equation (TDSE)

$$i\hbar \frac{\partial \Psi(\vec{x},t)}{\partial t} = \hat{H}\Psi(\vec{x},t) \tag{2.1.1}$$

where the *Hamiltonian* $\hat{H}$ represents the kinetic and potential energy of the system, and $\Psi(\vec{x},t)$ is the *wavefunction*, which encodes the state of the system at each given time t. The wavefunction itself does not bear any physical meaning, but its square $\Psi^*(\vec{x},t)\Psi(\vec{x},t)$ represents the probability distribution of particles in the system at the positions described by $\vec{x}$.

If the probability distribution is time-independent, the system is said to be found in a *stationary* state. The wavefunction can then be written as

$$\Psi(\vec{x},t) = \Psi(\vec{x}) \cdot e^{\frac{-E \cdot t}{\hbar}} \tag{2.1.2}$$

where $\Psi(\vec{x})$ is the time-independent wavefunction, which is an eigenfunction of the Hamiltonian $\hat{H}$, E is the corresponding eigenvalue, representing the total energy of the system. The eigenvalue equation of the Hamiltonian is called the time-independent Schrödinger equation (TISE):

$$\hat{H}\Psi(\vec{x}) = E \cdot \Psi(\vec{x}) \tag{2.1.3}$$

Let us consider a molecular system consisting of $\mathcal{N}$ electrons with positions $\vec{r}_i$, charge e, mass m_e and N nuclei with positions $\vec{R}_A$, nuclear charges $Z_A e$, and masses M_A. For such a system, the Hamiltonian consists of a sum of kinetic energy operators for each particle and potential energy operators resulting from the Coulombic interaction of the particles with each other:

$$\hat{H} = \hat{T}_{\mathrm{e}}(\vec{r}) + \hat{T}_{\mathrm{n}}(\vec{R}) + \hat{V}_{\mathrm{en}}(\vec{R},\vec{r}) + \hat{V}_{\mathrm{nn}}(\vec{R}) + \hat{V}_{\mathrm{ee}}(\vec{r}) \tag{2.1.4}$$

For convenience, all quantities will be expressed in atomic units in the following, i. e. m_e, $\hbar$ and e are set to 1, and M_A is expressed in units of m_e. The kinetic energy operators $\hat{T}_{\mathrm{e}}$ and $\hat{T}_{\mathrm{n}}$ for the electrons and nuclei respectively are expressed as

$$\hat{T}_{\mathrm{e}} = -\sum_{i=1}^{\mathcal{N}} \frac{1}{2}\nabla_i^2; \qquad \hat{T}_{\mathrm{n}} = -\sum_{A=1}^{N} \frac{1}{2M_A}\nabla_A^2 \tag{2.1.5}$$

and the potential energy operators, i. e. nuclear-electron attraction $\hat{V}_{\mathrm{en}}$, nuclear-nuclear repulsion $\hat{V}_{\mathrm{nn}}$ and electron-electron repulsion $\hat{V}_{\mathrm{ee}}$ as

$$\hat{V}_{\mathrm{en}} = -\sum_{i=1}^{\mathcal{N}} \sum_{A=1}^{N} \frac{Z_A}{r_{iA}}; \qquad \hat{V}_{\mathrm{nn}} = \sum_{A=1}^{N} \sum_{B>A}^{N} \frac{Z_A Z_B}{r_{AB}} \tag{2.1.6}$$

$$\hat{V}_{\mathrm{ee}} = \sum_{i=1}^{\mathcal{N}} \sum_{j>i}^{\mathcal{N}} \frac{1}{r_{ij}} \tag{2.1.7}$$

where the denominators represent the distance between the particles: $r_{ij} = |\vec{r}_i - \vec{r}_j|$, $r_{AB} = |\vec{R}_A - \vec{R}_B|$ and $r_{iA} = |\vec{R}_A - \vec{r}_i|$.

Employing the TISE 2.1.3 with the Hamiltonian 2.1.4 leads to a coupled multidimensional equation, which does not have an analytical solution for systems larger than two particles (e. g. the hydrogen atom). For larger atoms and molecules approximations must be made.

The first approximation which is usually made in quantum chemistry is the Born-Oppenheimer approximation.[59] It is based on the fact that the nuclei are about 10^3 times heavier than electrons and thus move much slower, allowing for separation of nuclear and electronic motion. The total wavefunction $\Psi(\vec{x}) = \Psi(\vec{R},\vec{r})$ can be written as a product of the electronic and nuclear part:

$$\Psi(\vec{r},\vec{R}) = \psi_{\mathrm{e}}(\vec{r},\bar{R}) \cdot \psi_{\mathrm{n}}(\vec{R}) \tag{2.1.8}$$

where $\bar{R}$ indicates the parametric dependence of the electronic wavefunction ψ_{e} on nuclear coordinates. It is thus possible to solve the electronic Schrödinger equation

$$\hat{H}_{\mathrm{e}}\psi_{\mathrm{e}} = E_{\mathrm{e}}\psi_{\mathrm{e}} \tag{2.1.9}$$

for a given set of nuclear coordinates $\bar{R}$ (a given molecular geometry), where the electronic Hamiltonian $\hat{H}_{\mathrm{e}}$ contains only the electron-nucleus and electron-electron interaction terms $\hat{T}_{\mathrm{e}}$, $\hat{V}_{\mathrm{en}}$ and $\hat{V}_{\mathrm{ee}}$. The total energy of the system is then just the sum of the electronic energy E_{e} and the nuclear repulsion energy V_{nn}, which can be calculated from Eq. 2.1.6.

We may solve the electronic Schrödinger equation for a sufficiently large set of molecular geometries, constructing a potential energy surface (PES). PES can be then employed to study molecular dynamics, which will be covered in Section 2.4. For now, we will focus on the solutions of the electronic Schrödinger equation, which constitutes the realm of quantum chemistry.

2.2 QUANTUM CHEMICAL METHODS

2.2.1 The Hartree-Fock Method

Even after the separation of the nuclear and electronic degrees of freedom, the electronic Schrödinger equation still contains the coupled motion of all electrons, and thus cannot be solved without further approximations. A reasonable approximation is expressing the many-electron wavefunction as a Slater determinant

$$\Psi(\vec{x}_1,\vec{x}_2,\dots,\vec{x}_n)=\frac{1}{\sqrt{n!}}\begin{vmatrix}\chi_1(\vec{x}_1) & \chi_1(\vec{x}_2) & \cdots & \chi_1(\vec{x}_n)\\ \chi_2(\vec{x}_1) & \chi_2(\vec{x}_2) & \cdots & \chi_2(\vec{x}_n)\\ \vdots & \vdots & \ddots & \vdots\\ \chi_n(\vec{x}_1) & \chi_n(\vec{x}_2) & \cdots & \chi_n(\vec{x}_n)\end{vmatrix} \tag{2.2.1}$$

which is essentially the product of one-electron wavefunctions (spin orbitals) $\chi_i(\vec{x}_i)$, antisymmetrised to satisfy the Pauli principle[60(p. 29)]. Applying the variational principle[60(p. 196)] to minimise the energy of the Slater determinant with respect to the spin orbitals yields the Hartree-Fock (HF) equations:[61]

$$\hat{f}_i\chi_v(\vec{x}_i)=\varepsilon_v\chi_v(\vec{x}_i) \tag{2.2.2}$$

where $\hat{f}_i$ is the *Fock operator* and ε_v are the *orbital energies*. The Fock operator is an effective one-electron operator of the form

$$\hat{f}_i=\hat{T}_{\mathrm{e},i}+\hat{V}_{\mathrm{en},i}+\hat{v}_i^{\mathrm{HF}} \tag{2.2.3}$$

where $T_{\mathrm{e},i}$ is the kinetic energy of the ith electron, $\hat{V}_{\mathrm{en},i}$ is the sum of the nuclear-electron attractions of the ith electron to all the nuclei (cf. Eqs. 2.1.5 and 2.1.6) and $\hat{v}_i^{\mathrm{HF}}$ is the average potential acting on the ith electron due to the presence of all the other electrons. The essence of the Hartree-Fock approximation is thus the decoupling of the electronic motion in single-particle Hartree-Fock equations by averaging out the electron-electron interactions. However, the Hartree-Fock equations are not entirely independent of each other: the average potential $\hat{v}_i^{\mathrm{HF}}$ depends on all spin orbitals, i. e. on the solution of all the HF equations. Thus, the Fock operator must be constructed and the HF equations must be solved iteratively until self-consistency (i. e. until the newly constructed Fock operator yields the orbitals which are the same as the ones used to construct it).

Following the variational principle, the total Hartree-Fock energy may be calculated as the expectation value of the Hamiltonian:

$$\begin{aligned}E_0^{\mathrm{HF}}&=\left\langle\Psi\middle|\hat{H}^{\mathrm{HF}}\middle|\Psi\right\rangle=\sum_{i=1}^{n}\left\langle\Psi\middle|\hat{T}_{\mathrm{e},i}+\hat{V}_{\mathrm{en},i}+\frac{1}{2}\hat{v}_i^{\mathrm{HF}}\middle|\Psi\right\rangle=\\ &\sum_{i=1}^{n}\varepsilon_i-\frac{1}{2}\sum_{i=1}^{n}\sum_{j=1}^{n}\left\langle\chi_i(\vec{r}_1)\chi_i(\vec{r}_1)\middle|\frac{1}{r_{12}}\middle|\chi_j(\vec{r}_2)\chi_j(\vec{r}_2)\right\rangle-\\ &\left\langle\chi_i(\vec{r}_1)\chi_j(\vec{r}_1)\middle|\frac{1}{r_{12}}\middle|\chi_i(\vec{r}_2)\chi_j(\vec{r}_2)\right\rangle\end{aligned} \tag{2.2.4}$$

where n denotes the number of occupied orbitals and we have introduced the bra-ket notation:

$$\left\langle\Psi\middle|\hat{A}\middle|\Psi\right\rangle=\int\Psi^*\hat{A}\Psi\,\mathrm{d}\vec{x}_1\dots\mathrm{d}\vec{x}_n. \tag{2.2.5}$$

Eqn. 2.2.4 is more commonly written in a short-hand (“chemists'”) notation:

$$E_0^{\mathrm{HF}}=\sum_{i=1}^{n}\varepsilon_i-\frac{1}{2}\sum_{i=1}^{n}\sum_{j=1}^{n}(ii|jj)-(ij|ji) \tag{2.2.6}$$

Here the *Coulomb integral* $(ii|jj)$ gives the average Coulombic repulsion between the electrons, and the *exchange integral* $(ij|ji)$ represents the *exchange* interaction, which arises due to the Pauli principle.

2.2.2 *Electron Correlation*

Although the Hartree-Fock approximation yields qualitatively good results for ground states of many molecules, it does not treat the electron correlation – dependence of the electron motion on the instantaneous positions of other electrons. Electron correlation can be classified[62–64] as *dynamic*, which keeps the electrons apart in the course of their motion and *static*, which requires more than one Slater determinant to describe the ground state wavefunction, and is present e. g. in dissociating molecules, excited states and many transition-metal compounds. If the static correlation is small, the Hartree-Fock approximation is qualitatively valid and constitutes a good starting point for *post-Hartree-Fock* or *single reference correlation* methods such as configuration interaction,[65(Ch. 4), 60(Ch. 10.10)] Møller-Plesset perturbation theory (MPx)[66] or the coupled-cluster method,[60(Ch. 10.14)] which allow for accurate calculation of energy and wavefunction corrections incorporating dynamic correlation. On the other hand, strong static correlation requires the presence of several Slater determinants in the wavefunction, and therefore the HF wavefunction is not a good approximation for the true wavefunction anymore. In such cases, multiconfigurational methods such as multiconfigurational self-consistent field (MCSCF) (cf. Section 2.2.3) must be used.

Characterisation of static correlation in a molecule is crucial because it allows identifying cases where multiconfigurational methods are necessary to describe the system. Traditionally, assessment of the multiconfigurational character of a wavefunction can be performed based on certain intrinsic values obtained from e. g. Møller-Plesset or coupled cluster calculations[67] or on occupation numbers of natural orbitals.[68] Recently, a new method to characterise static correlation based on quantum information theory has been developed in the groups of Noack and Reiher;[64,69,70] it has been applied in this work and will be explained in Section 2.2.5 in detail.

2.2.3 *Configuration Interaction and Multiconfigurational Self-Consistent Field*

The configuration interaction (CI) method is the conceptually simplest method to form a wavefunction based on multiple Slater determinants. Suppose, we use n_{orb} spin orbitals, of which n_{el} are occupied. In addition to the Hartree-Fock ground state Slater determinant $|\Psi_0\rangle$ (which can be referred to as the *reference determinant*), we may form a set of excited determinants, $\left|\Psi_{ab\ldots}^{rs\ldots}\right\rangle$, where electrons have been excited from occupied orbitals $a, b, \ldots$ to unoccupied orbitals $r, s, \ldots$ The CI wavefunction is then given as a linear combination of these determinants:

$$\begin{aligned} |\Phi_0\rangle = c_0\,|\Psi_0\rangle + \sum_{r} c_a^r\,|\Psi_a^r\rangle + \sum_{r<s} c_{ab}^{rs}\,\left|\Psi_{ab}^{rs}\right\rangle + \\ \sum_{r<s<t} c_{abc}^{rst}\,\left|\Psi_{abc}^{rst}\right\rangle + \sum_{r<s<t<u} c_{abcd}^{rstu}\,\left|\Psi_{abcd}^{rstu}\right\rangle + \ldots \end{aligned} \tag{2.2.7}$$

The Slater determinants are mutually orthogonal, and thus represent a suitable basis for an expansion of the exact wavefunction $|\Phi_0\rangle$. If all possible excitations are included in the CI expansion, it is called the *full CI* expansion and becomes an exact solution to the electronic TISE in the limit of $n_{\mathrm{orb}} \to \infty$.

Obtaining the CI wavefunction and energy is again a variational problem, and distils to constructing and finding the eigenvectors of the CI Hamiltonian matrix with matrix elements $\left\langle \Psi_0 \middle| \hat{H}^{\mathrm{HF}} \middle| \Psi_{ab\ldots}^{rs\ldots} \right\rangle$, which form the coefficients $c_{ab\ldots}^{rs\ldots}$. If the Hartree-Fock determinant is a good approximation, its coefficient will dominate the expansion: $c_0 \gg c_{ab\ldots}^{rs\ldots}$.

Unfortunately, employing the full CI expansion is impractical for all but the smallest systems. The size of the full CI expansion for a system with the total spin S is given by the Weyl formula[71(p. 234)]:

$$N_{\mathrm{FCI}} = \frac{2S+1}{n_{\mathrm{orb}}+1}\binom{n_{\mathrm{orb}}+1}{n_{\mathrm{el}}/2-S}\binom{n_{\mathrm{orb}}+1}{n_{\mathrm{el}}/2+S+1} \tag{2.2.8}$$

and thus grows factorially with the number of electrons and orbitals. In order to perform feasible CI calculations, the CI expansion needs to be truncated. Truncating the expansion at a certain level of excitations represents one possible approach. Most commonly, the expansion is usually truncated after the doubly-excited determinant resulting in the CI singles-doubles (CISD) method. CISD works well for obtaining dynamic correlation energy with single reference (Hartree-Fock) wavefunctions, since double excitations give the largest contributions to the dynamic correlation energy.[65(p. 236)]

On the other hand, describing static correlation needs a true multiconfigurational wavefunction, which, in addition to the optimisation of the CI coefficients $c_{ab\ldots}^{rs\ldots}$, requires also the orbitals χ_ν to be optimised: if more than one determinant dominates the expansion, orbitals optimised for only one of them might not be the best choice to describe the different electronic configuration reflected by the other dominant determinants. Such orbital optimisation combined with a (general) truncated CI expansion is called the *multiconfigurational self-consistent field* (MCSCF) method. For excited state calculations, instead of optimising the energy of one single state, one may optimise the weighted average of the energy of several (ground and excited) states, resulting in the *state-averaged* MCSCF (SA-MCSCF).

In MCSCF, a different approach to the CI truncation is more common. For instance, one can select an orbital subspace (the "active space") containing both occupied and virtual orbitals and perform a full CI expansion only in the active space. Such CI expansion is called the *complete active space* CI (CAS-CI) method, or, if the orbital optimisation is performed, the *Complete Active Space Self-Consistent Field* (CASSCF) method.[72] CASSCF provides the most complete description of the system within the active space, but it faces the same scaling problem as full CI when the active space has to be increased (cf. Eqn. 2.2.8). Presently, CASSCF is limited to active spaces of approximately 16 electrons in 16 orbitals. There have been several attempts to overcome this scaling problem. The first approach is, again, based on the truncation of the CI expansion. The restricted active space SCF (RASSCF) method[73] introduces two additional subspaces, RAS 1 and 3, where the maximum number of excitations from RAS 1 and to RAS 3 is restricted to a given number of electrons (RAS 2 is equivalent to CAS in CASSCF). The generalised active space (GAS)[74] concept takes this idea one step further and introduces an arbitrary number of subspaces. The partitioning of the three methods is schematically compared in Fig. 7.

Although restriction of the excitations in the RAS and GAS methods increases the usable size of the active space, it does so at the expense of neglecting certain Slater determinants and introducing additional complexity in partitioning the orbitals into multiple active spaces. density matrix renormalisation group (DMRG)[75,76] is a conceptually different algorithm, which constructs and optimises a CAS-CI-like wavefunction, but scales at a polynomial instead of factorial computational cost with the active space size without neglecting any of the Slater determinants. DMRG will be explained in more detail in Section 2.2.4.

Provided all important orbitals are present in the active space, MCSCF methods are able to describe static correlation properly. At this point it should be noted that the main problem of multiconfigurational methods and probably the most significant reason for the lack of their widespread adoption is not

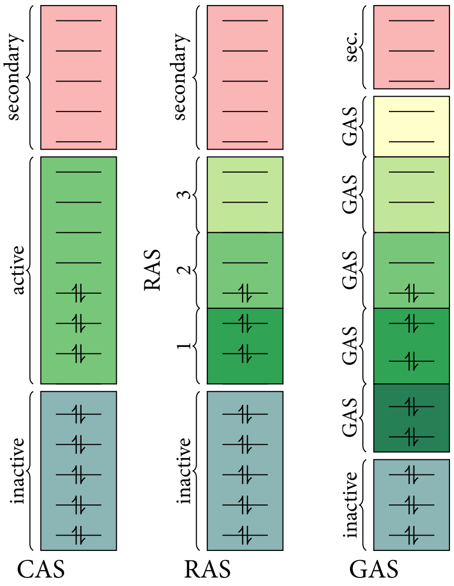

Figure 7: Illustration of orbital partitioning schemes for different MCSCF methods.

the prohibitive computational scaling, but the arbitrariness of the active space selection: the active orbitals must be selected carefully for each system and problem studied, based on the previous knowledge of the system, chemical intuition and previous user experience. For example, description of the static correlation in the ground state requires all orbitals contributing to the static correlation to be present in the active space.[64] Description of the bond breaking requires all of the orbitals participating in the bond.[70] With excited states the situation becomes even more complicated: the active space should comprise at least the orbitals participating in the excitations. Additionally, some so-called "correlating" orbitals may be required to capture the static correlation of the corresponding excited states: e. g. a π orbital for each π^* orbital. Interestingly enough, for 3d transition metal complexes an additional set of higher d shells is required in the active space, whereas for 4d metals such as Ru they are not mandatory.[77,78]

Once a MCSCF calculation has been performed, dynamic correlation can be accounted for, similarly to the single-reference wavefunction cases, with *multireference correlation* methods, such as perturbation theory (e. g. complete active space second order perturbation theory, CASPT2[79] or its multi-state variants[80,81]) or multireference CI.[82,83]

2.2.4 *Density Matrix Renormalisation Group*

The DMRG represents an alternative approach to the construction and optimisation of a full CI wavefunction. The first step in the DMRG ansatz is the representation of the full CI wavefunction (Eqn. 2.2.7) as the *matrix product state* (MPS):[84]

$$|\Phi_0\rangle = \sum_{\sigma} \mathbf{M}^{\sigma_1}\mathbf{M}^{\sigma_2}\cdots\mathbf{M}^{\sigma_L}|\sigma\rangle \tag{2.2.9}$$

where the product of matrices $\mathbf{M}^{\sigma_1}\cdots\mathbf{M}^{\sigma_L}$ represents the CI coefficient, and $|\sigma\rangle$ is the occupation number vector of the Slater determinant, which runs over all possible occupations of L orbitals. The vector space spanned by $|\sigma\rangle$ is a direct product of vector spaces spanned by the orbital occupation number vectors $|\sigma_n\rangle$:

$$|\sigma\rangle = \bigotimes_{n=1}^{L}|\sigma_n\rangle \tag{2.2.10}$$

Each $|\sigma_n\rangle$ thus represents four possible occupations of the (spatial) orbital n: doubly-occupied, spin-up, spin-down and empty. Each matrix $\mathbf{M}^{\sigma_n}$ operates only on one orbital, thus an MPS may be easily separated by the orbitals.

Exact representation of a full CI wavefunction constructed from L orbitals requires a 4^L-dimensional vector $|\sigma\rangle$ and matrices $\mathbf{M}^{\sigma_n}$. It still scales exponentially, so the MPS representation on its own does not solve the problem of the full CI scaling yet. However, the separability of the MPS is the key to the DMRG optimisation procedure, which constructs and optimises an approximation to the MPS with reduced dimensions of no more than $16m^2$, where m is a parameter which controls the accuracy of the approximation.

DMRG OPTIMISATION. At first, the active space is partitioned in the *system* and the *environment*, with two orbitals in between. The initial system size is chosen such that the dimension of the matrices (including the CI Hamiltonian) operating on the system does not exceed m. Then, the *superblock* Hamiltonian $\hat{H}_{\text{SB}}$ is constructed from the system and the environment, each augmented by one orbital in between. The dimension of $\hat{H}_{\text{SB}}$ then

$$\dim \hat{H}_{\text{SB}} = \dim \hat{H}_{\text{sys}} \cdot \dim \hat{H}_{\text{env}} \cdot 4 \cdot 4 = 16m^2 \tag{2.2.11}$$

i. e. the product of the dimension of the Hamiltonias of the augmented system and the augmented environment. Although the environment is usually larger than the system, the dimension of the enviromnent Hamiltonian may not exceed m, and so an approximate guess for $\hat{H}_{\text{env}}$ is necessary in the beginning. The superblock Hamiltonian is constructed and diagonalised, yielding the CI coefficients c_{ij}. From the CI coefficient, a *reduced density matrix* ρ^s with the dimension of $4m$ and matrix elements

$$\rho^s_{ii'} = \sum_{j\in\text{env}} c^*_{ij} c_{i'j} \tag{2.2.12}$$

is constructed by summing over the coefficients that belong to the augmented environment part of the Hamiltonian. Diagonalisation of ρ^s yields $4m$ eigenvectors, out of which m are used to construct a $m \times 4m$ transformation matrix $\mathbf{O}$, which reduces the dimensionality of the augmented system from $4m$ to m by a similarity transformation (Fig. 8). As a result, now the augmented system has the dimension m even after incorporating another orbital.

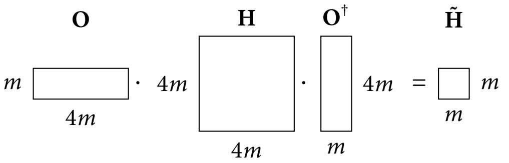

Figure 8: Illustration of the dimension reduction by a similarity transformation with matrix **O**.

Now the environment shrinks by one orbital, and the optimisation is repeated with the new system and environment until the environment consists only of one orbital. Such series of optimisations is called a *sweep*. Once the environment cannot shrink anymore, the sweep direction is reversed, and the environment and the system swap their roles. One DMRG iteration consists of a forward and a reverse sweep. The whole optimisation process is outlined in Fig. 9.

Unlike the truncated CI methods, DMRG has only one parameter m which controls the accuracy. m values of the order of magnitude 10^4, which are feasible on modern computers, are able to approximate the full CI wavefunction almost to numerical accuracy.[84] More details on the DMRG method and the MPS formalism can be found in Refs. 76,85,86.

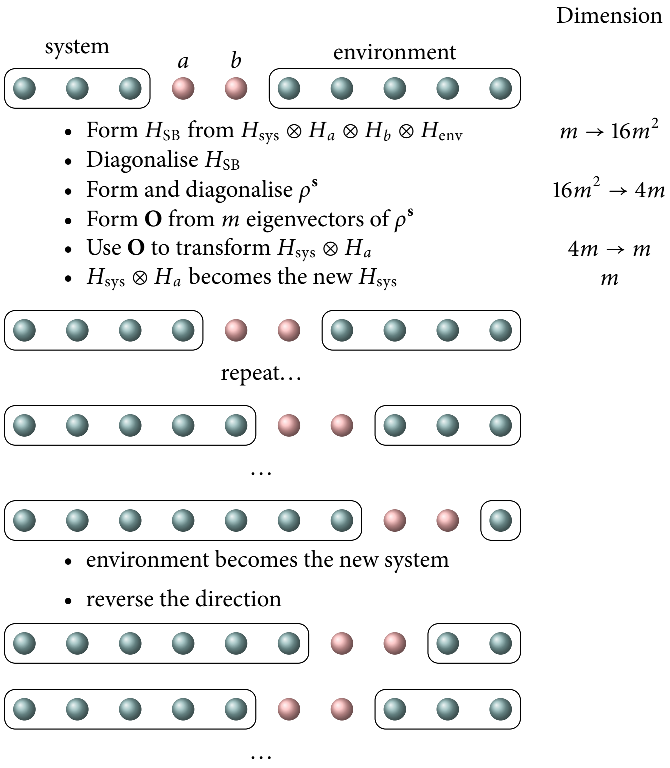
Dimension
system
a
b
environment
• Form H_{SB} from $H_{\mathrm{sys}} \otimes H_a \otimes H_b \otimes H_{\mathrm{env}}$
$m \rightarrow 16m^2$
• Diagonalise H_{SB}
• Form and diagonalise ρ^s
$16m^2 \rightarrow 4m$
• Form $\mathbf{O}$ from m eigenvectors of ρ^s
• Use $\mathbf{O}$ to transform $H_{\mathrm{sys}} \otimes H_a$
$4m \rightarrow m$
• $H_{\mathrm{sys}} \otimes H_a$ becomes the new H_{sys}
m
repeat…
…
• environment becomes the new system
• reverse the direction
…

Figure 9: Schematic view of the DMRG optimisation procedure.

2.2.5 *Orbital Entanglement Analysis*

The ability to separate the MPS wavefunction into contributions from single orbitals allows quantifying orbital interactions, which represent electron correlation.[69] This is achieved by calculating the *von Neumann entropy*, a concept from quantum information theory and *orbital entanglement*. Let us again separate a MPS (Eqn. 2.2.9) in system and environment, where the system consists only of one orbital i. The reduced density matrix for the system $\rho^{s,i}$ can then be constructed as in Eqn. 2.2.12 and diagonalised – its eigenvalues ω_α yield the expression for the *one-orbital von Neumann entropy* for the orbital i:

$$S_i = \sum_{\alpha} \omega_\alpha \log \omega_\alpha \tag{2.2.13}$$

A similar expression can be obtained for the *two-orbital entropy* S_{ij} by allowing the system to comprise two orbitals instead of one. Now one can define *orbital entanglement* for two orbitals i and j:

$$I_{ij} = \frac{1}{2}\left(S_i + S_j - S_{ij}\right)\left(1 - \delta_{ij}\right) \tag{2.2.14}$$

which is a means to quantify the interaction of orbitals i and j, as well as electron correlation.

2.2.6 *Density Functional Theory*

Density functional theory (DFT) constitutes an alternative approach to the wavefunction-based methods mentioned so far for describing the molecular electronic structure. Unlike the wavefunction-based methods, DFT considers the electron density $\rho(x, y, z)$ as its basic variable, and operates with *functionals*, i. e. functions of functions. For instance, the total energy of the system $E[\rho]$ is expressed as the functional of the density.

Hohenberg and Kohn[87(p. 33)] formulated the two theorems fundamental for DFT. The first theorem states that all properties of the system are uniquely represented by the ground state density, establishing the equivalence of the electron density and the wavefunction representations. The second theorem states that $E[\rho]$ yields the lowest energy with the true ground state density ρ_0, allowing us to apply the variational principle to calculate the ground state density and energy.

Similar to the wavefunction theories, the total energy functional in DFT can be split into several contributions:

$$E[\rho] = T[\rho] + V_{\text{en}}[\rho] + J[\rho] + E_{\text{xc}}[\rho] \tag{2.2.15}$$

where $T[\rho]$ represents the kinetic energy of the electrons, $V_{\text{en}}[\rho]$ – the nuclear-electron attraction, $J[\rho]$ the Coulombic attraction of the electrons and the $E_{\text{xc}}[\rho]$ is the *exchange-correlation energy*, which considers the exchange interaction as well as electron correlation. In practice, exact expressions for neither $T[\rho]$ nor $E_{\text{xc}}[\rho]$ do not exist. An approximation for $T[\rho]$ is most commonly obtained in the *Kohn-Sham formalism*.[88] Here, the concept of a wavefunction is re-introduced as a wavefunction of non-interacting electrons, but with the same electron density ρ_{KS} as the real density ρ:

$$\rho_{\text{KS}} = \sum_i \chi_i^* \chi_i = \rho \tag{2.2.16}$$

Since the electrons are non-interacting, it is natural to formulate this Kohn-Sham wavefunction as a Slater determinant (Eqn. 2.2.1), and the total kinetic energy of the Kohn-Sham wavefunction can be calculated from Eqn. 2.1.5:

$$T_{\text{KS}}[\rho] = \sum_{i=1}^{n} \left\langle \chi_i \middle| -\frac{1}{2}\nabla_i^2 \middle| \chi_i \right\rangle \tag{2.2.17}$$

Combining the variational principle with the Kohn-Sham scheme results in *Kohn-Sham equations*, which are similar to Hartree-Fock equations (Eqn. 2.2.2), but with the Fock operator defined as

$$\hat{f}_i = \hat{T}_{\text{e},i} + \hat{V}_{\text{en},i} + \hat{J}_i + \hat{v}_i^{\text{xc}} \tag{2.2.18}$$

where the first two terms are analogous to their Hartree-Fock counterparts (cf. Eqn. 2.2.3) and $\hat{J}_i$ and $\hat{v}_i^{\text{xc}}$ are the contributions from the Coulombic attraction and the exchange-correlation interactions, respectively. (The differences between the exact and the Kohn-Sham kinetic energy is also incorporated into $\hat{v}_i^{\text{xc}}$.)

Similarly to the HF equations, the Kohn-Sham equations are solved self-consistently and yield expressions for the ground state energy and other properties. The main difference to Hartree-Fock is that Kohn-Sham equations do employ electron correlation, and, if an exact expression for $\hat{v}^{\text{xc}}$ (or $E_{\text{xc}}[\rho]$) was known, they would yield an exact ground state energy of the system. In practice, approximate expressions for E_{xc} are constructed: a large number of approximate exchange-correlation functionals has been published so far, with different suitability for various applications and chemical problems. Most commonly, improvement of the functionals is achieved by increasing the number of variables on which the functional depends. This is equivalent to climbing the “Jacob’s ladder of density functionals”.[89] Yet, climbing the Jacob’s ladder does not imply systematic improvement of the functionals, but only enables the creation of new, often heavily parametrised functionals to address new chemical problems.

The similarity of the Kohn-Sham equations to the Hartree-Fock equations enables Kohn-Sham DFT to treat electron correlation at a similar computational cost and scaling as Hartree-Fock, i. e. in general better than traditional post-Hartree-Fock methods. The favourable scaling and the simplicity for the end user (it is a black-box method unlike of the multiconfigurational methods, although the user has to select a suitable functional) have contributed to the very widespread usage of DFT for many systems, especially for larger molecules such as transition metal complexes with extensive ligands.[90] However, DFT is not without drawbacks. In addition to the large number of existing exchange-correlation functionals and lack of the systematic improvement, DFT employs one Slater determinant due to the Kohn-Sham formalism, and, as a consequence, does not handle static correlation well. Additionally, DFT shows the so-called *delocalisation* or *self-interaction error*[91,92] and cannot handle well long-range interactions such as London dispersion interactions, but empirical dispersion corrections such as the D3 correction from Grimme[93] or dispersion-corrected functionals such as ωB97xD from M. Head-Gordon's group[94] have addressed this problem.

DFT AND EXCITED STATES. Although DFT is a ground-state only theory, it allows the calculation of excited state energies and properties to some extent. This is possible when the excited state of interest has a different spatial or spin symmetry and is the ground state in the respective symmetry. Energy differences from such calculations are called ΔSCF energies and provide good estimation of e. g. singlet-triplet energy gaps.[90,95] In this work, in addition to calculating singlet-triplet gaps (including calculation of emission wavelengths) the ΔSCF method has been used to calculate adiabatic energy gaps between two triplet states at their respective minima.

If the desired excited states are not accessible by the ΔSCF method, one can employ the time-dependent DFT (TD-DFT).[96,97] The idea of TD-DFT is based on the solution of the time-dependent Schrödinger equation 2.1.1 with a Hamiltonian including a time-dependent perturbation of an electric field. Using the linear response theory, instead of explicitly solving the TDSE, one can obtain the *density response function*:[98]

$$\begin{aligned}\Xi(\vec{r},\vec{r}',\omega) = \lim_{\eta\to 0}\sum_k\Bigg(&\frac{\langle\Psi_0|\rho(\vec{r})|\Psi_k\rangle\langle\Psi_k|\rho(\vec{r}')|\Psi_0\rangle}{\omega-(E_k-E_0)+i\eta}- \\ &\frac{\langle\Psi_0|\rho(\vec{r}')|\Psi_k\rangle\langle\Psi_k|\rho(\vec{r})|\Psi_0\rangle}{\omega+(E_k-E_0)+i\eta}\Bigg)\end{aligned} \tag{2.2.19}$$

where Ψ_0 and Ψ_k are ground and excited states respectively and ω is the oscillation frequency of the field. The density response function has its poles when the denominator becomes zero, i. e. when ω becomes the excitation energy: $E_k - E_0 = \omega$. From the numerator one can calculate the transition dipole moments $\langle\Psi_k\,|\,\mu\,|\,\Psi_0\rangle$, which determine the transition intensity, or oscillator strength f:

$$f = \frac{2}{3}\,\langle\Psi_k\,|\,\mu\,|\,\Psi_0\rangle^2\cdot(E_k-E_0) \tag{2.2.20}$$

Due to a more favourable computational scaling than the ab-initio methods, TD-DFT is widely employed and has been remarkably successful in calculating excited state properties in many systems.[90,95,98,99] However, the success of TD-DFT is not universal, and is plagued by the drawbacks of the ground-state DFT, and additionally the inability to describe double excitations, as well as the poor estimation of excitation energies of Rydberg and charge transfer excitations.[96,100] The latter problem has been partially addressed by the development of long-range corrected functionals,[101] but also with mixed success.

2.2.7 *Density Fitting and Cholesky Decomposition*

Two-electron integrals, such as the Coulomb and exchange integrals in Eqn. 2.2.6 depend on the product of four basis functions χ_i (hence they are often referred to as four-centre integrals). Their calculation thus scales as the fourth power of the number of χ_i, and, therefore, quickly becomes a bottleneck for large-scale ab-initio and DFT calculations. Hence, approaches to reduce this scaling have been devised. The *Density fitting* or *resolution-of-identity* (RI) approach, which dates back to the 1973 papers of Whitten and Baerends[102] considers the expansion of two-electron integrals in an *auxiliary basis set*. Consider, for example, a generalised form of Coulomb and exchange integrals $(ij|kl)$ in spatial orbitals ϕ_i:

$$\begin{aligned}(ij|kl) = \int \phi_i^*(\vec{r}_1)\phi_j(\vec{r}_1)\frac{1}{r_{12}}\phi_k^*(\vec{r}_2)\phi_l(\vec{r}_2)\,\mathrm{d}\vec{r}_1\,\mathrm{d}\vec{r}_2 \\ = \int \rho_{ij}\frac{1}{r_{12}}\rho_{kl}(\vec{r}_2)\,\mathrm{d}\vec{r}_1\,\mathrm{d}\vec{r}_2\end{aligned} \tag{2.2.21}$$

which may be represented as a repulsion between two electron densities $\rho_{ij}(\vec{r}_1) = \phi_i^*(\vec{r}_1)\phi_j(\vec{r}_1)$ and $\rho_{kl}(\vec{r}_2) = \phi_k^*(\vec{r}_2)\phi_l(\vec{r}_2)$.[103] The densities may be expanded in an auxiliary basis set $\bar{\phi}_P$:

$$\rho_{ij}(\vec{r}) \approx \sum_P d_P^{ij}\bar{\phi}_P(\vec{r}) \tag{2.2.22}$$

where the coefficients d_P^{ij} are determined by fitting, i. e. a minimisation of the error between the real and expanded density or the corresponding two-electron integrals. Combining equations 2.2.21 and 2.2.22, the approximated two-electron integral may be recast in the following form[103]:

$$\begin{aligned}(ij|kl) &\approx \sum_P\sum_Q d_P^{ij}d_Q^{kl}\int \bar{\phi}_P(\vec{r}_1)\frac{1}{r_{12}}\bar{\phi}_Q(\vec{r}_2)\,\mathrm{d}\vec{r}_1\,\mathrm{d}\vec{r}_2 \\ &= \sum_P\sum_Q (ij|P)\mathbf{J}_{PQ}^{-1}(Q|kl)\end{aligned} \tag{2.2.23}$$

where

$$(ij|P) = \int \phi_i^*(\vec{r}_1)\phi_j(\vec{r}_1)\frac{1}{r_{12}}\bar{\phi}_P(\vec{r}_1)\,\mathrm{d}\vec{r}_1\,\mathrm{d}\vec{r}_2$$

and

$$\mathbf{J}_{PQ} = \int \bar{\phi}_P(\vec{r}_1)\frac{1}{r_{12}}\bar{\phi}_Q(\vec{r}_2)\,\mathrm{d}\vec{r}_1\,\mathrm{d}\vec{r}_2$$

thus instead of calculating two-electron (four-centre) integrals, one may calculate three-centre integrals of the form $(ij|P)$, which scales as the third power of the number of basis functions.

In the conventional density fitting approach, as implemented in the majority of the quantum chemical codes, the auxiliary basis sets are optimised for different methods and catalogued in libraries. A slightly different approach first proposed by Beebe and Linderberg[104] and popularised by Pedersen et al.[105] is based on the approximate representation of two-electrons integrals by vectors obtained from the Cholesky decomposition of the two electron integrals if represented as a matrix:

$$(ij|kl) \approx \sum_{K=1}^{J} L_{ij}^{K} L_{kl}^{K} \tag{2.2.24}$$

where L_{ij}^{K} are the elements of the *Cholesky vectors* obtained from the intermediate iterations of the Cholesky decomposition of the two-electron integral matrix. Due to the iterative nature of the Cholesky decomposition, the number of the Cholesky vectors J can be easily chosen such that the maximum error of the decomposition does not exceed a certain pre-defined threshold, allowing an easy control of the accuracy. Pedersen et al.[105] have also shown that the Cholesky vectors can be related to the density fitting coefficients (cf. Eqn. 2.2.22), thus providing equivalence between Cholesky decomposition and density fitting procedures. However, Cholesky decomposition provides an advantage over conventional density fitting in the sense that it does not require a catalogued auxiliary basis set, but allows construction of the optimum auxiliary basis set on the fly.

For calculations on large molecules such as transition metal complexes the usage of two-electron integral approximations such as density fitting or Cholesky decomposition has become inevitable.

2.3 ADDITIONAL CORRECTIONS

2.3.1 *Relativistic effects*

The Schrödinger equation is nonrelativistic, and thus does not account for relativistic effects, which become important in chemistry and physics of heavy atoms such starting with 3*d* transition metals and beyond. Thus, incorporation of relativistic effects becomes mandatory for accurate calculations on ruthenium complexes. The most accurate relativistic methods based on Dirac equation and four-component wavefunctions are currently feasible for small molecules only,[106] but more computationally feasible approximations employing two or one-component wavefunctions have been devised. The two-component approximations most used today, namely the Zeroth Order Regular Approximations (ZORA)[107] or the second-order Douglas-Kroll-Hess (DKH) transformation[108] provide the accuracy needed for most chemical applications.

Relativistic effects can be divided into spin-independent *scalar relativistic effects* (e. g. relativistic orbital expansion and contraction) and the *spin-orbit couplings* (SOCs), which arise due to the interaction of the spin with the angular momentum, formulated in the relativistic Hamiltonians. Calculations involving only scalar relativistic effects can also be performed in a non-relativistic framework without extra computational cost employing the *effective core potentials* (ECPs)[109] which replace the core shells of a heavy atom. Calculation of spin-orbit couplings requires relativistic calculations: it is available e. g. for multiconfigurational wavefunctions[110] or TD-DFT.[111]

2.3.2 *Solvent Effects*

Since the majority of experiments performed on transition metal complexes are performed in solution, accurate reproduction of experimental data with the theoretical methods require modelling of solvent effects. Interactions of the solute with the solvent may be classified into bulk effects, arising from the interaction of a solute molecule with the bulk solvent, such as electrostatic interaction, i. e. interactions of the solute charges with the solvent charge distribution, and molecular effects, arising from interaction of a solute molecule with single solvent molecules, such as the formation of hydrogen bonds with solvent molecules. In many cases the description of the bulk effects is sufficient, and the solvent may be modelled by the so-called *continuum models* such as PCM[112] or COSMO,[113] where a solute molecule is placed into a cavity embedded into a solvent continuum with a given dielectric constant: such description is able to recover bulk electrostatic effects and is computationally inexpensive at the same time.

In case of explicit solvent-solute molecular interactions bulk effects are not sufficient anymore, and explicit solvent molecules must be present in the description of the system. If only a few solvent molecules are important, these may be treated at the same level of theory as the solute. For large amount of solvent molecules this becomes computationally expensive, and the bulk solvent is represented either as continuum model or explicitly, but with interactions described by classical molecular mechanics. The latter approach is called quantum mechanics/molecular mechanics (QM/MM) approach.[114]

2.4 DYNAMICS

Section 2.2 covered different approaches to the solution of the electronic Schrödinger equation, while the nuclear motion, which allows us to perform molecular dynamics and thus describe time-dependent phenomena has remained untouched so far. This gap is going to be filled in this section. In dealing with time-dependent phenomena, non-stationary states are present and thus a full time-dependent Schrödinger equation 2.1.1 must be solved. For a time-independent Hamiltonian (e. g. in the absence of external fields), the TDSE is usually solved by propagation in discrete time steps Δt:

$$\Psi(\vec{x}, t + \Delta t) = \exp\left(-\frac{\mathrm{i}}{\hbar}\hat{H}\Delta t\right)\Psi(\vec{x}, t) \tag{2.4.1}$$

If we want to describe photodynamical processes, which occur in excited electronic states, we must involve these states in the description of the time-dependent wavefunction. Therefore, it may be expressed as a linear combination of the stationary states, which are obtained as the solutions of the electronic Schrödinger equation employing the Born-Oppenheimer approximation:

$$\Psi(\vec{x}, t) = \sum_i c_i(t)\Psi_i(\vec{x}) \tag{2.4.2}$$

so that the propagation of the wavefunction is reduced to the propagation of the coefficients $c_i(t)$. The Born-Oppenheimer approximation does not hold when several $\Psi_i(\vec{x})$ become close in energy: in those cases, the *nonadiabatic couplings* (NACs) between the states become important (see below).

Direct solution of Eq. 2.4.1, i. e. the quantum mechanical propagation of the nuclear wavefunction is performed in *quantum dynamics*.[115] Since quantum mechanics is non-local, it requires the pre-computation of the PES of the $\Psi_i(\vec{x})$ in all $3N - 6$ nuclear vibrational degrees of freedom prior to the propagation, which is feasible only for small molecules with $N <= 4$. For larger molecules, only a subset of nuclear degrees can be considered, which does not describe the system fully.

SURFACE HOPPING DYNAMICS. If one wishes to treat larger molecules in all degrees of freedom, one needs to drop the requirement of non-locality of the quantum dynamics. This is achieved when the nuclei are propagated according to the classical Newtonian equation of motion on potential surfaces created by the electrons:

$$M_A \frac{\mathrm{d}^2 \vec{R}_A(t)}{\mathrm{d}t^2} = \vec{F}_A = -\nabla_A E_\mathrm{e}\left(\vec{R}(t)\right) \tag{2.4.3}$$

The force $\vec{F}_A$ which acts on the nucleus A depends only on the current position of all nuclei, therefore the electronic energy and its gradient has to be calculated only at the current position of the nuclei each time step. In *surface hopping dynamics*,[116] the nuclei are propagated classically on the PES of one state. The electronic wavefunction is propagated according to[117]

$$\frac{\mathrm{d}c_i(t)}{\mathrm{d}t} = -\frac{\mathrm{i}}{\hbar} c_i(t) E_i(t) - \sum_{j=1}^{N_\mathrm{s}} c_j(t) \sigma_{ij}(t) \tag{2.4.4}$$

where $E_i(t)$ is the energy of the state where the nuclei are propagated (equivalent to $E_\mathrm{e}(\vec{R}(t))$ in Eqn. 2.4.3) and $\sigma_{ij}(t)$ are the NACs, which account for the non-Born-Oppenheimer behaviour of the electronic states as they become closer in energy. Usually, NACs are derived from the derivatives of the electronic wavefunction with respect to the nuclear coordinates, or, alternatively, from the overlaps of the electronic wavefunctions at different timesteps:[117,118]

$$\sigma_{ij}(t) \approx \frac{1}{2\Delta t}\left(\left\langle \Psi_i\left(t-\frac{\Delta t}{2}\right) \middle| \Psi_j\left(t+\frac{\Delta t}{2}\right)\right\rangle - \left\langle \Psi_i\left(t+\frac{\Delta t}{2}\right) \middle| \Psi_j\left(t-\frac{\Delta t}{2}\right)\right\rangle\right) \tag{2.4.5}$$

At each time step, there is a certain probability of switching (*hopping*) to another state, which in general depends on the electronic wavefunction and the NACs. Usually an algorithm devised by Tully[119] is employed, which minimises the number of state switches. To counter the stochastic effects of the probabilistic hopping, and, to a certain extent, to simulate the distribution of a wavepacket obtained in quantum dynamics, surface hopping dynamics is usually performed with a set of independent trajectories.

SURFACE HOPPING DYNAMICS AND SOC. The standard surface hopping formulation in Eqn. 2.4.4 only allows for coupling of states with NACs; thus other couplings such as spin-orbit couplings, which are relevant for states of different spin multiplicities, cannot be included easily. A simple scheme for estimating the hopping probability between two states of different multiplicities employing the Landau-Zener formula has been employed e. g. by Merchán et al.[120] and also in this work:

$$P^\mathrm{ISC} = 1 - \exp\left(-\frac{\pi}{4}\xi\right); \qquad \xi = \frac{8(H^\mathrm{SO})^2}{\vec{g}_a \cdot \vec{v}_a}. \tag{2.4.6}$$

where H^SO is the spin-orbit coupling and $\vec{g}_a \cdot \vec{v}_a$ is the dot product of the gradient difference vector for the two states and the velocity vector at the hopping geometry.

A more general propagation scheme, which allows for incorporation of different types of couplings on the same footing (which, in addition to nonadiabatic and spin-orbit couplings, also includes coupling by electric fields) has been developed recently in the González group,[121] however its application to transition metal complexes is currently still under development.

3

RUTHENIUM NITROSYL COMPLEXES

This chapter presents the results of the studies on ruthenium nitrosyls. Section 3.1 describes a series of ground state studies of a nitrosyl complex abbreviated RuHIndNO (see below), namely a study of its cis-trans isomerisation mechanism and a multiconfigurational study of the electronic structure of the ground and first excited triplet state, investigating electron correlation and the NO ligand non-innocence in the Ru–NO bond. Section 3.2 covers the photochemical studies of excited state properties of Ru nitrosyls aimed at unravelling of their NO photodissociation mechanism. First, a quantum chemical and surface hopping dynamics study investigates the NO photodissociation mechanism of a Ru nitrosyl complex, which is known to release NO upon exposure to UV light. Next, we investigate the excited state picture in another ruthenium nitrosyl complex featuring a dye coordinated *trans* to the NO ligand, which has been used to tune its absorption wavelength. Sections 3.1 and 3.2.1 will present summaries of the respective published articles, which will be reprinted at the end of this chapter.

3.1 GROUND STATE STUDIES ON RUHINDNO

Trans-[RuCl$_4$(NO)(1H-indazole)]$^-$ (RuHIndNO, Fig. 10a) is a potential intermediate in the mechanism of action of KP1019,[5] (Fig. 10b) a promising anti-cancer drug candidate. RuHIndNO itself has been shown to suppress the growth of human cancer cell lines, along with its *cis* isomer.[122] During the synthesis of KP1019, a *cis*↔*trans* isomerisation of RuHIndNO has been observed, which called for theoretical investigation. The mechanism of this isomerisation reaction has been studied in a joint theoretical and experimental collaboration with the groups of Profs. Vladimir B. Arion (University of Vienna) and Dominique Luneau (University of Lyon 1). This study is presented in Section 3.1.1.

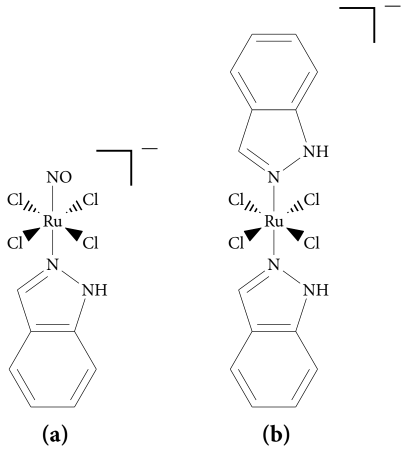

Figure 10: RuHIndNO (a) and the anion of its precursor KP1019 (b).

Due to the non-innocent nature of the nitrosyl ligand, our interest in this complex went beyond the mechanistic study and called for additional investigations of the electronic structure of the Ru–NO bond, which we carry out in Section 3.1.2. First, we perform geometry optimisations of the RuHIndNO conformers with a linear and a bent NO coordination (corresponding to the ground and the lowest triplet states of RuHIndNO respectively) and calculations of the energy gap with multiconfigurational methods and compare these values with values obtained from DFT calculations. This work has been performed in a collaboration with the groups around Prof. Dr. Roland Lindh (Uppsala University) and Prof. Dr. Thomas Bondo Pedersen (University of Oslo), who developed a novel implementation of the CASSCF gradient calculation using Cholesky decomposition which was employed in this study. Subsequently, we use a multiconfigurational wavefunction expressed in terms of localised orbitals and orbital entanglement analysis based on a multiconfigurational DMRG wavefunction to analyse the electronic structure and characterise static and dynamic correlation in the Ru coordination sphere, as well as to assign oxidation states to the metal and the NO ligand. The orbital entanglement analysis has been performed in collaboration with the group of Prof. Dr. Markus Reiher (ETH Zurich), where the code for DMRG and orbital entanglement analysis has been developed.

3.1.1 *Mechanism elucidation of the cis-trans isomerisation*

The synthesis of RuHIndNO yielded both *cis* and *trans* isomers with the *cis* isomer prevailing, despite the expectation to obtain predominantly the *trans* isomer due to the *trans* effect of the NO ligand.[123] A ^{1}H NMR study confirmed the experimental occurrence of the isomerisation. Given the difference in the growth-suppressive activities on cancer cell lines by the *cis* and *trans* isomer,[122] the study of the isomerisation mechanism allows for further insight into the mode of action of these complexes, as well as better stereoselectivity control during the synthesis.

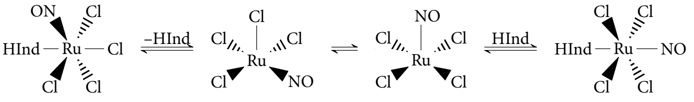

(a) Dissociative mechanism

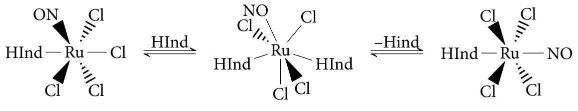

(b) Associative mechanism

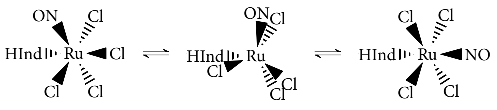

(c) Twist mechanism

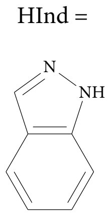

Figure 11: The three isomerisation mechanisms considered in this study.

Three different mechanisms were considered in this study (Fig. 11). The dissociative mechanism (Fig. 11a) is initiated by the detachment of one of the indazole ligands, resulting in a pentacoordinated ruthenium transition state allowing for the migration of one of the chloride ligands to a coordination site occupied formerly by the indazole ligand. The reattachment of the indazole at another coordination site completes the process. The associative mechanism (Fig. 11b) starts with an attachment of a second indazole ligand to form a heptacoordinated transition state, followed by the dissociation of the other indazole ligand from another coordination site which forms the second isomer. The twist mechanism (Fig. 11c) does not change the bonds in the Ru coordination sphere: rather, the octahedral coordination sphere is rotated around the metal centre via the trigonal prismatic transition state.

Geometry optimisations using DFT were employed to locate transition states and intermediates present in each mechanism. DFT calculations using the accurate B2GP-PLYP double-hybrid functional[124] showed that the dissociative mechanism shows the lowest activation barrier, followed by associative and twist mechanisms. The calculated activation barrier for the dissociative mechanism showed a very good agreement with the experimental activation enthalpy obtained from fitting the experimental population rates to the Eyring equation.

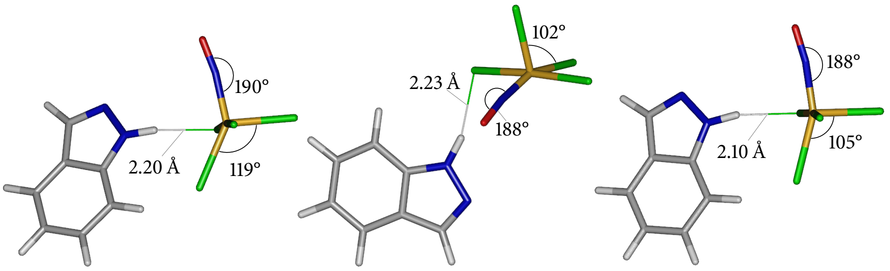

(a) **(b)** **(c)**

Figure 12: Transition state ((a)) and the additional transition state (b) and an intermediate (c) formed upon dissociation of the indazole from the *cis* isomer. Analogous compounds for (b) and (c) for the *trans* isomers can be found in Appendix 3.A.1.

A remarkable feature of the dissociative mechanism is that the indazole ligand does not detach completely, but, rather remains loosely attached to the complex via a H–Cl hydrogen bond (Fig. 12a) and forms an additional transition state (Fig. 12b) and a local minimum (Fig. 12c) with a pentacoordinated Ru, starting from both *cis* and *trans* isomers. The pentacoordinated transition states and intermediates are more stable than the transition states with higher coordination numbers, e. g. the hexacoordinated (albeit distorted) twist transition state or the heptacoordinated associative one. Noteworthy, the twist transition state can easily expulse an indazole ligand at only slightly larger Ru–indazole distances leading to a pentacoordinated ruthenium.

All structures shown in Fig. 12 show a slight bending of the Ru–N–O angle. The bending is attributed to the NO non-innocence, i. e. the ability of NO to partially donate another electron pair to the Ru after the indazole ligand has dissociated, and may contribute to the stabilisation of the pentacoordinated transition states and intermediates of the complex.

This study has been published in an article titled *"Mechanism Elucidation of the cis-trans Isomerization of an Azole Ruthenium–Nitrosyl Complex and Its Osmium Counterpart"* in *Inorganic Chemistry, 52, p. 6260*, which will be reprinted at the end of this chapter.

3.1.2 *Multiconfigurational studies of the electronic structure*

The non-innocent nature of the NO ligand motivated a further study of the electronic structure of RuHIndNO employing multiconfigurational methods. First, geometry optimisations of the ground (S_0) and the lowest triplet state (T_1) of RuHIndNO were performed with the CASSCF method, and the obtained geometries were compared to those optimised with BP86,[125,126] B3LYP[126,127] and M06L[128] DFT functionals. The CASSCF geometry optimisation employed the newly-developed implementation of CASSCF gradients employing Cholesky decomposition developed in the groups of Profs. Lindh and Pedersen.

The main difference between the S_0 and T_1 geometries (Fig. 13) is the coordination mode of the NO ligand: NO coordinates linearly in S_0, yielding a Ru–N–O angle (denoted ϕ in Fig. 13) of almost 180°, but bends in T_1, decreasing ϕ to 138°. The S_0 geometry is very similar among CASSCF and all DFT functionals, and also agrees very well with the X-ray structure. On the other hand, the T_1 geometries show a discrepancy in the relative positioning of the NO (i. e. the dihedral angle $\theta_{\mathrm{Cl_2-Ru-N_1-O_1}}$ in Fig. 13) and the indazole ligand (the di-

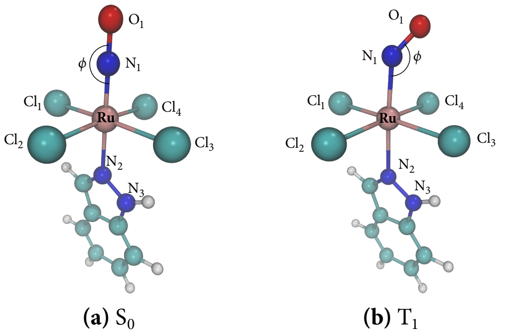

Figure 13: CASSCF optimised geometries for S_0 and T_1 states of RuHIndNO.

hedral angle $\theta_{Cl_3-Ru-N_2-N_3}$) to the remaining coordination sphere. CASSCF does not encompass dynamic correlation correctly, whereas DFT lacks proper description of static correlation, therefore the similarity of the S_0 geometries calculated with CASSCF and DFT is very encouraging.

The calculation of energy differences between different spin states is a common procedure in assessing the accuracy of different methods for transition metal complexes,[129–132] as spin-state energetics plays an important role in their reactivity. Thus, we compared singlet-triplet energy gaps calculated with CASPT2 and DFT functionals mentioned above at both S_0 and T_1 geometries. At S_0 geometries, CASPT2 and all tested DFT functionals yield similar singlet-triplet energy gaps, but the discrepancies grow for the T_1 geometry, reflecting the differences in the T_1 geometries calculated with different methods. Therefore, for both geometries and singlet-triplet energy gaps, in the ground state we obtain similar results with multiconfigurational methods and DFT functionals, whereas for the T_1 state we see larger differences, not only between multiconfigurational methods and DFT, but also between different DFT functionals.

A CASSCF wavefunction transformed to the basis of localised orbitals was employed to analyse the electronic structure of the Ru coordination sphere and in particular of the Ru–NO bond. The CASSCF active space was chosen to include the most important orbitals contributing to the bonds in Ru coordination sphere, and comprised 16 electrons in 13 orbitals in total (Fig. 14a). Upon localisation, the orbitals transformed to five Ru 4*d* orbitals, two pairs of NO π and π^* orbitals, one pair of indazole π and π^* orbitals, one combination of *p* orbitals on the Cl atoms (denoted σ_{Cl}) as well as the NO σ orbital (Fig. 14b). The localised orbital basis allows each individual configuration from the multiconfigurational CASSCF wavefunction to be given a well-defined occupation number in terms of localised orbitals, such as e. g. d^5 or NO^+ configurations. Calculation of the overall contribution of certain classes of configurations (e. g. d^5 or d^6) allows assigning oxidation states to the ruthenium centre and to the NO ligand, thus providing a means to resolve the oxidation state ambiguity in $\{RuNO\}^6$ nitrosyls. For both S_0 and T_1 states of RuHIndNO, despite different geometries and a different electronic state, the wavefunctions show approximately equal contributions of Ru d^5 and d^6 configurations which leads to the Ru oxidation state of approximately 2.5. As for the NO configurations, NO^0 is a predominant configuration, whereas NO^+ and NO^- bear roughly the same contribution and cancel out the net charge of the NO: thus, the NO ligand may be considered neutral. In the T_1 state, compared to the S_0 state, the NO^0 and NO^- character is increasing at the expense of NO^+ character, giving NO a partially negative charge. A similar analysis has been performed previously by Radoń et al.[29] for a series of Fe nitrosyls, yet the authors considered the joint metal and NO orbital occupation instead of distinguishing between the

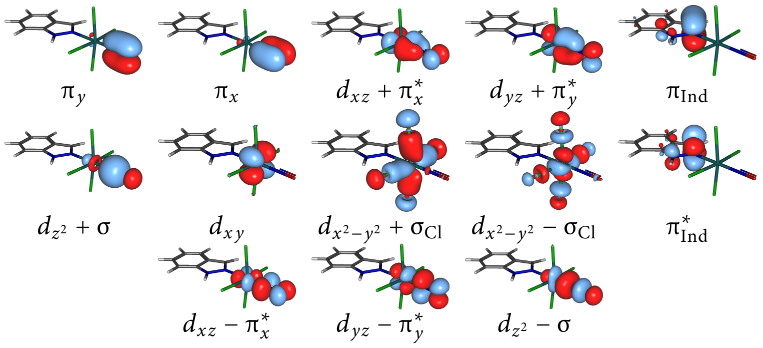

(a) Natural orbitals

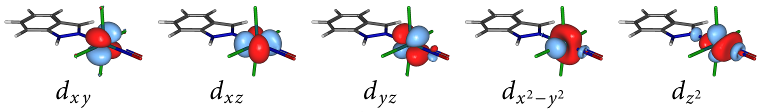

Ru *d* orbitals

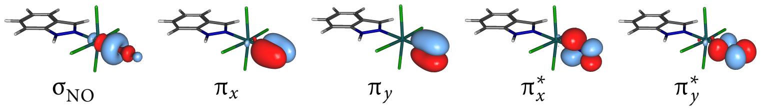

NO orbitals

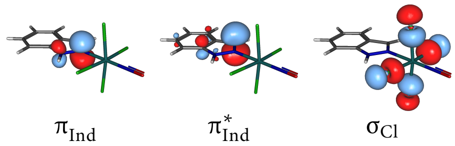

Indazole and Cl orbitals

(b) Localised orbitals

Figure 14: Natural (a) and localised (b) orbitals from the (16,13) active space employed in CASSCF calculations in RuHIndNO.

metal and NO, describing the structures merely as a superposition of $\mathrm{Fe^{III}(NO)^-}$ and $\mathrm{Fe^{II}(NO)^\circ}$ configurations. In line with these results, we report that also in RuHIndNO both $\mathrm{Ru^{II}(NO)^+}$ and $\mathrm{Ru^{III}(NO)^\circ}$ configurations are present in the S_0 and T_1 wavefunctions, although the $\mathrm{Ru^{II}(NO)^\circ}$ configuration (with a missing electron on one of the other ligands) is more prominent than $\mathrm{Ru^{II}(NO)^+}$, especially in the T_1 state.

Although CASSCF calculations show one dominant configuration (in the basis of natural orbitals, see Fig. 14a) with the weight over 77% for both S_0 and T_1 states of RuHIndNO, one finds non-negligible contributions of other configurations, particularly excitations involving orbital participating in the Ru–NO π bond ($(d_{xz} + \pi_x^*) \rightarrow (d_{xz} - \pi_x^*)$ and $(d_{yz} + \pi_y^*) \rightarrow (d_{yz} - \pi_y^*)$ excitations). These excitations contribute to the mixed covalent-ionic character of the Ru–NO bond and to the multiconfigurational character of the wavefunction. Noteworthy, a similar situation was found in $[\mathrm{Ru(PaPy_3)(NO)}]^{2+}$, which is discussed in Section 3.2.1. To further explore the multiconfigurational character of the RuHIndNO wavefunction and to characterise the static and dynamic correlation present in the Ru–NO bond, a DMRG calculation followed by an orbital entanglement analysis was performed. The important role of the orbitals participating in the Ru–NO π bond (i. e. $(d_{xz} \pm \pi_x^*)$ and $(d_{yz} \pm \pi_y^*)$ linear combinations) in static correlation is confirmed by their large single-orbital entropy and strong entanglement among each other. In contrast, the correlation present in other orbitals is primarily dynamic. Thus, the entanglement analysis reveals that the electron correlation present in the Ru–NO σ bond and other Ru–ligand bonds is predominantly dynamic, whereas the Ru–NO π bond shows static correlation and requires a multiconfigurational treatment for accurate results.

Another orbital entanglement analysis was employed to assess the importance of additional orbitals for the active space, in particular of the importance of another orbital pair for the Ru–NO bond and the so-called double-shell effect known to be important in $3d$ transition metals.[78] The previous (16,13) active space was extended by five additional orbitals: another $d_{z^2} \pm \sigma^*_{\mathrm{NO}}$ pair, potentially contributing to the Ru–NO σ bond, and three Ru $5d$ ("double-shell") orbitals, resulting in an extended active space of 18 electrons in 18 orbitals. The resulting active space was beyond reach for a conventional CASSCF calculation, thus the calculation was performed with DMRG. The entanglement picture of the larger active space is almost identical to that of the smaller one, with the additional orbitals playing a negligible role in correlation effects. Thus, the double d shell effect can be neglected in RuHIndNO.

Given the multiconfigurational character and the presence of static correlation in the RuHIndNO ground state wavefunction, it seems puzzling how the geometry and singlet-triplet energy gap calculated with DFT and multiconfigurational methods give results close to each other. One possible answer is given by the work of Cremer[133] which states that DFT is able to recover some static correlation effects, although in an unsystematic and unspecified manner, which "does not necessarily guarantee an improved description for a specific multireference system". The discrepancies between results S_0 and T_1 states in RuHIndNO (and also discrepancies in the results for various DFT functionals for the latter) provide an example of such unsystematicity. Notably, the unsystematic behaviour of various DFT functionals in TM nitrosyl systems has been demonstrated earlier, e. g. in studies comparing spin densities by Radoń and Pierloot[28] or by Boguslawski et al.[134], and is well-known in TM compounds beyond nitrosyls.[130] Although DFT errors in TM chemistry may be alleviated by an appropriate parametrisation of DFT functionals, in particular altering the amount of exact exchange,[129] an optimum functional parametrisation for the description of static correlation in one class of compounds is rarely transferable to another class of compounds.[130] The present study is another demonstration of the fact, that while DFT is able to perform successfully in many systems with significant static correlation (which is good news for computational chemistry of large transition metal complexes), multiconfigurational methods should be preferred to study such systems. In cases where DFT usage is unavoidable due to the high computational cost of the multiconfigurational methods, the latter could provide results for tuning DFT functionals to obtain better results.

The study summarised in this section has been published in two papers which will be reprinted at the end of this chapter: the part including geometry optimisations and the singlet-triplet energy gap calculations has been published jointly with the CASSCF analytic gradient formalism employed in the present study and developed in the groups of Profs. Lindh and Pedersen. The article is titled *"Analytical gradients of complete active space self-consistent field energies using Cholesky decomposition: Geometry optimization and spin-state energetics of a ruthenium nitrosyl complex"* and appeared in the *Journal of Chemical Physics, 140, p. 174103*. The part including the CASSCF localised orbitals study, DMRG calculations and entanglement analyses has been published in an article titled "Orbital entanglement and CASSCF analysis of the Ru–NO bond in a Ruthenium nitrosyl complex" as a part of the "Theoretical chemistry developments: from electronic structure to simulations" themed collection in *Physical Chemistry Chemical Physics, 17, p. 14383*.

3.2 EXCITED STATE STUDIES OF NO PHOTORELEASING RUTHENIUM NITROSYLS

3.2.1 *Photodissociation mechanism in a NO photoreleasing complex*

$[Ru(PaPy_3)(NO)]^{2+}$ (Fig. 15a) belongs to the group of metal nitrosyls complexated by a polypyridyl chelate ligand $PaPy_3H$ (N,N-bis(2-pyridylmethyl)amine-N-ethyl-2-pyridine-2-carboxamide, Fig. 15b), which have been synthesised by Mascharak and co-workers.[15,16,18] These nitrosyls release NO upon irradiation with UV or visible light and have been employed in NO delivery to different biological targets.[18,21]

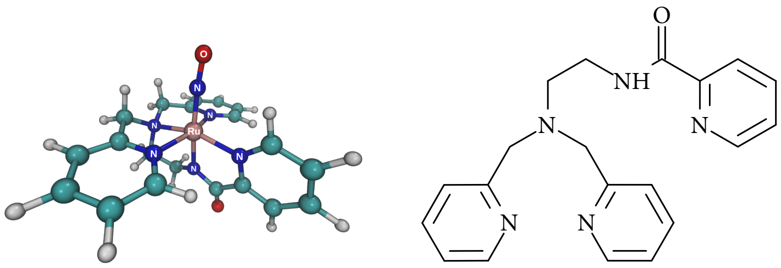

(a) $[Ru(PaPy_3)(NO)]^{2+}$ **(b)** $PaPy_3H$

Figure 15: Structure of $[Ru(PaPy_3)(NO)]^{2+}$ and of the $PaPy_3H$ ligand.

In this study we employ TD-DFT and accurate multiconfigurational spin-corrected calculations as well as surface-hopping dynamics to obtain insights into the NO photodissociation mechanism in $[Ru(PaPy_3)(NO)]^{2+}$. First, we calculate the UV-vis absorption spectrum of $[Ru(PaPy_3)(NO)]^{2+}$ and characterise its low-lying excited singlet and triplet states. Although previous studies on metal nitrosyls[27,38,39] showed satisfactory agreement of the TD-DFT absorption spectra with the experimental ones, we opted for the usage of the more accurate multiconfigurational CASPT2 method for the description of the excited states. Due to a relatively large size of $[Ru(PaPy_3)(NO)]^{2+}$, these calculations became computationally feasible only with the advent of Cholesky decomposition-based density fitting. We also perform TD-DFT calculations with the BP86 functional for comparison, and investigate the solvent effect on the excited state description by performing all calculations both in gas phase and including an implicit solvent model.

CASPT2 predicts two bright states, S_2 and S_4 at the lower end of the absorption spectrum (Fig. 16). S_4 is the brightest state, and is a MLCT transition from a Ru–NO bonding orbital into the corresponding antibonding orbital, with some admixture of a ligand to ligand charge transfer (LLCT) transition from the n orbital at the amide group located trans to the NO ligand (cf. Fig. 16b). The second brightest state is the S_2 state, which is a pure MLCT transition from another Ru d orbital to a Ru–NO π^* antibonding orbital. The character of both of these states indicates their possible dissociative nature, hinting at the possibility of NO dissociation from these states. Also the dark states lying in the vicinity of these bright states show a similar state character.

The spectrum calculated with CASPT2 agrees well with the experimental spectrum (cf. Fig. 16a). The inclusion of the solvent induces a slight blue-shift of the peaks, which shifts the brightest S_4 peak closer to the experimental value, and the introduction of the spin-orbit coupling has a negligible effect on the overall shape of the spectrum. The TD-DFT calculation employing the BP86 functional, are able to reproduce the essential features of the absorption spectrum, i. e. the character of the majority of the low-lying states and the relative position of the brightest state. However, a quantitative agreement is

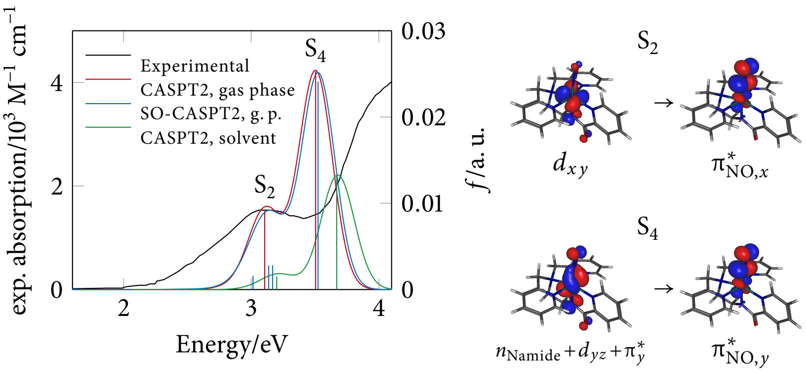

(a) (b)

Figure 16: Experimental and theoretical absorption spectrum (calculated with CASPT2) of $[Ru(PaPy_3)(NO)]^{2+}$ (a) and the characters of its bright excited states (b).

not achieved: BP86 expectedly[100] systematically underestimates the excitation energies of the low-lying excited states by up to 1 eV due to their charge transfer character.

Although already the dissociative character of the low-lying bright states (Fig. 16b) hints at a "direct" NO photodissociation mechanism,[39] in which the dissociative states are populated directly after excitation, we sought to obtain a more detailed insight into the photodissociation mechanism with a surface hopping molecular dynamics study. Surface hopping dynamics requires a recalculation of electronic energy and gradients at every time step, and hence the usage of a multiconfigurational method in the dynamics would not be possible despite the computational cost reduction introduced by Cholesky decomposition-based density fitting. Given that TD-DFT with the BP86 functional is able to reproduce the essential features of the absorption spectrum at a small fraction of the cost of the multiconfigurational CASPT2/CASSCF calculation, it was employed in the dynamics study.

The dynamics simulations show that after being excited into the bright S_4 state, already in the first 10 fs, a large fraction of the trajectories undergoes intersystem crossing (ISC) to one of the neighbouring triplet states, which also have a MLCT dissociative character. Such ultrafast ISC is in line with experimental findings in other transition metal complexes, where ultrafast ISC timescales, in some cases even less than 30 fs, have been measured.[49–51,135,136] Additionally, in the first 30 fs we observe a rapid Ru–NO bond extension in the majority of the trajectories occurring both in singlet and triplet states, which corresponds to the beginning of the NO dissociation. This time scale is not enough for the most trajectories to relax to the lowest excited state, although the relaxation to the S_1 or T_1 state is not much slower and occurs to a large extent within 100 fs, accompanied by NO bending. Thus, NO is dissociating from the higher excited states, in which the mechanism (Fig. 17) resembles the "direct" mechanism postulated earlier:[38,39] however, the dissociation is not confined to one particular state but rather occurs from a manifold of singlet and triplet states of a similar MLCT dissociative character populated by fast internal conversion and intersystem crossing. Given the very efficient ISC, the dissociation from triplet states is more probable.

The Ru–NO bond extension (and in some cases the NO bend) is accompanied by a rise of the multiconfigurational character of the ground state and by lowering the first excited state, leading to a degeneracy of the ground state with either the S_1 or T_1 state. Unfortunately, DFT and TD-DFT cannot handle such situations, leading to crashes of many trajectories shortly after around 30–50 fs. Nevertheless, the relevant processes for the NO photodissociation (ISC,

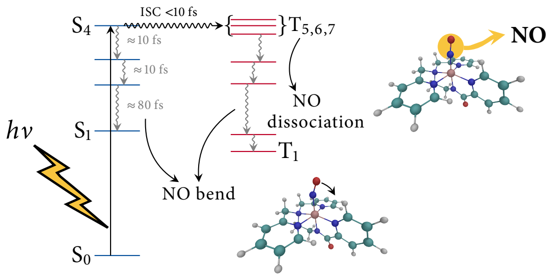

Figure 17: Photodissociation mechanism in $[Ru(PaPy_3)(NO)]^{2+}$.

internal conversion, initiation of the NO photodissociation and NO bending) have been observed within this timescale so that the mechanism shown in Fig. 17 described above can be postulated despite the very short duration of the simulations.

This study has been published as an article titled "Theoretical Spectroscopy and Photodynamics of a Ruthenium Nitrosyl Complex" in *Inorganic Chemistry, 53, p. 6415* as part of the *Insights into Spectroscopy and Reactivity from Electronic Structure Theory* forum and will be reprinted at the end of the chapter.

3.2.2 *Insights into dye-mediated NO photodissociation*

Tuning the absorption wavelength in NO photoreleasing complexes towards visible light bears advantages for PDT: visible light has a larger penetration depth and is less harmful for surrounding tissues than UV light. In a quest for a Ru nitrosyl which releases NO under visible light, Rose et al.[19] attempted a new strategy for tuning the absorption wavelength of NO releasing complexes by coordinating a dye to a Ru centre. As a dye, resorufin (Fig. 18a) with an absorption maximum of 600 nm was chosen, resulting in the **R1** complex (Fig. 18b). The tuning was successful: experimental UV-vis absorption spectrum of **R1** shows an absorption maximum of 500 nm, compared to the peaks of 387 and 310 nm in the spectrum of $[Ru(PaPy_3)(NO)]^{2+}$. This section presents a computational investigation on the influence of the dye ligand on the Ru nitrosyl photochemistry by calculating the absorption spectrum and characterising

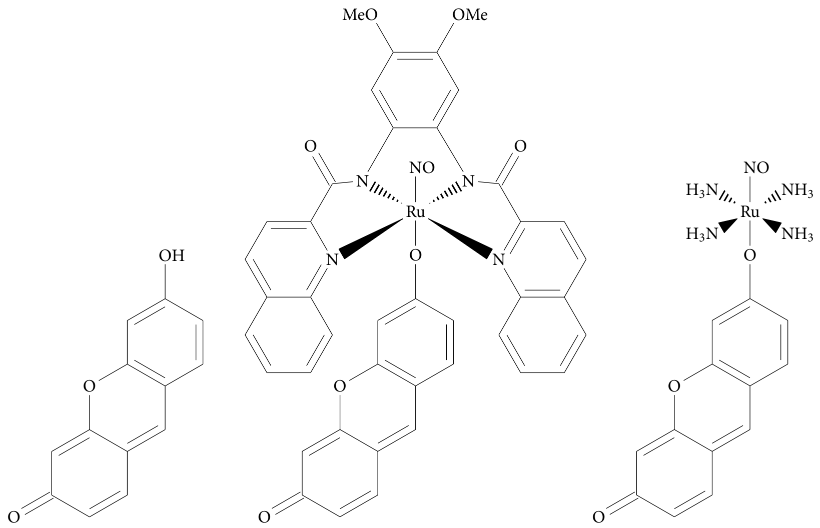

(a) Resorufin **(b) R1** **(c) R2**

Figure 18: (a): Resorufin, the dye employed for the photosensitisation of the NO complex, (b): complex prepared by Rose et al.[19], (c): a simplified complex used in this study.

the lowest excited states of **R2**, (Fig. 18c) a simplified model of **R1** with the equatorial ligand replaced by ammonia. The equatorial ligand is not expected to have a qualitative impact on the photochemistry of **R1**. Indeed, a previous experimental investigation on **R1** homologa[137] showed that the absorption maximum of the complex remains at 500 nm despite the variation of the equatorial ligand.

Computational Details

Similarly to the $[\mathrm{Ru(PaPy_3)(NO)}]^{2+}$ complex, the geometry optimisation was performed with DFT followed by a multiconfigurational calculation of several lowest-lying singlet excited states. For the geometry optimisation, which was performed with the Gaussian 09 D.01 program package,[138] the B3LYP functional and the def2-TZVPP[139] basis set, with a relativistic ECP for Ru have been employed. For the absorption spectrum, single-point CASSCF/CASPT2 calculations have been performed with the MOLCAS 8.0[140] program package. As the basis set, the ANO-RCC all-electron basis set[141] of a triple-zeta quality (VTZP) has been employed for Ru, and double-zeta (VDZP) for the remaining atoms. ANO-RCC is an all-electron basis set, so no ECPs were employed: relativistic effects were recovered with the second-order DKH Hamiltonian. For computational savings, the Cholesky-decomposition based density fitting has been used.

The active space selection (cf. Fig. 19) was motivated by a compromise between an adequate and balanced description of the Ru coordination sphere in the ground and excited states of interest and the computational feasibility. Similarly to other Ru complexes, the active space includes five Ru 4*d* orbitals, two π, π^* pairs for NO and further two linear combinations of σ orbitals centered at the nitrogen atoms coordinated to the metal, which interact with $d_{x^2-y^2}$ and d_{z^2} orbitals (the so-called *d* correlating orbitals, referred to as $\sigma_{\mathrm{NH_3}}$ and σ_{NO} in Fig. 19) for an adequate description of the latter *d* orbitals. The d_{z^2} orbital with its correlating orbital constitute the Ru–NO σ bond. Only one π orbital located the dye ligand was incorporated: its corresponding π^* counterpart was exchanged by another orbital in the active space upon CASSCF optimisation, and a CASSCF calculation with an additional dye π, π^* pair (at the expense of the NO π, π^* pair to keep the active space size manageable) did not show any low-lying excited state where this pair would be involved, so it was not included in the final active space. In total, the active space comprises 16 electrons in 12 orbitals. Twelve lowest singlet states were calculated in the state-averaged CASSCF calculation, followed by a multi-state CASPT2 calculation[80] for all states, where an IPEA shift[142] of 0.25 a. u. and a level shift[143] of 0.3 a. u. has been employed. Neither a solvent model nor spin-orbit coupling calculations were used since highly accurate excitation energies are not required to investigate the influence of the substituent on the photochemistry of the complex.

Results

Table 1 characterises several lowest singlet states in **R2**, calculated with MS-CASPT2. The two bright states, S_1 and S_7, may be assigned to the peaks of the experimental absorption spectrum in **R1**. The excitation energy of S_1 deviates by 0.69 eV from the experimental peak of **R1**. However, this is not surprising given that **R1** has an additional equatorial ligand and the solvent effects have not been considered in the calculations. Otherwise, the agreement between the peaks is remarkably good: the S_7 excitation energy and the relative intensities of the S_1 and the S_7 peaks match very well (Fig. 20).

One immediately notices several changes when comparing the lowest singlet excited states of **R2** with those of $[\mathrm{Ru(PaPy_3)(NO)}]^{2+}$. The most prominent

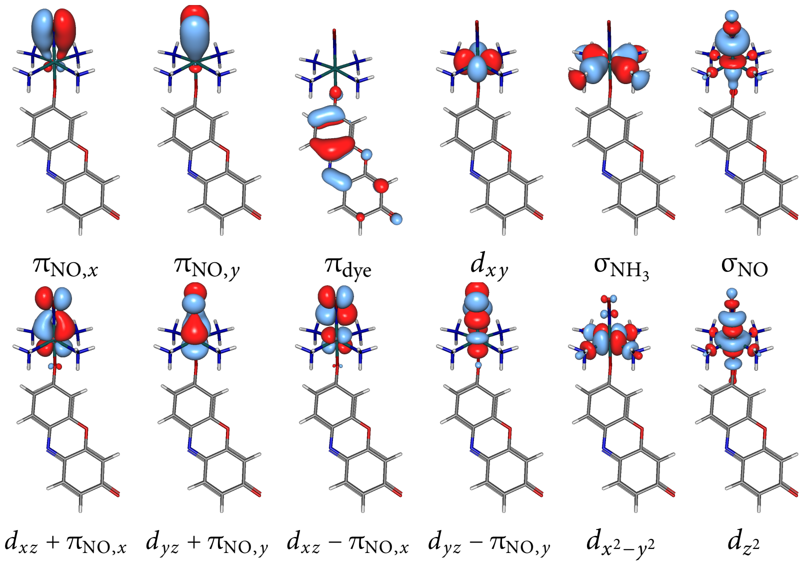

Figure 19: Active space used in the CASSCF calculation of **R2**.

St.	ΔE	Character	f	exp. ΔE
S_1	1.79	$\pi_{\mathrm{dye}} \rightarrow d_{xz} - \pi_{\mathrm{NO},x}$	0.486	2.48
S_2	1.83	$\pi_{\mathrm{dye}} \rightarrow d_{yz} - \pi_{\mathrm{NO},y}$	0.001	
S_3	2.22	$\pi_{\mathrm{dye}} \rightarrow d_{x^2-y^2}$	0.000	
S_4	2.61	$\pi_{\mathrm{dye}} \rightarrow d_{x^2-y^2}$	0.015	
S_5	2.73	$d_{xz,yz} + \pi_{\mathrm{NO},x,y} \rightarrow d_{xz,yz} - \pi_{\mathrm{NO},x,y}$	0.000	
S_6	3.02	$d_{xy} \rightarrow d_{xz} + \pi_{\mathrm{NO},x}$	0.019	
S_7	3.08	$\pi_{\mathrm{dye}} \rightarrow d_{z^2}$	0.234	3.10
S_8	3.34	$d_{xy} \rightarrow d_{xz} + \pi_{\mathrm{NO},x}$	0.003	
S_9	3.41	$d \rightarrow d$ and $d \rightarrow d - \pi_{\mathrm{NO}}$ mix	0.000	
S_{10}	4.08	$d_{xz,yz} + \pi_{\mathrm{NO},x,y} \rightarrow d_{xz,yz} - \pi_{\mathrm{NO},x,y}$	0.000	
S_{11}	4.24	double excitation mix	0.000	

Table 1: MS-CASPT2 excitation energies in eV, state characters and oscillator strengths for the lowest single excited states of **R2**. Bright states are highlighted in green. The last column shows absorption maxima (also in eV) of the experimental absorption spectrum[19] of **R1**, assigned to the corresponding bright states of **R2**.

change is the participation of the dye π orbital in the lower excited states, which completely changes the character of the states which are populated upon photo-excitation. Although the S_1 state is an excitation into a Ru–NO π^* antibonding orbital ($d_{xz} - \pi_{\mathrm{NO},x}$) with an NO dissociative nature as in $[\mathrm{Ru(PaPy_3)(NO)}]^{2+}$, the state has now a LLCT character. MLCT states such as the bright states found in $[\mathrm{Ru(PaPy_3)(NO)}]^{2+}$ are also present, but as dark states and at higher excitation energies (e. g. S_5 or S_8). Thus, MLCT states do not play a primary role in the excitation process anymore, in contrast to $[\mathrm{Ru(PaPy_3)(NO)}]^{2+}$. Interestingly enough, it is only the dye π orbital which participates in the transition, and not its π^* counterpart, which is exchanged by other orbitals during the CASSCF optimisation. No intra-ligand $\pi \rightarrow \pi^*$ transitions on the dye were observed among the calculated states, although experimentally the uncoordinated dye is reported to have an absorption maximum at 600 nm (2.06 eV) assigned to the $\pi \rightarrow \pi^*$ transitions,[19] i. e. below the absorption maximum of the **R1** complex. This is in contrast to previous DFT calculations on **R1** homologa,[144] claiming that the dye $\pi \rightarrow \pi^*$ transition is retained in the complex as the brightest transition, and a subsequent energy transfer process leads to the NO dissociation. According to our results, the NO dissociation would be facilitated by the new low-lying LLCT excitation from the resorufin π orbital into the Ru–NO antibonding orbital instead.

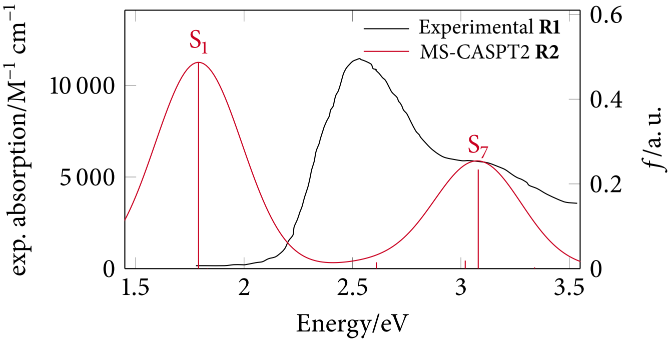

Figure 20: Stick and convoluted calculated spectrum of **R2** and experimental absorption spectrum of **R1**, obtained from Ref. 19.

In addition to S_1, **R2** shows another absorption maximum, the S_7 state, which is another excitation from the dye π orbital, but this time into a d_{z^2} orbital. Although the d_{z^2} orbital shows some admixture of the NO σ orbital and therefore could be technically described as a Ru–NO σ^* antibonding orbital, the majority of the electron density is located on the metal (cf. Fig. 19), and thus the S_7 state is unlikely to be dissociative. A NO dissociation mechanism involving excitation into the S_7 state would require an internal conversion to one of the lower-lying MLCT or LLCT NO dissociative states, and/or an intersystem crossing into their triplet analoga. Thus, in **R2** a combined NO dissociation mechanism is possible: the "direct" pathway[38,39] by populating the S_1 state, and the "indirect" pathway[38] via internal conversion to other singlets. Although triplet states and intersystem crossing were not considered in this study, given the intersystem crossing efficiency of $[Ru(PaPy_3)(NO)]^{2+}$ it is very likely that both of these mechanisms wold be accompanied by a similarly efficient ISC and dissociation from triplet states.

APPENDIX 3.A ATTACHED PAPERS

APPENDIX 3.A.1

Mechanism Elucidation of the cis-trans Isomerization of an Azole Ruthenium–Nitrosyl Complex and Its Osmium Counterpart

Anatolie Gavriluta, Gabriel E. Büchel, Leon Freitag, Ghenadie Novitchi, Jean Bernard Tommasino, Erwann Jeanneau, Paul-Steffen Kuhn, Leticia González, Vladimir B. Arion, and Dominique Luneau

Inorg. Chem., **2013**, 52, 6260–6272.
`http://dx.doi.org/10.1021/ic4004824`

Contributions:

ANATOLIE GAVRILUTA, GABRIEL E. BÜCHEL, GHENADIE NOVITCHI, JEAN BERNARD TOMMASINO, ERWANN JEANNEAU, PAUL-STEFFEN KUHN, VLADIMIR B. ARION, AND DOMINIQUE LUNEAU conceived the idea, performed the synthesis, characterisation, the NMR kinetics and electrochemical study and wrote parts of the manuscript.

LEON FREITAG performed DFT calculations and wrote parts of the manuscript.

LETICIA GONZÁLEZ planned and supervised the DFT calculations and was involved in the preparation of the final manuscript.

Reprinted with permission from Inorg. Chem., **2013**, 52, 6260–6272.
Copyright 2013, American Chemical Society.

Inorganic Chemistry
Article
pubs.acs.org/IC
Terms of Use

Mechanism Elucidation of the *cis*−*trans* Isomerization of an Azole Ruthenium−Nitrosyl Complex and Its Osmium Counterpart

Anatolie Gavriluta,[†,‡] Gabriel E. Büchel,[†,‡] Leon Freitag,[§] Ghenadie Novitchi,*[,†,∥]
Jean Bernard Tommasino,[†] Erwann Jeanneau,[†] Paul-Steffen Kuhn,[‡] Leticia González,*[,§]
Vladimir B. Arion,*[,‡] and Dominique Luneau*[,†]

[†]Université Claude Bernard Lyon 1, Laboratoire des Multimatériaux et Interfaces (UMR 5615), Campus de la Doua, 69622 Villeurbanne Cedex, France

[‡]University of Vienna, Institute of Inorganic Chemistry, Währinger Strasse 42, A-1090 Vienna, Austria

[§]University of Vienna, Institute of Theoretical Chemistry, Währinger Strasse 17, A-1090 Vienna, Austria

[∥]Laboratoire National des Champs Magnétiques Intenses-CNRS, Université Joseph Fourier, 25 Avenue des Martyrs, 38042 Grenoble Cedex 9, France

Ⓢ *Supporting Information*

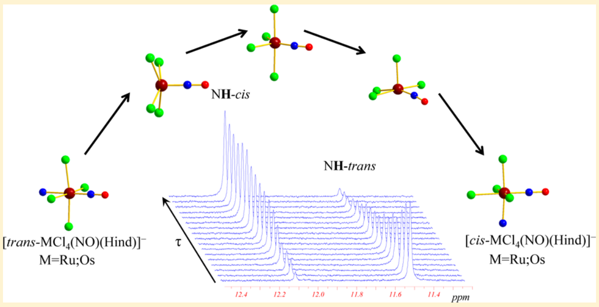

ABSTRACT: Synthesis and X-ray diffraction structures of *cis* and *trans* isomers of ruthenium and osmium metal complexes of general formulas (nBu$_4$N)[*cis*-MCl$_4$(NO)(Hind)], where M = Ru (**1**) and Os (**3**), and (nBu$_4$N)[*trans*-MCl$_4$(NO)(Hind)], where M = Ru (**2**) and Os (**4**) and Hind = 1*H*-indazole are reported. Interconversion between *cis* and *trans* isomers at high temperatures (80−130 °C) has been observed and studied by NMR spectroscopy. Kinetic data indicate that isomerizations correspond to reversible first order reactions. The rates of isomerization reactions even at 110 °C are very low with rate constants of 10^{-5} s^{-1} and 10^{-6} s^{-1} for ruthenium and osmium complexes, respectively, and the estimated rate constants of isomerization at room temperature are of ca. 10^{-10} s^{-1}. The activation parameters, which have been obtained from fitting the reaction rates at different temperatures to the Eyring equation for ruthenium [$\Delta H^{\ddagger}_{cis\text{-}trans} = 122.8 \pm 1.3$; $\Delta H^{\ddagger}_{trans\text{-}cis} = 138.8 \pm 1.0$ kJ/mol; $\Delta S^{\ddagger}_{cis\text{-}trans} = -18.7 \pm 3.6$; $\Delta S^{\ddagger}_{trans\text{-}cis} = 31.8 \pm 2.7$ J/(mol·K)] and osmium [$\Delta H^{\ddagger}_{cis\text{-}trans} = 200.7 \pm 0.7$; $\Delta H^{\ddagger}_{trans\text{-}cis} = 168.2 \pm 0.6$ kJ/mol; $\Delta S^{\ddagger}_{cis\text{-}trans} = 142.7 \pm 8.9$; $\Delta S^{\ddagger}_{trans\text{-}cis} = 85.9 \pm 3.9$ J/(mol·K)] reflect the inertness of these systems. The entropy of activation for the osmium complexes is highly positive and suggests the dissociative mechanism of isomerization. In the case of ruthenium, the activation entropy for the *cis* to *trans* isomerization is negative [−18.6 J/(mol·K)], while being positive [31.0 J/(mol·K)] for the *trans* to *cis* conversion. The thermodynamic parameters for *cis* to *trans* isomerization of [RuCl$_4$(NO)(Hind)]$^-$, viz. $\Delta H° = 13.5 \pm 1.5$ kJ/mol and $\Delta S° = -5.2 \pm 3.4$ J/(mol·K) indicate the low difference between the energies of *cis* and *trans* isomers. The theoretical calculation has been carried out on isomerization of ruthenium complexes with DFT methods. The dissociative, associative, and intramolecular twist isomerization mechanisms have been considered. The value for the activation energy found for the dissociative mechanism is in good agreement with experimental activation enthalpy. Electrochemical investigation provides further evidence for higher reactivity of ruthenium complexes compared to that of osmium counterparts and shows that intramolecular electron transfer reactions do not affect the isomerization process. A dissociative mechanism of *cis*↔*trans* isomerization has been proposed for both ruthenium and osmium complexes.

■ INTRODUCTION

Metal−nitrosyl complexes have attracted considerable attention because of their electron-transfer properties,[1−6] light-induced linkage isomerism,[7] and catalytic activities in organic synthesis.[8,9] They are also among the essentials in teaching coordination chemistry. It is the noninnocent nitrosyl molecule (NO) that mainly causes their interesting properties. It is also what makes it often difficult to assign an oxidation number to the metal center, so the electronic structure of the {M(NO)} moiety remains a field of current interest.[10−15] The relatively strong binding of the nitrosyl ligand to transition metal ions enables many substitution reactions on the metal centers. Along this, the strong *trans* effect of the nitrosyl ligand plays an important role in the chemical reactivity, electronic structure, and stereochemistry of the initial and final complexes.[16,17] It follows a great versatility of the complexes. They have long been limited to transition metal ions,[15,16,18] but have recently crossed the f-element border with the report of an actinide complex.[19]

Received: February 28, 2013
Published: May 15, 2013

© 2013 American Chemical Society

Metal-nitrosyl complexes are not only interesting for their physical and chemical properties. They have also been increasingly investigated for biomedical applications as suppliers or scavengers of NO[18,20−22] since being recognized as biologically relevant.[23] In this regard, a very well documented example of a coordination compound containing NO in clinical use is sodium nitroprusside ($Na_2[Fe(CN)_5(NO)]$), which has been amply studied for its photochemical properties[24] and is now the strongest available vasodilator.[22,25]

Metal−nitrosyl complexes, particularly those of the platinum group, are of interest to us as potential anticancer agents that may kill the cancer cells by releasing a cocktail of NO and metal complex.[26] In the field of anticancer metal drugs, it is well-known that the reactivity and biological properties can vary significantly with the isomeric compounds. The classical example of contrasting biological activity is cisplatin, which is the first clinically used metal-based anticancer agent, whereas its *trans* isomer shows no biological activity.[27,28] Two other platinum(II) complexes in clinical use today, namely *cis*-diamine(cyclobutane-1,1-dicarboxylato-*O*,*O*′)platinum(II) (carboplatin) and (1*R*,2*R*)-diaminocyclohexane-oxalatoplatinum(II) (oxaliplatin), are also *cis*-configured complexes. It follows that the *cis* geometry was for a long time considered as a prerequisite for anticancer activity,[29,30] and therefore, the *trans*-configured complexes have attracted little attention of researchers. The situation has changed, however, in recent years after several classes of *trans*-configured complexes have been reported to exhibit higher cytotoxicity than the corresponding *cis* isomers[31] with some of them exhibiting antitumor activity in vivo, with a lack of cross-resistance to cisplatin.[32] Cellular accumulation experiments have shown that accumulation in the SW480 cells of *trans*-configured platinum(II) complexes with acetone oxime and 3-pentanone oxime was up to 50 times higher than that of platinum(II) complexes and resulted in pronounced DNA strand cleavage for trans complexes, and a lack of DNA degradation for *cis* complexes.[33] All of these examples are concerned with square-planar platinum complexes. In the case of octahedral ruthenium and osmium complexes, the exploration of such structure−activity relationships is hindered by the low number of available compounds, although some rare examples of well-documented isomers have been reported in the literature.[34−37] In particular, the antiproliferative activity of (H_2trz)[*trans*-$RuCl_4(Htrz)_2$], where Htrz = 1*H*-1,2,4-triazole, was found higher than that of the corresponding *cis* isomer in human cancer cell lines SW480 (colon carcinoma), HT29 (colon carcinoma), and SK-BR-3 (mammary carcinoma). These examples show the crucial need in the field of antiproliferative complexes, as for any pharmaceutics, to control the stereochemistry and to know about the interconversion processes in between the isomeric forms. This goes well beyond the scope of metallopharmaceutics, given that stereochemistry studies are the basis of coordination chemistry.

With this in mind and as a tribute to Alfred Werner Nobel prize celebrations, we report herein on the synthesis, structure, and spectroscopic and electrochemical properties of the *trans* and *cis* isomers of the ruthenium− and osmium−nitrosyl complexes of the general formula (*n*-Bu_4N)[$MCl_4(NO)$(Hind)] where M = Ru or Os and Hind = 1*H*-indazole (Scheme 1). This is completed by in depth studies of their relative thermodynamic stabilities and of the *trans* ↔ *cis* isomerization mechanism that has been investigated experimentally by NMR and theoretically by DFT calculations in a complementary way.

Scheme 1. Compounds Reported in This Work[a]

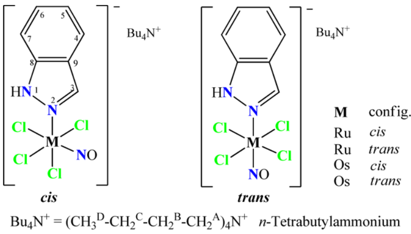

[a] Atom labeling was introduced for assignment of resonances in NMR spectra.

■ EXPERIMENTAL SECTION

Starting Materials. $Na_2[RuCl_5(NO)]\cdot 6H_2O$ was synthesized as previously reported in the literature.[38] $(H_2ind)_2[RuCl_5(NO)]$ (Hind = 1*H*-indazole) was prepared by heating the sodium salt with indazole in a 1:2 molar ratio in 6 M HCl. The starting compound (*n*-$Bu_4N)_2[OsCl_5(NO)]$ was synthesized as previously reported in the literature.[39] OsO_4 (99.8%) was purchased from Johnson Matthey. $NH_2OH\cdot HCl$, $K_2C_2O_4\cdot H_2O$, and indazole were from Aldrich.

(H_2ind)[*cis*-$RuCl_4$(NO)(Hind)] and (H_2ind)[*trans*-$RuCl_4$(NO)(Hind)]. A suspension of $(H_2ind)_2[RuCl_5(NO)]$ (230 mg, 0.36 mmol) in 1-propanol (8 mL) was heated at 75 °C for 6 h. The solvent was removed *in vacuo*, and the residue was extracted with chloroform. Fractioned crystallization afforded pink crystals of the *trans* isomer (first fraction), which was filtered off, washed with diethyl ether, and dried *in vacuo*. Yield: 47 mg, 21%. The second fraction crystallized as a *cis* isomer was filtered off, washed with diethyl ether, and dried *in vacuo*. Yield: 79 mg, 36%. Analytical data for *cis* isomer: Anal. Calcd for $C_{14}H_{13}RuCl_4N_5O\cdot 0.25\ CHCl_3$ (M_r = 540.01 g/mol): C, 31.69; H, 2.47; N, 12.96. Found: C, 31.64; H, 2.57; N, 13.28. ESI-MS in MeOH (negative): *m*/*z* 243 $[RuCl_4]^-$, 273 $[RuCl_4(NO)]^-$, 391 $[RuCl_4(NO)(Hind)]^-$. ESI-MS in MeOH (positive): *m*/*z* 119 $(H_2ind)^+$. MIR, ν, cm^{-1}: 614, 649, 840, 925, 965, 999, 1091, 1125, 1150, 1175, 1214, 1237, 1278, 1358, 1379, 1435, 1475, 1513, 1582, 1629 (C═N), 1854 (NO), 2993, 3127 (NH), 3308. UV−vis (CH_3CN), λ_{max}, nm (ε, M^{-1} cm^{-1}): 258 (21 517), 294 sh (15 948), 373 sh (154), 453 (68), 539 sh (46). ^1H NMR (DMSO-d_6, 500.32 MHz), δ, ppm: 7.10 (t, $1H_{5'}$, *J* = 7.01 Hz), 7.24 (t, $1H_5$, *J* = 7.21 Hz), 7.34 (t, $1H_{6'}$, *J* = 7.30 Hz), 7.49 (t, $1H_6$, *J* = 7.16 Hz), 7.52 (d, $1H_{7'}$, *J* = 7.45 Hz), 7.77 (d, $2H_{4'/7}$, *J* = 9.61 Hz), 7.90 (d, $1H_4$, *J* = 8.15 Hz), 8.06 (s, $1H_{3'}$), 8.62 (s, $1H_3$), 13.28 (s, $1H_1$). $^{13}C\{^1H\}$ NMR (DMSO-d_6, 125.77 MHz), δ, ppm: 110.54 ($C_{7'}$), 111.62 ($C_{5'}$), 120.64 ($C_{4'/7}$), 120.94 ($C_{4'/7}$), 121.50 (C_4), 121.92 (C_9), 122.33 (C_5), 123.24 ($C_{9''}$), 126.35 ($C_{6''}$), 129.07 (C_6), 133.78 ($C_{3'}$), 137.80 (C_3), 140.10 (C_8), 141.04 ($_{C8'}$). ^{15}N NMR (DMSO-d_6, 50.68 MHz), δ, ppm: 163.44 (N_1). Suitable crystals for the X-ray diffraction study were grown by slow evaporation of a solution of the cis isomer in chloroform. Analytical data for the *trans* isomer: Anal. Calcd for $C_{14}H_{13}RuCl_4N_5O\cdot CHCl_3$ (M_r = 629.54 g/mol): C, 28.62; H, 2.24; N, 11.12. Found: C, 28.83; H, 2.05; N, 10.97. ESI-MS in MeOH (negative): *m*/*z* 243 $[RuCl_4]^-$, 273 $[RuCl_4(NO)]^-$, 391 $[RuCl_4(NO)(Hind)]^-$. ESI-MS in MeOH (positive): *m*/*z* 119 $(H_2ind)^+$. MIR, ν, cm^{-1}: 588, 615, 657, 731, 739, 861, 899, 962, 999, 1091, 1121, 1148, 1228, 1270, 1298, 1358, 1449, 1471, 1511, 1582, 1635 (C═N), 1891 (NO), 2995, 3158, 3232 (NH), 3317. UV−vis (CH_3CN), λ_{max}, nm (ε, M^{-1} cm^{-1}): 260 (21 883), 283 sh (16 175), 383 sh (99), 504 (36), 597 (19). ^1H NMR (DMSO-d_6, 500.32 MHz), δ, ppm: 7.10 (t, $1H_{5'}$, *J* = 7.11 Hz), 7.22 (t, $1H_5$, *J* = 7.21 Hz), 7.34 (t, $1H_{6'}$, *J* = 7.23 Hz), 7.51 (t, $1H_6$, *J* = 7.34 Hz), 7.54 (d, $1H_{7'}$, *J* = 7.35 Hz), 7.76 (d, $1H_{4'}$, *J* = 7.76 Hz), 7.79 (d, $1H_7$, *J* = 7.75 Hz), 7.90 (d, $1H_4$, *J* = 8.25 Hz), 8.07 (s, $1H_{3'}$), 8.63 (s, $1H_3$), 12.95 (s, $1H_1$). $^{13}C\{^1H\}$ NMR (DMSO-d_6, 125.77 MHz), δ, ppm: 110.54 ($C_{7'}$), 112.13 (C_7), 120.64 ($C_{5'}$), 120.94 ($C_{4'}$), 121.01 (C_9), 121.94 (C_4), 122.36 (C_5), 123.23 ($C_{9'}$), 126.36 ($C_{6'}$), 129.40 (C_6), 133.78 ($C_{3'}$), 138.21 (C_3), 140.14 (C_8), 140.33

($C_{8'}$). ^{15}N NMR (DMSO-d_6, 50.68 MHz), δ, ppm: 161.97 (N_1). Suitable crystals for the X-ray diffraction study were grown by slow evaporation of a solution of the *trans* isomer in chloroform.

(Bu$_4$N)[*cis*-RuCl$_4$(NO)(Hind)] (1). To a solution of (H$_2$ind)[*cis*-RuCl$_4$(NO)(Hind)] (43 mg, 0.08 mmol) in 20 mL of water *n*-Bu$_4$NCl was added (30 mg, 0.1 mmol). The solution becomes immediately cloudy and product **1** precipitates after several minutes. The pale pink precipitate was filtered off washed with diethyl ether (2 × 10 mL) and dried *in vacuo*. Yield: 33 mg, 61%. Anal. Calcd for $C_{23}H_{42}Cl_4N_4ORu$ (M_r = 633.49 g/mol): C, 43.61; H, 6.68; N, 8.84. Found: C, 43.67; H, 6.50; N, 8.78. ESI-MS in MeOH (negative): *m/z* 391 [RuCl$_4$(NO)(Hind)]$^-$. ESI-MS in MeOH (positive): *m/z* 242 Bu$_4$N$^+$. IR, ν, cm^{-1}: 658, 677, 729, 764, 782, 848, 869, 963, 1091, 1114, 1241, 1358, 1381, 1442, 1476, 1508, 1623, 1846 (NO), 2873, 2959, 3250. ^{1}H NMR (DMSO-d_6, 500.32 MHz), δ, ppm: 0.95 (t, 12H$_D$, J = 7.2 Hz), 1.32 (sxt, 8H$_C$, J = 7.2 Hz), 1.57 (qui, 8H$_B$, J = 7.8 Hz), 3.17 (t, 8H$_A$, J = 7.7 Hz), 7.23 (t, 1H$_5$, J = 7.21 Hz), 7.49 (t, 1H$_6$, J = 7.16 Hz), 7.77 (d, 1H$_{4/7}$, J = 9.61 Hz), 7.89 (d, 1H$_4$, J = 8.15 Hz), 8.62 (s, 1H$_3$), 13.28 (s, 1H$_1$). Suitable crystals for X-ray diffraction study were grown by slow evaporation of the mother liquor.

(Bu$_4$N)[*trans*-RuCl$_4$(NO)(Hind)] (2). To a solution of (H$_2$ind)-[*trans*-RuCl$_4$(NO)(Hind)] (40 mg, 0.08 mmol) in 20 mL of water *n*-Bu$_4$NCl was added (30 mg, 0.1 mmol). The solution becomes immediately cloudy and product **2** precipitates after several minutes. The pale pink precipitate was filtered off washed with diethyl ether (2 × 10 mL) and dried *in vacuo*. Yield: 34 mg, 68%. Anal. Calcd for $C_{23}H_{42}Cl_4N_4ORu$ (M_r = 633.49 g/mol): C, 43.61; H, 6.68; N, 8.84. Found: C, 43.53; H, 6.54; N, 8.74. IR, ν, cm^{-1}: 591, 659, 737, 747, 757, 784, 833, 879, 965, 1002, 1097, 1238, 1282, 1360, 1378, 1459, 1476, 1514, 1629, 1875 (NO), 2872, 2960, 3302. ESI-MS in MeOH (negative): *m/z* 391 [RuCl$_4$(NO)(Hind)]$^-$. ESI-MS in MeOH (positive): *m/z* 242 Bu$_4$N$^+$. ^{1}H NMR (DMSO-d_6, 500.32 MHz), δ, ppm: 0.95 (t, 12H$_D$, J = 7.2 Hz), 1.32 (sxt, 8H$_C$, J = 7.2 Hz), 1.57 (qui, 8H$_B$, J = 7.8 Hz), 3.17 (t, 8H$_A$, J = 7.7 Hz), 7.23 (t, 1H$_{5/6}$, J = 7.2 Hz), 7.51 (t, 1H$_{5/6}$, J = 7.6 Hz), 7.78 (d, 1H$_{4/7}$, J = 8.8 Hz), 7.92 (d, 1H$_{4/7}$, J = 8.3 Hz), 8.68 (s, 1H$_3$), 12.96 (s, 1H$_1$). Suitable crystals for X-ray diffraction study were grown by slow evaporation of the mother liquor.

(Bu$_4$N)[*cis*-OsCl$_4$(NO)(Hind)] (3) and (Bu$_4$N)[*trans*-OsCl$_4$(NO)-(Hind)] (4). A mixture of indazole (100 mg, 0.85 mmol) and (*n*-Bu$_4$N)$_2$[OsCl$_5$(NO)] (500 mg, 0.56 mmol) in *n*-butanol (10 mL) was heated at 105 °C for 24 h. The solution was allowed to stand in an open beaker, and after 2 days the red crystals of the *cis* isomer were filtered off, washed with 1:2 water/ethanol (3 × 10 mL) and diethyl ether (3 × 5 mL), and dried *in vacuo*. Yield: 210 mg, 52%. The volume of the filtrate was reduced to one-third, and slow diffusion of diethyl ether afforded the formation of blue crystals of the *trans* isomer. These were filtered off, washed with 1:2 water/ethanol (3 × 3 mL) and diethyl ether (3 × 1 mL), and dried *in vacuo*. Yield: 101 mg, 25%.

Analytical Data for 3. Anal. Calcd for $C_{23}H_{42}OsCl_4N_4O$ (M_r = 722.65 g/mol): C, 38.23; H, 5.86; N, 7.75. Found: C, 38.48; H, 5.66; N, 7.62. ESI-MS in CH$_3$CN (negative): *m/z* 332 [OsCl$_4$]$^-$, 362 [OsCl$_4$(NO)]$^-$, 480 [OsCl$_4$(NO)(Hind)]$^-$. IR, ν, cm^{-1}: 437, 657, 761, 846, 878, 967, 1004, 1091, 1153, 1240, 1279, 1359, 1380, 1476, 1625, 1805 (NO), 2873, 2960, 3258. UV−vis (CH$_3$CN), λ_{max}, nm (ε, M^{-1} cm^{-1}): 248 (11 573), 393 (sh, 6178), 511 (921). ^{1}H NMR (DMSO-d_6, 500.13 MHz), δ, ppm: 0.93 (t, 12H$_D$, J = 7.3 Hz), 1.31 (sxt, 8H$_C$, J = 7.3 Hz,), 1.57 (qui, 8H$_B$, J = 7.7 Hz,), 3.16 (t, 8H, J = 8.4 Hz,), 7.26 (t, 1H, J = 7.5 Hz, H$_6$), 7.49 (t, 1H, J = 7.6 Hz, H$_5$), 7.78 (d, 1H, J = 8.1 Hz, H$_4$), 7.91 (d, 1H, J = 8.2 Hz, H$_7$), 8.62 (s, 1H, H$_3$), 13.49 (s, 1H, H$_1$). ^{13}C[40] NMR (DMSO-d_6, 125.77 MHz), δ, ppm: 13.47 (C$_D$), 19.18 (C$_C$), 23.07 (C$_B$), 57.54 (C$_A$), 111.11 (C$_4$), 121.33 (C$_7$), 121.98 (C$_6$), 129.12 (C$_5$), 137.79 (C$_3$), 140.78 (C$_{8,9}$). ^{15}N NMR (DMSO-d_6, 50.69 MHz), δ, ppm: 65.6 (N from Bu$_4$N$^+$), 187.6 (N$_2$), 194.2 (d, N$_1$). X-ray diffraction quality single crystals of **3** were picked from the reaction vessel.

Analytical Data for 4. Anal. Calcd for $C_{23}H_{42}OsCl_4N_4O$ (M_r = 722.65 g/mol): C, 38.23; H, 5.86; N, 7.75. Found: C, 38.49; H, 5.74; N, 7.61. ESI-MS in CH$_3$CN (negative): *m/z* 332 [OsCl$_4$]$^-$, 362 [OsCl$_4$(NO)]$^-$, 480 [OsCl$_4$(NO)(Hind)]$^-$. IR, ν, cm^{-1}: 437, 520, 594, 616, 660, 736, 757, 832, 878, 967, 1005, 1096, 1150, 1238, 1284, 1361, 1378, 1476, 1517, 1630, 1838, 2871, 2960, 3300. UV−vis (CH$_3$CN), λ_{max}, nm (ε, M^{-1} cm^{-1}): 254 (9207), 270 (8145), 300 (sh, 3808), 579 (116). ^{1}H NMR (DMSO-d_6, 500.13 MHz), δ, ppm: 0.93 (t, 12H$_D$, J = 7.3 Hz), 1.31 (sxt, 8H$_C$, J = 7.3 Hz,), 1.56 (qui, 8H$_B$, J = 7.2 Hz,), 3.16 (t, 8H, J = 8.3 Hz,), 7.23 (t, 1H, J = 7.5 Hz, H$_6$), 7.52 (t, 1H, J = 7.7 Hz, H$_5$), 7.76 (d, 1H, J = 8.5 Hz, H$_4$), 7.90 (d, 1H, J = 8.2 Hz, H$_7$), 8.58 (s, 1H, H$_3$), 13.00 (s, 1H, H$_1$). ^{13}C[40] NMR (DMSO-d_6, 125.77 MHz), δ, ppm: 13.47 (C$_D$), 19.18 (C$_C$), 23.05 (C$_B$), 57.53 (C$_A$), 111.63 (C$_4$), 120.26 (C$_9$),121.56 (C$_7$), 122.11 (C$_6$), 129.39 (C$_5$), 138.30 (C$_3$), 139.69 (C$_8$). ^{15}N NMR (DMSO-d_6, 50.69 MHz) δ, ppm: 65.6 (N from Bu$_4$N$^+$), 185.0 (N$_2$), 238.7 (N$_1$). Suitable crystals of **4** for X-ray diffraction analysis were obtained from mother liquor after isolation of **3** by slow diffusion of diethyl ether.

Physical Measurements. Elemental analyses were performed by the Microanalytical Service of the Faculty of Chemistry of the University of Vienna.

MIR spectra of **1** and **2** were obtained by using an ATR unit with a Perkin-Elmer 370 FTIR 2000 instrument (4000−400 cm^{-1}), while ESI mass spectrometry was carried out with a Bruker Esquire 3000 instrument (Bruker Daltonics, Bremen, Germany) by using methanol as solvent. Expected and measured isotope distributions were compared. The ^{1}H, ^{13}C, and ^{15}N NMR spectra were recorded at 500.32, 125.82, and 50.70 MHz on a Bruker DPX500 (Ultrashield Magnet) d_6-DMSO (2.50 ppm) or $C_2D_2Cl_4$ (5.98 ppm). 2D ^{13}C^{1}H HSQC, ^{15}N^{1}H HSQC, ^{13}C^{1}H HMBC, and ^{1}H^{1}H COSY experiments were performed.

IR spectra of **3** and **4** were recorded in the solid state on a NICOLET spectrophotometer in the 400−4000 cm^{-1} range, while UV−vis spectra were recorded on a Perkin-Elmer Lambda 35 UV−vis spectrophotometer using samples dissolved in CH$_3$CN. Mass spectra were recorded on an ion trap mass spectrometer (LCQ, Thermo, Bremen, Germany) equipped with an electrospray (ESI) ion source in the positive and negative ion mode. The spray voltage for the positive and negative ion mode is respectively 4 kV and −3 kV. The capillary transfer temperature is 200 °C. For ^{1}H and ^{13}C NMR experiments, all samples were prepared under a N$_2$ atmosphere in 5 mm NMR tubes. The chemical shifts were referred to TMS using the residual signals from the solvent d_6-DMSO (2.50 ppm) or $C_2D_2Cl_4$ (5.98 ppm). The 2D NMR spectra were recorded on a Bruker AV500 spectrometer and kinetic ^{1}H NMR spectra on a Bruker DRX-300 spectrometer.

Electrochemical Measurements. Electrochemical measurements were performed using an AMEL 7050 all-in-one potentiostat, using a standard three-electrode setup with a glassy carbon electrode, a platinum auxiliary electrode, and a SCE (saturated calomel electrode) as the reference electrode. Deareation of solutions was accomplished by passing a stream of N$_2$ through the solution for 30 min prior to the measurement and then maintaining a blanket atmosphere of N$_2$ over the solution during the measurement. The complex solution in CH$_3$CN was 1 or 2 mM in the supporting electrolyte of 0.1 M (*n*-Bu$_4$N)PF$_6$. Under these experimental conditions, the ferrocene/ferricinium couple, used as an internal reference for potential measurements, was located at $E_{1/2}^{ox}$ = +0.425 V. The cyclic voltammetry of a mixture of **3** and **4** was characterized by two reversible oxidation waves corresponding to each isomer studied separately, whereas no separation oxidation peak was observed with a mixture of **1** and **2**.

Kinetic Analysis. The integrals of NMR signals were obtained by fitting Lorentzian functions to the experimental spectra using the "NMRICMA 3.0"[41] program for MATLAB (see Supporting Information, Figure S1). The adjustable parameters are the resonance frequency, intensity, line width, baseline, and phasing. Data analyses were carried out with the nonlinear least-squares fitting program VISUALIZEUR-OPTIMISEUR[42] for MATLAB, using the Levenberg−Marquardt algorithm. Irreversible and reversible first-order reaction models were applied to analyze the time evolution of *trans* and *cis* Ru and Os isomer concentrations. The experimental data were fitted according to eqs 1−4 where A_0^T and B_0^T correspond to initial concentrations of *trans* and *cis* isomers, respectively. The samples were heated in an external constant temperature steam sterilizer at the desired temperature, whose value is assumed to be accurate within

Table 1. Crystal Data, Data Collection Parameters, and Structure Refinement Details for $(Bu_4N)[\textit{cis}\text{-}MCl_4(NO)(Hind)]$ (M = Ru (1); Os (3)) and $(Bu_4N)[\textit{trans}\text{-}MCl_4(NO)(Hind)]$ (M = Ru (2); Os (4))

compound	1	2	3	4
empirical formula	$C_{23}H_{42}Cl_4N_4ORu$	$C_{23}H_{42}Cl_4N_4ORu$	$C_{23}H_{42}Cl_4N_4OOs$	$C_{23}H_{42}Cl_4N_4OOs$
fw	633.48	633.48	722.61	722.62
space group	$P2_1/n$	$P2_1/c$	$P2_1/n$	$P2_1/c$
a [Å]	12.4091(4)	10.0975(5)	12.35414(12)	10.0836(7)
b [Å]	52.5720(15)	15.8422(9)	52.4121(4)	15.8530(10)
c [Å]	13.7339(4)	18.9705(10)	13.87637(13)	18.9740(10)
α [deg]				
β [deg]	100.7330(10)	100.759(2)	100.7569(9)	101.298(7)
γ [deg]				
V [Å^3]	8802.9(5)	2981.3(3)	8827.14(14)	2974.3(3)
Z	12	4	12	4
λ [Å]	0.70713	0.71073	1.54184	0.71070
ρ_{calcd} [g cm^{-3}]	1.434	1.411	1.631	1.614
cryst size [mm^3]	0.14 × 0.14 × 0.10	0.15 × 0.02 × 0.02	0.27 × 0.17 × 0.14	0.57 × 0.29 × 0.15
T [K]	150(2)	150(2)	100(2)	100(2)
μ [mm^{-1}]	0.921	0.906	11.698	4.668
R_1[a]	0.0715	0.0310	0.0316	0.0304
wR_2[b]	0.1288	0.0641	0.0860	0.0697
GOF[c]	1.064	1.025	1.042	1.033

[a] $R_1 = \sum||F_o| - |F_c||/\sum|F_o|$. [b] $wR_2 = \{\sum[w(F_o^2 - F_c^2)^2]/\sum[w(F_o^2)^2]\}^{1/2}$. [c] $\mathrm{GOF} = \{\sum[w(F_o^2 - F_c^2)^2]/(n - p)\}^{1/2}$, where n is the number of reflections and p is the total number of parameters refined.

Table 2. Selected Bond Lengths (Å) and Angles (deg) (experimental and calculated) for Compounds *cis*-$(Bu_4N)[MCl_4(NO)(Hind)]$ (M = Ru (1), Os (3)) and *trans*-$(Bu_4N)[MCl_4(NO)(Hind)]$ (M = Ru (2), Os (4))

	X-ray				B3LYP/6-31G*			
bond	1[a]	2	3[a]	4	1	2	3	4
M−N1	2.092(4)	2.104(2)	2.080(4)	2.114(3)	2.151	2.204	2.161	2.182
M−Cl_{eq}(av)	2.350(19)	2.360(3)	2.373(9)	2.368(3)	2.469	2.451	2.406	2.438
M−Cl_{ax}	2.3675(13)		2.3728(11)		2.405		2.390	
M−N3	1.784(5)	1.717(2)	1.8220(9)	1.763(3)	1.747	1.735	1.732	1.715
N3−O1	1.041(6)	1.144(3)	1.1346(12)	1.133(4)	1.171	1.167	1.161	1.157
M−N3−O1	176.1(5)	178.2(2)	176.4(4)	178.0(4)	178.7	179.7	179.5	179.8

[a] Quoted parameters refer to crystallographically independent complex anions not affected by the disorder.

±0.5 K. The temperature was monitored by a thermometer situated near the NMR sample tubes. NMR spectra of the investigated samples were measured at room temperature (20 °C) after rapid sample cooling using a water bath. Due to extremely low isomerization process rates in these systems, the time during NMR measurements is neglected. The time used in kinetic analysis (τ) corresponds to the heating time at indicated temperatures.

Crystallographic Structure Determination. X-ray diffraction measurements for ruthenium complexes **1** and **2** were performed on a Bruker X8 APEXII CCD diffractometer at 150 K with Mo Kα monochromated radiation. Diffraction data for osmium complexes **3** and **4** were collected on Gemini R and Gemini A Ultra diffractometers from Agilent Technologies Ltd. at 100 K with Cu Kα and Mo Kα graphite-monochromated radiation, respectively, both equipped with a CCD camera and controlled by the CrysAlisPro Software (Agilent Technologies, versions 1.171.33.55 and 1.171.34.49). The data on ruthenium complexes were processed using SAINT software,[43] and those on osmium complexes with the CrysAlisPro package.[44] For all crystals, an analytical absorption correction was applied using the modeled faces of the crystal.[45] Crystal data, data collection parameters, and structure refinement details are given in Table 1. The structures were solved by direct methods and refined by full-matrix least-squares techniques. All non-hydrogen atoms in **1**, **2**, and **4** were refined with anisotropic displacement parameters, while the non-hydrogen atoms of indazole in **3** (vide infra) were refined isotropically. H atoms were inserted in calculated positions and refined with a riding model. The nitrosyl ligand in **1** and **3** was found to be disordered over three positions in the equatorial plane of the metal. One of three crystallographically independent complex anions in **1** and two of three in **3** were found to be affected by this disorder. In addition, the indazole ligand in one crystallographically independent anion of **3** was found to be disordered over two positions with a s.o.f. of 0.5:0.5. The disorder was solved by using SADI, DFIX, and EADP instructions implemented in SHELXL. The following software programs and computer were used: structure solution, *SHELXS-97*; refinement, *SHELXL-97*;[46] molecular diagrams, *ORTEP-3*;[47] computer, Intel CoreDuo. Selected bond distances and angles for **1**−**4** are listed in Table 2.

Computational Details. The equilibrium geometries of the compounds **1**−**4** have been optimized in the gas phase combining the functional B3LYP[48,49] and the 6-31G* basis set for the light atoms. For ruthenium complexes **1** and **2** and osmium compounds **3** and **4**, the Stuttgart−Dresden 28-electron quasi-relativistic effective core potential (MWB28)[50] and the analogous 60-electron pseudopotential (MWB60),[50] respectively, have been used to account for the scalar relativistic effects. The possible transition state structures for the *cis*↔*trans* isomerization reaction of the Ru complexes were calculated at the same level of theory. In all the calculations, only the anions of all compounds have been considered, i.e., without any counterions. To verify the nature of the minima and the transition states, as well as to analyze the NO stretching frequency, harmonic vibrational frequency calculations have been carried out. Following the work of Scott and Radom,[51] the calculated harmonic vibrational frequencies were refined with a scaling factor of 0.9614 to account for the anharmonicity.

The mechanistic study of the $[RuCl_4(NO)(Hind)]^-$ *cis*↔*trans* isomerization requires high accuracy of the relative energies of the species. Therefore, additional single-point calculations on the optimized structures have been carried out on all Ru species using the double-hybrid B2GP-PLYP[52] functional and the 6-311G* basis set and MWB28 pseudopotential. The B2GP-PLYP functional has been used previously for accurate calculations of thermochemical data of late transition metal reactions.[53] These single point calculations have been carried out both in the gas phase and incorporating solvent effects in DMSO using the integral equation formalism (IEF)[54,55] of the polarizable continuum model (PCM).[56−58] To estimate the overall effect of the solvent on the relative energies and geometries of the species, two additional calculations have been carried out: (i) a B3LYP/6-311G* single-point calculation using the PCM on the B3LYP/6-31G* gas-phase optimized geometries (labeled as PCM-B3LYP/6-311G*//B3LYP/6-31G*) and (ii) a PCM-B3LYP/6-31G* optimization (on compounds **1** and **2** and one transition state for the dissociative mechanism). The PCM-B3LYP/6-31G* geometries showed negligible differences from the gas-phase B3LYP/6-31G* ones, and relative PCM-B3LYP/6-31G* energies deviated by less than 3 kJ/mol from the values calculated at the PCM-B3LYP/6-311G*//B3LYP/6-31G* level of theory. Therefore, gas-phase B3LYP/6-31G* geometries have been used for all subsequent calculations in the whole study. All calculations have been carried out with the Gaussian 09 program package.[59]

■ RESULTS AND DISCUSSION

Syntheses. Anderson rearrangement reaction of $(H_2ind)_2[RuCl_5(NO)]$ in alcohols at elevated temperatures yielded (H_2ind)[*cis*-$RuCl_4(NO)(Hind)$] and (H_2ind)[*trans*-$RuCl_4(NO)(Hind)$], which were separated by fractioned crystallization. A metathesis reaction with a small excess of $(n\text{-}Bu_4N)Cl$ afforded complexes **1** and **2**, respectively.

The isomeric osmium−nitrosyl complexes **3** and **4** were obtained by reaction of $(n\text{-}Bu_4N)_2[OsCl_5(NO)]$ with 1*H*-indazole in a 1:1.5 molar ratio in *n*-butanol at 105 °C for 24 h with an overall yield between 75 and 80%. Fractioned crystallization of the reaction mixture afforded 2/3 of the red *cis* isomer **3**, and then by slow diffusion of diethyl ether into the concentrated filtrate, 1/3 of blue crystals of the *trans*-isomer **4** were afforded.

The reactivity of pentahalonitrosyl metalate $[MX_5(NO)]^{2-}$ (M = Ru, Os; X = Cl, Br, I) increases in the order $Cl^- < Br^- < I^-$ and Os < Ru, and the ligand substitution should be favored in the *trans* position to the NO group due to the well-known *trans* effect.[17] However, in our case, the main compounds isolated were the *cis* isomers **1** and **3**. The lower yield of *trans* isomers **2** and **4** suggests that they are transient species, transforming into the *cis* forms under reaction conditions (*n*-propanol at 75 °C for ruthenium, *n*-butanol at 105 °C for osmium). This prompted us to study the *trans*/*cis* conversion by ^{1}H NMR in detail.

The peak with *m*/*z* 391 in the negative ion mode ESI mass spectra of **1** and **3** was assigned to $[RuCl_4(NO)(Hind)]^-$, while signals at *m*/*z* 480, 362, and 332 for **2** and **4** were attributed to $[OsCl_4(NO)(Hind)]^-$, $[OsCl_4(NO)]^-$, and $[OsCl_4]^-$, respectively. All compounds possess an $S = 0$ ground state as confirmed by magnetic measurements and NMR spectra. In IR spectroscopy, *cis* isomers are characterized by lower ν(NO) wavenumbers than the *trans* species. In particular, the ν(NO) for **1** and **3** is seen at 1846 and 1805 cm^{-1}, while that of **2** and **4** are at 1875 and 1838 cm^{-1}, respectively.

Crystal Structures. The crystal structures of **1**−**4** contain essentially octahedral Ru and Os complexes of the general formula $(n\text{-}Bu_4N)[MCl_4(NO)(Hind)]$ (M = Ru or Os; Hind = 1*H*-indazole; Figure 1). Complexes **1** and **3** crystallized in the monoclinic space group $P2_1/n$, while **2** and **4** crystallized in the monoclinic space group $P2_1/c$. Compounds **1** and **3** are *cis* isomers, in which three chlorido ligands and one NO molecule are bound to ruthenium (**1**) or osmium (**3**) in the equatorial plane, and the axial sites are occupied by an indazole heterocycle and a fourth chlorido ligand. In *trans* isomers **2** and **4**, the equatorial plane is occupied by four chlorides and the axial positions by NO and the indazole heterocycle. Crystal data and structure refinement parameters for **1**−**4** are shown in Table 1.

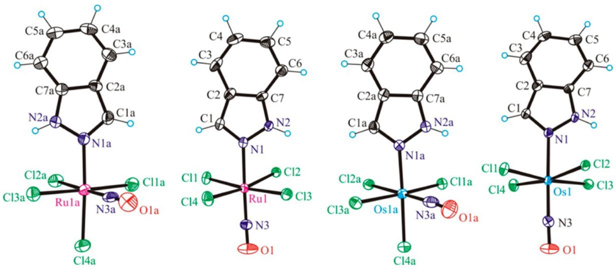

Figure 1. ORTEP views of the [*cis*-$RuCl_4(NO)(Hind)]^-$, [*trans*-$RuCl_4((NO)(Hind)]^-$, *cis*-$[OsCl_4(NO)(Hind)]^-$, and *trans*-$[OsCl_4(NO)(Hind)]^-$ complex anions in **1**−**4** (from left to right). Thermal ellipsoids are drawn at the 50% probability level.

Selected bond lengths and angles of the compounds **1**−**4**, as obtained from the crystal structures and theoretical calculations, are shown in Table 2. All complexes show a distorted octahedral coordination geometry around the metal center and a linear NO binding. In the *cis* compounds, NO lies in one plane with the equatorial Cl^- ligands, while in the *trans* compounds the Cl^- ligands are slightly bent out-of-plane toward the indazole ligand. In the calculated structures, we observe slightly longer (by ca. 0.1 Å) M−Cl bonds and a slightly more linear NO coordination compared to the crystal structures (Table 2). Otherwise, the optimized geometries are in good agreement with the X-ray structures.

Kinetic Study by NMR Spectroscopy. It is well-known that isomerization processes[60−76] as well as exchange/substitution reactions[77−80] at the metal center in platinum group (Ru, Rh, Pd, Os, Ir, Pt) metal complexes are much slower in comparison with those for 3d and 4f metal complexes.[81,82] Platinum group metal complexes are kinetically very inert and thermodynamically more stable. In addition, they have low isomerization rate constants. The two ruthenium isomers **1** and **2** and two related osmium isomers **3** and **4** presented in this work are in accord with these general rules. High resolution NMR spectroscopy is an appropriate technique to characterize isomers in solution and to monitor their mutual transformations.

The assignment of NMR signals of the coordinated 1*H*-indazole has been performed based on 2D NMR spectroscopy (see Supporting Information, Figures S2−S4) and was correlated with the spectra of the noncoordinated 1*H*-indazole.[83] A marked difference in the chemical shifts of NH and CH protons of the coordinated 1*H*-indazole ligand in *cis* and *trans* isomers (Figure 2) allows for the determination of population rates and an investigation of the kinetics of isomerization.

A typical series of time-dependent ^{1}H NMR spectra upon isomerization of [*trans*-$RuCl_4(NO)(Hind)]^-$ to [*cis*-

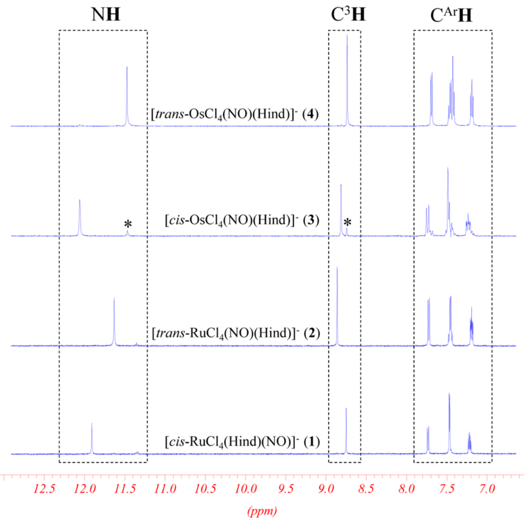

Figure 2. Selected region of ^{1}H NMR (500 MHz; 25 °C) spectra of (n-Bu$_4$N)[*cis*-MCl$_4$(NO)(Hind)] (M = Ru (**1**), Os (**3**)) and (n-Bu$_4$N)[*trans*-MCl$_4$(NO)(Hind)] (M = Ru (**2**), Os (**4**)) in $C_2D_2Cl_4$.

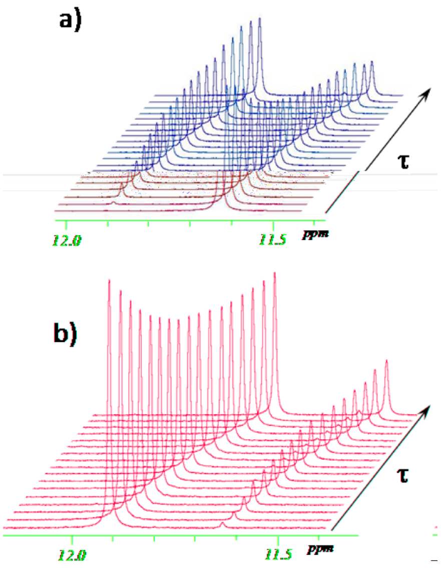

Figure 3. Evolution of ^{1}H NMR spectra (500 MHz) in the **NH** region of the [*trans*-RuCl$_4$(NO)(Hind)]$^-$ (*a*) and [*cis*-RuCl$_4$(NO)(Hind)]$^-$ (*b*) isomers as a function of time (τ = [0−3] × 10^5 s) at 100 °C in $C_2D_2Cl_4$ ($C_{0(\text{trans})}$ = 14.5 mmol/L; $C_{0(\text{cis})}$ = 13.7 mmol/L) showing the formation of the *cis* and *trans* isomers, respectively.

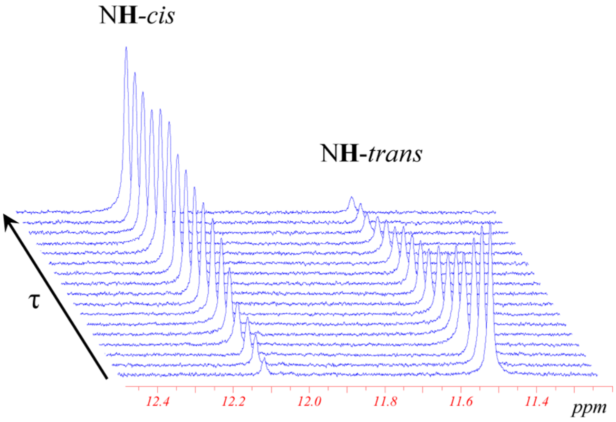

Figure 4. Evolution of ^{1}H NMR spectra (300 MHz) of the [*trans*-OsCl$_4$(NO)(Hind)]$^-$ isomer in the **NH** region as a function of time (τ = [0−3] × 10^5 s) at 120 °C in $C_2D_2Cl_4$ (C_0 = 15.26 mmol/L) showing the formation of the *cis* isomer (for complete aromatic region spectrum, see Supporting Information Figure S5).

RuCl$_4$(NO)(Hind)]$^-$ ([t−c]) and [*cis*-RuCl$_4$(NO)(Hind)]$^-$ to [*trans*-RuCl$_4$(NO)(Hind)]$^-$ ([c−t]) is shown in Figure 3, while that of [*trans*-OsCl$_4$(NO)(Hind)]$^-$ conversion into [*cis*-OsCl$_4$(NO)(Hind)]$^-$ and vice versa is displayed in Figure 4. From Figures 3a and 4, a progressive decrease of the **NH** signal intensity with time, corresponding to the *trans* isomer, and an increase of the signal corresponding to the *cis* isomer is seen. After 72 h of heating at 100 °C, [*trans*-RuCl$_4$(NO)(Hind)]$^-$ is partially converted into [*cis*-RuCl$_4$(NO)(Hind)]$^-$, and the *trans*−*cis* equilibrium is reached. Similarly, starting from the [*cis*-RuCl$_4$(NO)(Hind)]$^-$ isomer, the same equilibrium ratio between the *cis* and *trans* isomers is reached after 72 h of heating the solution at 100 °C. These time-dependent NMR spectra and the same equilibrium ratios between *cis* and *trans* isomers indicate the reversibility of the isomerization process.

The *trans* to *cis* conversion is also detected in the case of the [*trans*-OsCl$_4$(NO)(Hind)]$^-$ anion. However, the isomerization occurs slower and can be efficiently monitored only upon heating at temperatures higher than 100 °C. As can be seen from Figure 4, heating at 120 °C for 96 h leads to an almost complete conversion of the *trans* isomer into the *cis* one. According to the kinetic analysis (see below), the conversion of the *cis* isomer into the *trans* isomer in the case of osmium complexes also takes place, but only *trans* to *cis* transformation was experimentally investigated because of the very low conversion rate of *cis* species into *trans*.

Plots of population evolution of *cis* and *trans* isomeric species of ruthenium and osmium complexes versus heating times at different temperatures are shown in Figures 5, 6, and S6−S9.

For the estimation of population rates upon isomerization, the NH and C^3**H** signals of coordinated 1*H*-indazole in *cis* and

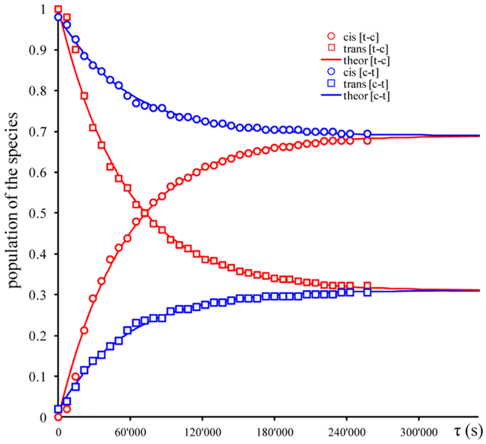

Figure 5. Time evolution of populations for [*cis*-RuCl$_4$(NO)(Hind)]$^-$ (○) and [*trans*-RuCl$_4$(NO)(Hind)]$^-$ (□) isomers at 100 °C in $C_2D_2Cl_4$ for *cis* to *trans* [c−t] (blue) and *trans* to *cis* [t−c] (red) isomerization processes. The solid lines are the best fits with activation parameters indicated in the text (for fitted plots at 90, 105, and 110 °C, see Supporting Information Figures S6 and S7).

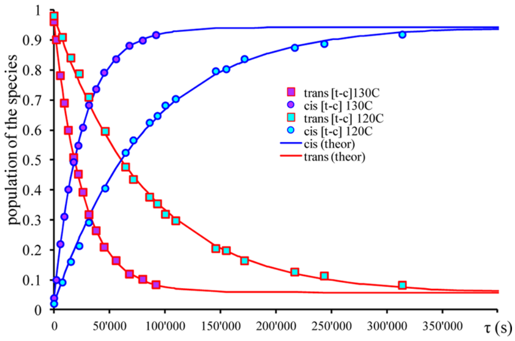

Figure 6. Time evolution of populations for [*cis*-OsCl$_4$(NO)(Hind)]$^-$ (○) and [*trans-Os*Cl$_4$(NO)(Hind)]$^-$ (□) isomers at 120 and 130 °C in C$_2$D$_2$Cl$_4$ for *trans* to *cis* [t−c] isomerization processes. The solid lines are the best fits with activation parameters indicated in the text (see also Figure S8 in the Supporting Information).

trans complexes from NMR spectra were used. Analogously to other isomerization processes,[73,74,84−86] the reversible first order kinetics are assumed for ruthenium and osmium complexes (see eqs 1 and 2).

$$A \rightleftarrows B \tag{1}$$

$$-\frac{dA_\tau^T}{d\tau} = \frac{dB_\tau^T}{d\tau} = k_1 A_\tau^T - k_{-1} B_\tau^T \tag{2}$$

In eqs 1 and 2, *A* is *trans* and *B* is *cis* isomer. Concentration evolution of *trans* (A_τ^T) and *cis* (B_τ^T) isomers as functions of time (τ) at different temperatures (T) were analyzed (by nonlinear least-squares fits) according to a reversible first order model via the eqs 3 and 4:[87,88]

$$\left[\frac{A_\tau^T}{A_\tau^T + B_\tau^T}\right] = \left[\frac{A_0^T}{A_0^T + B_0^T}\right]\left\{\left(\frac{1}{k_1 + k_{-1}}\right)(k_{-1} + k_1\,\mathrm{e}^{-(k_1+k_{-1})\tau})\right\} + \left[\frac{B_0^T}{A_0^T + B_0^T}\right]\left\{\left(\frac{k_{-1}}{k_1 + k_{-1}}\right)(1 - \mathrm{e}^{-(k_1+k_{-1})\tau})\right\} \tag{3}$$

$$\left[\frac{B_\tau^T}{A_\tau^T + B_\tau^T}\right] = \left[\frac{B_0^T}{A_0^T + B_0^T}\right]\left\{\left(\frac{1}{k_1 + k_{-1}}\right)(k_1 + k_{-1}\,\mathrm{e}^{-(k_1+k_{-1})\tau})\right\} + \left[\frac{B_0^T}{A_0^T + B_0^T}\right]\left\{\left(\frac{k_1}{k_1 + k_{-1}}\right)(1 - \mathrm{e}^{-(k_1+k_{-1})\tau})\right\} \tag{4}$$

Appropriate temperature values 80−110 °C for **1** and **2** and 105−130 °C for **3** and **4** were used in this analysis. The best fits of experimental data were obtained by using eqs 3 and 4 (Table 3). Initially, the conversion of [*trans*-OsCl$_4$(NO)(Hind)]$^-$ into [*cis*-OsCl$_4$(NO)(Hind)]$^-$ was analyzed as a first order irreversible process. The deviation of experimental data from the theoretical ones at high temperatures (120 and 130 °C) at longer time intervals (see Figure S9) suggested applying the reversible first order isomerization law. The activation parameters ($\Delta H^\#$ and $\Delta S^\#$) have been estimated using two methods (Table 4). In the first one (method I), the corresponding values of k_1 and k_{-1} at different temperatures have been obtained after fitting the experimental population rates with those calculated via eqs 3 and 4 and analysis by the logarithmic Eyring eq 5:

$$\ln\frac{k}{T} = -\frac{\Delta H^\#}{R} \times \frac{1}{T} + \ln\frac{k_\mathrm{B}}{h} + \frac{\Delta S^\#}{R} \tag{5}$$

In the second method (method II), the experimental population ratios at different temperatures were fitted simultaneously by using the reversible first order model (eqs 4 and 5) with constraining eq 5. In this case, two enthalpies of activation ($\Delta H^\ddagger_{cis-trans}$ and $\Delta H^\ddagger_{trans-cis}$) and two entropies of activation ($\Delta S^\ddagger_{cis-trans}$ and $\Delta S^\ddagger_{trans-cis}$) were used as variable parameters (Table 4). The results obtained from both methods are similar. The second method was not applied in the case of osmium complexes because of the absence of experimental data for *cis* to *trans* transformation.

The best fit for activation parameters ($\Delta H^\ddagger$, $\Delta S^\ddagger$) and calculated Gibbs energy ($\Delta G^\ddagger$) for the isomerization reactions of [*cis*-MCl$_4$(NO)(Hind)]$^-$ (M = Ru (**1**), Os (**3**)) and [*trans*-MCl$_4$(NO)(Hind)]$^-$ (M = Ru (**2**), Os (**4**)) in C$_2$D$_2$Cl$_4$ are quoted in Table 4 (see also Figure 7). The obtained enthalpies of isomerization is approximately two times as high as that

Table 3. Rate Constants *k* (s^{-1}) with Standard Deviations in Parentheses and Equilibrium Constant *K* at Different Temperatures for the Isomerization Reactions of [*cis*-MCl$_4$(NO)(Hind)]$^-$ (M = Ru (1), Os (3)) and [*trans*-MCl$_4$(NO)(Hind)]$^-$ (M = Ru (2), Os(4)) in C$_2$D$_2$Cl$_4$

	process	*k*(80 °C) × 10^{-6}	*k*(90 °C) × 10^{-6}	*k*(100 °C) × 10^{-6}	*k*(105 °C) × 10^{-6}	*k*(110 °C) × 10^{-6}	*k*(120 °C) × 10^{-6}	*k*(130 °C) × 10^{-6}
[*cis*-RuCl$_4$(NO)(Hind)]$^-$ (**1**)	*cis* → *trans*	0.58(8)	1.78(2)	5.51(6)	8.3(1)	20.1(7)		
[*trans*-RuCl$_4$(NO)(Hind)]$^-$ (**2**)	*trans* → *cis*	1.05(6)	2.66(3)	12.2(1)	19.5(2)	50.1(5)		
[RuCl$_4$(NO)(Hind)]$^-$	$K = (k_{c-t})(k_{t-c})$	0.55	0.57	0.45	0.42	0.40		
cis-[OsCl$_4$(NO)(Hind)]$^-$ (**3**)	*cis* → *trans*[a]				0.04(1)	0.08(1)	0.6(1)	2.3(2)
trans-[OsCl$_4$(NO)(Hind)]$^-$ (**4**)	*trans* → *cis*				1.26(1)	2.68(2)	11.4(1)	36.6(7)
[OsCl$_4$(NO)(Hind)]$^-$	$K = (k_{c-t})(k_{t-c})$				0.03	0.03	0.05	0.06

[a] The kinetic parameters were obtained from reversible first order law analysis of *trans* to *cis* conversion data of *trans*-[OsCl$_4$(NO)(Hind)]$^-$ (**4**).

Table 4. Activation Parameters ($\Delta H^{\ddagger}$, $\Delta S^{\ddagger}$, $\Delta G^{\ddagger}$) for the isomerization of [*cis*-$MCl_4(NO)(Hind)]^-$ (M = Ru (1), Os(3)) and [*trans*-$MCl_4(NO)(Hind)]^-$ (M = Ru (2), Os(4)) in $C_2D_2Cl_4$[a]

		$\Delta H^{\ddagger}$ (kJ/mol)		$\Delta S^{\ddagger}$ (J/(mol·K))		$\Delta G^{\ddagger}$(25 °C) (kJ/mol)	$\Delta G^{\ddagger}$(110 °C) (kJ/mol)
compound	process	method I	method II	method I	method II	method I	method I
[*cis*-$RuCl_4(NO)(Hind)]^-$ (**1**)	*cis* → *trans*	124.1 ± 0.3	122.8 ± 1.3	−14.9 ± 0.7	−18.7 ± 3.6	128.5	129.8
[*trans*-$RuCl_4(NO)(Hind)]^-$ (**2**)	*trans* → *cis*	143.7 ± 0.5	138.8 ± 1.0	28.5 ± 1.4	31.0 ± 2.7	135.2	132.8
[*cis*-$OsCl_4(NO)(Hind)]^-$ (**3**)	*cis* → *trans*[b]	200.7 ± 0.7		142.7 ± 8.9		161.7	146.0
[*trans*-$OsCl_4(NO)(Hind)]^-$ (**4**)	*trans* → *cis*	168.2 ± 0.6		85.4 ± 3.9		144.9	135.5

[a] Estimation from method I by fitting k_1 and k_{-1} by Eyring equation (eq 5) and by method II, simultaneously fitting the all population ratios at different temperatures via eqs 3 and 4 with constraining eq 5. [b] The kinetic parameters were obtained from reversible first order law analysis of *trans* to *cis* conversion data of **4**.

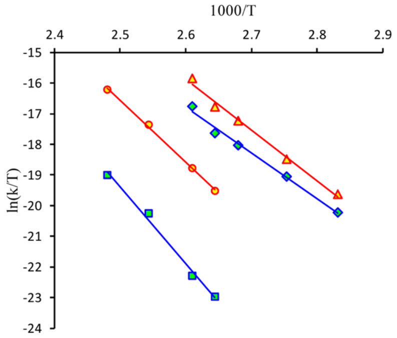

Figure 7. Eyring plots for the isomerization reactions of [$MCl_4(NO)(Hind)]^-$ *trans* to *cis* (in red) (M = Ru (**2**) (Δ), Os (**4**) (○)) and *cis* to *trans* (in blue) (M = Ru (**1**) (◊), Os (**3**) (□)) in $C_2D_2Cl_4$. The solid lines are the best fits with activation parameters quoted in Table 4.

reported for *trans* to *cis* isomerization of [$Os(tpy)Cl_2(N)]^+$, where tpy = terpyridine ($\Delta H^{\#} = 78 \pm 8$ kJ/mol $\Delta S^{\#} = 79 \pm 10$ J/mol·K),[84] while the entropy factors are similar.[84]

The equilibrium constants at different temperatures were obtained as a ratio between the rate constant for *trans→cis* and *cis→trans* isomerizations (Table 3). The equilibrium constants (K_i) for isomerization of [$RuCl_4(NO)(Hind)]^-$ are not changing much with temperature and vary slightly between 0.57 and 0.40, indicating the low thermodynamic differences between *cis* and *trans* isomers.

The thermodynamic parameters ($\Delta H° = 13.5 \pm 1.5$ kJ/mol; $\Delta S° = -5.2 \pm 3.4$ J/(mol·K)) for [$RuCl_4(NO)(Hind)]^-$ isomerization have been obtained by fitting the experimental data with eq 6 (see van't Hoff plot in Figure S10 of Supporting Information):

$$\ln K = -\frac{\Delta H°}{RT} + \frac{\Delta S°}{R} \qquad (6)$$

The enthalpy of isomerization reaction obtained from van't Hoff plot is close to value obtained from difference between two enthalpy of activation ($\Delta H° = \Delta H^{\ddagger}_{trans-cis} - \Delta H^{\ddagger}_{cis-trans}$) $\Delta H°$ = 16 kJ/mol (method I) and 19.6 kJ/mol (method II). For osmium complexes, the equilibrium constants have low values (0.03−0.06) and suggest the dominant stability of the *cis* isomer. This result is in accordance with the evolution of NMR spectra for [*trans*-$OsCl_4(NO)(Hind)]^-$ (Figure 4), which was almost completely transformed into the *cis* isomer upon heating.

Note that the isomerization also occurs in DMSO-d_6 (see Figure S11). However, the isomerization in DMSO is accompanied by the ligand substitution process (DMSO/indazole). Detailed investigation of isomerization in different solvents and of exchange/substitution reactions will be part of a separate work.

Electrochemistry. The cyclic voltammograms of ruthenium and osmium complexes **1**−**4** in CH_3CN containing 0.10 M $TBAPF_6$ as the supporting electrolyte using a glassy carbon working electrode and a saturated calomel electrode (SCE) as a reference electrode are shown in Figures S12 and 8, respectively. The redox processes occur exclusively on the complex anions [$MCl_4(NO)(Hind)]^-$, where M = Ru or Os. The cyclic voltammograms of **1** and **2** showed a large irreversible reduction wave at −1.0 V and an irreversible oxidation wave at 1.77 V vs SCE (Figure S12). The multiscan cyclic voltammetry on the oxidation peak at 0.1 V/s is characterized by a dramatic decrease of the peak intensity, presumably due to nonconductor deposit generation. The peak intensities (normalized vs concentration) are similar for **1** and **2**, and one-electron processes were determined by calibration with the Fc/Fc^+ couple. In the isomeric mixture, **1** and **2** cannot be distinguished by cyclic voltammetry since the phenomenon of deposit was encountered again during the coulometry with a fast and abnormal decrease of the current intensity. The ruthenium complexes are generally more reactive than the related osmium compounds. This seems to affect their redox processes, in which, both the oxidized and reduced species generated are unstable.

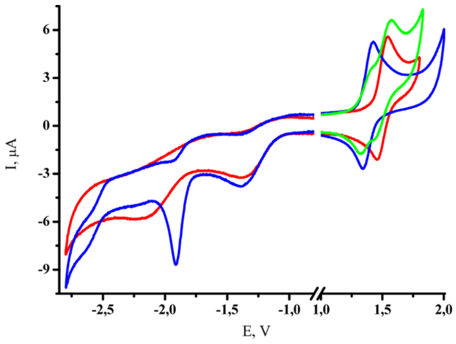

Figure 8. Cyclic voltammetry of [*cis*-$OsCl_4(NO)(Hind)]^-$ (red), [*trans*-$OsCl_4(NO)(Hind)]^-$ (blue), and their mixture (green) at 100 mV/s on GC electrode (3 mm) in 0.1 M $TBAPF_6$ in CH_3CN (see also Figure S17).

The cyclic voltammograms of the osmium complexes **3** and **4** display two irreversible reductions and a reversible oxidation wave (Figure 8) with $E_{1/2}$ = 1.40 and 1.52 V vs SCE for *trans* **3** and *cis* **4** complexes, respectively (Figure 8). The difference in redox potentials indicates that the two isomers can be identified by standard cyclic voltammetry measurement (see Experimental Section and Figure 8). The linear dependence of the oxidation peak current I_p versus the square-root of the scan rate potential between 0.025 and 0.3 V/s for **3** and **4** is indicative of a diffusion-controlled process. Moreover, the oxidation peak intensities (at the same concentration) of **3** and **4** are similar (Figure 8). The exhaustive electrolysis of **4** performed at 2.00 V exhibited a one-electron oxidation accompanied by development of a new visible absorption band with λ_{max} at 519 nm (Figures S13 and S14). The cyclic voltammetry followed after electrolysis showed the same reversible wave, indicating the stability of the oxidized state of **4** under an inert atmosphere. Similar electrochemical behavior was reported for $[OsCl_5(NO)]^{2-}$.[89−91]

Thus, we can assign a reversible one-electron oxidation for these two isomers as follows:

$$\underset{\textit{cis}\text{ or trans}}{[OsCl_4(NO)(Hind)]^-} \rightleftharpoons \underset{\textit{cis}\text{ or trans}}{[OsCl_4(NO)(Hind)]} + e$$

An exhaustive electrolysis of **3** at 2.00 V resulted in the appearance of a new visible band with λ_{max} at 502 nm (Figures S15 and S16). Unexpectedly, the determined electron apparent number value was $n_{app} = 2$ (Figure S18). The voltammograms recorded immediately after coulometry showed the disappearance of all the initial redox processes. So, the oxidized form of **3** appeared to be stable at the time scale of the cyclic voltammetry but unstable at the time scale of the coulometry. From the NMR experiment at room temperature, cis isomer **3** undergoes a slow isomerization into **4**. By association with the electrochemical results, a general mechanism can be proposed as summarized in Scheme 2:

Scheme 2. *cis*−*trans* Isomerization Reactions (Red Outline) Associated with the Redox Processes (Black Outline)

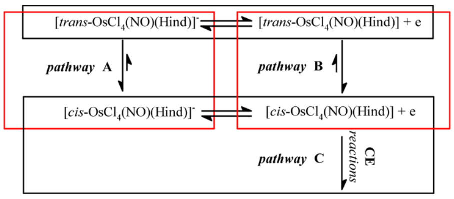
[trans-OsCl$_4$(NO)(Hind)]$^-$
[trans-OsCl$_4$(NO)(Hind)] + e
pathway A
pathway B
[cis-OsCl$_4$(NO)(Hind)]$^-$
[cis-OsCl$_4$(NO)(Hind)] + e
pathway C
CE reactions

The same isomerization reaction can be envisaged from the one-electron oxidized form of **4** in agreement with the mechanism presented in Scheme 2. Some examples of a redox-induced *cis*−*trans* isomerization of metal complexes are well-documented in the literature.[92] In order to prove whether pathway B in Scheme 2 is indeed operative in our case, the multiscan cyclic voltammetry of **4** at a slow scan rate of potential was performed to generate the 1e oxidized species of **4** at the electrode, which could hypothetically convert into the corresponding isomer (1e oxidized form of **3**). However, no mixture of one-electron oxidized species of **4** and **3** was observed in the diffusion layer during the experiment. This result indicates that (i) pathway B is not operative or (ii) the rate of the transformation of 1e oxidized species of **4** into the corresponding oxidized form of **3** is very slow, and we cannot observe it on the time scale of our experiments. Finally, on the time scale of the coulometry, we observed a more complex mechanism which led to the degradation of the oxidized form of **3** after two electrons transfer according to pathway C. We can suggest a CE mechanism in which the chemical reaction C can be considered slow on the time scale of the cyclic voltammetry.[93] Indeed, the system **3**/1e oxidized **4** is reversible in cyclic voltammetry, even at a slow scan rate of the potential. On the coulometry time scale, the process is irreversible because a chemical reaction occurs followed by an irreversible 1e oxidation reaction in accord with a general ECE mechanism with a global apparent electron number value $n_{app} = 2$.

Computational Study. The theoretical analysis starts with a brief comparison of the calculated NO stretching vibrational frequencies of **1**−**4** to their experimental values. This allows for verifying the experimental distinguishability of the *cis* and *trans* isomers by the ν(NO) wavenumber in the IR spectrum, that is the most prominent peak in the IR spectra of all investigated compounds. It deserved particular attention for two reasons: first, it is the peak with the highest intensity, and second, its vibrational frequency differs for the *cis* and *trans* isomers due to different *trans* effects of the chlorido and indazole ligands.

Table 5 shows calculated and experimental wavenumber values for the NO vibrational frequency. The *trans* isomers (**2** and **4**) show an NO absorption frequency which is larger by ca. 30 cm^{-1} than that of the corresponding *cis* isomers. Although calculations overestimate the NO absorption frequency by ca. 20 cm^{-1} on average, the error is systematic; i.e., the difference between the NO frequencies in *trans* and *cis* compounds is almost the same. Thus, the calculations support the distinguishability of the *cis* and *trans* isomers by their NO vibrational frequencies. The good agreement between the experimental and the B3LYP/6-31G* geometries validates the employed method for the calculation of equilibrium geometries.

Table 5. Experimental and Scaled NO Stretching Vibrations (in cm^{-1}) at the B3LYP/6-31G* Level of Theory

complex	1	2	3	4
calculated	1863	1892	1829	1860
experimental	1846	1875	1805	1838

In the following, we discuss the *cis*↔*trans* isomerization mechanism of the $[RuCl_4(NO)(Hind)]^-$ complex. We present and compare activation energies for three different isomerization pathways: the dissociative mechanism with intermediates, the associative mechanism, and the twist mechanism. The outlines for the three mechanisms showing the involved transition states and intermediates are given in Figure 9, showing the most relevant geometrical parameters. All the optimized values can be found in the Supporting Information (Tables S1−S9). Although the mechanisms are described only in the *cis* → *trans* direction, they are thermodynamically reversible, and hence the described reaction paths are also valid for the reverse reaction.

The Dissociative Mechanism. Starting from the *cis* structure, the dissociative mechanism (Figure 9A) is found to consist of three key steps: (i) the dissociation of the indazole ligand, (ii) migration of a Cl^- ligand around the metal center from the axial to the equatorial position, and (iii) reassociation of the indazole ligand. Each of the three substeps shows a transition state and metastable intermediates. After the ligand dissociation (step i), the system is found in a metastable intermediate (a local minimum along the reaction coordinate, labeled *cis-min*) showing a distorted square-pyramidal coordination geometry around Ru. This minimum presents a hydrogen bond-like interaction of the NH group of the indazole with one of the Cl ligands. The H−Cl bond length in *cis-min* is 2.10 Å and remains in the range of 2.10−2.38 Å throughout all intermediates and transition states. The Cl−Ru−

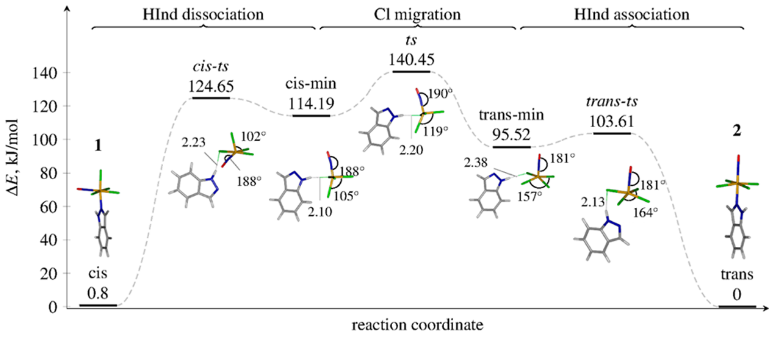

A) dissociative mechanism

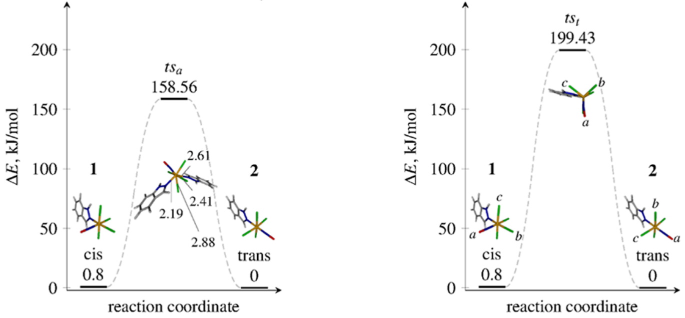

B) associative mechanism **C) twist mechanism**

Figure 9. Schematic representation of three *cis*−*trans* isomerization mechanisms investigated for $[RuCl_4(NO)(Hind)]^-$: dissociative (A), associative (B), and twist (C). The involved transition states and the reaction intermediates are shown, together with the most relevant geometrical parameters (in Å and degrees) obtained at the B3LYP/6-31G* level of theory in the gas phase. The relative energies are calculated at the PCM-B2GP-PLYP/6-311G*//B3LYP/6-31G* level of theory. The labels *cis-ts*, *ts*, and *trans-ts* refer to transition states, while *cis-min* and *trans-min* are intermediates. For a better illustration of the twist mechanism (c), the letters *a*, *b*, and *c* mark the NO−Cl−Cl triangle. Upon the isomerization, the triangle rotates around the ruthenium atom, as shown in the figure.

Cl angle increases from 90° in the *cis* compound to 102° in the *cis-min* structure.

The ligand dissociation from the *cis* complex is immediately accompanied with an NO bending up to 9° out of the Ru−Cl−N plane: this is most likely due to the noninnocent character of the NO ligand, i.e. the ability of NO to donate another electron pair to ruthenium after the indazole ligand has dissociated. Upon conversion to the *trans* structure, NO becomes linear again during step ii. In step ii, the *cis-min* structure is easily converted to another, more stable *trans-min* intermediate via the transition state *ts*, which shows a trigonal-bipyramidal coordination geometry around Ru. Both the *cis-min* and the *trans-min* structures show a square-pyramidal coordination geometry with the Ru atom coming out from the basal plane. In the *cis-min* structure, one of the Cl^- ligands is bound apically, while in the *trans-min* structure, all four Cl^- ligands are equatorially bound. The Cl^- migrates from the apical position in *cis-min* to the equatorial position in *trans-min*, while the rest of the coordination sphere remains almost unchanged—only the Cl−Ru−Cl angle changes from 105° in *cis-min* via 119° in *ts* to 158° in *trans-min*. Step iii, the final step, is the reversion of the step i, where an indazole ligand reassociates to the square-pyramidal coordination polyhedron and completes the isomerization process. The dissociative mechanism described herein is similar to that of Berry pseudorotation in PF_5.[94−97] In our case, the square-pyramidal transition states (*cis-ts* and *trans-ts*) are more stable than the trigonal-bipyramidal intermediate (*ts*). This can be explained by a large crystal field splitting of 4d orbitals of ruthenium.

The Associative and the Twist Mechanisms. The associative mechanism involves coordination of a second indazole ligand to ruthenium, resulting in a pentagonal−bipyramidal coordination geometry around ruthenium in the transition state (Figure 9B). The transition state (labeled ts_a) is asymmetric: the Ru−indazole bond lengths for the indazoles attached *cis* and *trans* relatively to the NO are 2.19 and 2.41 Å, respectively. The Ru−Cl bond lengths are not identical either. One of them involving the chlorido ligand between the two indazole ligands is of 2.88 Å, while the other Ru−Cl bonds are shorter at 2.41 Å. Inspection of the vibrational normal mode associated with the imaginary frequency shows that ts_a is also a transition state for the indazole vs chlorido ligand substitution reaction: while in a direct *cis*↔*trans* isomerization one would expect a transition state with an imaginary frequency associated with an asymmetric indazole−indazole stretch, the found saddle point normal mode is a linear combination of the indazole−indazole and indazole−chlorido asymmetric stretches.

The twist mechanism (Figure 9C) is likewise mediated by one transition state (ts_t), where the NO−Cl−Cl triangle (marked with *a*, *b*, and *c* in Figure 9C) rotates on top of the central atom and the three remaining ligands. This transition state shows a trigonal-prismatic coordination geometry around ruthenium. Along with the NO−Cl−Cl rotation, the indazole ligand rotates slightly around the Ru−N bond, so that the two H atoms of the indazole close to other chlorido ligands can maintain hydrogen bond-like interactions with them. The vibrational normal-mode analysis of the transition state shows a low frequency corresponding to the Ru−indazole stretching normal mode. A relaxed potential energy surface scan at the B3LYP/6-31G* level of theory along with the normal modethe Ru-indazole stretching coordinate has revealed that at slightly longer Ru−indazole distances (2.481 Å) this coordinate

Table 6. Electronic Energies (in kJ/mol, Relative to the *trans* Compound 2 for cis (1) and trans (2) Minima), Transition States and Associated Intermediates Calculated at Different Levels of Theory

	(A) dissociative mechanism							(B) associative	(C) twist
method	*cis* (1)	*cis-ts*	*cis-min*	*ts*	*trans-min*	*trans-ts*	*trans* (2)	ts_a	ts_t
$B3LYP_{gas}$[a]	15.28	96.03	91.29	92.12	72.85	86.6	0	139.19	193
$B3LYP_{sol}$[b]	−3.94	111.99	107.65	125.3	90.56	94.82	0	140.47	189.09
$B2GP\text{-}PLYP_{gas}$[c]	27.61	118.38	109.04	112.08	87.02	105.99	0	163.68	192.58
$B2GP\text{-}LYP_{sol}$[d]	0.8	124.65	114.19	140.45	95.52	103.61	0	158.56	199.43
ΔH^0	16.0			138.8[e]			0	138.8[e]	138.8[e]

[a] B3LYP/6-31G*. [b] PCM-B3LYP/6-311G*//B3LYP/6-31G*. [c] B2GP-PLYP/6-311G*//B3LYP/6-31G*. [d] PCM-B2GP-PLYP/6-311G*//B3LYP/6-31G*. [e] Activation enthalpy is obtained without explicit considerations of a particular transition state.

becomes dissociative; in other words, an indazole ligand dissociates very easily from the twist transition state.

Relative Thermodynamic Stabilities and Activation Energies. Table 6 quotes the relative energies of **1** and **2** and all the transition state species involved in the isomerization reaction. The enthalpy $\Delta H°$ for the isomerization reaction is taken from Table 4, and it is equal to the difference between activation enthalpy obtained from kinetic study $\Delta H^{\ddagger}$ for the *trans* → *cis* and *cis* → *trans* reactions. This value corresponds to the rate limiting step transition state (*ts* in Figure 9A). The experimental enthalpy for the *cis* compound is calculated as the difference of the experimental activation enthalpies $\Delta H^{\ddagger}$ for the *cis* → *trans* and *trans* → *cis* isomerization, also taken from Table 4 (method II):

$$\Delta H^{\circ} = \Delta H^{\ddagger}_{trans\rightarrow cis} - \Delta H^{\ddagger}_{cis\rightarrow trans}$$

All calculated energies are relative to the *trans* compound **2**. Moreover, electronic energies are used instead of calculated enthalpies: B3LYP/6-31G* enthalpies at 298 K show that the deviations of electronic energies from enthalpies are under 1 kJ/mol. A comparison of calculated electronic energies with experimental activation enthalpy as performed here introduces errors which are negligible in comparison to the intrinsic error of the method.

As can be clearly seen, the thermodynamic values obtained with B3LYP and B2GP-PLYP functionals are substantially different, confirming the need of a highly accurate functional for estimating energetics. However, the inclusion of the solvent with the PCM method is reflected in a similar manner for both B3LYP and B2GP-PLYP functionals. For instance, in the dissociative mechanism, the *cis* isomer is stabilized by ca. 19 kJ/mol and ca. 27 kJ/mol, respectively, as compared to the *trans*, while the limiting step transition state (*ts*) is destabilized (by 33 and 28 kJ/mol), increasing the total activation energy for the reaction. The increase of the activation energy for the dissociative mechanism is consistent with the fact that it is harder for the ligand to escape the metal coordination sphere to initiate a reaction when the molecule is trapped in a solvent cage. This is not relevant for the twist mechanism, where no dissociation is required to initiate the reaction. Accordingly, the solvent effect on the activation barrier is much smaller (less than 10 kJ/mol).

Conspicuously, the B3LYP/6-31G* gas phase result for the relative *cis*—*trans* thermodynamic stability (15.3 kJ/mol) is very close to the experimental value (13.5 kJ/mol). However, the inclusion of the solvent effects changes the value down to −3.9 kJ/mol, leading to the *cis* isomer being thermodynamically more stable than the *trans*, in contrast to the experiment. This evidences the importance of including solvent effects. Both the gas phase and PCM values obtained with the B2GP-PLYP functional are in line with the experiment, although the solvated value predicts both *cis* and *trans* isomers as almost degenerate. We attribute the discrepancy between the experimental and B2GP-PLYP calculated value at least in part to the fit errors in the Eyring plots.

The best value for the activation energy in the dissociative mechanism is given by the PCM-B2GP-PLYP/6-311G* (140.45 kJ/mol, see *ts* energy in Table 6), remarkably close to the experimental activation enthalpy (138.8 kJ/mol). At the same level of theory, the corresponding energies for the associative and twist mechanisms are higher in energy, i.e. ca. 159 and 200 kJ/mol, respectively. It is important to note that regardless of the functional and the exact comparison with the experimental value, the activation energy for the dissociative mechanism is the lowest. Therefore, we propose the dissociative mechanism as the primary mechanism for the *cis*↔*trans* isomerization of the ruthenium complexes.

■ CONCLUSION

In this work, we report on the synthesis and crystal structures of ruthenium and osmium compounds of the general formula $(Bu_4N)[MCl_4(NO)(Hind)]$, where M = Ru or Os and Hind = 1*H*-indazole. All compounds have an octahedral $\{MCl_4N_2\}$ structure and have been isolated as *cis* and *trans* isomers. The negative charge of each complex is counterbalanced by one tetrabutylammonium (Bu_4N^+) cation. A good solubility of the compounds in aprotic solvents assured by the presence of the (Bu_4N^+) cation allowed for the investigation of these compounds in solution by electrochemistry and NMR spectroscopy.

NMR spectroscopy showed that the *cis* and *trans* complexes are stable in DMSO and $C_2D_2Cl_4$ solutions at room temperature. In the case of ruthenium complexes, the *cis*↔*trans* isomerization in $C_2D_2Cl_4$ solution is discovered at temperatures above 80 °C. For osmium complexes, the isomerization process occurs at temperatures above 100 °C in accord with higher inertness of osmium complexes as compared to ruthenium counterparts. A kinetic investigation by NMR spectroscopy revealed that the isomerization reaction corresponds to a reversible first order process. The rates of isomerization reaction even at 110 °C are very low at 10^{-5} s^{-1} in the case of ruthenium and 10^{-6} s^{-1} in the case of osmium. The activation parameters, which have been obtained from fitting the reaction rates at different temperatures to the Eyring equation, are also in line with the inertness of these systems. The entropy of activation for the isomerization process of the osmium compounds is highly positive and suggests the dissociative mechanism of isomerization. In the case of ruthenium, the activation entropy for the *cis* to *trans* isomerization is negative (−18.6 J/(mol·K)), but positive for the *trans* to *cis* isomerization reaction (31.0 J/(mol·K)). The thermodynamic parameters for *cis/trans* isomerization of $[RuCl_4(NO)(Hind)]^-$, viz., $\Delta H^\circ = 13.5 \pm 1.5$ kJ/mol and $\Delta S^\circ = -5.2 \pm 3.4$ J/(mol·K), indicate the low difference between the energy of *cis* and *trans* isomers. The obtained thermodynamic parameters are consistent with kinetic results. Estimation of rates of the isomerization reactions at room temperature is on the order of 10^{-10} s^{-1}, representing one of the slowest isomerization processes reported so far.

The theoretical calculation of possible isomerization mechanisms has been carried out on ruthenium complexes with DFT methods. The dissociative, associative, and intramolecular twist isomerization mechanisms have been considered. The best value for the activation energy is given for the dissociative mechanism by the PCM-B2GP-PLYP/6-311G* method (140.5 kJ/mol), close to the experimental activation enthalpy (138.8 kJ/mol). At the same level of theory, the corresponding energies for the associative and twist mechanisms are higher in energy, i.e., ca. 159 and 200 kJ/mol, respectively. Electrochemical investigation confirmed higher reactivity of ruthenium complexes compared to those of osmium and showed that intramolecular electron transfer reactions do not affect the isomerization process. On the basis of the results above and also taking into account the high temperature of reactions, we propose the dissociative mechanism as the primary mechanism for the *cis*↔*trans* isomerization of both the ruthenium and osmium complexes.

■ ASSOCIATED CONTENT

Ⓢ Supporting Information

Crystallographic refinement details, NMR spectra, and results of kinetic analysis for **1**−**4**; results of theoretical calculation for **1** and **2**; and calculated structures (in xyz format) for **1**, **2**, and all transition states and intermediates for the theoretically investigated mechanism. This material is available free of charge via the Internet at http://pubs.acs.org.

■ AUTHOR INFORMATION

Corresponding Author

*E-mail: ghenadie.novitchi@lncmi.cnrs.fr (G. N.); leticia.gonzalez@univie.ac.at (L.G.); vladimir.arion@univie.ac.at (V. B. A.); luneau@univ-lyon1.fr (D. L.).

Notes

The authors declare no competing financial interest.

■ ACKNOWLEDGMENTS

We thank Dr. Jozef Kožišek and Alexander Roller for collection of X-ray data sets for complexes **3** and **4**, respectively. The authors also thank Professor André E. Merbach from École Polytechnique Fédérale de Lausanne (EPFL) and Dr. S. Shova from The State University of Moldova for useful discussions and suggestions. This work was done in the frame of an Austrian−French joint project supported in France by ANR (Agence Nationale de la Recherche) through project ANR-09-BLAN-0420-01 (VILYGRu) and in Austria by FWF (Fonds zur Förderung der Wissenschaftlichen Forschung) through the project I 374-N19. The PHC Amadeus is also greatly acknowledged for his support.

■ REFERENCES

(1) Baumann, F.; Kaim, W.; Baraldo, L. M.; Slep, L. D.; Olabe, J. A.; Fiedler, J. *Inorg. Chim. Acta* **1999**, *285*, 129−133.

(2) Ferlay, S.; Schmalle, H. W.; Francese, G.; Stoeckli-Evans, H.; Imlau, M.; Schaniel, D.; Woike, T. *Inorg. Chem.* **2004**, *43*, 3500−3506.

(3) Schaniel, D.; Woike, T. *Phys. Chem. Chem. Phys.* **2009**, *11*, 4391−4395.

(4) Schaniel, D.; Woike, T.; Behrnd, N. R.; Hauser, J.; Kramer, K. W.; Todorova, T.; Delley, B. *Inorg. Chem.* **2009**, *48*, 11399−11406.

(5) Zangl, A.; Klufers, P.; Schaniel, D.; Woike, T. *Dalton Trans.* **2009**, 1034−1045.

(6) Singh, P.; Sarkar, B.; Sieger, M.; Niemeyer, M.; Fiedler, J.; Zalis, S.; Kaim, W. *Inorg. Chem.* **2006**, *45*, 4602−4609.

(7) Cormary, B.; Ladeira, S.; Jacob, K.; Lacroix, P. G.; Woike, T.; Schaniel, D.; Malfant, I. *Inorg. Chem.* **2012**, *51*, 7492−7501.

(8) Zuech, E. A.; Hughes, W. B.; Kubicek, D. H.; Kittleman, E. T. *J. Am. Chem. Soc.* **1970**, *92*, 528−531.

(9) Wilson, S. T.; Osborn, J. A. *J. Am. Chem. Soc.* **1971**, *93*, 3068−3070.

(10) Videla, M.; Jacinto, J. S.; Baggio, R.; Garland, M. T.; Singh, P.; Kaim, W.; Slep, L. D.; Olabe, J. A. *Inorg. Chem.* **2006**, *45*, 8608−8617.

(11) Roncaroli, F.; Videla, M.; Slep, L. D.; Olabe, J. A. *Coord. Chem. Rev.* **2007**, *251*, 1903−1930.

(12) Montenegro, A. C.; Amorebieta, V. T.; Slep, L. D.; Martin, D. F.; Roncaroli, F.; Murgida, D. H.; Bari, S. E.; Olabe, J. A. *Angew. Chem., Int. Ed.* **2009**, *48*, 4213−4216.

(13) Serres, R. G.; Grapperhaus, C. A.; Bothe, E.; Bill, E.; Weyhermuller, T.; Neese, F.; Wieghardt, K. *J. Am. Chem. Soc.* **2004**, *126*, 5138−5153.

(14) Radon, M.; Broclawik, E.; Pierloot, K. *J. Phys. Chem. B* **2010**, *114*, 1518−1528.

(15) Hayton, T. W.; Legzdins, P.; Sharp, W. B. *Chem. Rev.* **2002**, *102*, 935−991.

(16) Baraldo, L. M.; Forlano, P.; Parise, A. R.; Slep, L. D.; Olabe, J. A. *Coord. Chem. Rev.* **2001**, *219*, 881−921.

(17) Sinitsyn, N. M.; Svetlov, A. A.; Bobrova, L. V. *Zh. Neorg. Khim.* **1980**, *25*, 780−783.

(18) McCleverty, J. A. *Chem. Rev.* **2004**, *104*, 403−418.

(19) Siladke, N. A.; Meihaus, K. R.; Ziller, J. W.; Fang, M.; Furche, F.; Long, J. R.; Evans, W. J. *J. Am. Chem. Soc.* **2012**, *134*, 1243−1249.

(20) Rose, M. J.; Mascharak, P. K. *Curr. Opin. Chem. Biol.* **2008**, *12*, 238−244.

(21) Tfouni, E.; Truzzi, D. R.; Tavares, A.; Gomes, A. J.; Figueiredo, L. E.; Franco, D. W. *Nitric Oxide-Biol. Chem.* **2012**, *26*, 38−53.

(22) Butler, A. R.; Megson, I. L. *Chem. Rev.* **2002**, *102*, 1155−1165.

(23) Ignarro, L. J.; Byrns, R. E.; Wood, K. S. *Circulation* **1986**, *74*, 287−287.

(24) Carducci, M. D.; Pressprich, M. R.; Coppens, P. *J. Am. Chem. Soc.* **1997**, *119*, 2669−2678.

(25) Khot, U. N.; Novaro, G. M.; Popovic, Z. B.; Mills, R. M.; Thomas, J. D.; Tuzcu, E. M.; Hammer, D.; Nissen, S. E.; Francis, G. S. *New Engl. J. Med.* **2003**, *348*, 1756−1763.

(26) Serli, B.; Zangrando, E.; Gianfeffara, T.; Yellowlees, L.; Alessio, E. *Coord. Chem. Rev.* **2003**, *245*, 73−83.

(27) Rosenberg, B.; Van Camp, L.; Trosko, J. E.; Mansour, V. H. *Nature* **1969**, *222*, 385−386.

(28) *Metal Complexes in Cancer Chemotherapy*; Keppler, B. K., Ed.; Wiley-VCH: Weinheim, Germany, 1993.

(29) Cleare, M. J.; Höschele, J. D. *Plat. Met. Rev.* **1973**, *17*, 2−13.

(30) Cleare, M. J.; Höschele, J. D. *Bioinorg. Chem.* **1973**, *2*, 187−210.

(31) Scaffidi-Domianello, Y. Y.; Meelich, K.; Jakupec, M. A.; Arion, V. B.; Kukushkin, V. Y.; Galanski, M.; Keppler, B. K. *Inorg. Chem.* **2010**, *49*, 5669−5678 (and references therein).

(32) Coluccia, M.; Nassi, A.; Boccarelli, A.; Giordano, D.; Cardellicchio, N.; Locker, D.; Leng, M.; Sivo, M.; Intini, F. P.; Natile, G. *J. Inorg. Biochem.* **1999**, *77*, 31−35.

(33) Bartel, C.; Bytzek, A. K.; Scaffidi-Domianello, Y. Y.; Grabmann, G.; Jakupec, M. A.; Hartinger, C. G.; Galanski, M.; Keppler, B. K. *J. Biol. Inorg. Chem.* **2012**, *17*, 465−474.

(34) Arion, V. B.; Reisner, E.; Fremuth, M.; Jakupec, M. A.; Keppler, B. K.; Kukushkin, V. Y.; Pombeiro, A. J. L. *Inorg. Chem.* **2003**, *42*, 6024−6031.
(35) Stepanenko, I. N.; Cebrian-Losantos, B.; Arion, V. B.; Krokhin, A. A.; Nazarov, A. A.; Keppler, B. K. *Eur. J. Inorg. Chem.* **2007**, 400−411.
(36) Kolf, S.; Preetz, W. *Z. Anorg. Allg. Chem.* **1999**, *625*, 411−416.
(37) Ni, W. X.; Man, W. L.; Yiu, S. M.; Ho, M.; Cheung, M. T. W.; Ko, C. C.; Che, C. M.; Lam, Y. W.; Lau, T. C. *Chem. Sci.* **2012**, *3*, 1582−1588.
(38) Bučinský, L.; Büchel, G. E.; Ponec, P.; Breza, M.; Kožíšek, J.; Gall, M.; Biskupič, S.; Fronc, M.; Schiessl, K.; Cuzan, O.; Prodius, D.; Turta, C.; Shova, S.; Zajac, D. A.; Arion, V. B. *Eur. J. Inorg. Chem.* **2013**, 2505−2519.
(39) Bhattacharyya, R.; Saha, A. M.; Ghosh, P. N.; Mukherjee, M.; Mukherjee, A. K. *J. Chem. Soc., Dalton Trans.* **1991**, 501−510.
(40) Fritz, H. P.; Keller, H. J.; Schwarzhans, K. E. *J. Organomet. Chem.* **1967**, *7*, 105.
(41) Helm, L. *NMRICMA 3.0*; Institut des Sciences et Ingénierie Chimiques, EPFL: Lausanne, Switzerland, 2003.
(42) Yerly, F. *VISUALIZEUR-OPTIMISEUR*; EPFL: Lausanne, Switzerland, 2001.
(43) *SAINT-Plus*, version 7.06a; *APEX2*; Bruker-Nonius AXS Inc.: Madison, WI, 2004.
(44) *CrysAlisPro*; Oxford Diffraction Ltd.: Abingdon, England, 2009.
(45) Clark, R. C.; Reid, J. S. *Acta Crystallogr.* **1995**, *A51*, 887−897.
(46) Sheldrick, G. *Acta Crystallogr., Sect. A* **2008**, *64*, 112−122.
(47) Johnson, G. K. *Report ORNL-5138*; OAK Ridge National Laboratory: Oak Ridge, TN, 1976.
(48) Becke, A. D. *J. Chem. Phys.* **1993**, *98*, 5648−5652.
(49) Lee, C. T.; Yang, W. T.; Parr, R. G. *Phys. Rev. B* **1988**, *37*, 785−789.
(50) Andrae, D.; Haussermann, U.; Dolg, M.; Stoll, H.; Preuss, H. *Theor. Chim. Acta* **1990**, *77*, 123−141.
(51) Scott, A. P.; Radom, L. *J. Phys. Chem.* **1996**, *100*, 16502−16513.
(52) Karton, A.; Tarnopolsky, A.; Lamere, J. F.; Schatz, G. C.; Martin, J. M. L. *J. Phys. Chem. A* **2008**, *112*, 12868−12886.
(53) Escudero, D.; Weisheit, T.; Weigand, W.; González, L. *Dalton Trans.* **2010**, *39*, 9505−9513.
(54) Cances, E.; Mennucci, B. *J. Math. Chem.* **1998**, *23*, 309−326.
(55) Mennucci, B.; Cances, E.; Tomasi, J. *J. Phys. Chem. B* **1997**, *101*, 10506−10517.
(56) Miertus, S.; Scrocco, E.; Tomasi, J. *Chem. Phys.* **1981**, *55*, 117−129.
(57) Cammi, R.; Tomasi, J. *J. Comput. Math.* **1995**, *16*, 1449−1458.
(58) Scalmani, G.; Frisch, M. J. *J. Chem. Phys.* **2010**, *132*, 114110.
(59) Frisch, M. J.; Trucks, G. W.; Schlegel, H. B.; Scuseria, G. E.; Robb, M. A.; Cheeseman, J. R.; Scalmani, G.; Barone, V.; Mennucci, B.; Petersson, G. A.; Nakatsuji, H.; Caricato, M.; Li, X.; Hratchian, H. P.; Izmaylov, A. F.; Bloino, J.; Zheng, G.; Sonnenberg, J. L.; Hada, M.; Ehara, M.; Toyota, K.; Fukuda, R.; Hasegawa, J.; Ishida, M.; Nakajima, T.; Honda, Y.; Kitao, O.; Nakai, H.; Vreven, T.; Montgomery, J. A., Jr.; Peralta, J. E.; Ogliaro, F.; Bearpark, M.; Heyd, J. J.; Brothers, E.; Kudin, K. N.; Staroverov, V. N.; Kobayashi, R.; Normand, J.; Raghavachari, K.; Rendell, A.; Burant, J. C.; Iyengar, S. S.; Tomasi, J.; Cossi, M.; Rega, N.; Millam, J. M.; Klene, M.; Knox, J. E.; Cross, J. B.; Bakken, V.; Adamo, C.; Jaramillo, J.; Gomperts, R.; Stratmann, R. E.; Yazyev, O.; Austin, A. J.; Cammi, R.; Pomelli, C.; Ochterski, J. W.; Martin, R. L.; Morokuma, K.; Zakrzewski, V. G.; Voth, G. A.; Salvador, P.; Dannenberg, J. J.; Dapprich, S.; Daniels, A. D.; Farkas, Ö.; Foresman, J. B.; Ortiz, J. V.; Cioslowski, J.; Fox, D. J. *Gaussian 09*; Gaussian, Inc.: Wallingford, CT, 2009.
(60) Krause, R. A.; Krause, K. *Inorg. Chem.* **1980**, *19*, 2600−2603.
(61) Ferreira, V.; Krause, R. A.; Larsen, S. *Inorg. Chim. Acta* **1988**, *145*, 29−38.
(62) Breher, F.; Ruegger, H.; Mlakar, M.; Rudolph, M.; Deblon, S.; Schonberg, H.; Boulmaaz, S.; Thomaier, J.; Grutzmacher, H. *Chem.—Eur. J.* **2004**, *10*, 641−653.
(63) Mebi, C. A.; Frost, B. J. *Inorg. Chem.* **2007**, *46*, 7115−7120.
(64) Kakoti, M.; Chaudhury, S.; Deb, A. K.; Goswami, S. *Polyhedron* **1993**, *12*, 783−789.
(65) Dovletoglou, A.; Meyer, T. J. *J. Am. Chem. Soc.* **1994**, *116*, 215−223.
(66) Bakhmutov, V. I.; Bertran, J.; Esteruelas, M. A.; Lledos, A.; Maseras, F.; Modrego, J.; Oro, L. A.; Sola, E. *Chem.—Eur. J.* **1996**, *2*, 815−825.
(67) Bakhmutov, V. I.; Visseaux, M.; Baudry, D.; Dormond, A.; Richard, P. *Inorg. Chem.* **1996**, *35*, 7316−7324.
(68) Guido, E.; D'Amico, G.; Russo, N.; Sicilia, E.; Rizzato, S.; Albinati, A.; Romeo, A.; Plutino, M. R.; Romeo, R. *Inorg. Chem.* **2011**, *50*, 2224−2239.
(69) Hughes, R. P.; Meyer, M. A.; Tawa, M. D.; Ward, A. J.; Williamson, A.; Rheingold, A. L.; Zakharov, L. N. *Inorg. Chem.* **2004**, *43*, 747−756.
(70) Alibrandi, G.; Scolaro, L. M.; Romeo, R. *Inorg. Chem.* **1991**, *30*, 4007−4013.
(71) Shafaatian, B.; Akbari, A.; Nabavizadeh, S. M.; Heinemann, F. W.; Rashidi, M. *Dalton Trans.* **2007**, 4715−4725.
(72) Ashby, M. T. *J. Am. Chem. Soc.* **1995**, *117*, 2000−2007.
(73) Lu, K. L.; Lo, H. U.; Lin, Y. C.; Wang, Y. *Inorg. Chem.* **1992**, *31*, 4499−4502.
(74) Haynes, A.; McNish, J.; Pearson, J. M. *J. Organomet. Chem.* **1998**, *551*, 339−347.
(75) Yang, F. Z.; Wang, Y. H.; Chang, M. C.; Yu, K. H.; Huang, S. L.; Liu, Y. H.; Wang, Y.; Liu, S. T.; Chen, J. T. *Inorg. Chem.* **2009**, *48*, 7639−7644.
(76) Smith, D. C.; Gray, G. M. *J. Chem. Soc., Dalton Trans.* **2000**, 677−683.
(77) Rapaport, I.; Helm, L.; Merbach, A. E.; Bernhard, P.; Ludi, A. *Inorg. Chem.* **1988**, *27*, 873−879.
(78) Steblerrothlisberger, M.; Hummel, W.; Pittet, P. A.; Burgi, H. B.; Ludi, A.; Merbach, A. E. *Inorg. Chem.* **1988**, *27*, 1358−1363.
(79) Helm, L.; Nicolle, G. M.; Merbach, A. E. *Adv. Inorg. Chem.* **2005**, *57*, 327−379.
(80) Helm, L.; Merbach, A. E. *Chem. Rev.* **2005**, *105*, 1923−1959.
(81) Riblet, F.; Novitchi, G.; Scopelliti, R.; Helm, L.; Gulea, A.; Merbach, A. E. *Inorg. Chem.* **2010**, *49*, 4194−4211.
(82) Novitchi, G.; Riblet, F.; Helm, L.; Scopelliti, R.; Gulea, A.; Merbach, A. E. *Magn. Reson. Chem.* **2004**, *42*, 801−806.
(83) Elguero, J.; Fruchier, A.; Tjiou, E. M.; Trofimenko, S. *Khim. Geterotsikl. Soedin.* **1995**, 1159−1179.
(84) Williams, D. S.; Coia, G. M.; Meyer, T. J. *Inorg. Chem.* **1995**, *34*, 586−592.
(85) Bae, B. J.; Park, J. E.; Kim, Y.; Park, J. T.; Suh, I. H. *Organometallics* **1999**, *18*, 2513−2518.
(86) Cotton, F. A.; Dikarev, E. V.; Wong, W. Y. *Inorg. Chem.* **1997**, *36*, 3268−3276.
(87) Atwood, J. D. *Inorganic and Organometallic Reaction Mechanisms*; Wiley-VCH: Weinheim, Germany, 1997.
(88) Bielski, B. H. J.; Capellos, C. *Kinetic Systems; Mathematical Description of Chemical Kinetics in Solution*; RE Krieger: New York, 1980.
(89) Ooyama, D.; Nagao, N.; Nagao, H.; Sugimoto, Y.; Howell, F. S.; Mukaida, M. *Inorg. Chim. Acta* **1997**, *261*, 45−52.
(90) Svetlov, A. A.; Sinitsyn, N. M. *Zh. Neorg. Khim.* **1986**, *31*, 2902−2914.
(91) Svetlov, A. A.; Sinitsyn, N. M.; Kravchenko, V. V. *Zh. Neorg. Khim.* **1990**, *35*, 336−343.
(92) Pombeiro, A. J. L.; da Silva, M.; Lemos, M. *Coord. Chem. Rev.* **2001**, *219*, 53−80.
(93) Amatore, C.; Azzabi, M.; Calas, P.; Jutand, A.; Lefrou, C.; Rollin, Y. *J. Electroanal. Chem.* **1990**, *288*, 45−63.
(94) Berry, R. S. *J. Chem. Phys.* **1960**, *32*, 933−938.
(95) Tobe, M. L. *Inorganic Reaction Mechanisms*; Nelson: London, 1972.
(96) Ugi, I.; Marquard., D.; Klusacek, H.; Gillespi., P.; Ramirez, F. *Acc. Chem. Res.* **1971**, *4*, 288−296.
(97) Koga, N.; Morokuma, K. *Chem. Rev.* **1991**, *91*, 823−842.

APPENDIX 3.A.2

Analytical gradients of complete active space self-consistent field energies using Cholesky decomposition: Geometry optimization and spin-state energetics of a ruthenium nitrosyl complex

Mickaël G. Delcey, Leon Freitag, Thomas Bondo Pedersen, Francesco
Aquilante, Roland Lindh and Leticia González

J. Chem. Phys. **2014**, *140*, 174103.
`http://dx.doi.org/10.1063/1.4873349`

Contributions:

MICKAËL G. DELCEY developed and implemented the theory, wrote parts of the manuscript.

LEON FREITAG performed the calculations and wrote parts of the manuscript.

THOMAS BONDO PEDERSEN, FRANCESCO AQUILANTE AND ROLAND LINDH conceived the theory, supervised its development and helped in preparation of the manuscript.

LETICIA GONZÁLEZ conceived the idea and the application of the theory, supervised the calculations and helped in preparation of the manuscript.

Reprinted with permission from J. Chem. Phys. **2014**, *140*, 174103. Copyright 2014, AIP Publishing LLC.

THE JOURNAL OF CHEMICAL PHYSICS **140**, 174103 (2014)

Analytical gradients of complete active space self-consistent field energies using Cholesky decomposition: Geometry optimization and spin-state energetics of a ruthenium nitrosyl complex

Mickaël G. Delcey,[1] Leon Freitag,[2] Thomas Bondo Pedersen,[3] Francesco Aquilante,[1,4]
Roland Lindh,[1,5,a)] and Leticia González[2,b)]
[1]*Department of Chemistry – Ångström, The Theoretical Chemistry Programme, Uppsala University, Box 518, 751 20 Uppsala, Sweden*
[2]*Institut für Theoretische Chemie, Universität Wien, Währinger Straße 17, 1090 Vienna, Austria*
[3]*Centre for Theoretical and Computational Chemistry, Department of Chemistry, University of Oslo, P.O. Box 1033 Blindern, 0315 Oslo, Norway*
[4]*Dipartimento di Chimica "G. Ciamician," Università di Bologna, V. F. Selmi 2, 40126 Bologna, Italy*
[5]*Uppsala Center for Computational Chemistry - UC$_3$, Uppsala University, Box 518, 751 20 Uppsala, Sweden*

(Received 4 January 2014; accepted 14 April 2014; published online 2 May 2014)

We present a formulation of analytical energy gradients at the complete active space self-consistent field (CASSCF) level of theory employing density fitting (DF) techniques to enable efficient geometry optimizations of large systems. As an example, the ground and lowest triplet state geometries of a ruthenium nitrosyl complex are computed at the DF-CASSCF level of theory and compared with structures obtained from density functional theory (DFT) using the B3LYP, BP86, and M06L functionals. The average deviation of all bond lengths compared to the crystal structure is 0.042 Å at the DF-CASSCF level of theory, which is slightly larger but still comparable with the deviations obtained by the tested DFT functionals, e.g., 0.032 Å with M06L. Specifically, the root-mean-square deviation between the DF-CASSCF and best DFT coordinates, delivered by BP86, is only 0.08 Å for S_0 and 0.11 Å for T_1, indicating that the geometries are very similar. While keeping the mean energy gradient errors below 0.25%, the DF technique results in a 13-fold speedup compared to the conventional CASSCF geometry optimization algorithm. Additionally, we assess the singlet-triplet energy vertical and adiabatic differences with multiconfigurational second-order perturbation theory (CASPT2) using the DF-CASSCF and DFT optimized geometries. It is found that the vertical CASPT2 energies are relatively similar regardless of the geometry employed whereas the adiabatic singlet-triplet gaps are more sensitive to the chosen triplet geometry. © *2014 AIP Publishing LLC.* [http://dx.doi.org/10.1063/1.4873349]

I. INTRODUCTION

Almost half a century ago, the pioneering work of Pulay[1] on the "force method" marked the era of analytical derivative techniques in quantum chemistry. Since then the vast computational advantage of analytical evaluations of energy derivatives rather than naive numerical differentiation has been assessed over and over again.[2] Modern-day quantum chemistry is therefore shaped around electronic structure models that provide a manageable theoretical and algorithmic formulation of energy derivatives, first of all for variational wave functions and density functional theory (DFT). Efficient analytical energy derivatives can also be computed for nonvariational wave functions by means of the Lagrangian technique.[3] A comprehensive description of analytical energy derivative techniques can be found in, for example, Refs. 2 and 3 and references therein.

A variational wave function theory in widespread use is the complete active space self-consistent field (CASSCF) method.[4,5] The CASSCF approach to the many-electron problem is very general in the sense that it defines a mean-field wave function that is qualitatively correct even for some of the most difficult problems in quantum chemistry. These include the determination of the spin states of radical species and the electronic structure of molecules with low-lying excited states such as transition metal and heavy element containing species. More generally, for the description of chemical bonds and their dissociation, for the energetics of chemical and photochemical reactions, and often for excited electronic states, CASSCF is the most adequate starting point for subsequent quantitative treatments of electron correlation. All these situations share the distinctive feature of a large nondynamical component of the correlation energy. Despite the curse of dimensionality of the CASSCF method, for situations where a suitable and tractable active space can be chosen, correcting the CASSCF energy by means of second-order perturbation theory—the CASSCF/CASPT2 protocol[6]—is often sufficient to obtain a quantitative description of problems featuring strong electron correlation.[7]

Storage and handling of large arrays of electron repulsion integrals (ERIs) present an additional practical limitation of the CASSCF/CASPT2 protocol. In recent years, the range of system sizes tractable with CASSCF/CASPT2 has

---

a)Electronic mail: roland.lindh@kemi.uu.se
b)Electronic mail: leticia.gonzalez@univie.ac.at

This article is copyrighted as indicated in the article. Reuse of AIP content is subject to the terms at: http://scitation.aip.org/termsconditions. Downloaded to IP: 77.80.43.215 On: Tue, 28 Jul 2015 11:52:01

been substantially widened thanks to the development of the Cholesky decomposition (CD)[8–10] and the related *ab initio* density fitting (DF)[11,12] approximation to the ERIs. With the advent of a variety of CD- and DF-based CASSCF/CASPT2 algorithms,[13–16] electronic structure studies on large, often transition metal-containing, molecules are no longer limited to DFT investigations.

In this paper we shall use a newly developed DF-CASSCF analytical gradient algorithm, which is an extension of existing DF-based analytical derivative theory.[17–30] Werner *et al.*[31] have recently presented a DF-CASPT2 gradient algorithm: in their case the calculation of the DF-CASSCF contributions to the gradient uses a straightforward implementation with a potential fourth-order scaling with system size. In the context of a CASPT2 geometry optimization this is acceptable, given the higher scaling of the CASPT2 component of the gradient calculation. However, in various situations, especially for photochemical studies, an improved computational scaling of DF-CASSCF gradients is needed. For the dominant exchange-type contributions, we use a previously developed screening technique[29] which reduces the computational scaling from quartic to cubic.

As a demonstration of the capabilities of the gradient algorithm, ground and first triplet state equilibrium geometries of the *trans*-$[\mathrm{RuCl_4(NO)(1H\text{-}indazole)}]^-$ complex (RuHIndNO), which has recently been synthesized and characterized in Ref. 32, will be optimized at the DF-CASSCF level of theory. The obtained geometries will be compared with those optimized with DFT using some popular functionals commonly employed for transition metal complexes. Additionally, singlet-triplet energy gaps using DFT and DF-CASSCF geometries will be calculated using DF-CASPT2.

II. THEORY

The CD approximation to ERIs[8–10] has made a significant impact on the applicability of CASSCF and CASPT2.[13–16] At the time of the first application of the CD approximation to CASSCF wavefunctions,[13] analytical gradients for the CD representation of the ERIs had not been formulated yet and, indeed, it was unclear if an analytical formulation would be possible at all (a numerical approach was proposed by O'Neal and Simons in 1989).[33] Formulating the CD approach as a special case of DF,[34–37] analytical integral gradients were eventually provided by Aquilante, Lindh, and Pedersen[26] and an implementation of CD-based Hartree-Fock (HF) forces has been reported recently.[29] In this work, we extend this analytical gradient formulation to DF-CASSCF. As discussed above, our approach differs from the DF-CASSCF gradient formulation of Werner *et al.*[31] mainly in the use of screening in the HF-type exchange contributions. A brief account of the theory is presented in this section, while algorithmic details, a more thorough performance analysis, and the extension to state-averaged CASSCF will be presented in a forthcoming publication.

In the CD framework, the atomic orbital (AO) ERIs are approximated by Cholesky vectors $L^J_{\mu\nu}$ according to[8,9]

$$(\mu\nu|\kappa\sigma) \approx \sum_{J=1}^{M} L^J_{\mu\nu} L^J_{\kappa\sigma}, \tag{1}$$

where we have used Mulliken notation and greek letters denote AOs. The number of Cholesky vectors, M, typically range from 3 to 8 times the number of AOs N, depending on the desired integral accuracy (higher accuracy requires more vectors). As shown in detail in Refs. 12 and 26 the CD expression can be recast in the DF form[34–37]

$$(\mu\nu|\kappa\sigma) \approx \sum_{K=1}^{M}\sum_{L=1}^{M} C^K_{\mu\nu}(K|L)C^L_{\kappa\sigma}, \tag{2}$$

with $C^K_{\mu\nu}$ denoting fitting coefficients determined from the equations

$$(K|\mu\nu) = \sum_L (K|L)C^L_{\mu\nu}. \tag{3}$$

The indices K, L represent auxiliary basis functions, here corresponding to the Cholesky vector indices J of Eq. (1).[12,26] The first integral derivative with respect to a nuclear coordinate can now be evaluated analytically from the standard DF expression

$$\begin{aligned}(\mu\nu|\kappa\sigma)^{(1)} \approx{}& \sum_K C^K_{\mu\nu}(K|\kappa\sigma)^{(1)} + \sum_K C^K_{\kappa\sigma}(K|\mu\nu)^{(1)}\\ &-\sum_{KL} C^K_{\mu\nu}(K|L)^{(1)}C^L_{\kappa\sigma}.\end{aligned} \tag{4}$$

The contribution from the ERIs to the total molecular gradient is then given by

$$E^{(1)} \approx 2\sum_{K\mu\nu} P^K_{\mu\nu}(K|\mu\nu)^{(1)} - \sum_{KL} P_{KL}(K|L)^{(1)}, \tag{5}$$

where P_{KL} and $P^K_{\mu\nu}$ are two- and three-index effective densities, respectively, computed as

$$P_{KL} = \sum_{\mu\nu\kappa\sigma} C^K_{\mu\nu} d_{\mu\nu\kappa\sigma} C^L_{\kappa\sigma} \tag{6}$$

and

$$P^K_{\mu\nu} = \sum_{\kappa\sigma} d_{\mu\nu\kappa\sigma} C^K_{\kappa\sigma}, \tag{7}$$

with $d_{\mu\nu\kappa\sigma}$ the 2-body density matrix of the system.

For an optimal implementation, it is useful to separate the 2-body density matrix in distinct contributions. For CASSCF, those are the Coulomb, the exchange and the non-separable active terms. The construction of the effective densities arising from the two former is essentially the same as in our DF-HF implementation described in Refs. 26 and 29. The Coulomb term is rather straightforward:

$$P^K_{\mu\nu} = V^K D_{\mu\nu}, \tag{8}$$

$$P_{KL} = V^K V^L, \tag{9}$$

with

$$V^K = \sum_{\mu\nu} D_{\mu\nu} C^K_{\mu\nu}, \tag{10}$$

and $D_{\mu\nu}$ the 1-body density matrix.

This article is copyrighted as indicated in the article. Reuse of AIP content is subject to the terms at: http://scitation.aip.org/termsconditions. Downloaded to IP: 77.80.43.215 On: Tue, 28 Jul 2015 11:52:01

The exchange term does not factorize so easily. An efficient implementation was done by first Cholesky decomposing the 1-body density matrix

$$D_{\mu\kappa} = \sum_i X_{\mu i} X_{\kappa i}, \tag{11}$$

creating Cholesky orbital coefficients $X_{\mu i}$. From those, one can form the MO-transformed fitting coefficients C_{ij}^K and then compute the effective densities as

$$P_{KL} = \sum_{ij} C_{ij}^K C_{ij}^L, \tag{12}$$

$$P_{\mu\nu}^K = \sum_{ij} C_{ij}^K X_{\mu i} X_{\nu j}. \tag{13}$$

Because of the use of Cholesky orbitals, an efficient screening procedure can be used, reducing the scaling to an effective quadratic scaling.[29] This term remains the most expensive for small to medium-sized molecules, even though other terms still scale cubically. This implementation is significantly more efficient with atomic natural orbital (ANO) basis sets than with correlation-consistent basis sets, as the cost reduction in the computation of integral derivatives is greater with ANOs.[29]

Only one contribution cannot be handled in analogy to HF theory, namely, the active-active contribution to the CASSCF energy, which involves the non-separable two-body density matrix d_{tuvx},

$$E_a = \sum_{tuvx} d_{tuvx} (tu|vx), \tag{14}$$

where t, u, v, x denote active molecular orbitals (MOs). Invoking the DF approximation, the active-active contribution to the energy gradient becomes

$$\begin{aligned} E_a^{(1)} \approx\; & 2 \sum_K \sum_{tuvx} d_{tuvx} C_{tu}^K (K|vx)^{(1)} \\ & - \sum_{KL} \sum_{tuvx} d_{tuvx} C_{tu}^K (K|L)^{(1)} C_{vx}^L. \end{aligned} \tag{15}$$

The two-body density matrix in MO basis is symmetric ($d_{tuvx} = d_{vxtu}$) but not definite. It can be eigenvalue decomposed according to

$$d_{tuvx} = \sum_p Q_{tu}^p \lambda_p Q_{vx}^p = \sum_p \mathrm{sgn}(\lambda_p) W_{tu}^p W_{vx}^p, \tag{16}$$

where $W_{tu}^p = \sqrt{|\lambda_p|} Q_{tu}^p$ and the function sgn(∗) returns the sign of its argument. Since the number of active orbitals is normally very small compared to the number of inactive and secondary orbitals, the cost of this transformation is negligible. This allows us to form the intermediate quantity

$$Z_K^p = \sum_{tu} W_{tu}^p C_{tu}^K, \tag{17}$$

for which the most expensive step is the MO transformation of the fitting coefficients ($MN^2 a + MNa^2$), where a is the number of active orbitals. One can then form the active-active contribution to the two-index effective density matrix P_{KL} as

$$P_{KL} \approx \sum_p \mathrm{sgn}(\lambda_p) Z_K^p Z_L^p, \tag{18}$$

at the cost of $M^2 a^2$ operations, and the contribution to the three-index effective density matrix $P_{\mu\nu}^K$ becomes

$$P_{\mu\nu}^K \approx \sum_t X_{\mu t} \sum_u \left\{ \sum_p \mathrm{sgn}(\lambda_p) Z_K^p W_{tu}^p \right\} X_{\nu u}, \tag{19}$$

where $\boldsymbol{X}$ is the MO coefficient matrix. The overall cost of this step is $MN^2 a$, i.e., cubic scaling with system size (for fixed a). Owing to a small prefactor and $a \ll N$, the (quadratic-scaling) exchange contributions remain the most expensive for small to medium-sized molecules. In practice, this means that the computational cost of DF-CASSCF gradients is comparable to that of DF-HF gradients.

III. COMPUTATIONAL DETAILS

The single-state DF-CASSCF gradients have been implemented in a development version of the MOLCAS quantum chemical software package,[38] which has been used to perform the geometry optimization of the lowest singlet and triplet (S_0 and T_1) electronic states of the RuHIndNO nitrosyl complex. The ANO-RCC-VTZP all-electron basis set[39] and the atomic compact CD auxiliary basis set[11] generated using the CD threshold 0.0001 a.u. (acCD-4) have been used for all atoms including Ru. The molecule has 22 atoms and the number of basis functions adds up to 618 without auxiliaries.

For CASSCF calculations of RuHIndNO, it is desired that the active space comprises the five 4*d* orbitals of the Ru atom, the Ru-Cl bonding orbitals, the whole indazole π system, the two pairs of NO π and π^* orbitals, and possibly also the NO σ and σ^* orbitals, making a total of 27 electrons in 24 orbitals. Unlike in 3*d* transition metals,[40,41] Ru does not require the double-shell *d* orbitals in the active space as long as other correlating orbitals are present;[42] this is the case here. Since such an active space is not computationally feasible for the current CASSCF implementation, we restrict our active space to 16 electrons in 13 orbitals. The starting guess for the optimization employed the five Ru 4*d* orbitals, two pairs of NO π and π^* orbitals, one pair of indazole π and π^* orbitals, one combination of Cl *n* orbitals, which mix with the $d_{x^2-y^2}$ orbitals, and the NO σ orbital, which mixes with the d_{z^2} orbital and therefore participates in the bond formed between the metal and nitrosyl.

Although the same starting guess was used for the singlet and triplet states, the orbitals obtained in the CASSCF energy optimization are not identical. In particular, as the d_{xy} orbital in the S_0 state is strictly non-bonding it was replaced by a Ru–σ_{Ind} orbital, and the correlating pair of the n_{Cl} and $d_{x^2-y^2}$ orbitals has been replaced by another correlating pair consisting of d_{z^2} and σ_{NO}^* orbitals. The resulting final orbitals and corresponding occupation numbers of the optimized S_0 and T_1 geometries are collected in Figs. 1(a) and 1(b), respectively. Every attempt to replace these orbitals manually so that the S_0 and T_1 use the same active space in state-specific calculations was not successful. A number of test calculations indicate that only upon inclusion of the two subsequent roots, i.e., by doing state-average calculation of three states, the starting active space is kept. Since state-averaging three states to describe the S_0 state would deteriorate the quality of the ground

This article is copyrighted as indicated in the article. Reuse of AIP content is subject to the terms at: http://scitation.aip.org/termsconditions. Downloaded to IP: 77.80.43.215 On: Tue, 28 Jul 2015 11:52:01

state wavefunction, we opt for employing single root calculations, at the expense that the active spaces for the singlet and triplet states are not identical. The differences between the active spaces are not as pronounced as they might seem: another optimization of the S_0 state, performed with a smaller active space (14 active electrons in 12 orbitals), identical to the active space of the T_1 state but with the non-bonding d_{xy} orbital removed, resulted in the geometry which is almost identical to the geometry optimized with the active space shown in Fig. 1(a).

For the sake of comparison, the geometries of the S_0 and T_1 states have been also optimized with DFT using the B3LYP,[43,44] M06L,[45] and BP86[46–48] functionals and the def2-TZVPP[49] basis set. The latter functionals have been chosen in view of their good performance in optimizing geometries of transition metal complexes.[41,50–53] For Ru, the MWB28 effective core potential[54] (ECP) has been used. For B3LYP, the DF approximation featuring the chain-of-spheres approximation for the calculation of the Hartree-Fock exchange[55] and for the BP86 functional the RI-J and MARI-J[56,57] approximations are employed. The triplet geometry is optimized within the unrestricted Kohn-Sham procedure. The DFT calculations with the B3LYP functional have been performed using the ORCA 2.9.1 and 3.0[58] suite of programs, the BP86 functional with the TURBOMOLE 6.5 program package,[59] and the M06L functional with the Gaussian 09 D.01 program package.[60]

Vertical singlet-triplet gaps have been evaluated from single point calculations for the T_1 and S_0 states at the S_0 and T_1 geometries, respectively, using DFT with the aforementioned functionals and CASSCF. Adiabatic singlet-triplet gaps are computed using the corresponding relaxed geometries. In addition, CASPT2 calculations are conducted on the state of interest (S_0 or T_1) using a level-shift[61] of 0.3 a.u. Also for these single-point CASPT2 calculations, the acCD-4 auxiliary basis set was used.

IV. RESULTS AND DISCUSSION

A. RuHIndNO geometries

The Ru nitrosyl moiety in RuHIndNO shows similarities to the Fe nitrosyl complexes studied by Radoń, Broclawik, and Pierloot.[41] Just as in the Fe systems, the interaction between Ru and ligands is strongly covalent. In the linear structures, the d_{xz} and d_{yz} orbitals interact with NO π^* orbitals, forming two bonding and two antibonding orbitals denoted $d \pm \pi^*_{x,y}$ in Fig. 1. The d_{z^2} and the NO σ orbital form another pair of bonding and antibonding orbitals denoted $d_{z^2} \pm \sigma$.

The weights of the dominant configurations of the S_0 and T_1 CASSCF wavefunctions in the natural orbital basis are below 100% (76% − 82%, depending on the state and geometry), indicating that a single configuration is not completely sufficient to describe the states. For comparison, the weight of the leading determinant in a full valence CAS of the F_2 and N_2 electronic singlet ground states is about 93%. The remaining ∼20% of the RuHIndNO wavefunction is distributed among many configurations, each with a weight below 2%, similar to the situation encountered in Fe nitrosyl complexes,[41] although to a minor extent. Among the participating configurations are

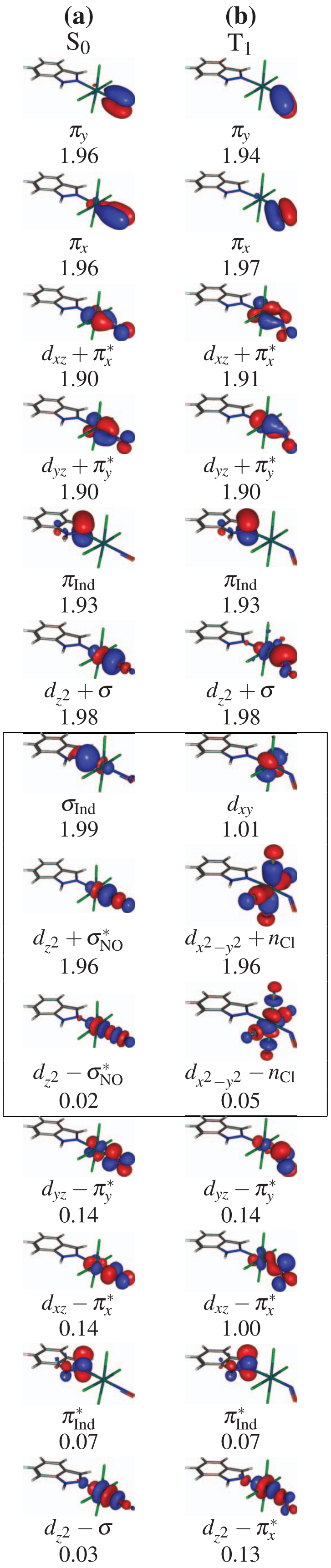

FIG. 1. Active space orbitals and their occupation numbers used in the optimization of the (a) S_0 and (b) T_1 electronic states. The orbitals differing between the active spaces are highlighted in a box.

This article is copyrighted as indicated in the article. Reuse of AIP content is subject to the terms at: http://scitation.aip.org/termsconditions. Downloaded to IP: 77.80.43.215 On: Tue, 28 Jul 2015 11:52:01

TABLE I. Most relevant parameters of the DF-CASSCF and B3LYP optimized geometries of the S_0 and T_1 states. Angles reported in degrees and distances in Å.

	S_0					T_1			
	Expt.	DF-CASSCF	BP86	B3LYP	M06L	DF-CASSCF	BP86	B3LYP	M06L
ϕ	178	180	179	180	180	138	140	139	140
$\theta_{Cl_2-Ru-N_1-O_1}$	…	…	…	…	…	139	134	134	124
$\theta_{Cl_3-Ru-N_2-N_3}$	29.4	− 2.8	− 1.5	− 2.1	0.0	− 3.0	− 0.1	− 8.6	3.5
$d_{N_1-O_1}$	1.144	1.139	1.164	1.146	1.150	1.129	1.183	1.161	1.166
d_{Ru-N_2}	2.104	2.215	2.166	2.174	2.192	2.338	2.229	2.190	2.285
d_{Ru-N_1}	1.717	1.718	1.711	1.700	1.702	1.936	1.838	1.867	1.838
d_{Ru-Cl_1}	2.371	2.416	2.381	2.393	2.386	2.415	2.376	2.386	2.376
d_{Ru-Cl_2}	2.375	2.414	2.391	2.398	2.395	2.412	2.372	2.377	2.340
d_{Ru-Cl_3}	2.386	2.444	2.439	2.438	2.443	2.431	2.415	2.417	2.374
d_{Ru-Cl_4}	2.375	2.414	2.391	2.398	2.395	2.399	2.350	2.364	2.325

S_0 geometry

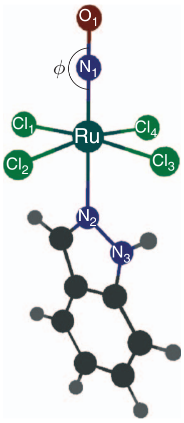

T_1 geometry

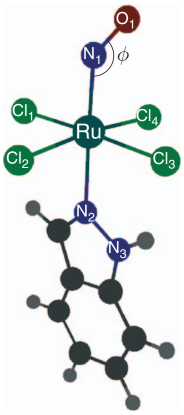

the intra-ligand $\pi\pi^*$ excitations in indazole and single and double excitations from the $(d, \pi^*)_b$ to the $(d, \pi^*)_a$ orbitals. In the T_1 state an electron is excited to the $(d_{z^2}, \pi^*_y)_a$ orbital. These excitations confirm the strong covalent interaction between Ru and the NO ligand.

The DF-CASSCF optimized geometry of RuHIndNO shall be compared to the geometries optimized by the single-configurational DFT and the experimental crystal structure from Ref. 32. Table I collects the most important geometrical parameters of the DF-CASSCF and DFT S_0 and T_1 optimized geometries and the experimental data. RuHIndNO shows a distorted octahedral coordination with four chloride ligands in the equatorial plane and the NO and indazole ligands at the axial sites.

The largest difference between the S_0 and T_1 structures is the Ru-N-O bending angle ϕ (Table I). Regardless of the employed method, the S_0 optimized structure shows almost linear NO coordination, while in the T_1 structure the NO is bent. The crystal structure is also linear; therefore, both the DF-CASSCF and DFT are consistent with the fact that the S_0 is the electronic ground state. More subtle differences between the S_0 and the T_1 geometries include the Ru-N_1 and Ru-N_2 bond lengths, which are slightly longer in the T_1 structure compared with the S_0 one (both in the DF-CASSCF and DFT optimized geometries). The relative orientation of the indazole heterocycle with respect to the equatorial plane containing the Cl atoms ($\theta_{Cl_3-Ru-N_2-N_3}$) is very similar in the S_0 DF-CASSCF and all DFT structures, but different from the X-ray structure. This difference is explained with the interaction of the indazole ligand with another, free indazole molecule present in the crystal (see Ref. 32).

The other relevant dihedral angle, $\theta_{Cl_2-Ru-N_1-O_1}$, showing relative orientation of the bent NO to the remaining coordination sphere also differs slightly in the DFT and DF-CASSCF structures for the triplet state: CASSCF show the largest bend, which decreases in B3LYP and BP86 geometries and even more so in the M06L geometry. In general this dihedral angle has the largest deviation between all DFT structures, showing a spread of 10° between B3LYP and M06L.

The average deviation of all bond lengths compared to the crystal structure is 0.042 Å at the DF-CASSCF level of theory, which is slightly larger but still comparable with the deviations obtained by M06L (0.032 Å), B3LYP (0.030 Å), and BP86 (0.026 Å). One also should note that a direct comparison of the optimized gas phase structures and the crystal one is not completely possible due to crystal packaging distortions. Also for this reason, the latter averages were made only considering bond distances. Since BP86 provides the least deviation, this geometry will be used as a DFT reference for more detailed comparisons with the DF-CASSCF geometry.

In general, the DF-CASSCF bond distances are slightly larger than those calculated by DFT, regardless of the functional, both in the S_0 and T_1 structures. The largest discrepancy between the BP86 and DF-CASSCF bond

This article is copyrighted as indicated in the article. Reuse of AIP content is subject to the terms at: http://scitation.aip.org/termsconditions. Downloaded to IP: 77.80.43.215 On: Tue, 28 Jul 2015 11:52:01

TABLE II. Timings and disk usage for one iteration of the optimization of RuHIndNO. *Conv.* labels the algorithm using conventional integrals. The first row provides total runtimes and the subsequent three rows give the runtime for the indicated tasks. The last column shows the speedup for the timings and the ratio of disk usages for the last row.

	Conv.	DF	Ratio
Runtime/min	1244	96	13
Integrals	573	18	32
CASSCF	374	49	8
Gradients	297	29	10
Disk usage/GB	185	15	12

lengths is in the Ru–N_2 bond length, with greater difference in the T_1, although the Ru–Cl bond lengths are also slightly longer in the ground state DF-CASSCF structure than in the DFT or crystal structure.

The root-mean-square deviation between the DF-CASSCF and BP86 coordinates (minimized by translation and rigid rotation using the Kabsch algorithm)[62] is only 0.08Å for S_0 and 0.11 Å for T_1. Since DFT accounts for dynamical correlation and one would expect it to be better than CASSCF for optimizing geometries, it is very encouraging to see that the differences between the two methods are small.

B. Performance and error assessment

In order to assess the performance of the DF-CASSCF algorithm we have compared the runtime needed for one iteration of the geometry optimization. The comparison of the full optimization runtime with and without the DF approximation is not possible, since RuHIndNO is too large to be optimized using conventional (non-direct) integrals. The speedup obtained for one iteration should be indicative for the whole optimization, since the optimization should converge in the same, or very nearly the same, number of iterations regardless of whether DF is employed or not. Therefore, to compare the timings, one full iteration (integral calculation, CASSCF single-point calculation, and gradient calculation), both with and without the DF approximation has been performed on the B3LYP S_0 geometry of RuHIndNO (which also served as a starting guess for the DF-CASSCF geometry optimizations discussed in Sec. IV A). The timings and disk usage are given in Table II. The overall speedup of 13 times for a single iteration arises from speedups in each of the tasks. The greatest speedup (32-fold) is observed for the integral calculation, reflecting the large computational effort required for the conventional calculation of four-center ERIs with the ANO-RCC-VTZP basis set. The DF approximation speeds up the CASSCF gradient calculation by one order of magnitude in this case. A significant contribution to the overall speedup is the reduced disk space requirement with DF, which implies reduced input-output latency. A better speedup is expected for larger molecules and/or larger basis sets.

Figure 2 displays the absolute value of a relative error due to the DF approximation of the norm of the gradient at each atom of RuHIndNO. Evidently, the errors due to the DF approximation are small. The mean and median errors are 0.25% and 0.22%, respectively, and the maximum error is 0.89% for the nitrosyl oxygen atom. For comparison, the B3LYP geometry is also used for one optimization step employing RI-BP86 and BP86 gradients and the obtained mean and median errors are 1.55% and 0.97%, respectively, with a maximum of 6.1%. It is reasonable to claim, therefore, that the DF-CASSCF gradient calculations are accurate, even with a relatively high CD threshold of 0.0001 a.u. for the generation of the auxiliary basis.

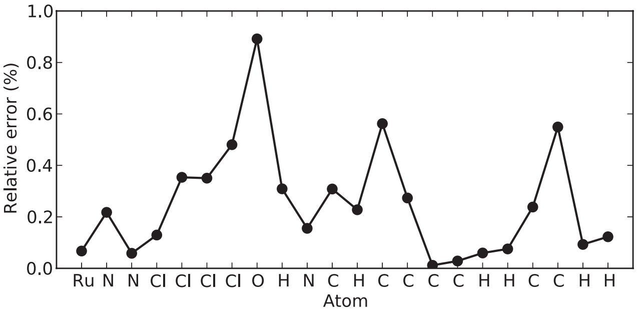

FIG. 2. Relative errors of the norm of the gradient for each atom of RuHIndNO. The atoms have been ordered according to increasing distance from Ru.

C. Singlet-triplet gaps

The relative stability of S_0 and T_1 structures and the corresponding vertical and adiabatic singlet-triplet energy gaps are listed in Table III. The energies are reported at the BP86 and at the CASPT2 level of theory, where the latter has been calculated both using the DF-CASSCF and the BP86 geometries. For comparison, the energies are also calculated with the B3LYP and M06L functionals at the geometries optimized at the same level of theory (denoted B3LYP//B3LYP and M06L//M06L, respectively).

Regardless of the geometry or the method employed to compute the energies, the S_0 state is always more stable than the T_1. At the BP86 level of theory using the BP86 geometry (denoted BP86//BP86), the vertical singlet-triplet gap amounts to 1.61 eV. The CASPT2 calculation yields 1.87 (1.81) eV for the DF-CASSCF (BP86) structure. The small difference of the CASPT2 result on DF-CASSCF and BP86 geometries of only 0.06 eV confirms both that the S_0 is the electronic ground state and that the S_0 geometry predicted by DF-CASSCF is very similar to the one predicted by BP86.

TABLE III. Vertical ($\Delta E_{\mathrm{ST}}^{\mathrm{v}}$) and adiabatic ($\Delta E_{\mathrm{ST}}^{\mathrm{a}}$) singlet-triplet gaps at different levels of theory. The energy of the electronic ground state S_0 at the T_1 geometry is given by $E_{S_0(T_1)}$. All energies reported in eV.

Method	$\Delta E_{\mathrm{ST}}^{\mathrm{v}}$	$\Delta E_{\mathrm{ST}}^{\mathrm{a}}$	$E_{S_0(T_1)}$
CASPT2//DF-CASSCF	1.87	1.52	1.56
CASPT2//BP86	1.81	1.16	0.96
BP86//BP86	1.61	1.16	1.05
B3LYP//B3LYP	1.70	0.83	1.03
M06L//M06L	1.51	0.96	0.93

This article is copyrighted as indicated in the article. Reuse of AIP content is subject to the terms at: http://scitation.aip.org/termsconditions. Downloaded to IP: 77.80.43.215 On: Tue, 28 Jul 2015 11:52:01

In contrast, the estimates for the adiabatic singlet-triplet energy gap ($\Delta E^{\mathrm{a}}_{\mathrm{ST}}$ in Table III), obtained at the triplet geometry, depend more strongly on the geometry employed. While this gap amounts to 1.16 eV for both CASPT2 and BP86 levels of theory at the BP86 geometry, it increases up to 1.52 eV at the CASPT2//DF-CASSCF level of theory. These discrepancies can be attributed to the deviations in the dihedral angle θ between the CASSCF and BP86 T_1 geometry. Indeed, similar deviations are observed in the $E_{S_0(T_1)}$ energies, but not in $\Delta E^{\mathrm{v}}_{\mathrm{ST}}$ energies, which depend on the S_0 geometry.

BP86 functional underestimates $\Delta E^{\mathrm{v}}_{\mathrm{ST}}$ by 0.2 eV as compared to CASPT2 but yields very similar values to CASPT2 for the other two energies. Other functionals clearly underestimate the vertical and the adiabatic gaps. The values of $E_{S_0(T_1)}$ are fairly similar for all DFT geometries but differs for the DF-CASSCF geometry calculated at CASPT2 level, but since no experimental value is available for the singlet-triplet gap of RuHIndNO, no conclusion can be drawn.

In summary, it can be seen that the relative singlet-triplet energies of RuHIndNO depend on the geometry and this is particularly true for the T_1 geometry. The DFT calculations seem to predict smaller energy gaps than CASPT2. Among the tested functionals BP86 shows the closest result to the CASPT2 calculation, the vertical $\Delta E^{\mathrm{v}}_{\mathrm{ST}}$ gap 0.2 eV smaller than the CASPT2 value.

Unlike the Fe nitrosyl complexes of Ref. 41 that show spin state energy differences within 1–10 kcal/mol, this nitrosyl Ru system shows much larger singlet-triplet energy gaps, and the spin crossover cannot be achieved thermally, but only photochemically.

V. CONCLUSIONS

We have performed geometry optimizations for the lowest singlet and triplet states of RuHIndNO, a Ru nitrosyl complex, using multiconfigurational and density-functional methods. A new algorithm relying on density fitting has been employed to optimize geometries at the CASSCF level of theory (DF-CASSCF), which would otherwise be too computationally demanding. While errors in atomic gradients are below 0.9%, a 13-fold speedup of the optimization results from the DF approximation with auxiliary basis sets generated by Cholesky decomposition, which thus paves the way for CASSCF optimizations of relatively large transition metal complexes. This is especially relevant for the study of complexes with large static correlation contributions, for which the use of methods such as CASSCF is mandatory. The results show that the ground state of the Ru nitrosyl complex is a singlet, as reflected in the linear NO coordination, which is consistent with the experimental X-ray structure.[32] The DF-CASSCF ground state geometry is in good agreement with that obtained with (single-configurational) DFT methods, whereas the first triplet excited state shows a slightly different positioning of the NO and indazole ligands when optimized with DFT versus DF-CASSCF. Interestingly, this slightly different positioning of the ligands is enough to introduce discrepancies in the singlet-triplet energies calculated with CASPT2 and DFT.

ACKNOWLEDGMENTS

All the calculations have been performed on the HP computers of the Theoretical Chemistry group of the University of Vienna. This work has been supported by the Research Council of Norway through a Centre of Excellence Grant (Grant No. 179568/V30). The Swedish Research Council and the eSSENCE program are acknowledged for financial support. We gratefully acknowledge the University of Vienna for financial support and Vladimir Arion and Gabriel Büchel for fruitful discussions. Author F.A. was supported primarily by the Italian Ministry of Education and Research (MIUR) under Grant No. RBFR1248UI.

[1] P. Pulay, Mol. Phys. **17**, 197 (1969).
[2] *Geometrical Derivatives of Energy Surfaces and Molecular Properties*, NATO ASI Series C: Mathematical and Physical Sciences Vol. 186, edited by P. Jørgensen and J. Simons (D. Reidel Publishing Company, Dordrecht, Netherlands, 1986).
[3] T. Helgaker and P. Jørgensen, “Calculation of geometrical derivatives in molecular electronic structure theory,” in *Methods in Computational Molecular Physics*, edited by S. Wilson and G. H. F. Diercksen (Plenum, New York, 1992), pp. 353–421.
[4] H.-J. Werner and W. Meyer, J. Chem. Phys. **73**, 2342 (1980).
[5] B. O. Roos, P. R. Taylor, and P. E. Siegbahn, Chem. Phys. **48**, 157 (1980).
[6] K. Andersson, P. A. Malmqvist, B. O. Roos, A. J. Sadlej, and K. Wolinski, J. Phys. Chem. **94**, 5483 (1990).
[7] L. González, D. Escudero, and L. Serrano-Andrés, ChemPhysChem **13**, 28–51 (2012).
[8] N. H. F. Beebe and J. Linderberg, Int. J. Quantum Chem. **12**, 683 (1977).
[9] H. Koch, T. B. Pedersen, and A. Sánchez de Merás, J. Chem. Phys. **118**, 9481 (2003).
[10] F. Aquilante, L. Boman, J. Boström, H. Koch, T. B. Pedersen, A. S. de Merás, and R. Lindh, “Cholesky decomposition techniques in electronic structure theory,” in *Challenges and Advances in Computational Chemistry and Physics*, edited by M. G. Papadopoulos, R. Zalesny, P. G. Mezey, and J. Leszczynski (Springer, 2011), Vol. 13, pp. 301–344.
[11] F. Aquilante, T. B. Pedersen, L. Gagliardi, and R. Lindh, J. Chem. Phys. **130**, 154107 (2009).
[12] T. B. Pedersen, F. Aquilante, and R. Lindh, Theor. Chem. Acc. **124**, 1 (2009).
[13] F. Aquilante, T. B. Pedersen, B. O. Roos, A. Sánchez de Merás, and H. Koch, J. Chem. Phys. **129**, 024113 (2008).
[14] F. Aquilante, P.-A. Malmqvist, T. B. Pedersen, A. Ghosh, and B. O. Roos, J. Chem. Theory Comput. **4**, 694 (2008).
[15] F. Aquilante, T. K. Todorova, T. B. Pedersen, L. Gagliardi, and B. O. Roos, J. Chem. Phys. **131**, 034113 (2009).
[16] D. Roca-Sanjuán, F. Aquilante, and R. Lindh, WIREs Comput. Mol. Sci. **2**, 585 (2012).
[17] F. Weigend and M. Häser, Theor. Chem. Acc. **97**, 331 (1997).
[18] C. Hättig, J. Chem. Phys. **118**, 7751 (2003).
[19] A. Köhn and C. Hättig, J. Chem. Phys. **119**, 5021 (2003).
[20] P. Deglmann, K. May, F. Furche, and R. Ahlrichs, Chem. Phys. Lett. **384**, 103 (2004).
[21] M. Schütz, H.-J. Werner, R. Lindh, and F. R. Manby, J. Chem. Phys. **121**, 737 (2004).
[22] Y. M. Rhee, R. A. DiStasio, Jr., R. C. Lochan, and M. Head-Gordon, Chem. Phys. Lett. **426**, 197 (2006).
[23] R. A. DiStasio, Jr., R. P. Steele, Y. M. Rhee, Y. Shao, and M. Head-Gordon, J. Comput. Chem. **28**, 839 (2007).
[24] R. A. DiStasio, Jr., R. P. Steele, and M. Head-Gordon, Mol. Phys. **105**, 2731 (2007).
[25] F. Neese, T. Schwabe, and S. Grimme, J. Chem. Phys. **126**, 124115 (2007).
[26] F. Aquilante, R. Lindh, and T. B. Pedersen, J. Chem. Phys. **129**, 034106 (2008).
[27] Y. M. Rhee, D. Casanova, and M. Head-Gordon, J. Chem. Theory Comput. **5**, 1224 (2009).
[28] S. Loibl, F. R. Manby, and M. Schütz, Mol. Phys. **108**, 477 (2010).
[29] J. Boström, F. Aquilante, T. B. Pedersen, and R. Lindh, J. Chem. Theory Comput. **9**, 204 (2013).

This article is copyrighted as indicated in the article. Reuse of AIP content is subject to the terms at: http://scitation.aip.org/termsconditions. Downloaded to IP: 77.80.43.215 On: Tue, 28 Jul 2015 11:52:01

[30] J. Boström, V. Veryazov, F. Aquilante, T. B. Pedersen, and R. Lindh, Int. J. Quantum Chem. **114**, 321 (2014).
[31] W. Győrffy, T. Shiozaki, G. Knizia, and H.-J. Werner, J. Chem. Phys. **138**, 104104 (2013).
[32] A. Gavriluta, G. E. Büchel, L. Freitag, G. Novitchi, J. B. Tommasino, E. Jeanneau, P.-S. Kuhn, L. González, V. B. Arion, and D. Luneau, Inorg. Chem. **52**, 6260 (2013).
[33] D. W. O'Neal and J. Simons, Int. J. Quantum Chem. **36**, 673 (1989).
[34] J. L. Whitten, J. Chem. Phys. **58**, 4496 (1973).
[35] B. I. Dunlap, J. W. D. Connolly, and J. R. Sabin, J. Chem. Phys. **71**, 4993 (1979).
[36] M. Feyereisen, G. Fitzgerald, and A. Komornicki, Chem. Phys. Lett. **208**, 359 (1993).
[37] O. Vahtras, J. Almlöf, and M. W. Feyereisen, Chem. Phys. Lett. **213**, 514 (1993).
[38] F. Aquilante, L. de Vico, N. Ferré, G. Ghigo, P.-Å. Malmqvist, P. Neogrády, T. B. Pedersen, M. Pitoňák, M. Reiher, B. O. Roos, L. Serrano-Andrés, M. Urban, V. Veryazov, and R. Lindh, J. Comput. Chem. **31**, 224 (2010).
[39] B. O. Roos, R. Lindh, P.-A. Malmqvist, V. Veryazov, and P.-O. Widmark, J. Phys. Chem. A **109**, 6575 (2005).
[40] K. Pierloot, Mol. Phys. **101**, 2083 (2003).
[41] M. Radoń, E. Broclawik and K. Pierloot, J. Phys. Chem. B **114**, 1518 (2010).
[42] D. Escudero and L. González, J. Chem. Theory Comput. **8**, 203 (2012).
[43] A. D. Becke, J. Chem. Phys. **98**, 5648 (1993).
[44] C. Lee, W. Yang, and R. G. Parr, Phys. Rev. B **37**, 785 (1988).
[45] Y. Zhao and D. G. Truhlar, J. Chem. Phys. **125**, 194101 (2006).
[46] A. D. Becke, Phys. Rev. A **38**, 3098 (1988).
[47] J. P. Perdew, Phys. Rev. B **33**, 8822 (1986).
[48] S. H. Vosko, L. Wilk, and M. Nusair, Can. J. Phys. **58**, 1200 (1980).
[49] F. Weigend and R. Ahlrichs, Phys. Chem. Chem. Phys. **7**, 3297 (2005).
[50] C. J. Cramer and D. G. Truhlar, Phys. Chem. Chem. Phys. **11**, 10757 (2009).
[51] M. Radoń and K. Pierloot, J. Phys. Chem. A **112**, 11824 (2008).
[52] C. E. Diesendruck, E. Tzur, A. Ben-Asuly, I. Goldberg, B. F. Straub, and N. G. Lemcoff, Inorg. Chem. **48**, 10819 (2009).
[53] C. Adlhart and P. Chen, Angew. Chem. Int. Ed. **41**, 4484 (2002).
[54] D. Andrae, U. Häußermann, M. Dolg, H. Stoll, and H. Preuß, Theo. Chim. Acta **77**, 123 (1990).
[55] F. Neese, F. Wennmohs, A. Hansen, and U. Becker, Chem. Phys. **356**, 98 (2009).
[56] K. Eichkorn, O. Treutler, H. Öhm, M. Häser, and R. Ahlrichs, Chem. Phys. Lett. **240**, 283 (1995).
[57] M. Sierka, A. Hogekamp, and R. Ahlrichs, J. Chem. Phys. **118**, 9136 (2003).
[58] F. Neese, WIREs Comput. Mol. Sci. **2**, 73 (2012).
[59] TURBOMOLE V6.5 2013, a development of University of Karlsruhe and Forschungszentrum Karlsruhe GmbH, 1989–2007, TURBOMOLE GmbH, since 2007; available from http://www.turbomole.com.
[60] M. J. Frisch, G. W. Trucks, H. B. Schlegel *et al.*, Gaussian 09, Revision D.01, Gaussian, Inc., Wallingford, CT, 2009.
[61] B. O. Roos and K. Andersson, Chem. Phys. Lett. **245**, 215 (1995).
[62] W. Kabsch, Acta Cryst. A **32**, 922 (1976).

This article is copyrighted as indicated in the article. Reuse of AIP content is subject to the terms at: http://scitation.aip.org/termsconditions. Downloaded to IP: 77.80.43.215 On: Tue, 28 Jul 2015 11:52:01

APPENDIX 3.A.3

Orbital entanglement and CASSCF analysis of the Ru–NO bond in a Ruthenium nitrosyl complex

Leon Freitag, Stefan Knecht, Sebastian F. Keller, Mickaël G. Delcey, Francesco Aquilante, Thomas Bondo Pedersen, Roland Lindh, Markus Reiher and Leticia González

Phys. Chem. Chem. Phys., **2015**, *17*, 14383–14392.
`https://doi.org/10.1039/c4cp05278a`

Contributions:

LEON FREITAG planned, performed and evaluated all quantum chemical calculations and prepared the first draft of the manuscript.

STEFAN KNECHT helped with DMRG calculations and entanglement analyses, was involved in the development of the MAQUIS DMRG code employed and contributed to the preparation of the final version of the manuscript.

SEBASTIAN F. KELLER was involved in the development of the MAQUIS DMRG code.

MICKAËL G. DELCEY, FRANCESCO AQUILANTE, THOMAS BONDO PEDERSEN AND ROLAND LINDH were involved in the development of the Cholesky decomposition-based density fitting method employed in the study to perform CASSCF and DMRG calculations. They also helped in preparation of the final version of the manuscript.

MARKUS REIHER supervised the DMRG calculations and entanglement analyses and was involved in preparation of the final version of the manuscript.

LETICIA GONZÁLEZ conceived the project, supervised the CASSCF calculations, localised orbital analysis and partially DMRG calculations and entanglement analysis and helped in preparation of the final manuscript.

Copyright 2015, Royal Society of Chemistry. This article is licensed under a Creative Commons Attribution 3.0 Unported Licence.

PCCP

PAPER

View Article Online
View Journal | View Issue

Cite this: *Phys. Chem. Chem. Phys.*, 2015, **17**, 14383

Open Access Article. Published on 10 March 2015. Downloaded on 09/08/2015 17:10:04.
This article is licensed under a Creative Commons Attribution 3.0 Unported Licence.

Orbital entanglement and CASSCF analysis of the Ru–NO bond in a Ruthenium nitrosyl complex

Leon Freitag,[a] Stefan Knecht,[b] Sebastian F. Keller,[b] Mickaël G. Delcey,[c] Francesco Aquilante,[cd] Thomas Bondo Pedersen,[e] Roland Lindh,[f] Markus Reiher*[b] and Leticia González*[a]

Received 13th November 2014,
Accepted 23rd February 2015

DOI: 10.1039/c4cp05278a

www.rsc.org/pccp

Complete active space self-consistent field (CASSCF) wavefunctions and an orbital entanglement analysis obtained from a density-matrix renormalisation group (DMRG) calculation are used to understand the electronic structure, and, in particular, the Ru–NO bond of a Ru nitrosyl complex. Based on the configurations and orbital occupation numbers obtained for the CASSCF wavefunction and on the orbital entropy measurements evaluated for the DMRG wavefunction, we unravel electron correlation effects in the Ru coordination sphere of the complex. It is shown that Ru–NO π bonds show static and dynamic correlation, while other Ru–ligand bonds feature predominantly dynamic correlation. The presence of static correlation requires the use of multiconfigurational methods to describe the Ru–NO bond. Subsequently, the CASSCF wavefunction is analysed in terms of configuration state functions based on localised orbitals. The analysis of the wavefunctions in the electronic singlet ground state and the first triplet state provides a picture of the Ru–NO moiety beyond the standard representation based on formal oxidation states. A distinct description of the Ru and NO fragments is advocated. The electron configuration of Ru is an equally weighted superposition of $\mathrm{Ru^{II}}$ and $\mathrm{Ru^{III}}$ configurations, with the $\mathrm{Ru^{III}}$ configuration originating from charge donation mostly from Cl ligands. However, and contrary to what is typically assumed, the electronic configuration of the NO ligand is best described as electroneutral.

1 Introduction

The electronic structure and properties of transition metal nitrosyl complexes have been a subject of interest in inorganic and bioinorganic chemistry for a long time. Nitric oxide (NO) plays a role in neurotransmission, blood pressure control and even control of tumour growth.[1] A number of transition metal nitrosyl complexes have been employed in photodynamical therapy to deliver targeted NO to biological tissues.[2] Particularly interesting are ruthenium nitrosyls, since they are postulated to be intermediates[3,4] in the mechanism of action of novel ruthenium anticancer drugs such as NAMI-A[5] and KP1019.[6] Understanding the electronic structure of the metal–NO moiety is therefore essential to rationalise the mechanisms for NO delivery from nitrosyl complexes and thus obtain a fundamental understanding of the mode of action of ruthenium anti-cancer drugs.

Furthermore, NO is a well-known non-innocent ligand in coordination chemistry,[7] which leads to an intricate and ambiguous electronic structure of the transition metal nitrosyls. NO can attach to the metal both in a linear or a bent configuration, depending on the electronic structure of the metal, charge of the free NO and the remaining coordination sphere. The metal-nitrosyl moiety M–NO usually shows strongly delocalised electron density and a strong covalency. Enemark and Feltham[8,9] have suggested to describe the electronic structure of this moiety as $\{\mathrm{M(NO)}\}^n$, with n being the total number of electrons in the metal d and nitrosyl π* orbitals. Within this framework, however, the electronic character of neither the Ru nor the NO fragment is known, and it is not possible to assign a particular oxidation state to either fragment. For example, it is unclear whether $\{\mathrm{RuNO}\}^6$ structures should be treated as $\mathrm{Ru^{II}{-}NO^{+}}$ or $\mathrm{Ru^{III}{-}NO^{0}}$. A correct description of the oxidation states of the metal and ligands is important, *e.g.*, for the study of the redox processes involved in the metabolism of redox-active anti-cancer drugs.

Attempts to resolve the ambiguity in the metal–NO bond and to assign oxidation states to the metal and the ligands have

---

[a] *Institut für theoretische Chemie, Universität Wien, Währinger Str. 17, 1090 Vienna, Austria. E-mail: leticia.gonzalez@univie.ac.at*

[b] *ETH Zürich, Laboratory of Physical Chemistry, Vladimir-Prelog-Weg 2, 8093 Zürich, Switzerland. E-mail: markus.reiher@phys.chem.ethz.ch*

[c] *Department of Chemistry – Ångström, The Theoretical Chemistry Programme, Uppsala University, Box 518, 751 20 Uppsala, Sweden*

[d] *Dipartimento di Chimica "G. Ciamician", Università di Bologna, V. F. Selmi 2, 40126 Bologna, Italy*

[e] *Centre for Theoretical and Computational Chemistry, Department of Chemistry, University of Oslo, P.O. Box 1033 Blindern, 0315 Oslo, Norway*

[f] *Uppsala Center for Computational Chemistry - UC$_3$, Uppsala University, Box 518, 751 20 Uppsala, Sweden*

Open Access Article. Published on 10 March 2015. Downloaded on 09/08/2015 17:10:04. This article is licensed under a Creative Commons Attribution 3.0 Unported Licence.

been carried out in many theoretical, spectroscopic and electrochemical studies.[4,10–14] It has been largely accepted that most linear $\{RuNO\}^6$ complexes[15] and many $\{FeNO\}^6$ complexes[16] are best described as M^{II}–NO^+. Interestingly, and in contrast to this picture, a recent extensive joint experimental and computational study[4] on one particular $\{RuNO\}^6$ complex concluded that the physical electronic structure of the Ru–NO moiety is better described by Ru^{III}–NO^0, rather than Ru^{II}–NO^+.

The majority of computational studies on transition metal complexes employ density functional theory (DFT).[17] However, many structures belong to the class of the so-called strongly correlated systems which cannot be described by Kohn–Sham DFT[18] due to its single Slater determinant approximation. In this respect, Kohn–Sham DFT is conceptually similar to Hartree–Fock theory, which does not incorporate electron correlation (*i.e.* movement of electrons depending on the instantaneous positions of other electrons). Electron correlation can be classified as[19–21] *dynamic* and *static* (split further into static and nondynamic correlation by some authors[19,21]). Dynamic correlation is responsible for keeping the electrons apart and is found in any quantum mechanical system with more than one electron. Static correlation corresponds to significant mixtures of several electronic configurations and is largely present, *e.g.*, in dissociating molecules and many transition metal compounds. While dynamic correlation can be effectively described by DFT and post-Hartree–Fock methods, such as Møller–Plesset perturbation theory or coupled cluster (CC) methods, the proper description of static correlation requires several Slater determinants or configurations in the *ansatz*. Multiconfigurational methods – such as the complete active space self consistent field (CASSCF),[22] the restricted active space SCF (RASSCF),[23] or the density matrix renormalization group (DMRG)[24] method in its quantum chemical formulation[25] as well as their corresponding refinements by second-order perturbation theory[23,26,27] – are then mandatory to describe such systems.

Sizova *et al.*[11] were the first to apply a multiconfigurational/valence-bond treatment to a variety of $\{RuNO\}^6$ complexes. Radoń *et al.*[13] applied CASSCF localised orbitals and spin densities to analyse the Fe–NO bond in several $\{FeNO\}^7$ complexes, as well as calculated the doublet-quartet energy gap with CASPT2/CASSCF. Recently, we have also used CASPT2/CASSCF to study the electronic structure of another $\{RuNO\}^6$ complex.[14] Boguslawski *et al.*[28] compared the CASSCF spin densities of several Fe–NO complexes with DFT results, deeming both unsatisfactory. This unpleasant situation could only be resolved by calculating the spin density from a large-CAS DMRG wavefunction, in which the complete double-d shell correlation effects could be taken into account.[29] Double-d shell correlation effects are related to the presence of a large number of electrons in compact d shells, resulting in large radial correlation effects in these shells. The second more diffuse d shell gives additional flexibility to describe such correlation effects, and for many 3d transition metal compounds the second d shell must be present to obtain quantitative accuracy with the CASPT2 method.[30]

The last example illustrates the major limitation of CASSCF – the factorial growth of computational time with the number of correlating electrons and orbitals. Presently, CASSCF calculations are typically limited to active spaces comprising approximately 16 electrons in 16 orbitals. Over the past few decades, several attempts have been made to overcome the CASSCF factorial scaling problem and allow the usage of larger active spaces: the RASSCF method introduces additional subspaces with a restricted number of excitations; the generalised active space (GAS)[31] concept takes the RAS concept one step further by introducing an arbitrary number of subspaces. RAS and GAS methods allow us to extend the active spaces at the price of having to choose a restriction of the excitation levels; however this degree of freedom makes these methods less straightforward to use than CASSCF. Recently, the GAS method has been combined with Löwdin's partitioning technique[32] resulting in the SplitGAS method,[33] which, despite its demonstrated capability to effectively employ up to 10^{22} Slater determinants, still requires algorithmic advances and further development before it can be widely used.

The conceptually different DMRG algorithm employs the reduced density matrix of the system studied to construct and optimise a CAS-like wavefunction, allowing for a polynomial instead of factorial scaling with the number of active orbitals. As a consequence, DMRG allows much larger active spaces than conventional CASSCF, explaining its value for calculations on transition metal complexes dominated by strong static electron correlation[34] and its remarkable success in transition metal chemistry in recent years.[29,35]

Using the DMRG algorithm, n-orbital reduced density matrices are easily obtained from the full density matrix by tracing out contributions from all orbitals in the complementary set of orbitals in the active space. As a consequence, entanglement measures such as the single-orbital entropy[36] and mutual information[37,38] calculated from the one-orbital and two-orbital reduced density matrix, respectively, are easily accessible. These orbital-based entanglement measures can be applied to examine the multi-reference character of the electronic wave function. In particular, they can be correlated with the amount of static and dynamic electron correlation in an electronic wavefunction[21] or exploited to study chemical bonding in molecule formation and dissociation processes.[39] Thus, they complement the traditional orbital-based correlation measures such as the natural orbital and geminal analysis.[40]

In addition to the factorial scaling with the active space size, the cost of multiconfigurational calculations also scales as $O(n^4)$ with the number of basis functions. Efficient calculations on large molecules, including large transition metal complexes, cannot be performed unless this scaling is reduced. Using approximate representations of the electron repulsion integrals based on density-fitting (DF) and Cholesky decomposition (CD)[41] reduces the scaling to cubic, thus enabling multiconfigurational calculations on larger molecules.[42] Analytical gradients employing combined DF and CD techniques extend the applicability to geometry optimisations.[43,44]

In this work we investigate the electronic structure of the $\{RuNO\}^6$ moiety in the *trans*-[$RuCl_4(NO)(1H$-indazole)]-complex (RuHIndNO),[45] which is closely related to the anti-cancer drug KP1019. We perform CASSCF calculations of the S_0 and T_1 state of RuHIndNO, describe the electronic structure of the coordination sphere around Ru and analyse the wavefunction in

Open Access Article. Published on 10 March 2015. Downloaded on 09/08/2015 17:10:04. This article is licensed under a Creative Commons Attribution 3.0 Unported Licence.

terms of contributions of different configurations and natural orbital occupation numbers. Note that CASPT2/CASSCF singlet-triplet energy splittings have been addressed in ref. 44. Here we also perform orbital entanglement analyses[21,38,39] based on DMRG calculations of the S_0 state. We examine different types of electron correlation present in the Ru–ligand bonds and assess the ability of multiconfigurational methods to describe the Ru–NO coordination sphere in RuHIndNO.

To shed more light on the electronic structure of the $\{RuNO\}^6$ complex, we transform the CASSCF wavefunctions of the S_0 and T_1 states into a localised orbital basis and analyse the Ru–NO bond and the Ru coordination sphere in terms of configuration state functions (CSFs) based on localised orbitals; we compare the results obtained from the localised orbital analysis to the Mulliken population of Ru d orbitals based on both single-configurational DFT and the CASSCF wavefunction. At the end of our analysis we adress the non-innocence of the NO ligand: in particular, whether NO is to be considered ionic or neutral and the true 4d occupation of the Ru center.

Noting the importance of the double-d shell effects in transition metal compounds,[29,30,46] we also investigate the double-d-shell effect using entanglement analysis. We perform another DMRG calculation with an active space incorporating another pair of correlating orbitals and a second d shell on Ru.

2 Computational details

Geometry optimisation of the lowest singlet (S_0) and the triplet state (T_1) has been performed with DFT, using the BP86 functional[47,48] and the def2-TZVPP basis set.[49,50] For Ru, the MWB28 effective core potential[51] (ECP) has been used, and RI-J and MARI-J[52] approximations were employed for computational efficiency. The triplet geometry has been optimised with the unrestricted Kohn–Sham procedure. The DFT calculations have been performed using the TURBOMOLE 6.5[53] suite of programs.

Using the optimised S_0 and T_1 geometries, single-point CASSCF calculations employing the ANO-RCC-VTZP basis set[54] and atomic compact Cholesky decomposition (acCD)-based algorithms[41] with the Cholesky decomposition threshold of 10^{-4} have been performed with the MOLCAS 7.8 program package.[55] Mulliken population analyses have been done at the CASSCF and PBE[56] levels of theory with the ANO-RCC-VTZP basis set, as implemented in MOLCAS.[57]

The choice of the CASSCF active space is motivated by its feasibility for a configuration analysis of the Ru coordination sphere. Accordingly, all Ru 4d orbitals and the ligand orbitals interacting with them must be included, resulting in a total active space of 13 orbitals with 16 electrons (denoted (16,13)), including the five Ru 4d orbitals, two pairs of NO π and π^* orbitals, one pair of indazole π and π^* orbitals, one combination of p orbitals on the Cl atoms (denoted σ_{Cl}) as well as the NO σ orbital. The last two orbitals are particularly important because they participate in the covalent bond formed between the metal and the NO and Cl ligands, respectively; accordingly, each of them mixes with the d_{z^2} and the $d_{x^2-y^2}$ orbitals of the Ru atom, respectively. A fair comparison of the CASSCF wavefunction analyses on the S_0 and T_1 geometry should be done using the same active spaces in both calculations. For RuHIndNO, this can be only achieved in the S_0 calculation by a state-average (SA)-CASSCF calculation over the lowest three singlet states. Thus, the T_1 calculation was similarly averaged over three states, to ensure that the deterioration of the wavefuction quality due to state averaging is similar in both spin states. The resulting orbitals and corresponding natural orbital occupation numbers of the optimised S_0 and T_1 geometries are collected in Fig. 1a and b, respectively.

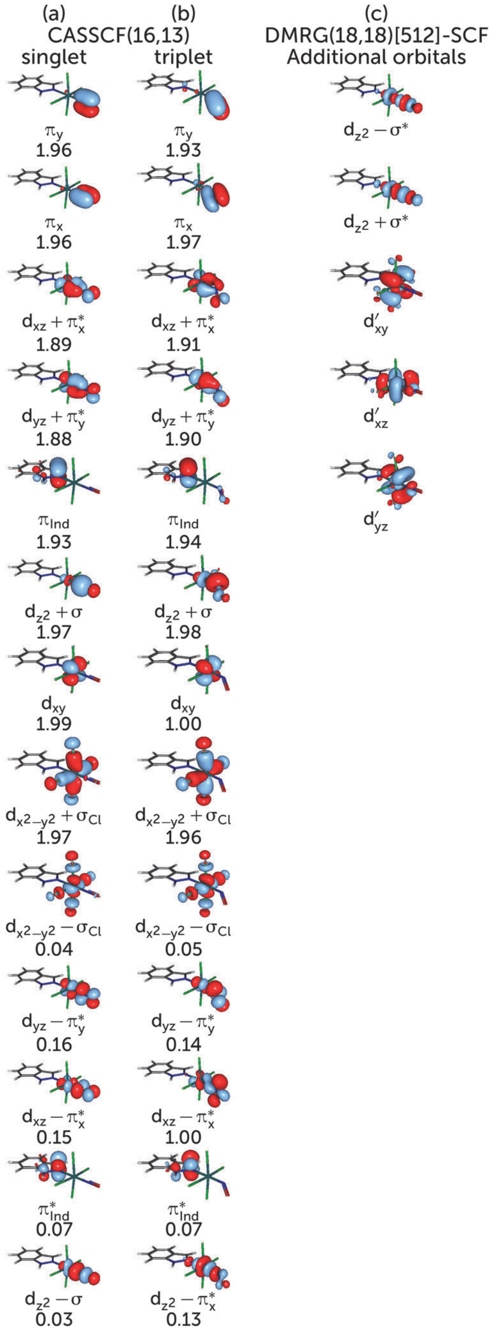

Fig. 1 Active space orbitals and their respective occupation numbers used in the optimization of the S_0 (a) and T_1 (b) electronic states using CASSCF calculations. Panel (c) shows the additional orbitals used in the DMRG(18,18)[512]-SCF calculation. Double-shell d orbitals are indicated with a prime. The remaining orbitals correspond to those in column (a).

Open Access Article. Published on 10 March 2015. Downloaded on 09/08/2015 17:10:04.
This article is licensed under a Creative Commons Attribution 3.0 Unported Licence.

For the entanglement measures, a DMRG-CASCI calculation based on the optimised CASSCF orbitals (*cf.* Fig. 1a) has been performed for the S_0 state employing the same geometry, active space and basis set as in the CASSCF calculation using the MAQUIS[58,59] DMRG program, interfaced to the development version of the MOLCAS program package. The number of renormalised active-subsystem states (m-value)[58] is set to 1000. With this value, the DMRG calculation reproduces the absolute energy of the CASSCF calculation up to 10^{-6} a.u., so that the properties of the DMRG wavefunction can be considered identical to those of the CASSCF wavefunction. This calculation will be denoted DMRG(16,13)[1000], using the shorthand notation DMRG($n_{\text{electrons}}$,n_{orbitals})[m]. From the CI-type expansion coefficients of the DMRG wavefunction, a density matrix is constructed, in which environment states can be traced out. These states are states defined on orbitals of the active space that are not considered part of a selected subsystem of orbitals. In the single-orbital case, the selected subsystem consists of only one spatial orbital with four possible states (empty, spin-up, spin-down and doubly-occupied) quantum-mechanically embedded into all other orbitals of the active space. States defined on these complementary orbitals are the environment states traced out in the (then) reduced density matrix. The four eigenvalues of this reduced density matrix, $w_{\alpha,i}$, enter a von Neumann entropy expression, which yields the single-orbital entropy, $s(1)_i$, for a given orbital i, which can be understood as a measure of the interaction of one orbital with all other orbitals:

$$s(1)_i = -\sum_{\alpha} w_{\alpha,i} \ln w_{\alpha,i} \tag{1}$$

In the same way, a two-orbital entropy, $s(2)_{i,j}$, can be calculated from the sixteen eigenvalues of the reduced density matrix that is valid for the subsystem consisting of the two selected orbitals i,j:

$$s(2)_{i,j} = -\sum_{\alpha} w_{\alpha,i,j} \ln w_{\alpha,i,j} \tag{2}$$

As this two-orbital entropy still contains single-orbital-entropy contributions, the two single-orbital entropies may be subtracted, which yields the mutual information, $I_{i,j}$, for orbitals i and j:

$$I_{i,j} = \frac{1}{2}\left(s(2)_{i,j} - s(1)_i - s(1)_j\right)\left(1 - \delta_{i,j}\right) \tag{3}$$

The central aspect of these measures is that the quantum entanglement of the states defined on one and two orbitals, respectively, has been properly encoded through the eigenvalues of the reduced density matrices.

To evaluate the correlation contribution of additional orbitals, including the second d shell effect, another DMRG calculation and entanglement analysis was performed with a larger active space. The previous (16,13) active space (Fig. 1a) was augmented with another pair of orbitals consisting of Ru d_{z^2} and NO σ* orbitals and the second Ru d_{xy}, d_{xz} and d_{yz} shells (*cf.* Fig. 1c). From all orbitals not present in the (16,13) active space, these orbitals were expected to give the largest contribution to the correlation in the Ru coordination sphere. The new active space consists of 18 electrons in 18 orbitals. Since this active space is out of reach for the traditional CASSCF implementation, the orbitals were optimised with the DMRG-SCF approach as implemented in the development version of MOLCAS. We carried out the DMRG(18,18)[512]-SCF orbital optimisation with the smaller ANO-RCC-MB basis set, augmented with an additional d shell on Ru because the ANO-RCC-VTZP basis set yielded additional p shells on N or O atoms of NO instead of the Ru double shell orbitals. The subsequent DMRG-CASCI step, which is based on the DMRG-SCF orbitals, was done increasing the m-value back to 1000, to be consistent with the DMRG(16,13)[1000] calculation. The orbital entanglement analysis was carried out for the DMRG-CASCI wavefunction, analogous to what has been explained before.

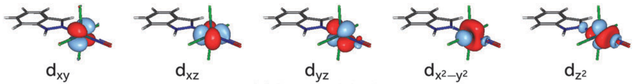

(a) Ru d orbitals

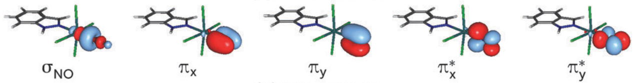

(b) NO orbitals

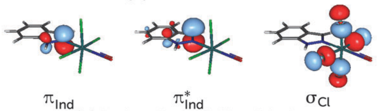

(c) Indazole and Cl orbitals

Fig. 2 Localised orbitals for the S_0 structure.

To perform the characterisation of the electronic structure in terms of CSFs based on localised orbitals, all active space orbitals have been localised using the Cholesky algorithm.[60] As for any rotation among the active orbitals only, this procedure does not change the total energy of the CASSCF wavefunction. The Cholesky localisation yielded orbitals predominantly localised on single atoms, including single p orbitals at the N and O atoms of NO. These were converted into a set of proper π and π* orbitals by forming normalised linear combinations of the form $\frac{1}{\sqrt{2}}(P_{\mathrm{N}} \pm P_{\mathrm{O}})$. This procedure yields π and π* orbitals almost exclusively localised on the NO molecule, and together with the other Cholesky orbitals they form the localised active space. The remaining Cholesky orbitals (*cf.* Fig. 2) are d orbitals localised on the metal, the σ orbital localised at the NO molecule and an orbital consisting of the p orbitals of the four Cl ligands. This localised active space is used in the discussion of the electronic structure of the complex.

3 Results and discussion

Based on the CASSCF wavefunction expressed in natural orbitals (*cf.* Fig. 1a), the singlet, S_0, and triplet, T_1, states are predominantly described by the electronic configurations (*cf.* Fig. 1a)

$$|S_0\rangle = |(d_{xz} + \pi_x^*)^2(d_{yz} + \pi_y^*)^2(d_{xy})^2(d_{xz} - \pi_x^*)^0\rangle$$

$$|T_1\rangle = |(d_{xz} + \pi_x^*)^2(d_{yz} + \pi_y^*)^2(d_{xy})^1(d_{xz} - \pi_x^*)^1\rangle$$

respectively (other active orbitals are, respectively, doubly- or unnocupied). Fig. 3 shows a schematic representation of these dominant configurations. In the S_0 linear structure, the d_{xz} and

This journal is © the Owner Societies 2015

Open Access Article. Published on 10 March 2015. Downloaded on 09/08/2015 17:10:04. This article is licensed under a Creative Commons Attribution 3.0 Unported Licence.

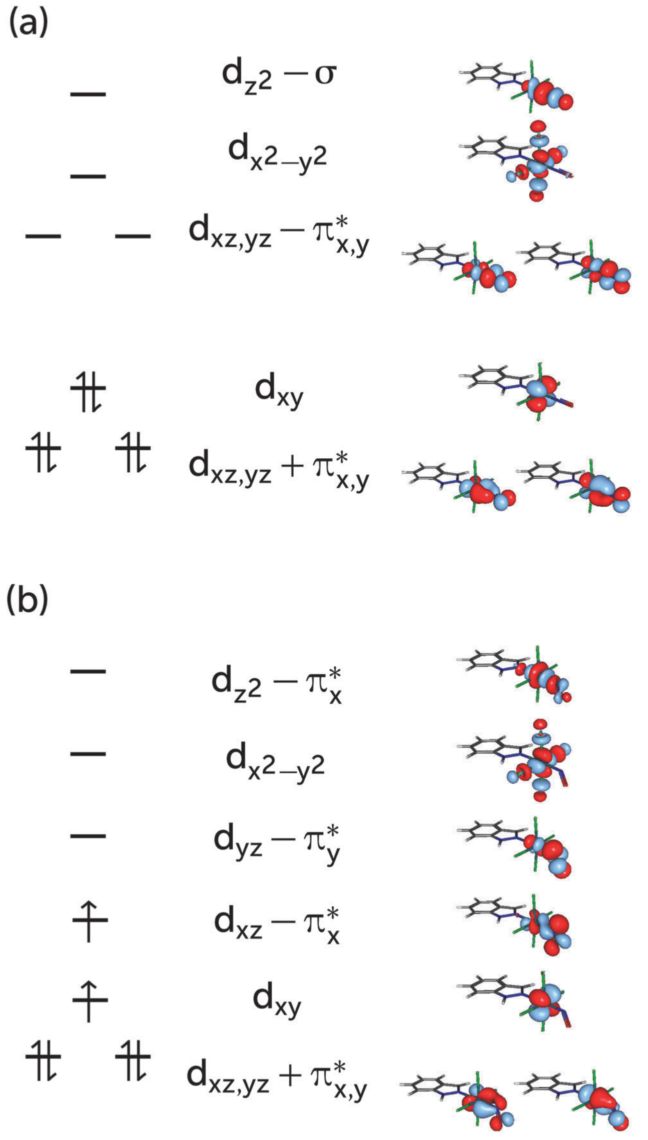

Fig. 3 Principal configurations expressed in terms of CASSCF natural orbitals for the S_0 (a) and the T_1 (b) state.

d_{yz} orbitals of Ru interact with π* orbitals of NO, forming two bonding and two antibonding orbitals, which are denoted $d_{xz,yz} \pm \pi_{x,y}^*$. d_{z^2} of Ru with the σ orbital of NO forms another pair of bonding and antibonding orbitals denoted $d_{z^2} \pm \sigma$ (*cf.* Fig. 1), again indicating a strongly covalent interaction of Ru with NO. The triplet dominant configuration is a $d_{xy} \rightarrow d_{xz} - \pi_x^*$ excitation with respect to $|S_0\rangle$. Since the latter orbital is an antibonding orbital, the Ru–NO bond is weaker in the T_1 structure than in the S_0 structure, where the d_{xy} orbital is doubly occupied. Indeed, the bond in the triplet geometry (1.838 Å) is longer than that of the singlet (1.718 Å).[44] Unlike the linear S_0 structure, the interaction of the d_{z^2} orbital with the π* orbitals of the NO ligand is not symmetry forbidden; therefore a linear combination $d_{z^2} - \pi_x^*$ is formed.

The major configurations discussed above correspond to 77% of the singlet and 78% of the triplet wavefunctions of RuHIndNO. These weights are lower than the typical value of over 90% for a molecule where the ground state is well described with a single configuration. The remaining ≈20% are distributed among many other configurations, each with weights below 3%. One might then be tempted to conclude that a single-configurational description is sufficient in this case, arguing that the remaining wavefunction contributions are negligible or that they arise due to the dynamic correlation of the system, present in every molecule. If that was the case, however, double excitations would dominate the remaining configurations and single excitations would have much less weight due to the Brilloin theorem. Indeed, one can find that the configuration with the second largest weight of (3% and 2%) in the S_0 and T_1 wavefunctions, respectively, is a local $\pi \rightarrow \pi^*$ double excitation on the indazole ligand; this configuration can be attributed to dynamic correlation between these orbitals. However, a number of single excitations with comparable weight are also present in the wavefunction, for instance, the $(d_{xz} + \pi_x^*) \rightarrow (d_{xz} - \pi_x^*)$ and $(d_{yz} + \pi_y^*) \rightarrow (d_{yz} - \pi_y^*)$ excitations in the S_0 wavefunction, and excitations to the $(d_{xz,yz} - \pi_{x,y}^*)$ and $d_{z^2} - \pi_x^*$ orbitals, in the T_1 state, which points to the presence of static correlation. For comparison, the former contributions amount to 18% of the S_0 wavefunction in the related $[Ru(PaPy_3)(NO)]^{2+}$ complex.[14]

The presence of both static and dynamic correlation in the Ru–NO bond of RuHIndNO is also reflected by the occupation numbers of the orbitals involved in the Ru–NO bonds, which differ significantly from the formal values of 2 (doubly occupied) and 0 (unoccupied). In the S_0 state these are the $(d_{xz,yz} + \pi_{x,y}^*)$ and $(d_{xz,yz} - \pi_{x,y}^*)$ orbitals with occupation numbers of 1.89, 1.88, 0.15 and 0.16 respectively (*cf.* Fig. 1). Similar occupation numbers for these orbitals are also found in the T_1 state, although here the role of the $(d_{yz} - \pi_y^*)$ orbital is taken over by the $(d_{z^2} - \pi_y^*)$ orbital: the occupation number of the former orbital is exactly 1, which indicates that it does not contribute to the electron correlation. The discrepancies from the formal uncorrelated values of 2 and 0 are also larger than those of the orbitals providing dynamic correlation only, *e.g.* the π, π* pair of indazole (π_{Ind} and π_{Ind}^*) (1.93/1.94 and 0.07). Not surprisingly, similar behaviour has been found in $\{FeNO\}^7$ complexes before,[13] although the effects are even more pronounced there – with occupation numbers of antibonding orbitals as large as 0.3.

Fig. 4 shows the single-orbital entropies and mutual information for the S_0 structure, as defined in eqn (1)–(3), as obtained from the DMRG(16,13)[1000] calculation. One can immediately recognise that orbitals 4, 5, 9 and 10 (corresponding to the $d_{xz,yz} \pm \pi_{x,y}^*$ orbitals) have the largest single-orbital entropy (as indicated by the size of the corresponding red circles in Fig. 4), while *e.g.* orbital 3 (d_{xy}) shows very low entropy. Orbitals 4, 5, 9 and 10 also show high entanglement with each other, and additionally 9 and 10 are also entangled with the $\pi_{x,y}$ orbitals, labelled 1 and 2. Large single-orbital entropies and strong entanglement with more than one orbital are a signature of static correlation. In contrast, small single-orbital entropies combined with weak entanglement among many orbitals or strong entanglement between two orbitals only is an indication of dynamic correlation. Accordingly, the $\pi_{x,y} - d_{xz,yz} - \pi_{x,y}^*$ orbitals (1, 2, 4, 5, 9, 10), corresponding to two Ru–NO π bonds, are strongly entangled

Open Access Article. Published on 10 March 2015. Downloaded on 09/08/2015 17:10:04.
This article is licensed under a Creative Commons Attribution 3.0 Unported Licence.

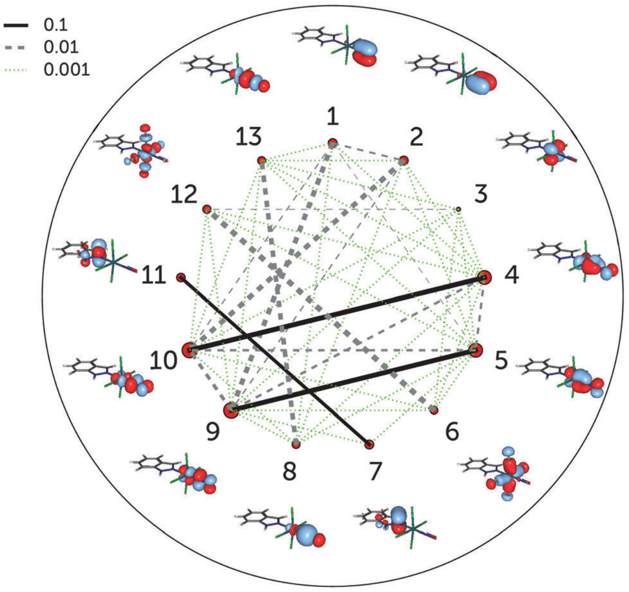

Fig. 4 Single-orbital entropy, $s(1)$, and mutual information, I, in the DMRG(16,13)[1000] (equivalent to the CASSCF) wavefunction of RuHIndNO. The size of the red circles next to the orbitals correlates with the magnitude of the corresponding single-orbital entropy. The lines connecting the dots represent the mutual information: solid lines indicate strong entanglement ($I > 0.1$), dashed grey lines stand for middle entanglement ($0.01 > I > 0.1$) and dotted green lines indicate weak entanglement ($0.001 > I > 0.01$). The line width is also proportional to the absolute value of I.

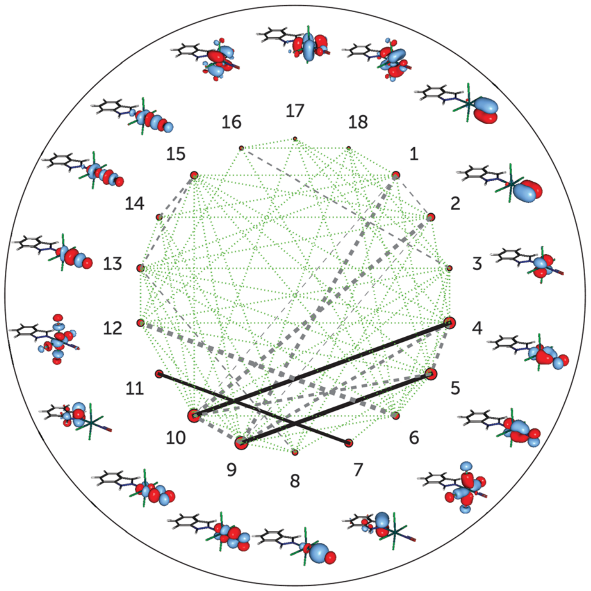

Fig. 5 Single-orbital entropy, $s(1)$, and mutual information, I, for the DMRG(18,18)[1000] wavefunction. Labels as in Fig. 4; additional orbitals have been labelled 14–18.

(*i.e.* interact strongly) and are responsible for static correlation. The entanglement of the orbitals 1 with 9 and 2 with 10 is due to dynamic correlation, as expected from $\pi\pi^*$ pairs. One can distinguish other orbital pairs which show largely dynamic correlation, *i.e.* have smaller single-orbital entropy and are strongly entangled only with each other, but not with other orbitals of the active space, such as orbitals 7 and 11 (π_{Ind} and π_{Ind}^*, which are again a textbook example of dynamic correlation), 6 and 12 ($d_{x^2-y^2} \pm \sigma_{\mathrm{Cl}}$) and 8 and 13 ($d_{z^2} \pm \sigma$). The latter two orbital pairs correspond to Ru bonds with chlorido ligands and the Ru–NO σ bond. The single-orbital entropy values correlate well with the deviation of the occupation numbers from 2 or 0 (recall Fig. 1a). The orbitals with the largest deviation (4, 5, 9, 10) show both static and dynamic correlation, whereas orbitals with smaller deviations (7 and 11, 6 and 12, 8 and 13) show mostly dynamic correlation.

The incorporation of the additional d_{z^2}–NO σ* pair and the double-shell d orbitals in the active space (DMRG(18,18)[1000] calculation) does not change the entanglement picture (Fig. 5). Compared to DMRG(16,13)[1000], only a few weak interactions with the newly added orbitals can be seen. The d_{z^2}–NO σ pair (orbitals 8 and 13) has similar single-orbital entropies to the newly added d_{z^2}–NO σ* orbitals (14 and 15) and is weakly-entangled with them; similarly weak is the interaction of the d_{xy} orbital (3) with its double shell (16). The entanglement of the two other double shells is even smaller – they are not affecting the entanglement in the Ru–NO bond in any way. Single-orbital entropies of other orbitals, present in the smaller active space, remain also unaffected. The few additional weak interactions added with the extension of the active space thus should be attributed to the dynamic correlation and do not affect the overall entanglement picture of the Ru coordination sphere found with the smaller (16,13) active space. The lack of strong entanglement and small single-orbital entropies of the double-shell d orbitals shows that their overall effect on the correlation is negligible, similar to what has been found by Pierloot and coworkers for the description of electronic excitations in other 4d transition metals.[30,46] The negligible effect of the double-shell d orbitals also explains why the orbital optimisation of the DMRG(18,18)[512]-SCF calculation could only be done with the small ANO-RCC-MB basis set, which excludes the additional p shells of the N, C and O atoms. If the larger ANO-RCC-VTZP basis set is used, the double-shell d orbitals will then be replaced by these p shells. Notably, a similar problem was faced in an earlier study of a ruthenocene complex reported by Phung *et al.*[61] We thus emphasise that despite the difference in the basis set, the entanglement picture is similar in both cases.

Summarising, the configurational analysis in terms of CASSCF natural orbitals and the entanglement analyses reveal that the Ru–NO σ bond and other Ru–ligand bonds exhibit mostly dynamic correlation and therefore they are well described with single-configurational methods, whereas the Ru–NO π bonds show static correlation and therefore require a multiconfigurational treatment. It is precisely the electronic structure of these π bonds that contributes to the non-innocence of the NO ligand and, hence, a multiconfigurational analysis is best suited to determine the electronic structure of the $\{\mathrm{RuNO}\}^6$ moiety.

An attempt to determine the electronic configuration of Ru can be performed with the help of Mulliken population analysis. For illustrative purposes and for the sake of comparison with the DFT work of Bučinský *et al.*,[4] we contrast Mulliken population differences of Ru 4d orbitals from wavefunctions obtained from

This journal is © the Owner Societies 2015

Open Access Article. Published on 10 March 2015. Downloaded on 09/08/2015 17:10:04.
This article is licensed under a Creative Commons Attribution 3.0 Unported Licence.

CASSCF and DFT calculations. The total Ru 4d atomic orbital population of the single-determinantal wavefunction is 6.47, in very good agreement with the total Ru d population of 6.54 obtained in a similar Ru nitrosyl complex by Bučinský *et al.*[4] The value obtained from the CASSCF wavefunction is 6.02. Given that a single-determinant wavefunction corresponds to a $\mathrm{Ru^{II}(d^6)–NO^+}$ configuration, *i.e.* to a theoretical Ru 4d occupation of 6, the Mulliken population analysis "overestimates" the d population by approximately half an electron (0.47). Assuming that the intrinsic overestimation of the Mulliken analysis is the same for both wavefunctions, a corrected Mulliken 4d population for the CASSCF wavefunction can be estimated to be 6.02 − 0.47 = 5.55 electrons. A d population value below 6 within a multiconfigurational calculation is due to the mixture of $\mathrm{Ru^{II}(d^6)–NO^+}$ and $\mathrm{Ru^{III}(d^5)–NO^0}$ configurations in the wavefunction. Although these values should be considered purely qualitative, the difference in Mulliken populations between single-determinant and the CASSCF wavefunction hints to the need of a multiconfiguration treatment.

Further insight into the Ru coordination sphere can be gained from transforming the CSFs into the basis of localised orbitals (Fig. 2) and analysing the CASSCF wavefunctions in terms of the transformed CSFs. The S_0 wavefunction expressed in terms of localised orbitals results in a very diffuse expansion, with a large amount of configurations having small but comparable weights, none above 6%. The configurations with the highest weights of 6% and 4% are $(\sigma_{\mathrm{Cl}})^2(d_{xy})^2(d_{yz})^2(d_{xz})^1(d_{z^2})^0(d_{x^2-y^2})^0(\pi_{\mathrm{Ind}})^1(\pi_{\mathrm{Ind}}{}^*)^1(\sigma_{\mathrm{NO}})^2(\pi_x)^2(\pi_y)^2(\pi_x{}^*)^1(\pi_y{}^*)^0$ and

$$(\sigma_{\mathrm{Cl}})^2(d_{xy})^2(d_{yz})^1(d_{xz})^2(d_{z^2})^0(d_{x^2-y^2})^0$$
$$(\pi_{\mathrm{Ind}})^1(\pi_{\mathrm{Ind}}{}^*)^1(\sigma_{\mathrm{NO}})^2(\pi_x)^2(\pi_y)^2(\pi_x{}^*)^0(\pi_y{}^*)^1$$

and include the $d_{xz} \to \pi_x{}^*$ and $d_{yz} \to \pi_y{}^*$ excitation, respectively, reflecting two $d \to \pi_{\mathrm{NO}}{}^*$ back dative bonds along both the x and y axes. Both of these configurations feature five electrons in Ru d orbitals and five electrons in the NO orbitals, which corresponds to a $\mathrm{Ru^{III}(d^5)–NO^0}$ character. The configuration with the next-largest contribution (3%) is of a $\mathrm{Ru^{II}(d^6)–NO^+}$ character:

$$(\sigma_{\mathrm{Cl}})^2(d_{xy})^2(d_{yz})^2(d_{xz})^2(d_{z^2})^0(d_{x^2-y^2})^0$$
$$(\pi_{\mathrm{Ind}})^1(\pi_{\mathrm{Ind}}{}^*)^1(\sigma_{\mathrm{NO}})^2(\pi_x)^2(\pi_y)^2(\pi_x{}^*)^0(\pi_y{}^*)^0$$

Due to the large number of contributing configurations, a detailed analysis of the character and contributions to the total wavefunction of each particular configuration is not feasible. Instead, we resort to calculating the collective weights of the configurations corresponding to the particular resonance structure. But rather than calculating only weights of *e.g.* $\mathrm{Ru^{II}–NO^+}$ to $\mathrm{Ru^{III}–NO^0}$ configurations (as done in the previous work of Radoń *et al.*[13]), we classify the CSFs into several classes based on the occupancy of either Ru or ligands, or the collective occupation of Ru and some ligands. The relative weights of configurations belonging to each class are shown in Table 1: in the first class, we consider only the occupation of Ru d orbitals (*cf.* Fig. 2a and Table 1a), then only the NO orbital occupancy (Fig. 2b and Table 1b) equal to n = 6 ($\mathrm{NO^-}$), 5 ($\mathrm{NO^0}$) or 4 ($\mathrm{NO^+}$), and finally the combined Ru d and NO occupancy (Table 1c).

Table 1 Contributions of all configurations in the S_0 and T_1 states with certain properties: (a) only Ru electron configuration taken into account; (b) Only NO electron configuration taken into account; (c) both Ru and NO electron configurations are taken into account; (d) the charge transfer from Cl to NO and Ru is considered

	Character	Contr. S_0 (%)	Contr. T_1 (%)
(a)	$\mathrm{Ru^{IV}(d^4)}$	7.7	8.9
	$\mathrm{Ru^{III}(d^5)}$	42.0	44.9
	$\mathrm{Ru^{II}(d^6)}$	39.9	38.4
(b)	$\mathrm{NO^-}$	18.3	23.1
	$\mathrm{NO^0}$	58.0	62.3
	$\mathrm{NO^+}$	21.5	12.2
(c)	$\mathrm{Ru^{IV}(d^4)}$ and $\mathrm{NO^-}$	7.3	8.2
	$\mathrm{Ru^{III}(d^5)}$ and $\mathrm{NO^0}$	31.9	31.2
	$\mathrm{Ru^{II}(d^6)}$ and $\mathrm{NO^+}$	14.3	8.8
	$\mathrm{Ru^{II}(d^6)}$ and $\mathrm{NO^0}$	24.7	28.7
(d)	$\mathrm{Ru^{II}(d^6)}$ and $(\sigma_{\mathrm{Cl}})^1$	24.6	28.7
	$\mathrm{NO^-}$ and $(\sigma_{\mathrm{Cl}})^1$	10.0	13.2

From the analysis of Table 1a we see that the contribution of $\mathrm{Ru^{II}(d^6)}$ and $\mathrm{Ru^{III}(d^5)}$ configurations to the S_0 state is almost the same, yielding a formal oxidation state of Ru of 2.5. This value is in accordance with the corrected Mulliken d population in the CASSCF wavefunction of 5.55 determined previously, despite the fact that Mulliken populations should be treated only qualitatively. A similar process is carried out with NO (Table 1b). The $\mathrm{Ru^{II}}$ to $\mathrm{Ru^{III}}$ ratios do not correspond to the ratios of ionic to neutral NO: the $\mathrm{NO^0}$ contribution is the predominant one in this complex (58%). Moreover, $\mathrm{NO^+}$ contributions are largely cancelled out by $\mathrm{NO^-}$ contributions.

Since the net charge (−1) of the complex cannot be explained with a Ru formal oxidation state of 2.5 and a $\mathrm{NO^0}$ ligand, we also consider the class of configurations combining the Ru and NO occupancies. Table 1c shows that the $\mathrm{Ru^{III}–NO^0}$ configurations have the largest collective weight, above 30%, which is 2.2 times as large as that of the $\mathrm{Ru^{II}–NO^+}$ configurations. This weight ratio is slightly smaller than the weight ratio of $\mathrm{NO^0}$ to $\mathrm{NO^+}$ configurations, which is approximately 2.7. This shows that the Ru–NO bond situation is dominated by a strong $d \to \pi_{\mathrm{NO}}{}^*$ back donation leading to $\mathrm{NO^0}$ and the d^6 character of Ru comes from elsewhere. Indeed, we find a large amount of configurations with $\mathrm{Ru^{II}(d^6)}$ and $\mathrm{NO^0}$ character, with an even larger weight than that of the $\mathrm{Ru^{II}(d^6)}$ and $\mathrm{NO^+}$ configurations. Table 1d reveals that these configurations entirely correspond to the $\sigma_{\mathrm{Cl}} \to d_{x^2-y^2}$ excitations, *i.e.* to a charge transfer from Cl ligands.

Summarising the configuration analysis for the S_0 state, we may conclude that the electronic structure of $\{\mathrm{RuNO}\}^6$ is a mixture of several important contributions from which the $\mathrm{Ru^{III}–NO^0}$ configurations are most important, indicating a strong $d \to \pi_{\mathrm{NO}}{}^*$ back donation. The $\mathrm{Ru^{II}–NO^+}$ configurations are about half as important if compared by total contributions to the wavefunction, and give Ru some of its $\mathrm{Ru^{II}}$ character. Despite the lesser significance of $\mathrm{Ru^{II}–NO^+}$ configurations, Ru shows a large amount of $\mathrm{Ru^{II}}$ character, almost equal to its $\mathrm{Ru^{III}}$ character by having a formal oxidation state of 2.5. A larger amount of the d^6 character of Ru, however, does not arise from these configurations,

Open Access Article. Published on 10 March 2015. Downloaded on 09/08/2015 17:10:04. This article is licensed under a Creative Commons Attribution 3.0 Unported Licence.

but rather from an electron transfer from the Cl ligands, which can be seen from the contribution of $Ru^{II}(d^6)$–$(\sigma_{Cl})^1$ configurations: this contribution is almost identical to that of $Ru^{II}(d^6)$–NO^0.

Very similar results are obtained for the T_1 state, despite its different molecular structure and electronic wavefunction. Most notably, the weights of Ru d^5 and d^6 configurations are alike and hence the formal oxidation state of Ru is also approximately 2.5. The CSFs with the largest weight have the same electronic configurations as in the case of S_0, albeit with a different spin and weights under 3%. At first glance, this is quite unexpected since the T_1 state involves an excitation to a metal–NO π^* antibonding orbital and Ru–NO back donation gets stronger. As such one would expect a withdrawal of electron density from the metal to NO. Indeed, we observe it to some extent, as the weight of NO^+ and $Ru^{II}(d^6)$–NO^+ configurations decreases compared to the S_0 state (8.8% in T_1 *vs.* 14.3% in S_0): the bent-coordinated NO has even less NO^+ contributions than the linear-coordinated one. However, this electron withdrawal from the metal is compensated by the stronger Ru → Cl dative bond: the cumulative weight of $Ru^{II}(d^6)$–$(\sigma_{Cl})^1$ configurations increases to 28.7%. This stronger dative bond compensates for the electron density loss on Ru due to a stronger back donation, yielding a similar Ru electronic configuration to that in S_0.

4 Conclusion

In this work, we have employed multiconfigurational methods to analyse the electronic structure of the lowest singlet and triplet states of RuHIndNO, a ruthenium nitrosyl complex. We performed a CASSCF calculation on the optimised geometries for the S_0 and T_1 states of RuHIndNO and analysed the resulting wavefunction both in terms of CASSCF natural orbitals and localised orbitals. The Ru–NO bond shows strong electronic correlation, both static and dynamic, which is supported by the weight of the dominant configuration being significantly below 100%, comparably large weights of single excitations and large fractional populations of the orbitals involved in this bond and the analysis of orbital entanglement. An orbital entanglement analysis based on the one- and two-orbital reduced density matrices calculated from the DMRG wavefunction of the S_0 state provides further evidence of strong static correlation in the Ru–NO π bonds, while the Ru–NO σ bond and other Ru–ligand bonds are largely dominated by dynamic correlation. An additional entanglement analysis based on a larger active-space calculation shows a negligible effect of the double-shell d orbitals on the static correlation effects. Furthermore, Mulliken Ru d orbital population based on the single-reference DFT and CASSCF wavefunction shows a discrepancy of approximately 0.5 electrons. In view of these results, we advocate the usage of multiconfigurational methods such as CASSCF to describe the correct bonding situation in the Ru–NO moiety.

CASSCF-type methods also allow for an extensive electronic structure analysis of the metal centre, ligands and metal-ligand bonds in the Ru coordination sphere. By a comparatively straightforward unitary transformation of the active-space orbitals, an operation which does not change the physical content of the wavefunction, we obtain a possibility to quantify the contributions from different electronic configurations and therefore to describe the electronic structure of $\{RuNO\}^6$ more precisely than any assigned formal oxidation state would do. As we have shown, a single structure *e.g.* Ru^{III}–NO^0 or Ru^{II}–NO^+ does not account for the complexity of the $\{RuNO\}^6$ electronic structure. Although the electronic structure of the RuHIndNO complex is a superposition of configurations like Ru^{III}–NO^0, Ru^{II}–NO^+ and many others, we gain more details about the structure when we describe the Ru and NO fragments of the Ru–NO bond separately. In this view, our results show that the electronic configuration of Ru consists of approximately equal amounts of $d^5(Ru^{III})$ and $d^6(Ru^{II})$ contributions, resulting in a formal Ru oxidation state of 2.5. The NO electronic configuration, on the other hand, shows a predominantly neutral character, which is in contrast to the commonly accepted picture of the Ru^{II}–NO^+ description. The NO neutral character arises mainly due to the d → π_{NO}^* back donation, but a dative contribution by the Cl ligands compensates the outflux of the electron density due to this back donation. This description of Ru and NO is almost the same for both the S_0 and T_1 state, despite the different electronic structures, with the only difference that metal → NO back donation is even stronger in the T_1 structure. This increase of the metal → NO back donation is additionally supported by the increase of the bond length in the triplet state.

Acknowledgements

Financial support from the University of Vienna, the COST Action CM1305 ''Explicit Control Over Spin-states in Technology and Biochemistry'', the Research Council of Norway through a Centre of Excellence Grant (Grant No. 179568/V30), the Italian Ministry of Education and Research (MIUR)-Grant No. RBFR1248UI, the Uppsala University, eSSENCE, and the Swedish Research Council (VR) is gratefully acknowledged. Furthermore, we thank Yingjin Ma for the help with the MAQUIS-MOLCAS interface, as well as Vladimir Arion and Gabriel Büchel for fruitful discussions.

References

1 (*a*) E. Culotta and D. E. Koshland, *Science*, 1992, **258**, 1862–1865; (*b*) F. C. Fang, *Nitric Oxide and Infection*, Springer, 1999; (*c*) L. J. Ignarro, *Nitric Oxide: Biology and Pathobiology*, Academic Press, 2000.

2 (*a*) P. Ford, J. Bourassa, K. Miranda, B. Lee, I. Lorkovic, S. Boggs, S. Kudo and L. Laverman, *Coord. Chem. Rev.*, 1998, **171**, 185–202; (*b*) P. C. Ford and I. M. Lorkovic, *Chem. Rev.*, 2002, **102**, 993–1018; (*c*) A. R. Butler and I. L. Megson, *Chem. Rev.*, 2002, **102**, 1155–1166; (*d*) J. L. Bourassa and P. C. Ford, *Coord. Chem. Rev.*, 2000, **200–202**, 887–900; (*e*) M. Hoshino, L. Laverman and P. C. Ford, *Coord. Chem. Rev.*, 1999, **187**, 75–102; (*f*) C. F. Works, C. J. Jocher, G. D. Bart, X. Bu and P. C. Ford, *Inorg. Chem.*, 2002, **41**, 3728–3739; (*g*) C. F. Works and P. C. Ford, *J. Am. Chem. Soc.*, 2000, **122**, 7592–7593; (*h*) A. K. Patra and P. K. Mascharak, *Inorg. Chem.*, 2003, **42**,

Open Access Article. Published on 10 March 2015. Downloaded on 09/08/2015 17:10:04. This article is licensed under a Creative Commons Attribution 3.0 Unported Licence.

7363–7365; (*i*) E. Tfouni, D. R. Truzzi, A. Tavares, A. J. Gomes, L. E. Figueiredo and D. W. Franco, *Nitric Oxide*, 2012, **26**, 38–53.

3 B. Serli, E. Zangrando, E. Iengo, G. Mestroni, L. Yellowlees and E. Alessio, *Inorg. Chem.*, 2002, **41**, 4033–4043.

4 L. Bučinský, G. E. Büchel, R. Ponec, P. Rapta, M. Breza, J. Kožíšek, M. Gall, S. Biskupič, M. Fronc, K. Schiessl, O. Cuzan, D. Prodius, C. Turta, S. Shova, D. A. Zając and V. B. Arion, *Eur. J. Inorg. Chem.*, 2013, 2505–2519.

5 (*a*) J. M. Rademaker-Lakhai, D. v. d. Bongard, D. Pluim, J. H. Beijnen and J. H. M. Schellens, *Clin. Cancer Res.*, 2004, **10**, 3717–3727; (*b*) E. Alessio, G. Mestroni, A. Bergamo and G. Sava, *Curr. Top. Med. Chem.*, 2004, **4**, 1525–1535.

6 C. G. Hartinger, S. Zorbas-Seifried, M. A. Jakupec, B. Kynast, H. Zorbas and B. K. Keppler, *J. Inorg. Biochem.*, 2006, **100**, 891–904.

7 (*a*) C. Jørgensen, *Coord. Chem. Rev.*, 1966, **1**, 164–178; (*b*) W. Kaim, *Eur. J. Inorg. Chem.*, 2012, 343–348.

8 J. Enemark and R. Feltham, *Coord. Chem. Rev.*, 1974, **13**, 339–406.

9 J. H. Enemark and R. D. Feltham, *J. Am. Chem. Soc.*, 1974, **96**, 5002–5004.

10 (*a*) M. Li, D. Bonnet, E. Bill, F. Neese, T. Weyhermüller, N. Blum, D. Sellmann and K. Wieghardt, *Inorg. Chem.*, 2002, **41**, 3444–3456; (*b*) R. G. Serres, C. A. Grapperhaus, E. Bothe, E. Bill, T. Weyhermüller, F. Neese and K. Wieghardt, *J. Am. Chem. Soc.*, 2004, **126**, 5138–5153; (*c*) P. Singh, B. Sarkar, M. Sieger, M. Niemeyer, J. Fiedler, S. Záliš and W. Kaim, *Inorg. Chem.*, 2006, **45**, 4602–4609; (*d*) G. F. Caramori and G. Frenking, *Organometallics*, 2007, **26**, 5815–5825; (*e*) G. F. Caramori and G. Frenking, *Croat. Chem. Acta*, 2009, **82**, 219–232; (*f*) G. F. Caramori, A. G. Kunitz, K. F. Andriani, F. G. Doro, G. Frenking and E. Tfouni, *Dalton Trans.*, 2012, **41**, 7327–7339; (*g*) A. G. De Candia, J. P. Marcolongo, R. Etchenique and L. D. Slep, *Inorg. Chem.*, 2010, **49**, 6925–6930; (*h*) J. Conradie and A. Ghosh, *J. Phys. Chem. B*, 2007, **111**, 12621–12624; (*i*) H.-Y. Cheng, S. Chang and P.-Y. Tsai, *J. Phys. Chem. A*, 2004, **108**, 358–361; (*j*) J. Oláh and J. N. Harvey, *J. Phys. Chem. A*, 2009, **113**, 7338–7345; (*k*) K. F. Andriani, G. F. Caramori, F. G. Doro and R. L. T. Parreira, *Dalton Trans.*, 2014, **43**, 8792–8804.

11 O. V. Sizova, V. I. Baranovski, N. V. Ivanova and V. V. Sizov, *Mol. Phys.*, 2003, **101**, 715–720.

12 M. Radoń and K. Pierloot, *J. Phys. Chem. A*, 2008, **112**, 11824–11832.

13 M. Radoń, E. Broclawik and K. Pierloot, *J. Phys. Chem. B*, 2010, **114**, 1518–1528.

14 L. Freitag and L. González, *Inorg. Chem.*, 2014, **53**, 6415–6426.

15 M. J. Rose and P. K. Mascharak, *Coord. Chem. Rev.*, 2008, **252**, 2093–2114.

16 F. Roncaroli, M. Videla, L. D. Slep and J. A. Olabe, *Coord. Chem. Rev.*, 2007, **251**, 1903–1930.

17 C. J. Cramer and D. G. Truhlar, *Phys. Chem. Chem. Phys.*, 2009, **11**, 10757–10816.

18 A. J. Cohen, P. Mori-Sánchez and W. Yang, *Science*, 2008, **321**, 792–794.

19 R. J. Bartlett and J. F. Stanton, in *Reviews in Computational Chemistry*, ed. K. B. Lipkowitz and D. B. Boyd, John Wiley & Sons, Inc., 1994, pp. 65–169.

20 O. Sinanoğlu and D. F. Tuan, *J. Chem. Phys.*, 1963, **38**, 1740–1748.

21 K. Boguslawski, P. Tecmer, Ö. Legeza and M. Reiher, *J. Phys. Chem. Lett.*, 2012, **3**, 3129–3135.

22 B. O. Roos, P. R. Taylor and P. E. Siegbahn, *Chem. Phys.*, 1980, **48**, 157–173.

23 P. A. Malmqvist, K. Pierloot, A. R. M. Shahi, C. J. Cramer and L. Gagliardi, *J. Chem. Phys.*, 2008, **128**, 204109.

24 (*a*) S. R. White, *Phys. Rev. Lett.*, 1992, **69**, 2863–2866; (*b*) S. R. White, *Phys. Rev. B: Condens. Matter Mater. Phys.*, 1993, **48**, 10345–10356.

25 (*a*) K. H. Marti and M. Reiher, *Z. Phys. Chem.*, 2010, **224**, 583–599; (*b*) G. K.-L. Chan and S. Sharma, *Annu. Rev. Phys. Chem.*, 2011, **62**, 465–481; (*c*) Y. Kurashige, *Mol. Phys.*, 2013, **112**, 1485–1494; (*d*) S. Wouters and D. van Neck, *Eur. Phys. J. D*, 2014, **68**, 272; (*e*) T. Yanai, Y. Kurashige, W. Mizukami, J. Chalupský, T. N. Lan and M. Saitow, *Int. J. Quantum Chem.*, 2015, **115**, 283–299; (*f*) S. Sharma and G. K.-L. Chan, *J. Chem. Phys.*, 2012, **136**, 124121; (*g*) Ö. Legeza, R. M. Noack, J. Sólyom and L. Tincani, in *Computational Many-Particle Physics*, ed. H. Fehske, R. Schneider and A. Weiße, Springer Berlin Heidelberg, 2008, pp. 653–664.

26 K. Andersson, P. A. Malmqvist, B. O. Roos, A. J. Sadlej and K. Wolinski, *J. Phys. Chem.*, 1990, **94**, 5483–5488.

27 (*a*) Y. Kurashige and T. Yanai, *J. Chem. Phys.*, 2011, **135**, 094104; (*b*) S. Sharma and G. K.-L. Chan, *J. Chem. Phys.*, 2014, **141**, 111101.

28 K. Boguslawski, C. R. Jacob and M. Reiher, *J. Chem. Theory Comput.*, 2011, **7**, 2740–2752.

29 K. Boguslawski, K. H. Marti, Ö. Legeza and M. Reiher, *J. Chem. Theory Comput.*, 2012, **8**, 1970–1982.

30 K. Pierloot, in *Computational Organometallic Chemistry*, ed. T. R. Cundari, Marcel Dekker Inc., New York, 2001, pp. 123–158.

31 D. Ma, G. Li Manni and L. Gagliardi, *J. Chem. Phys.*, 2011, **135**, 044128.

32 P.-O. Löwdin, *J. Chem. Phys.*, 1951, **19**, 1396–1401.

33 G. Li Manni, D. Ma, F. Aquilante, J. Olsen and L. Gagliardi, *J. Chem. Theory Comput.*, 2013, **9**, 3375–3384.

34 K. H. Marti, I. Malkin Ondík, G. Moritz and M. Reiher, *J. Chem. Phys.*, 2008, **128**, 014104.

35 (*a*) Y. Kurashige, G. K.-L. Chan and T. Yanai, *Nat. Chem.*, 2013, **5**, 660–666; (*b*) S. Wouters, T. Bogaerts, P. V. D. Voort, V. V. Speybroeck and D. V. Neck, *J. Chem. Phys.*, 2014, **140**, 241103; (*c*) S. Sharma, K. Sivalingam, F. Neese and G. K.-L. Chan, *Nat. Chem.*, 2014, **6**, 927–933; (*d*) J. Chalupský, T. A. Rokob, Y. Kurashige, T. Yanai, E. I. Solomon, L. Rulíšek and M. Srnec, *J. Am. Chem. Soc.*, 2014, **136**, 15977–15991.

36 Ö. Legeza and J. Sólyom, *Phys. Rev. B: Condens. Matter Mater. Phys.*, 2003, **68**, 195116.

37 Ö. Legeza and J. Sólyom, *Phys. Rev. Lett.*, 2006, **96**, 116401.

38 J. Rissler, R. M. Noack and S. R. White, *Chem. Phys.*, 2006, **323**, 519–531.

Open Access Article. Published on 10 March 2015. Downloaded on 09/08/2015 17:10:04.
This article is licensed under a Creative Commons Attribution 3.0 Unported Licence.

39 (*a*) K. Boguslawski, P. Tecmer, G. Barcza, Ö. Legeza and M. Reiher, *J. Chem. Theory Comput.*, 2013, **9**, 2959–2973; (*b*) M. Mottet, P. Tecmer, K. Boguslawski, Ö. Legeza and M. Reiher, *Phys. Chem. Chem. Phys.*, 2014, **16**, 8872–8880.

40 (*a*) P. Pulay and T. P. Hamilton, *J. Chem. Phys.*, 1988, **88**, 4926–4933; (*b*) M. S. Gordon, M. W. Schmidt, G. M. Chaban, K. R. Glaesemann, W. J. Stevens and C. Gonzalez, *J. Chem. Phys.*, 1999, **110**, 4199–4207.

41 (*a*) N. H. F. Beebe and J. Linderberg, *Int. J. Quantum Chem.*, 1977, **12**, 683–705; (*b*) H. Koch, A. Sánchez de Merás and T. B. Pedersen, *J. Chem. Phys.*, 2003, **118**, 9481–9484; (*c*) T. B. Pedersen, F. Aquilante and R. Lindh, *Theor. Chem. Acc.*, 2009, **124**, 1–10; (*d*) F. Aquilante, L. Boman, J. Boström, H. Koch, R. Lindh, A. Sánchez de Merás and T. B. Pedersen, in *Challenges and Advances in Computational Chemistry and Physics*, ed. M. G. Papadopoulos, R. Zalesny, P. G. Mezey and J. Leszczynski, Springer, 2011, vol. 13, pp. 301–344.

42 (*a*) F. Aquilante, T. B. Pedersen, R. Lindh, B. O. Roos, A. Sánchez de Merás and H. Koch, *J. Chem. Phys.*, 2008, **129**, 024113; (*b*) F. Aquilante, P.-Å. Malmqvist, T. B. Pedersen, A. Ghosh and B. O. Roos, *J. Chem. Theory Comput.*, 2008, **4**, 694–702; (*c*) F. Aquilante, T. K. Todorova, T. B. Pedersen, L. Gagliardi and B. O. Roos, *J. Chem. Phys.*, 2009, **131**, 34113; (*d*) D. Roca-Sanjuán, F. Aquilante and R. Lindh, *WIREs Comput. Mol. Sci.*, 2012, **2**, 585–603.

43 (*a*) F. Aquilante, R. Lindh and T. B. Pedersen, *J. Chem. Phys.*, 2008, **129**, 034106; (*b*) J. Boström, F. Aquilante, T. B. Pedersen and R. Lindh, *J. Chem. Theory Comput.*, 2013, **9**, 204–212.

44 M. G. Delcey, L. Freitag, T. B. Pedersen, F. Aquilante, R. Lindh and L. González, *J. Chem. Phys.*, 2014, **140**, 174103.

45 A. Gavriluta, G. E. Büchel, L. Freitag, G. Novitchi, J. B. Tommasino, E. Jeanneau, P.-S. Kuhn, L. González, V. B. Arion and D. Luneau, *Inorg. Chem.*, 2013, **52**, 6260–6272.

46 K. Pierloot, *Int. J. Quantum Chem.*, 2011, **111**, 3291–3301.

47 J. P. Perdew, *Phys. Rev. B: Condens. Matter Mater. Phys.*, 1986, **33**, 8822–8824.

48 A. D. Becke, *J. Chem. Phys.*, 1993, **98**, 5648–5652.

49 F. Weigend and R. Ahlrichs, *Phys. Chem. Chem. Phys.*, 2005, **7**, 3297–3305.

50 K. Eichkorn, F. Weigend, O. Treutler and R. Ahlrichs, *Theor. Chem. Acc.*, 1997, **97**, 119–124.

51 D. Andrae, U. Häußermann, M. Dolg, H. Stoll and H. Preuß, *Theor. Chim. Acta*, 1990, **77**, 123–141.

52 (*a*) K. Eichkorn, O. Treutler, H. Öhm, M. Häser and R. Ahlrichs, *Chem. Phys. Lett.*, 1995, **240**, 283–290; (*b*) M. Sierka, A. Hogekamp and R. Ahlrichs, *J. Chem. Phys.*, 2003, **118**, 9136–9148.

53 *TURBOMOLE V6.5 2013*, a development of University of Karlsruhe and Forschungszentrum Karlsruhe GmbH, 1989–2007, TURBOMOLE GmbH, since 2007, available from http://www.turbomole.com.

54 B. O. Roos, R. Lindh, P.-A. Malmqvist, V. Veryazov and P.-O. Widmark, *J. Phys. Chem. A*, 2005, **109**, 6575–6579.

55 F. Aquilante, L. de Vico, N. Ferré, G. Ghigo, P.-Å. Malmqvist, P. Neogrády, T. B. Pedersen, M. Pitoňák, M. Reiher, B. O. Roos, L. Serrano-Andrés, M. Urban, V. Veryazov and R. Lindh, *J. Comput. Chem.*, 2010, **31**, 224–247.

56 J. P. Perdew, K. Burke and M. Ernzerhof, *Phys. Rev. Lett.*, 1996, **77**, 3865–3868.

57 R. S. Mulliken, *J. Chem. Phys.*, 1955, **23**, 1833–1840.

58 S. F. Keller and M. Reiher, *Chimia*, 2014, **68**, 200–203.

59 M. Dolfi, B. Bauer, S. Keller, A. Kosenkov, T. Ewart, A. Kantian, T. Giamarchi and M. Troyer, *Comput. Phys. Commun.*, 2014, **185**, 3430–3440.

60 F. Aquilante, T. B. Pedersen, A. Sánchez de Merás and H. Koch, *J. Chem. Phys.*, 2006, **125**, 174101.

61 Q. M. Phung, S. Vancoillie, A. Delabie, G. Pourtois and K. Pierloot, *Theor. Chem. Acc.*, 2012, **131**, 1–9.

This journal is © the Owner Societies 2015

APPENDIX 3.A.4

Theoretical Spectroscopy and Photodynamics of a Ruthenium Nitrosyl Complex

Leon Freitag and Leticia González

Inorg. Chem., **2014**, *53*, 6415–6426.
`https://doi.org/10.1021/ic500283y`

Contributions:

LEON FREITAG planned, performed and evaluated the quantum chemical and surface-hopping dynamics calculations, adapted the dynamics code and prepared the draft of the manuscript.

LETICIA GONZÁLEZ conceived the idea, took part in planning and supervised the study and helped in preparation of the final manuscript.

Reprinted with permission from Inorg. Chem., **2014**, *53*, 6415–6426.
Copyright© 2014, American Chemical Society.

Inorganic Chemistry
Forum Article
pubs.acs.org/IC

Theoretical Spectroscopy and Photodynamics of a Ruthenium Nitrosyl Complex

Leon Freitag and Leticia González*

Institut für theoretische Chemie, Universität Wien, Währinger Straße 17, 1090 Vienna, Austria

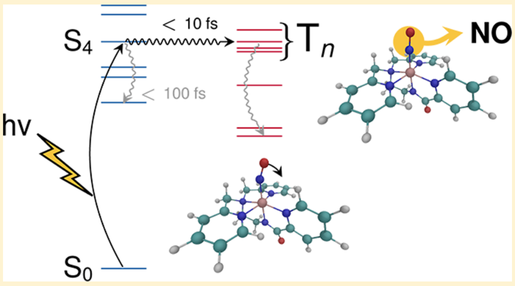

ABSTRACT: Photoactive transition-metal nitrosyl complexes are particularly interesting as potential drugs that deliver nitric oxide (NO) upon UV-light irradiation to be used, e.g., in photodynamic therapy. It is well-recognized that quantum-chemical calculations can guide the rational design and synthesis of molecules with specific functions. In this contribution, it is shown how electronic structure calculations and dynamical simulations can provide a unique insight into the photodissociation mechanism of NO. Exemplarily, $[Ru(PaPy_3)(NO)]^{2+}$ is investigated in detail, as a prototype of a particularly promising class of photoactive metal nitrosyl complexes. The ability of time-dependent density functional theory (TD-DFT) to obtain reliable excited-state energies compared with more sophisticated multiconfigurational spin-corrected calculations is evaluated. Moreover, a TD-DFT-based trajectory surface-hopping molecular dynamics study is employed to reveal the details of the radiationless decay of the molecule via internal conversion and intersystem crossing. Calculations show that the ground state of $[Ru(PaPy_3)(NO)]^{2+}$ includes a significant admixture of the $Ru^{III}(NO)^0$ electronic configuration, in contrast to the previously postulated $Ru^{II}(NO)^+$ structure of similar metal nitrosyls. Moreover, the lowest singlet and triplet excited states populate the antibonding metal d → π_{NO}* orbitals, favoring NO dissociation. Molecular dynamics show that intersystem crossing is ultrafast (<10 fs) and dissociation is initiated in less than 50 fs. The competing relaxation to the lowest S$_1$ singlet state takes place in less than 100 fs and thus competes with NO dissociation, which mostly takes place in the higher-lying excited triplet states. All of these processes are accompanied by bending of the NO ligand, which is not confined to any particular state.

INTRODUCTION

The study of the electronic structure and spectroscopic properties of transition-metal (TM) nitrosyl complexes has long been a subject of interest in inorganic and bioinorganic chemistry. Nitric oxide (NO) plays a role in many biological processes, such as neurotransmission, blood pressure control, or control of tumor growth.[1−3] Following these discoveries, various TM nitrosyl complexes have been investigated as potential carriers able to deliver NO on demand in biological tissues upon illumination, for example to be used in photodynamic therapy (PDT) to treat cancers.[4] Early studies on NO delivery focused on well-known salts, such as sodium nitroprusside $Na_2[Fe(CN)_5(NO)]$, Roussin's salts $(NH_4)[Fe_4S_3(NO)_7]$ and $Na_2[Fe_2S_2(NO)_4]$)[5,6] or metalloporphyrins, derived from heme.[7,8] However, more recently, in the pursuit to tune the quantum yield and wavelength suitable for the NO photorelease, a number of iron,[9,10] manganese,[11] and ruthenium nitrosyl complexes with other auxiliary ligands[12−16] have been synthesized. In this regard, quite promising is the series of metal nitrosyls $[M(PaPy_3)(NO)]^{2+}$ (M = Fe, Mn, Ru) synthesized by Mascharak and co-workers,[9,11,14] in which the photorelease wavelength is metal-dependent and additionally may be varied by modifying the auxiliary PaPy$_3$ ligand[17] (PaPy$_3$ = *N*,*N*′-bis(2-pyridylmethyl)amine-*N*-ethyl-2-pyridine-2-carboxamide; cf. Scheme 1).

An efficient design of metal−NO carrier complexes can be assisted by electronic structure calculations. In particular, because of its cost-efficiency ratio, density functional theory (DFT) and its time-dependent (TD-DFT) version have become the most popular formalisms to calculate ground- and excited-state properties of TM complexes.[18]

Scheme 1

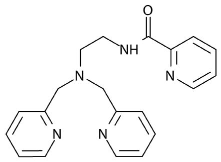

PaPy$_3$H

Excited-state TD-DFT studies on TM nitrosyls[19−23] suggest that metal-to-ligand charge-transfer (MLCT) $d_M \rightarrow \pi_{NO}$* states are responsible for their photolability. Yet, different dissociation mechanisms are possible. While in some metal complexes a direct mechanism of NO photorelease via direct population of the $d_M \rightarrow \pi_{NO}$* singlet excited state has been postulated, in others the initial excited state is a MLCT state located in a

Special Issue: Insights into Spectroscopy and Reactivity from Electronic Structure Theory

Received: February 4, 2014
Published: April 21, 2014

© 2014 American Chemical Society

dx.doi.org/10.1021/ic500283y | *Inorg. Chem.* 2014, 53, 6415−6426

different ligand (i.e., $d_M \rightarrow \pi_L^*$), and therefore internal conversion is required prior to dissociation in the antibonding $d_M \rightarrow \pi_{NO}^*$ state.[21,22] Moreover, intersystem crossing (ISC) into a $d_M \rightarrow \pi_{NO}^*$ triplet state can also be involved in the NO release.[21−23] These conclusions have been mainly obtained from the theoretical characterization of the absorption spectra obtained from vertical excitation energies and analysis of the Kohn−Sham DFT frontier orbitals of the equilibrium ground state and lowest triplet excited states. Further insight into the dissociation mechanism has also been gained from one-dimensional potential energy scans along the M−NO dissociation coordinate, as in refs 20 and 23.

Beyond stationary quantum-chemical calculations, dynamical simulations could help to reveal further details of the mechanism of NO delivery. In general, a dynamical study allows one to monitor the evolution of the nuclear geometries in time, providing a comprehensive picture of the different states and structures that are visited by the system after light irradiation.[24] In particular, trajectory surface-hopping molecular dynamics[25] is one of the methods most widely employed to simulate nonadiabatic photochemistry beyond the Born−Oppenheimer approximation. It has been employed successfully to explain a large number of ultrafast processes in organic molecules,[26,27] but its application to TM complexes is still in its infancy[28,29] because of the inherent difficulties and computational expenses involved in describing accurately TM complexes with quantum-chemical methods.[30]

Indeed, despite its popularity, the application of TD-DFT to describe the photochemistry of TM complexes is challenging because it requires a balanced description of excited states of very different character.[31] Moreover, the electronic structure of nitrosyl compounds is particularly complicated because of the additional problem of noninnocence of the NO ligand: In metal nitrosyls, NO does not have a clear oxidation state and can exist as NO^+, NO^-, and NO^0.[6,32−36]

Although previous studies on metal nitrosyl complexes[20−22] show satisfactory agreement of the experimental UV−vis absorption spectra with the results calculated with TD-DFT, the most appropriate method to treat these complexes is with multiconfigurational wave-function calculations, such as the complete active space self-consistent-field (CASSCF) method[37] and its second-order perturbation theory version (CASPT2).[38] Indeed, the pioneering work of Pierloot's group in the field of metal nitrosyl complexes[34,39,40] nicely illustrates that CASSCF and CASPT2 are the most adequate methods to describe the complicated electronic structure of these compounds. In general, however, CASSCF/CASPT2 calculations on large TM complexes have remained relatively sparse (see, e.g., refs 30, 31, and 41−43) mainly because of their extensive computational cost. Encouragingly, recent developments in approximation techniques for the two-electron integrals, such as density fitting and Cholesky decomposition,[44] have introduced significant savings of computational time and disk space allowing CASSCF/CASPT2 calculations to be carried out on large TM complexes.[45]

Another important aspect of TM complexes is that, because of the nature of the heavy atom, relativistic effects should be expected. The energies and also the character of the states can be affected by spin−orbit coupling (SOC), influencing their photochemical properties and decay pathways. However, because of the larger computational effort, only a few studies incorporate SOC in the calculation of UV−vis absorption spectra using CASSCF/CASPT2 methods.[46,47] The fact that states of different multiplicity are involved in many photophysical processes of TM complexes is well-known,[48,49] but most studies are limited to analyses of the geometries and orbitals of the lowest singlet and triplet states to explain the reactivity of the TM complex. Calculations including spin dynamics, even if in an approximated way, are exceptional.[29]

In this paper, we push theory in different ways to provide insight into the spectroscopy and reactivity of TM complexes. In particular, we focus on a ruthenium nitrosyl complex, $[Ru(PaPy_3)(NO)]^{2+}$, with the specific aim to learn about the NO dissociation mechanism. Such a study should help to understand the factors that influence the photostability and photodissociation wavelength of these complexes[14] and thus contribute to a rationalization of the drug design for PDT. From a theoretical point of view, this is a contemporary challenge because it implies going beyond the calculation of a UV spectrum for the equilibrium geometry, the optimization of the lowest minimum structures, or the computation of the potential energy curves along one reaction coordinate.[50] Here, we desire to obtain information about relevant geometrical features that are responsible for the reactivity (photodissociation) of metal nitrosyl complexes starting from the bright state. o the best of our knowledge, available studies on this family of complexes have only made use of DFT and TD-DFT and did not account for spin−orbit corrections. Here we shall compute spin-corrected energies and compare the results with the spin-free ones to determine the influence of SOC on the excited-state energies and excitation characters of these complexes. Additionally, we shall assess the applicability of TD-DFT in these compounds by computing the absorption spectra of $[Ru(PaPy_3)(NO)]^{2+}$ with multiconfigurational methods, i.e., with CASPT2. The results will be compared with TD-DFT calculations on metal $PaPy_3$ nitrosyls.[21,22] Finally, and most challenging, time-resolved insight into the NO photorelease mechanism and competing photoprocesses will be obtained by performing a trajectory surface-hopping molecular dynamics study at the TD-DFT level of theory within the singlet- and the triplet-state manifolds. This is, to our knowledge, the first full-dimensional dynamical study on TM nitrosyl complexes.

■ METHODS AND COMPUTATIONAL DETAILS

Quantum-Chemical Calculations. All DFT and TD-DFT calculations have been performed with the pure BP86[51,52] functional, which has also been employed in the same ruthenium complex and analogous manganese nitrosyl.[21] Moreover, BP86 has the advantage that it allows very fast and efficient computations by employing the resolution-of-identity (RI) approximation for calculating the electronic Coulomb term (RI-J)[53,54] and its multipole-accelerated version (MARI-J).[55] This will be especially important for time savings in the dynamical study, as detailed below. Optimization of the gas-phase equilibrium structure has been carried out using Ahlrichs' def2-SV(P) basis set.[56,57] Additionally, scalar relativistic effects in ruthenium have been accounted for using the quasi-relativistic 28-electron effective core potential (MWB28 ECP).[58] The lowest triplet state has been optimized within the unrestricted DFT formalism. Spin-free electronic excited states have been calculated by means of TD-DFT using the same functional and the def2-TZVPP basis set.[57,59] A total of 30 singlet and 30 triplet excited states have been computed. Solvent effects have been considered using the COSMO solvation model.[60] All of these calculations have been performed with the TURBOMOLE 6.5[61] program package.

Using the BP86 geometry, multiconfigurational spin-free and spin-corrected CASSCF/CASPT2 calculations have been obtained using the MOLCAS 7.8 program package.[62] The active space consisted of 18 electrons in 14 orbitals, including the five Ru 4d orbitals, two pairs of

NO π and π^* orbitals, two σ orbitals that form bonding−antibonding pairs with the Ru $d_{x^2-y^2}$ and d_{z^2} orbitals, respectively, and one $\pi-\pi^*$ pair located at the amide moiety; see Figure 1a. The all-electron ANO-RCC-VTZP basis set[63] has been used for the ruthenium atom and the ANO-RCC-VDZP basis set for other atoms: a CASSCF test calculation with this mixed basis set yielded results almost identical with a calculation with the ANO-RCC-VTZP basis set on all atoms.

(a) CASSCF/CASPT2

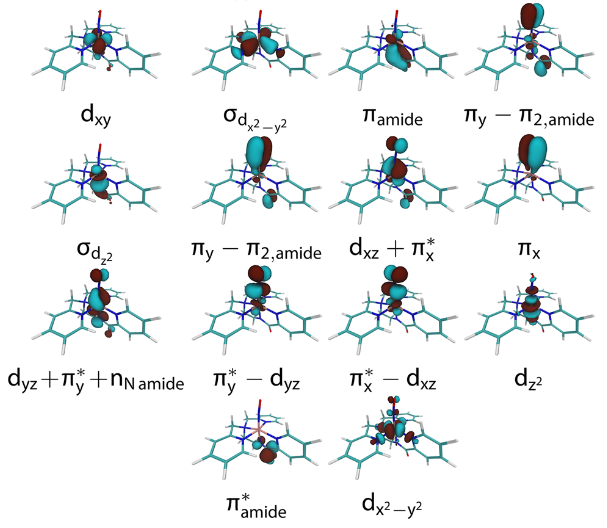

(b) DFT

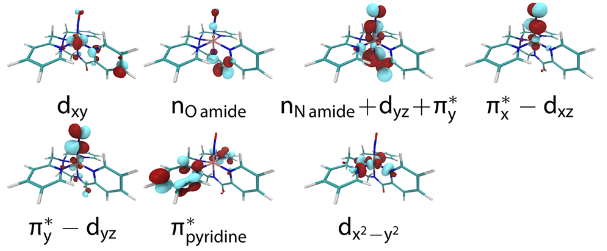

Figure 1. Active orbitals used in CASSCF/CASPT2 calculations (a) and the most important Kohn−Sham DFT orbitals (b). The orbital nomenclature $a \pm b$ indicates that orbital a interacts with b, and the orbital written first has a larger contribution to the resulting molecular orbital than the second one. The sign indicates bonding or antibonding interaction.

For singlet and triplet states, two separate CASSCF calculations have been performed, averaging over 5 singlets and 6 triplets, respectively. The CASPT2 calculations have been done within the multistate approach (MS-CASPT2)[64] using the same number of roots as that in the CASSCF. A level shift[65] of 0.3 a.u. was employed to avoid intruder states. Both CASSCF and MS-CASPT2 calculations employed the Cholesky decomposition-based density fitting approach.[44] The MS-CASPT2 calculations have been performed both in the gas phase and in acetonitrile using the conductor-like polarizable continuum model.[66] The SOC for the MS-CASPT2 wave functions has been calculated with the SO-RASSI method.[67]

Nonadiabatic Molecular Dynamics Simulations. In order to obtain a time-dependent insight of the photodissociation of NO in $[Ru(PaPy_3)(NO)]^{2+}$, nonadiabatic molecular dynamics simulations, where the nuclei move according to classical trajectories that follow Newton's equations in the potential calculated quantum mechanically at every time step, have been performed for the first time in these types of TM complexes. A Wigner distribution for a quantum harmonic oscillator at the ground electronic and vibrational state has been obtained from 400 uncorrelated geometries and velocities. This distribution was created using a geometry optimized with the BP86/def2-SV(P) protocol and a frequency calculation at the same level of theory. From the ensemble of generated geometries, a UV absorption spectrum has been obtained, as explained in ref 68. These calculations also serve to select a number of initial geometries as the initial conditions for the dynamics, according to their oscillator strength and excitation energy. For the nuclear motion, the Velocity Verlet[69] algorithm has been employed with a time step of 0.5 fs. At each time step, on-the-fly energies, gradients, and relevant couplings in the gas phase are calculated.

Ideally, in order to allow internal conversion to compete dynamically with ISC, a code such as SHARC,[70] recently implemented in our group and able to include nonadiabatic coupling and SOC simultaneously, should be used. Because the computation of the CASSCF/CASPT2 electronic properties for TM complexes is currently too time-consuming for on-the-fly calculations, simulations like those performed in smaller organic systems[71] are not possible yet and here we are content with employing TD-DFT. The derivation of TD-DFT-based trajectory surface hopping was given for the first time by Tapavicza et al.,[72] and current TD-DFT molecular dynamics simulations can also include nonadiabatic coupling between ground and excited states as well as between pairs of excited states (see, for instance, refs 73 and 74). Despite the difficulties that TD-DFT experiences to describe regions of near-degeneracy and thus photochemical funnels,[75] remarkable advances are evidenced in the last years in conjunction with nonadiabatic molecular dynamics.[76] However, we are not aware of any code that can currently perform molecular dynamics including on-the-fly TD-DFT SOC; therefore, here a pragmatic and approximate approach has been devised. Two sets of dynamical simulations have been run: one including singlet states and another one starting from triplets from which ISC is highly plausible. Within the singlet manifold, the ground and five lowest excited singlet states were considered and 97 trajectories were started in the S_4 state, according to the oscillator strength and excitation energy of the obtained spectrum. The dynamics of the second set of trajectories in the triplet manifold was executed as follows. The energy levels of the seven lowest triplet states were calculated along the 97 singlet trajectories, and once a triplet state was found close to the current state (<0.01 eV), a new trajectory was spawned with the velocity of the particle in the singlet state but starting in the corresponding triplet state. Only one spawning per trajectory has been performed, resulting in another set of 97 trajectories moving on the triplet-state surfaces. ISC is expected in regions of close degeneracy between singlet and triplet states and nonzero SOC.[47] Therefore, our "manual hopping" is justified as long as SOC is not negligible. This is ensured by looking at the character of the involved singlet and triplet states at the hopping geometries: If the character of the states is different, nonzero SOC is expected. This is an analogy to the El-Sayed rule[77] for organic systems: SOC is large if the transition involves a change of the molecular orbital type. If SOC is nonzero and the potentials are close enough, substantial ISC is expected.[71] As an additional criteria, ISC probabilities have been estimated a posteriori at the hopping geometries with the Landau−Zener model (as was done in refs 78 and 79) using the equation below, where the transition probability P_{ST}^{ISC} from a state S to a state T is given by

$$P_{ST}^{ISC} = 1 - \exp\left(-\frac{\pi}{4}\xi\right); \qquad \xi = \frac{8(H_{ST}^{SO})^2}{\vec{g}_a^{\,ST}\cdot\vec{v}_a}$$

Here, $\vec{g}_a^{\,ST}\cdot\vec{v}_a$ is the dot product of the gradient difference vector for the two states and the velocity vector, obtained at the hopping geometry from the dynamics simulations for each trajectory, and H_{ST}^{SO} is the SOC between the two states. The latter value is taken from the MS-CASPT2 calculations at the equilibrium geometry, as in ref 80. The fact that large probabilities have been found in all cases justifies the manual-hopping procedure. Note that a surface-hopping algorithm based on the Landau−Zener model probabilities instead of using the ad hoc "manual-hopping" procedure could have also been envisaged, given an efficient way to calculate the SOC at each time step would currently exist.

The on-the-fly energy and gradients of the involved singlet or triplet states have been calculated with the BP86 functional in its restricted variant and Ahlrich's def2-SV(P)[56] basis set, within the RI-J and MARI-J approximations, as implemented in the TURBOMOLE 6.5[61] program package. Nonadiabatic coupling is obtained via time-derivative coupling.[81,82]

A locally modified version of the NEWTON-X 1.4 program[83] has been employed to generate the initial conditions, to calculate the UV spectrum, and to simulate the dynamics along 200 fs.

■ RESULTS AND DISCUSSION

Quantum-Chemical Calculations. *Structural Properties.* The most relevant geometrical parameters of $[Ru(PaPy_3)(NO)]^{2+}$, optimized with DFT for the electronic ground state and lowest singlet (S_1) and triplet (T_1) states are collected in Table 1 (see also Figure 2), together with experimental data.[14]

Table 1. Selected BP86 Bond Lengths and Angles in the $[Ru(PaPy_3)(NO)]^{2+}$ Ground State, T_1 and S_1 Geometry, Compared with the Experimental[14] Structure[a]

	expt	S_0	T_1	S_1
r_{Ru-NO}/Å	1.780	1.807	1.980	1.868
θ_{Ru-N-O}/deg	173.2	172.4	137.5	156.6
$\phi_{O-N_1-Ru-N_2}$/deg			−105.2	0.78
r_{Ru-N_6}/Å	1.997	1.988	1.970	2.041

[a] Distances in angstroms and angles in degrees.

The calculated ground-state geometry is in good agreement with the experimental structure, and because it has already been extensively described in ref 14, we shall only concentrate on the geometrical parameters important for the excited-state transitions.

The most notable change in the geometries upon transition to either T_1 or S_1 is the bend of the nitrosyl ligand: from an almost linear coordination in the ground state (172.4°), the Ru−N−O angle is bent to 156.6° in S_1 or to 137.5° in T_1; see Figure 2. As discussed in the next section, the bend is due to the character of these states, which involve excitation from the $n_{N\ amide} + d_{yz} + \pi_y^*$ orbital (cf. Figure 1; T_1) or the $n_{O\ amide}$ orbital (S_1) to one of the NO π^* antibonding orbitals, i.e., a MLCT and ligand-to-ligand charge-transfer (LLCT) excitation, respectively. Such behavior has already been found in other nitrosyls.[8,34,39] The bending is smaller in S_1 than in T_1 because of less charge transfer (CT) from the metal and more pronounced LLCT character; for the same reason, the Ru−N_6 bond is elongated slightly in S_1 but not in T_1. The bending direction is also different in the excited states (see different dihedral angles $\phi_{O-N_1-Ru-N_2}$): while in S_1 the NO is bent toward N_2, in T_1 it is bent toward N_3.

Ground-State Electronic Structure. While free NO is a radical and contains one unpaired electron in its π^* orbital, both NO^+ and NO^- have closed-shell electronic configurations. In metal complexes, NO can bind to a metal center in different states, such as NO^+, NO^0, or NO^-, making the assignment of oxidation states to NO and the metal center difficult (noninnocency). Enemark and Feltham[84] have established a notation in which such an electronic configuration is represented as $\{M(NO)\}^n$ with n as the total amount of electrons in metal d and NO π^* orbitals. Accordingly, in $[Ru(PaPy_3)(NO)]^{2+}$, the electronic structure is denoted as $\{Ru(NO)\}^6$ and could describe both $Ru^{III}(NO)^0$ and $Ru^{II}(NO)^+$ structures.

On the basis of previous DFT calculations and of the IR stretching frequency of free and bound NO, it has been largely accepted that $\{Ru(NO)\}^6$ nitrosyls are best described as $Ru^{II}(NO)^+$,[36] a structure that corresponds to a d^6 closed-shell occupation of the Ru d orbitals. Our MS-CASPT2 calculations show that the closed-shell d^6 configuration $(d_{xy})^2(d_{xz} + \pi_x^*)^2(d_{yz} + \pi_y^* + n_{N\ amide})^2$ has a weight of 63% and thus the largest contribution to the wave function. Note that weights correspond to configurations built with natural orbitals. As seen in Figure 1, the d_{xz} and d_{yz} metal orbitals interact with the π_{NO}^* orbitals, forming corresponding bonding and antibonding combinations, which indicates strong covalency of the Ru−NO bond. The p_y orbital of the amide nitrogen ($n_{N\ amide}$) also contributes to the $d_{yz} + \pi_y^*$ bonding combination. Similar orbital interactions have been found in the DFT calculations of an analogous manganese complex.[21] Important to understanding the electronic structure of $[Ru(PaPy_3)(NO)]^{2+}$ is that, although the closed-shell configuration has the largest weight, two open-shell configurations, $(d_{xy})^2(d_{xz} + \pi_x^*)^2(d_{yz} + \pi_y^* + n_{N\ amide})^1(d_{yz} - \pi_y^*)^1$ and $(d_{xy})^2(d_{xz} + \pi_x^*)^1(d_{yz} + \pi_y^* + n_{N\ amide})^2(d_{xz} - \pi_x^*)^1$, which represent a back-donation of an electron into the π_{NO}^* orbital and therefore are synonyms of a $Ru^{III}(NO)^0$ structure, have weights of 10 and 8%, respectively [i.e., the total weight of dominant $Ru^{III}(NO)^0$ configurations is 18%]. This means that the ground-state structure of $[Ru(PaPy_3)(NO)]^{2+}$, otherwise accepted as $Ru^{II}(NO)^+$, has a significant contribution of $Ru^{III}(NO)^0$. It is interesting that, despite the fact that DFT cannot account for the admixing of the configurations, it provides good equilibrium geometries, as shown above.

Spin-Free and Spin−Orbit Excited States of $[Ru(PaPy_3)(NO)]^{2+}$. The lowest spin-free singlet and triplet vertical excitation energies, calculated with MS-CASPT2 and TD-

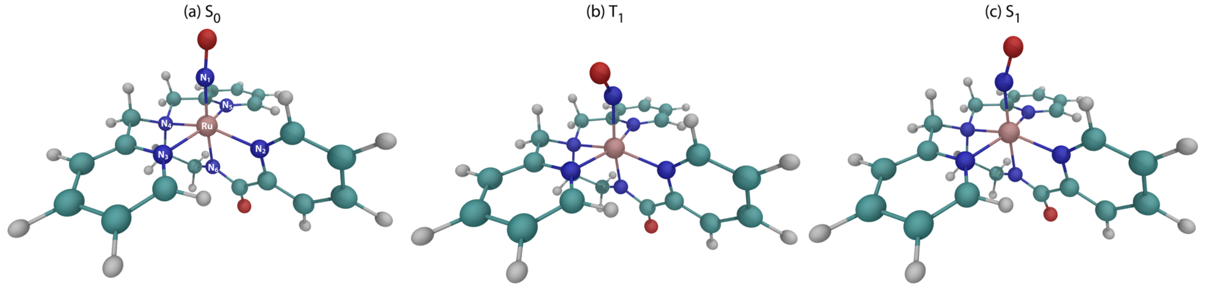

Figure 2. Optimized structure of $[Ru(PaPy_3)(NO)]^{2+}$ in the S_0 (a), T_1 (b), and S_1 (c) states.

Table 2. Spin-Free Lowest Singlet and Triplet Excitations in $[\mathrm{Ru(PaPy_3)(NO)}]^{2+}$ Calculated at Different Levels of Theory[a]

method	state	ΔE_{gas}	f_{gas}	ΔE_{solv}	f_{solv}	major contribution	gas c^2 (%)	solv c^2 (%)
CASPT2	T_1	2.46				$d_{yz} + \pi_y^* + n_{\mathrm{N\ amide}} \rightarrow \pi_x^* - d_{xz}$	35	
						$d_{xy} \rightarrow \pi_x^* - d_{xz}$	30	
	T_2	2.55				$d_{yz} + \pi_y^* + n_{\mathrm{N\ amide}} \rightarrow \pi_y^* - d_{yz}$	53	
	S_1	2.83	0.0003	3.05	0.0001	$d_{xy} \rightarrow \pi_x^* - d_{xz}$	58	63
						$d_{yz} + \pi_y^* + n_{\mathrm{N\ amide}} \rightarrow \pi_x^* - d_{xz}$	22	14
	T_3	3.02				$d_{xy} \rightarrow d_{x^2-y^2}$	53	
	T_4	3.09				$d_{xy} \rightarrow \pi_x^* - d_{xz}$	36	
						$d_{yz} + \pi_y^* + n_{\mathrm{N\ amide}} \rightarrow \pi_x^* - d_{xz}$	21	
	S_2	3.11	0.0091	3.20	0.0015	$d_{xy} \rightarrow \pi_y^* - d_{yz}$	76	67
	S_3	3.22	0.0003	3.32	0.0004	$d_{yz} + \pi_y^* + n_{\mathrm{N\ amide}} \rightarrow \pi_x^* - d_{xz}$	59	54
						$d_{xy} \rightarrow \pi_x^* - d_{xz}$	21	20
	T_5	3.13				$d_{xy} \rightarrow \pi_y^* - d_{yz}$	51	
	S_4	3.50	0.0253	3.67	0.0132	$d_{yz} + \pi_y^* + n_{\mathrm{N\ amide}} \rightarrow \pi_y^* - d_{yz}$	48	46
						$d_{xz} + \pi_x^* \rightarrow \pi_x^* - d_{xz}$	31	38
	T_6	3.54				$d_{xz} + \pi_x^* \rightarrow \pi_x^* - d_{xz}$	83	
BP86	T_1	1.66				$n_{\mathrm{N\ amide}} + d_{yz} + \pi_y^* \rightarrow \pi_y^* - d_{yz}$	71	
	T_2	1.84				$n_{\mathrm{N\ amide}} + d_{yz} + \pi_y^* \rightarrow \pi_x^* - d_{yz}$	77	
	S_1	1.99	0.0000	2.19	0.0002	$n_{\mathrm{N\ amide}} + d_{yz} + \pi_y^* \rightarrow \pi_x^* - d_{yz}$	98	80
	T_3	2.05				$n_{\mathrm{O\ amide}} \rightarrow \pi_x^* - d_{xz}$	85	
	T_4	2.16				$n_{\mathrm{O\ amide}} \rightarrow \pi_y^* - d_{yz}$	87	
	S_2	2.17	0.0002	2.75	0.0062	$n_{\mathrm{O\ amide}} \rightarrow \pi_x^* - d_{xz}$	69	31
						$n_{\mathrm{N\ amide}} + d_{yz} + \pi_y^* \rightarrow \pi_y^* - d_{yz}$	30	
	S_3	2.24	0.0011	2.73	0.0000	$n_{\mathrm{O\ amide}} \rightarrow \pi_y^* - d_{yz}$	77	63
						$d_{xy} \rightarrow \rightarrow \pi_y^* - d_{yz}$		32
	T_5	2.42				$d_{xy} \rightarrow \pi_x^* - d_{xz}$	99	
	T_6	2.50				$d_{xy} \rightarrow \pi_y^* - d_{yz}$	96	
	S_4	2.61	0.0352	2.50	0.0224	$n_{\mathrm{N\ amide}} + d_{yz} + \pi_y^* \rightarrow \pi_y^* - d_{yz}$	38	58
						$n_{\mathrm{O\ amide}} \rightarrow \pi_x^* - d_{xz}$	–	26
	S_5	2.72	0.0009	2.70	0.0041	$d_{xy} \rightarrow \pi_x^* - d_{xz}$	95	93
	S_6	2.82	0.0083	2.91	0.0352	$d_{xy} \rightarrow \pi_y^* - d_{yz}$	72	31
						$n_{\mathrm{O\ amide}} \rightarrow \pi_x^* - d_{xz}$	–	31
	T_7	2.83				$n_{\mathrm{N\ amide}} + d_{yz} + \pi_y^* \rightarrow \pi_{\mathrm{pyridine}}^*$	71	
	T_8	2.86				$n_{\mathrm{N\ amide}} + d_{yz} + \pi_y^* \rightarrow d_{x^2-y^2}$	70	
						$d_{xy} \rightarrow d_{x^2-y^2}$	8	

[a] The excitation energies (ΔE) in electronvolts, oscillator strengths f, main character of the transitions, and corresponding coefficients c^2 are provided. The "gas" subscript stands for properties calculated in the gas phase and the "solv" subscript for properties calculated in acetonitrile.

DFT/BP86, are collected in Table 2. Values for singlet excitations are reported in the gas phase and acetonitrile.

According to the MS-CASPT2 calculations, the lowest four singlet states are mainly MLCT transitions from the ruthenium center to antibonding Ru–NO ($\pi_x^* - d_{xz}$ and $\pi_y^* - d_{yz}$) orbitals. Two states are bright. The brightest state corresponds to S_4, is predicted at 3.50 eV, and is characterized by a $n_{\mathrm{N\ amide}} + d_{yz} + \pi_y^* \rightarrow \pi_y^* - d_{yz}$ transition, i.e., by a transition from a Ru–NO bonding orbital to the corresponding antibonding orbital with some admixing of a LLCT transition from the $n_{\mathrm{N\ amide}}$ orbital; see the orbitals in Figure 1a. The second brightest state is S_2; it is located at 3.11 eV and corresponds to a pure MLCT transition, $d_{xy} \rightarrow \pi_y^* - d_{yz}$. This transition would be forbidden in an octahedral ligand field but here becomes partially allowed because of deviations from the octahedral coordination geometry. The S_1 and S_3 states are much weaker in intensity and play little role in the absorption spectrum. The inclusion of acetonitrile in the calculation is reflected in a solvatochromic blue shift of 0.09−0.22 eV but does not alter the order of the singlet states. Noticeable is that the intensity of the S_2 state decreases in solution, so that the spectrum in acetonitrile is dominated by the bright S_4 state, which is now predicted at 3.67 eV.

The MS-CASPT2 results show a good agreement with the experimental spectrum, reproduced in Figure 3. The spectrum, recorded in acetonitrile,[21] shows a broad band around ca. 3.8 eV and a less intense one at ca. 3.2 eV. The low-energy peak can then be assigned to the weaker MLCT $d_{xy} \rightarrow \pi_y^* - d_{yz}$ transition ($S_0 \rightarrow S_2$), and the second, more intense shoulder is due to the brighter MLCT (and partially LLCT) $n_{\mathrm{N\ amide}} + d_{yz} + \pi_y^* \rightarrow \pi_y^* - d_{yz}$ transition (S_4). The latter transition is underestimated by MS-CASPT2 by about 0.2 eV. The convoluted absorption spectra obtained from the theoretical MS-CASPT2 calculations are also shown in Figure 3 for comparison.

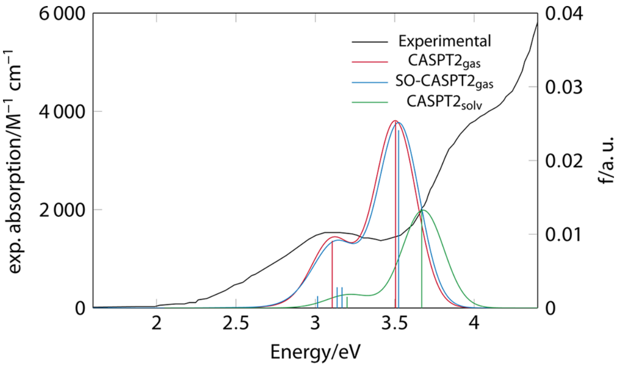

Figure 3. Convoluted spectra obtained with MS-CASPT2 in the gas phase (gas), including spin−orbit (SO) corrections, and in solution (solv). The experimental absorption spectrum of $[\mathrm{Ru(PaPy_3)(NO)}]^{2+}$ is also depicted, reproduced from ref 21 (solid line, left *y* axis).

The gas-phase TD-DFT/BP86 results agree qualitatively with those obtained by MS-CASPT2; see Table 2. The brightest state is also S_4, although underestimated by ca. 0.9 eV, with respect to the gas-phase MS-CASPT2 value. The character of the transition is the same, although the mixing of the orbitals differs slightly. The second bright state, found as S_2 with MS-CASPT2, is S_6 with BP86. This state is predicted at 2.82 eV and thus underestimated by ca. 0.3 eV from the MS-CASPT2 value. Because the errors in both excitations are different, the state order predicted by BP86 is different from that obtained with MS-CASPT2, and thus the assignment of the lowest experimental band is missing at the BP86 level of theory. Regarding the other singlet states, BP86 also finds a LLCT state (S_3) at 2.24 eV, which is not present at the MS-CASPT2 level of theory because the corresponding $n_{\mathrm{O\ amide}}$ orbital is not contained in the active space. Because the oscillator strength of this state is comparatively small, it is not expected to contribute to the spectrum. Inclusion of the solvent model in TD-DFT calculations has a more dramatic effect on the excited-state energies and properties than that in MS-CASPT2: the states mix more with each other, which is reflected in less systematic solvent shifts and oscillator strength changes.

BP86 calculations of higher-lying excited states show a high density of bright MLCT $d \rightarrow \pi_{\mathrm{pyridine}}^*$ and LLCT $\pi_{\mathrm{pyridine}}^* \rightarrow \pi_{\mathrm{pyridine}}^*$ transitions (cf. Figure 1b), which could contribute to the rising higher-energy band above 4 eV; see Figure 3. These states are not relevant for photodissociation of NO, and therefore they will not be further discussed.

Despite the fact that BP86 has been widely used for TM complexes,[85] it is well-known that non-range-separated functionals (such as BP86) do not optimally describe CT excitations.[86] In $[\mathrm{Ru(PaPy_3)(NO)}]^{2+}$, BP86 systematically underestimates the absorption energies with respect to both the experimental and MS-CASPT2 values. However, the magnitude of the error seems to be different depending on the CT character of the transition, which leads to different orders of the states and could lead to a misinterpretation of the spectrum. Excitations involving the $n_{\mathrm{N\ amide}}$ orbitals with partial LLCT character (such as S_1 and S_4) are underestimated by almost 1 eV (compare the BP86 and gas-phase MS-CASPT2 values in Table 2), while transitions involving the metal d_{xy} orbital (such as the S_6 at BP86) have a much smaller error. This difference can be explained by the larger spatial separation of the n_{Namide} and π_{NO}^* orbital compared to the metal d_{xy} orbital; see Figure 1b. The more accentuated the CT character, the more problematic is the description of the state. The LLCT S_3 state at 2.24 eV has a spatial separation of the frontier orbitals similar to that of the excitation involving the n_{Namide} orbital and is therefore expected to be red-shifted within by BP86 by a similar amount of energy.

Despite the errors, the qualitative description of the lowest singlet excited states with BP86 seems to be largely in accordance with the MS-CASPT2 results and supports the fact that the MLCT excitations into Ru−NO antibonding orbitals, which are highly relevant for NO photodissociation, lie at the lower end of the absorption spectrum and do not mix with other states.

The triplet states are, in principle, not important for the peak assignment in the absorption spectrum, but they are relevant for the photodissociation mechanism of NO. Just like their singlet counterparts, the lowest triplet excited states are also predominantly of MLCT character; see Table 2. An exception is the T_3 state, which at MS-CASPT2 is a ligand-field or d → d transition. This d → d transition shows by far the largest SOC to the ground state of 1013 $\mathrm{cm^{-1}}$, which is reflected in the absorption spectrum: the first bright state in the spin−orbit-coupled MS-CASPT2 calculation (labeled SO-CASPT2 in Figure 3) has a T_3 weight of approximately 76%. Its bright character is not attributed to the large ground-state SOC but rather to large SOC to the bright S_2 state. Figure 4 shows the most important SOC between the singlets and triplets, calculated at the MS-CASPT2 level of theory. As can be seen, the S_2 state has strong SOC with T_4 and T_5, which results in a splitting of the bright S_2 peak in the spin-free spectrum into three different transitions with large S_2 contributions. This splitting, however, is rather small, for the resulting three transitions are at most 0.15 eV apart. The brightest state, S_4, is only slightly influenced by SOC. It mixes with the closest-lying T_6 state, but the SOC is comparatively small (37 $\mathrm{cm^{-1}}$), and thus it blue-shifts by only 0.02 eV. The small SOC is compatible with the El-Sayed rule[77] in the sense that the S_4 and T_6 state characters are very similar, and therefore a small coupling is expected. For comparison, SOC between other states can reach values of up to 460 $\mathrm{cm^{-1}}$.

Despite SOC, the convoluted SO-CASPT2 spectrum is very similar to that obtained spin-free; see Figure 3. In other TM complexes, such as rhenium and iridium complexes, for

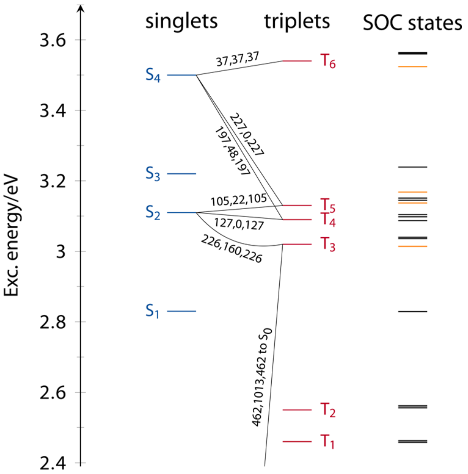

Figure 4. Important SOC (in cm^{-1}) calculated at the CASPT2 level of theory: bright spin−orbit states are shown in orange.

example, the influence of SOC has been shown to be larger.[46] Despite the fact that spin-free energies are sufficient to calculate the absorption spectrum, the presence of large SOC between singlet and triplet states undermines the importance of the triplet states for dissociation.

As in the case of the singlet states, TD-DFT/BP86 systematically underestimates MLCT triplet excitation energies by 0.62−0.89 eV, but this error is systematic and quantitatively similar for a given class of excitations.

NO Photodissociation Mechanism. According to the spin-free static calculations, the most optically active state in the near-UV region is the S_4 state. This is predominantly an MLCT state that populates the Ru−NO antibonding orbital, with an admixture of LLCT character from the amido nitrogen coordinated trans to NO. Between this state and the ground state, there is a manifold of other MLCT excited states (singlets and triplets) populating Ru−NO antibonding orbitals, which could easily be accessed by internal conversion (singlets) or ISC (triplets) and could all potentially lead to NO dissociation. The introduction of SOC does not change the absorption spectrum qualitatively; it only increases the density of states (cf. Figure 4).

This picture is compatible with the "direct" mechanism postulated earlier[21,22] in which NO dissociation is prompted by the direct population of a $d_M \rightarrow \pi_{NO}^*$ MLCT singlet excited state, with the addenda that the dissociation may occur also from the analogous triplet states after ISC. As such, it is then in contrast to the "indirect" mechanism postulated in the analogous $[Mn(PaPy_3)(NO)]^{2+}$ complex,[21] where internal conversion to the $d_M \rightarrow \pi_{NO}^*$ MLCT is required prior to dissociation.

In order to obtain more details about the actual NO photodissociation mechanism and the features that accompany this process, a gas-phase surface-hopping molecular dynamics study has been carried out. Dynamical simulations have been done at the TD-DFT/BP86/def2-SV(P) level of theory, which provides an overall qualitative picture of the spectroscopy of $[Ru(PaPy_3)(NO)]^{2+}$, despite the fact that the energies of the MLCT states are systematically underestimated with respect to the MS-CASPT2 ones.

From single-point vertical excitation calculations at the 400 initial conditions generated from the Wigner distribution, a total spectrum restricted to the lowest four excited singlet states has been calculated. This spectrum is obtained as the sum of the four contributions coming from the S_1−S_4 excited states. The spectra arising from each state, as well as the total absorption spectrum, are shown in Figure 5. One can see that the total UV spectrum almost entirely consists of the S_4 contribution, indicating that nonequilibrium geometries obtained from the zero-point-energy quantum distribution of the molecule also are excited primarily to the S_4 state. Therefore, all trajectories have been prepared in S_4 as the initial state, covering the full energy band. Recall that the obtained band corresponds to the experimental shoulder extending from ca. 3.5 to 4.2 eV.

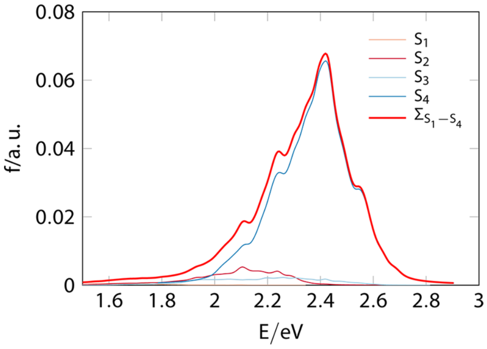

Figure 5. Absorption spectra of $[Ru(PaPy_3)(NO)]^{2+}$ calculated from excitation energies for a Wigner distribution of geometries. The total spectrum ($\sum_{S_1-S_4}$), as well as those obtained from each individual excitation, is depicted. The full-width at half-maximum employed to convolute the spectra was 0.05 eV.

The possibility of ISC from S_4 has been approximated with a Landau−Zener model, as explained in the Methods and Computational Details section. The obtained singlet−triplet transition probabilities should be considered upper limits, but with up to 90%, they point to a very efficient ISC. The most probable transitions are those from S_4 to the $d_{xy} \rightarrow \pi_{x-d_{xz}}^*$ and $d_{xy} \rightarrow \pi_{y-d_{yz}}^*$ MLCT T_5 and T_6 states (T_4 and T_5 in MS-CASPT2; recall Table 2) and to T_7. The calculated SOC values for $S_4 \rightarrow T_4$ (T_5 in BP86) and $S_4 \rightarrow T_5$ (T_6 in BP86) are 197 and 227 cm^{-1}, respectively (cf. Figure 4). For the $S_4 \rightarrow T_7$ transition, no probability could be calculated because the state is not present at the MS-CASPT2 level of theory and thus no SOC is available; however, here SOC is also expected to be large based on the El-Sayed propensity rule. Figure 6 depicts the time distribution at which ISC was obtained during the first 20 fs. From the 97 trajectories, 46% undergo ISC in the first 2 fs, 85% within the first 10 fs, and over 90% in the first 20 fs. These numbers should also be considered an upper bound because only one trajectory was spawned per singlet and back-transfer from the triplets is not allowed. However, it is clear that a large fraction of the initial S_4 population can undergo an ISC to a MLCT $d_{xy} \rightarrow \pi_{x-d_{xz}}^*$ or $d_{xy} \rightarrow \pi_{y-d_{yz}}^*$ triplet state already in the first 10 fs. This ultrafast ISC is in line with experiments done in other TM complexes, where extremely short time scales for ISC have been measured (even below 30 fs).[48]

Along the singlet and triplet trajectories, the most important changes in the geometry are stretching of the Ru−NO bond and bending of the NO ligand. The time evolution of these two geometrical parameters is shown in Figure 7. Most trajectories

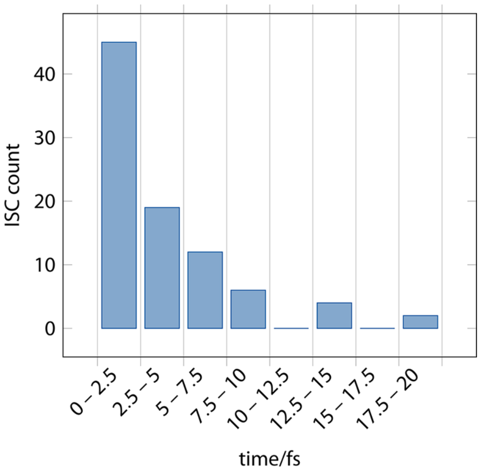

Figure 6. Number of ISC during the first 20 fs.

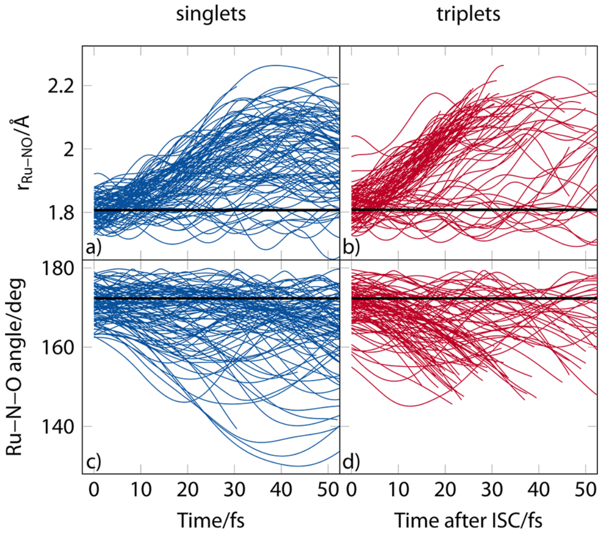

Figure 7. Time evolution of Ru–NO distances (a and b) and Ru–N–O angles (c and d) for each trajectory in singlet (a and c) and triplet (b and d) states in the first 50 fs. The solid black lines in each plot indicate the values at equilibrium.

clearly show an increase in the Ru–NO distance (Figure 7a,b) in the first 30 fs. Other Ru–N bonds oscillate randomly and do not increase their average value during the simulation time, indicating that they are not relevant for NO photorelease. NO dissociation appears to be slightly faster for the triplet trajectories than for the singlet ones. Unfortunately, a large number of triplet trajectories crash shortly after the Ru–N distance reaches 2.1–2.2 Å because at these extended Ru–N bond distances the S_0 and T_1 states become degenerate, a situation that DFT cannot handle. Therefore, Figure 7 is only plotted until 50 fs, a time for which we consider the results to be meaningful. Despite the limitations of TD-DFT, we interpret this Ru–NO bond extension as the beginning of NO dissociation and not just as a Ru–NO vibration because of its concerted nature.

The time scale of 20–30 fs, at which dissociation is initiated, is not enough for most trajectories to relax to the lowest excited state; i.e., NO readily dissociates in the triplet excited states. Note that singlet and triplet excitations within TD-DFT could be described with different accuracy, especially in geometries differing significantly from the equilibrium one, affecting the predicted dissociation times. However, because here we are only able to describe the beginning of the dissociation process, which takes place in an extremely short time scale, we expect this effect to hardly affect the reported time scales. Most of the triplet trajectories show NO dissociation in the $d_{xy} \rightarrow \pi_x^* - d_{xz}$, $d_{xy} \rightarrow \pi_y^* - d_{yz}$ MLCT states or sometimes in the $n_{\mathrm{N\ amide}} + d_{yz} + \pi_y^* \rightarrow \pi_{y-d_{yz}}^*$ state, either directly or involving one or two internal conversions between the triplet states.

The bond stretching observed in the singlet trajectories (Figure 7a) is also ascribed to NO dissociation. In this case, propagation of the singlet states does not suffer from the S_0–T_1 degeneracy problem because the T_1 state is not present in the calculation, but analysis is equally restricted to the first 50 fs because DFT cannot properly dissociate.[87,88]

Indeed, a CASSCF rigid scan of the Ru–NO distance while keeping all other coordinates frozen at the equilibrium geometry shows the dissociative nature of the singlet excited states (Figure 8a) and the increase of the ground-state weight of the open-shell $\mathrm{Ru^{III}(NO)^0}$ configuration built with natural orbitals (Figure 8b). At around 2 Å, both $\mathrm{Ru^{III}(NO)^0}$ and $\mathrm{Ru^{II}(NO)^+}$ electronic configurations reach 50% and, accordingly, the ground state cannot be described reliably by DFT anymore.

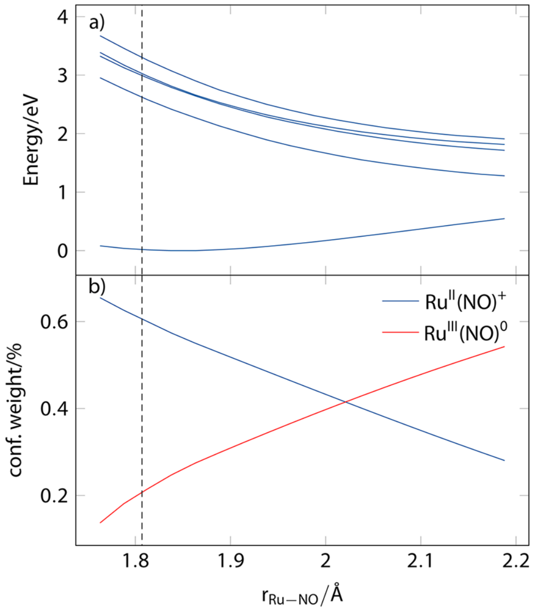

Figure 8. (a) Energies of the ground and the first four singlet excited states from the Ru–NO distance scan with CASSCF. All other geometry parameters were kept at their equilibrium geometry values. (b) Configuration weight of the principal $\mathrm{Ru^{II}(NO)^+}$ and $\mathrm{Ru^{III}(NO)^0}$ configurations in the ground state. The dashed black line indicates the equilibrium Ru–NO distance at the BP86 geometry.

The singlet trajectories show efficient internal conversion: within the first 50 fs, over 30% of the trajectories decay from S_4 to S_1 (Figure 9a). Note that the present TD-DFT implementation in NEWTON-X does not support hopping from S_1 to S_0, so trajectories can only be trapped in the S_1 state. The target S_1 state is also a MLCT or LLCT state, populating the NO π^* orbital either from the $n_{\mathrm{N\ amide}} + d_{yz}$, the $n_{\mathrm{O\ amide}}$, or a mixture of both, and from our Ru–NO analysis, population in

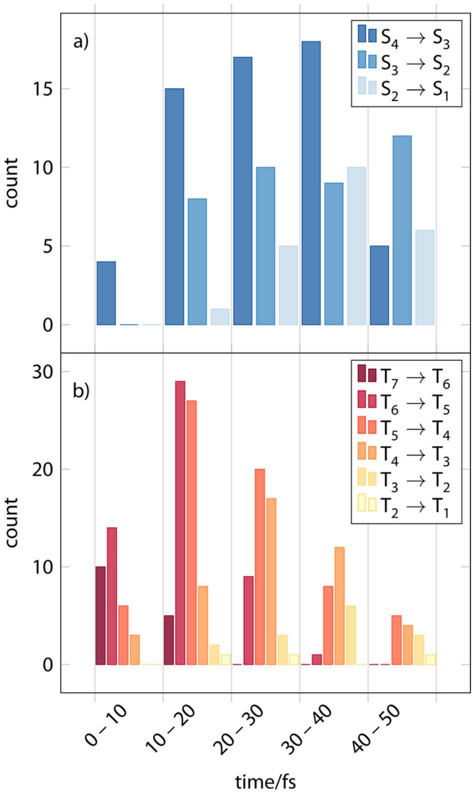

Figure 9. Frequency of internal conversions to the lowest excited states for the singlet (a) and triplet (b) trajectories in the first 50 fs.

this state does not prompt dissociation, in agreement with the fact that an equilibrium structure for the S_1 state can be optimized (see above).

Another key geometrical change present in most of the trajectories is bending of the NO ligand (Figure 7c,d). It is precisely the bending of NO that brings the S_0, S_1, and T_1 states close together, with the concomitant problem for TD-DFT terminating the calculation. During the first 20 fs, $[Ru(PaPy_3)(NO)]^{2+}$ evolves from mostly a linear structure to angles of ca. 150°. This bending is consistent with the optimized geometry of the S_1 and T_1 structures, which are also bent, and with the character of the lowest MLCT states because they represent excitation into a NO π^* antibonding orbital, i.e., a $Ru^{III}(NO)^0$ configuration, which is favored upon NO bending. NO bending is also found along the concerted Ru−NO bond elongation in triplets, but it is not a necessary requirement for dissociation.

In theoretical photochemistry, it is an usual goal to characterize conical intersections, which are the structures that facilitate an ultrafast funnel between two electronic states, i.e., radiationless internal conversion. As seen in Figure 9, the number of internal conversions among the singlet and among the triplet states, respectively, is relatively large in the first 50 fs. Already during the first 10 fs, $S_4 \to S_3$ internal conversion is taking place. After another 10 fs, the conical intersection mediating the $S_3 \to S_2$ transition is operative and gradually the nonadiabatic $S_2 \to S_1$ transition is also efficient. Internal conversion among the triplets (Figure 9b) is even more efficient because the distribution of sequential hops is rather generalized. Figure 10 shows a global mechanism of the deactivation of $[Ru(PaPy_3)(NO)]^{2+}$, summarizing all time scales and processes predicted by the present simulations.

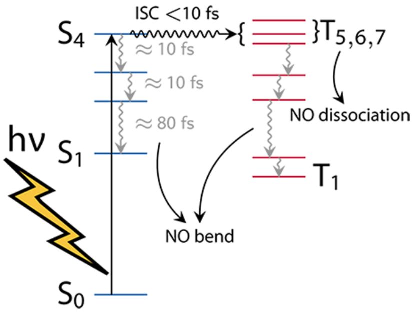

Figure 10. Schematic deactivation mechanism of $[Ru(PaPy_3)(NO)]^{2+}$.

In order to obtain insight into the geometrical changes that characterize the conical intersections among singlet and triplet states, respectively, a convoluted spectral distribution of selected parameters (Ru−NO bond length, Ru−N−O bond angle, and other Ru−N bonds) at the different hopping geometries is shown in Figure 11, together with the same convoluted distribution for the initial geometries generated with a Wigner distribution. The comparison between the different distributions indicates the temporal evolution of these parameters. The first thing to notice is that already the geometries belonging to the Wigner distributions include a broad spectrum of values. Then, it is obvious that the Ru−N

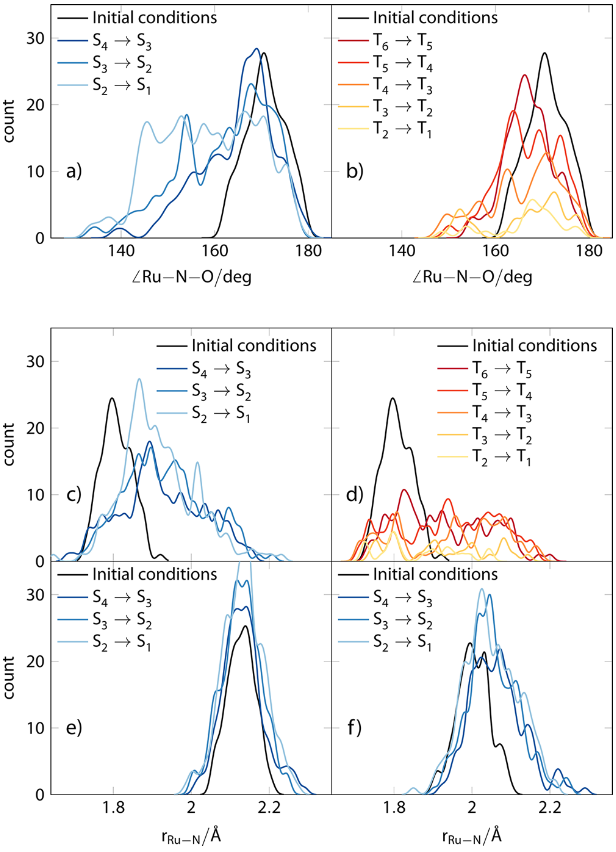

Figure 11. Gaussian convolution of the distribution of various geometrical parameters in singlet and triplet hopping geometries: (a and b) Ru−NO angles in singlet and triplet geometries; (c and d) Ru−NO distances in singlet and triplet geometries, (e and f) Ru−N_5 and Ru−N_6 distances in singlet hopping geometries.

bonds, different from NO (Figure 11e,f), show little change in the dynamics; that is, the peaks of the distributions do not show significant deviations at any of the hopping geometries, making it difficult to assign a particular value characteristic of a conical intersection.

In contrast, the distributions of the Ru−NO bond lengths and Ru−N−O angles for the singlets (Figure 11a,c) and triplets (Figure 11b,d) are significantly different from the initial values at all hopping geometries. The Ru−NO distance at the Franck−Condon geometry is 1.807 Å, which corresponds to the peak of the Wigner distribution. As can be seen (Figure 11c), after excitation to S_4 and internal conversion to S_3, the Ru−NO stretches on average to 1.9 Å. The next internal conversion from $S_3 \rightarrow S_2$ is accompanied by a broader distribution of Ru−NO bond distances, centered around 1.9 and 2.0 Å, while $S_2 \rightarrow S_1$ relaxation is characterized by an averaged distance smaller than 1.9 Å, indicating that the majority of the relaxation to S_1 occurs at a bond distance close to the equilibrium one. In the triplet states (Figure 11d), the distribution of Ru−NO bond lengths is significantly broader than that for the singlet states at any of the hopping geometries, making it difficult to assign a conical intersection with a particular value. While one still can locate a slight maximum for $T_6 \rightarrow T_5$ hop, at approximately 1.82 Å, still fairly close to the equilibrium geometry, this maximum is smeared out as the trajectories proceed nonadiabatically to lower triplet states, which is consistent with the dissociating behavior of some of the trajectories.

For the Ru−N−O bond angle dependence (Figure 11a,b), also broad distributions are obtained. Yet, the cascade of both singlet and triplet conical intersections is accompanied of bending of the NO fragment. The initial $S_4 \rightarrow S_3$ transition is so fast (10 fs; see Figure 9a) that the molecule does not have time to bend; therefore, a large peak is found at almost the same angle as that in the Franck−Condon geometry. Hops to the lower states show lower angles, which means that most of the bending occurs in the S_3 and S_2 states. In the triplet states, the change in the angle is faster, as we can see in the decrease of the maxima toward lower angles as the trajectories proceed to T_1 (although there always remains a small maximum close to the equilibrium values).

■ CONCLUSIONS

In this paper, we investigated the electronic structure of $[Ru(PaPy_3)(NO)]^{2+}$ ground and excited states using spin-corrected MS-CASPT2 calculations. Moreover, we obtained insight into the NO photodissociation mechanism using TD-DFT-based trajectory surface-hopping molecular dynamics.

The ground state of $[Ru(PaPy_3)(NO)]^{2+}$ is a singlet and shows linear NO coordination, in line with many other TM nitrosyls. In contrast, the excited states show significant bending of the NO ligand, which is attributed to CT from either the metal or the carboxamido group of PaPy to NO. Although this complex is usually considered to be of mainly $Ru^{II}(NO)^+$ character, our MS-CASPT2 calculations show a significant contribution of $Ru^{III}(NO)^0$ configurations to its ground state.

Excited-state MS-CASPT2 calculations reproduce well the UV−vis absorption spectra and show that the lowest singlet and the majority of lowest triplet excited states are MLCT excitations in the antibonding metal $d \rightarrow \pi_{NO}^*$ orbitals. Spin-corrected calculations show large SOC of the triplet states up to 1013 cm^{-1} with the ground state and up to 460 cm^{-1} between singlet and triplet excited states. The calculated SOC between singlets and triplets with similar character is an order of magnitude smaller, which is consistent with the El-Sayed rules, extrapolated to TM complexes. Although the large SOC values are not reflected quantitatively in the absorption spectrum, they can facilitate ultrafast ISC, which is calculated to happen to a significant amount already in the first 10 fs.

Within the first 50 fs, the trajectories propagating in both the singlet or triplet states show Ru−NO bond elongation, a fact that can be ascribed to Ru−NO dissociation. This dissociation is more accentuated in the $d_{xy} \rightarrow \pi_x^* - d_{xz}$ and $d_{xy} \rightarrow \pi_y^* - d_{yz}$ triplet MLCT states, which are populated after the ISC from the bright $d_{yz} + \pi_y^* + n_{\text{N amide}} \rightarrow \pi_y^* - d_{yz}$ MLCT state. A similar pathway is found in the singlet trajectories; in this case, however, radiationless internal conversion from S_4 to S_1 competes with NO dissociation. Unfortunately, full decay to the ground state cannot be observed within our TD-DFT dynamical calculations; therefore, absolute decay times are not provided, but both dissociation and internal conversion take place in less than 100 fs. All of these processes are accompanied by bending of the NO ligand, which is not confined to any particular state.

Besides stretching of the Ru−NO bond and bending of the NO ligand, no other characteristic geometrical feature is found to be relevant for NO photodissociation. Likewise, no particular geometry could be assigned to any of the different conical intersections mediating internal conversion within the singlet or triplet states, respectively. The hopping geometries show a very broad distribution of geometrical parameters, with a pattern similar to that obtained initially due to the zero-point energy.

In general, we found that the fully atomistic description of dynamical processes involving nonadiabatic effects, different multiplicities, and bond breaking is extremely challenging for the standard formulation of TD-DFT, as employed here in the on-the-fly calculations. However, and despite its limitations, surface-hopping nonadiabatic simulations are very useful to providing key insight into the photodynamics of this class of molecules. Clearly, the development of methods that are able to describe the photodynamics of TM complexes is an exciting and rewarding area of research, which we will surely see flourish in the coming years.

■ AUTHOR INFORMATION

Corresponding Author

*E-mail: leticia.gonzalez@univie.ac.at.

Notes

The authors declare no competing financial interest.

■ ACKNOWLEDGMENTS

We thank the University of Vienna for financial support and the COST Action CM1202 for inspiring a number of theoretical problems on ruthenium complexes. The authors also thank Vladimir Arion, as well as Sebastian Mai and Philipp Marquetand for enlightening discussions on nitrosyl complexes and dynamics, respectively. All of the calculations were performed in the HP computers of the Theoretical Chemistry Group at the University of Vienna.

■ REFERENCES

(1) (a) Culotta, E.; Koshland, D. E. *Science* **1992**, *258*, 1862−1865. (b) Fang, F. C. *Nitric Oxide and Infection*; Springer: Berlin, 1999. (c) Ignarro, L. J. *Nitric Oxide: Biology and Pathobiology*; Academic Press: New York, 2000.

(2) Rose, M. J.; Mascharak, P. K. *Curr. Opin. Chem. Biol.* **2008**, *12*, 238−244.

(3) Tfouni, E.; Truzzi, D. R.; Tavares, A.; Gomes, A. J.; Figueiredo, L. E.; Franco, D. W. *Nitric Oxide* **2012**, *26*, 38−53.

(4) Detty, M. R.; Gibson, S. L.; Wagner, S. J. *J. Med. Chem.* **2004**, *47*, 3897−3915.

(5) (a) Bourassa, J.; Lee, B.; Bernard, S.; Schoonover, J.; Ford, P. C. *Inorg. Chem.* **1999**, *38*, 2947−2952. (b) Conrado, C. L.; Bourassa, J. L.; Egler, C.; Wecksler, S.; Ford, P. C. *Inorg. Chem.* **2003**, *42*, 2288−2293.

(6) Jaworska, M.; Stasicka, Z. *J. Mol. Struct.* **2006**, *785*, 68−75.

(7) (a) Ford, P.; Bourassa, J.; Miranda, K.; Lee, B.; Lorkovic, I.; Boggs, S.; Kudo, S.; Laverman, L. *Coord. Chem. Rev.* **1998**, *171*, 185−202. (b) Hoshino, M.; Laverman, L.; Ford, P. C. *Coord. Chem. Rev.* **1999**, *187*, 75−102.

(8) Ford, P. C.; Lorkovic, I. M. *Chem. Rev.* **2002**, *102*, 993−1018.

(9) Patra, A. K.; Afshar, R.; Olmstead, M. M.; Mascharak, P. K. *Angew. Chem., Int. Ed.* **2002**, *41*, 2512−2515.

(10) Patra, A. K.; Rowland, J. M.; Marlin, D. S.; Bill, E.; Olmstead, M. M.; Mascharak, P. K. *Angew. Chem., Int. Ed.* **2003**, *42*, 6812−6823.

(11) Eroy-Reveles, A. A.; Leung, Y.; Beavers, C. M.; Olmstead, M. M.; Mascharak, P. K. *J. Am. Chem. Soc.* **2008**, *130*, 4447−4458.

(12) Works, C. F.; Ford, P. C. *J. Am. Chem. Soc.* **2000**, *122*, 7592−7593.

(13) Works, C. F.; Jocher, C. J.; Bart, G. D.; Bu, X.; Ford, P. C. *Inorg. Chem.* **2002**, *41*, 3728−3739.

(14) Patra, A. K.; Mascharak, P. K. *Inorg. Chem.* **2003**, *42*, 7363−7365.

(15) (a) Rose, M. J.; Olmstead, M. M.; Mascharak, P. K. *J. Am. Chem. Soc.* **2007**, *129*, 5342−5343. (b) Rose, M. J.; Mascharak, P. K. *Chem. Commun.* **2008**, 3933−3935. (c) Fry, N. L.; Mascharak, P. K. *Acc. Chem. Res.* **2011**, *44*, 289−298.

(16) Bohlender, C.; Wolfram, M.; Goerls, H.; Imhof, W.; Menzel, R.; Baumgaertel, A.; Schubert, U. S.; Mueller, U.; Frigge, M.; Schnabelrauch, M.; Wyrwa, R.; Schiller, A. *J. Mater. Chem.* **2012**, *22*, 8785−8792.

(17) Rose, M. J.; Olmstead, M. M.; Mascharak, P. K. *Polyhedron* **2007**, *26*, 4713−4718.

(18) Cramer, C. J.; Truhlar, D. G. *Phys. Chem. Chem. Phys.* **2009**, *11*, 10757−10816.

(19) Tfouni, E.; Krieger, M.; McGarvey, B. R.; Franco, D. W. *Coord. Chem. Rev.* **2003**, *236*, 57−69.

(20) De Candia, A. G.; Marcolongo, J. P.; Etchenique, R.; Slep, L. D. *Inorg. Chem.* **2010**, *49*, 6925−6930.

(21) Merkle, A. C.; Fry, N. L.; Mascharak, P. K.; Lehnert, N. *Inorg. Chem.* **2011**, *50*, 12192−12203.

(22) Fry, N. L.; Mascharak, P. K. *Dalton Trans.* **2012**, *41*, 4726−4735.

(23) Zheng, W.; Wu, S.; Zhao, S.; Geng, Y.; Jin, J.; Su, Z.; Fu, Q. *Inorg. Chem.* **2012**, *51*, 3972−3980.

(24) Full, J.; Daniel, C.; González, L. *Phys. Chem. Chem. Phys.* **2003**, *5*, 87−96.

(25) Tully, J. C. *J. Chem. Phys.* **1990**, *93*, 1061−1071.

(26) (a) Doltsinis, N. L.; Marx, D. *J. Theory Comput. Chem.* **2002**, *01*, 319−349. (b) González, L.; Marquetand, P.; Richter, M.; González-Vázquez, J.; Sola, I. In *Ultrafast Phenomena in Molecular Sciences*; de Nalda, R., Bañares, L., Eds.; Springer Series in Chemical Physics 107; Springer International Publishing: Cham, Switzerland, 2014; pp 145−170.

(27) Barbatti, M. *WIREs Comput. Mol. Sci.* **2011**, *1*, 620−633.

(28) Moret, M.-E.; Tavernelli, I.; Chergui, M.; Rothlisberger, U. *Chem.—Eur. J.* **2010**, *16*, 5889−5894.

(29) Tavernelli, I.; Curchod, B. F.; Rothlisberger, U. *Chem. Phys.* **2011**, *391*, 101−109.

(30) Pierloot, K. *Int. J. Quantum Chem.* **2011**, *111*, 3291−3301.

(31) González, L.; Escudero, D.; Serrano-Andrés, L. *ChemPhysChem* **2012**, *13*, 28−51.

(32) Jaworska, M. *Inorg. Chem. Commun.* **2006**, *9*, 284−289.

(33) Schenk, G.; Pau, M. Y. M.; Solomon, E. I. *J. Am. Chem. Soc.* **2004**, *126*, 505−515.

(34) Radoń, M.; Broclawik, E.; Pierloot, K. *J. Phys. Chem. B* **2010**, *114*, 1518−1528.

(35) Lahiri, G. K.; Kaim, W. *Dalton Trans.* **2010**, *39*, 4471−4478.

(36) Rose, M. J.; Mascharak, P. K. *Coord. Chem. Rev.* **2008**, *252*, 2093−2114.

(37) Roos, B. O.; Taylor, P. R.; Siegbahn, P. E. *Chem. Phys.* **1980**, *48*, 157−173.

(38) Andersson, K.; Malmqvist, P. A.; Roos, B. O.; Sadlej, A. J.; Wolinski, K. *J. Phys. Chem.* **1990**, *94*, 5483−5488.

(39) Kurtikyan, T. S.; Hayrapetyan, V. A.; Martirosyan, G. G.; Ghazaryan, R. K.; Iretskii, A. V.; Zhao, H.; Pierloot, K.; Ford, P. C. *Chem. Commun.* **2012**, *48*, 12088−12090.

(40) Radoń, M.; Pierloot, K. *J. Phys. Chem. A* **2008**, *112*, 11824−11832.

(41) Daniel, C. *Coord. Chem. Rev.* **2003**, *238−239*, 143−166.

(42) Pierloot, K. *Mol. Phys.* **2003**, *101*, 2083−2094.

(43) Gagliardi, L. In *Reviews in Computational Chemistry*; Lipkowitz, K. B., Cundari, T. R., Eds.; John Wiley & Sons, Inc.: New York, 2007; pp 249−284.

(44) (a) Pedersen, T.; Aquilante, F.; Lindh, R. *Theor. Chem. Acc.* **2009**, *124*, 1−10. (b) Aquilante, F.; Pedersen, T. B.; Lindh, R.; Roos, B. O.; Sánchez de Merás, A.; Koch, H. *J. Chem. Phys.* **2008**, *129*, 024113. (c) Aquilante, F.; Malmqvist, P.-A.; Pedersen, T. B.; Ghosh, A.; Roos, B. O. *J. Chem. Theory Comput.* **2008**, *4*, 694−702.

(45) Delcey, M.; Freitag, L.; Pedersen, T. B.; Aquilante, F.; Lindh, R.; González, L. *J. Chem. Phys.* **2014**, Accepted.

(46) (a) Brahim, H.; Daniel, C.; Rahmouni, A. *Int. J. Quantum Chem.* **2012**, *112*, 2085−2097. (b) Baková, R.; Chergui, M.; Daniel, C.; Vlček, A., Jr.; Záliš, S. *Coord. Chem. Rev.* **2011**, *255*, 975−989. (c) Vallet, V.; Strich, A.; Daniel, C. *Chem. Phys.* **2005**, *311*, 13−18. (d) Kayanuma, M.; Daniel, C.; Köppel, H.; Gindensperger, E. *Coord. Chem. Rev.* **2011**, 255−2703. (e) Heydová, R.; Gindensperger, E.; Romano, R.; Sýkora, J.; Vlček, A.; Záliš, S.; Daniel, C. *J. Phys. Chem. A* **2012**, *116*, 11319−11329.

(47) Marian, C. M. *WIREs Comput. Mol. Sci.* **2012**, *2*, 187−203.

(48) (a) Bhasikuttan, A. C.; Suzuki, M.; Nakashima, S.; Okada, T. *J. Am. Chem. Soc.* **2002**, *124*, 8398−8405. (b) Bhasikuttan, A. C.; Okada, T. *J. Phys. Chem. B* **2004**, *108*, 12629−12632. (c) McCusker, J. K. *Acc. Chem. Res.* **2003**, *36*, 876−887. (d) Cannizzo, A.; van Mourik, F.; Gawelda, W.; Zgrablic, G.; Bressler, C.; Chergui, M. *Angew. Chem., Int. Ed.* **2006**, *118*, 3246−3248. (e) Bräm, O.; Messina, F.; El-Zohry, A. M.; Cannizzo, A.; Chergui, M. *Chem. Phys.* **2012**, *393*, 51−57. (f) Gawelda, W.; Cannizzo, A.; Pham, V.-T.; van Mourik, F.; Bressler, C.; Chergui, M. *J. Am. Chem. Soc.* **2007**, *129*, 8199−8206. (g) Gawelda, W.; Pham, V.-T.; Benfatto, M.; Zaushitsyn, Y.; Kaiser, M.; Grolimund, D.; Johnson, S. L.; Abela, R.; Hauser, A.; Bressler, C.; Chergui, M. *Phys. Rev. Lett.* **2007**, *98*, 057401. (h) Bressler, C.; Milne, C.; Pham, V.-T.; ElNahhas, A.; Veen, R. M. v. d.; Gawelda, W.; Johnson, S.; Beaud, P.; Grolimund, D.; Kaiser, M.; Borca, C. N.; Ingold, G.; Abela, R.; Chergui, M. *Science* **2009**, *323*, 489−492. (i) Consani, C.; Prémont-Schwarz, M.; El Nahhas, A.; Bressler, C.; van Mourik, F.; Cannizzo, A.; Chergui, M. *Angew. Chem., Int. Ed.* **2009**, *48*, 7184−7187. (j) Cannizzo, A.; Milne, C.; Consani, C.; Gawelda, W.; Bressler, C.; van Mourik, F.; Chergui, M. *Coord. Chem. Rev.* **2010**, *254*, 2677−2686. (k) Bräm, O.; Messina, F.; Baranoff, E.; Cannizzo, A.; Nazeeruddin, M. K.; Chergui, M. *J. Phys. Chem. C* **2013**, *117*, 15958−15966. (l) Cannizzo, A.; Blanco-Rodríguez, A. M.; El Nahhas, A.; Šebera, J.; Záliš, S.; Vlček, A., Jr.; Chergui, M. *J. Am. Chem. Soc.* **2008**, *130*, 8967−8974. (m) Juban, E. A.; McCusker, J. K. *J. Am. Chem. Soc.* **2005**, *127*, 6857−6865. (n) Hedley, G. J.; Ruseckas, A.; Samuel, I. D.W. *J. Phys. Chem. A* **2009**, *113*, 2−4. (o) Burdzinski, G. T.; Ramnauth, R.; Chisholm, M. H.; Gustafson, T. L. *J. Am. Chem. Soc.* **2006**, *128*, 6776−6777. (p) Iwakura, I.; Kobayashi, T.; Yabushita, A. *Inorg. Chem.* **2009**, *48*, 3523−3528.

(49) Colvin, M. T.; Smeigh, A. L.; Giacobbe, E. M.; Conron, S. M. M.; Ricks, A. B.; Wasielewski, M. R. *J. Phys. Chem. A* **2011**, *115*, 7538−7549.

(50) (a) Full, J.; González, L.; Daniel, C. *J. Phys. Chem. A* **2001**, *105*, 184−189. (b) González, L.; Daniel, C. *J. Comput. Chem.* **2006**, *27*, 1781−1786. (c) Ambrosek, D.; Villaume, S.; Daniel, C.; González, L. *J.*

Phys. Chem. A **2007**, *111*, 4737−4742. (d) Gindensperger, E.; Köppel, H.; Daniel, C. *Chem. Commun.* **2010**, *46*, 8225. (e) Costa, P. J.; Calhorda, M. J.; Villaume, S.; Daniel, C. *New J. Chem.* **2008**, *32*, 1904.

(51) Perdew, J. P. *Phys. Rev. B* **1986**, *33*, 8822−8824.

(52) Becke, A. D. *J. Chem. Phys.* **1993**, *98*, 5648−5652.

(53) Vahtras, O.; Almlöf, J.; Feyereisen, M. W. *Chem. Phys. Lett.* **1993**, *213*, 514−518.

(54) Eichkorn, K.; Treutler, O.; Öhm, H.; Häser, M.; Ahlrichs, R. *Chem. Phys. Lett.* **1995**, *242*, 652−660.

(55) Sierka, M.; Hogekamp, A.; Ahlrichs, R. *J. Chem. Phys.* **2003**, *118*, 9136−9148.

(56) Schäfer, A.; Horn, H.; Ahlrichs, R. *J. Chem. Phys.* **1992**, *97*, 2571−2577.

(57) Weigend, F.; Ahlrichs, R. *Phys. Chem. Chem. Phys.* **2005**, *7*, 3297−3305.

(58) Andrae, D.; Häußermann, U.; Dolg, M.; Stoll, H.; Preuß, H. *Theor. Chim. Acta* **1990**, *77*, 123−141.

(59) Eichkorn, K.; Weigend, F.; Treutler, O.; Ahlrichs, R. *Theor. Chem. Acc.* **1997**, *97*, 119−124.

(60) Klamt, A.; Schüürmann, G. *J. Chem. Soc., Perkin Trans. 2* **1993**, 799−805.

(61) TURBOMOLE V6.5, 2013, a development of University of Karlsruhe and Forschungszentrum Karlsruhe GmbH, 1989−2007, TURBOMOLE GmbH, since 2007; available from http://www.turbomole.com.

(62) Aquilante, F.; de Vico, L.; Ferré, N.; Ghigo, G.; Malmqvist, P.-Å.; Neogrády, P.; Pedersen, T. B.; Pitoňák, M.; Reiher, M.; Roos, B. O.; Serrano-Andrés, L.; Urban, M.; Veryazov, V.; Lindh, R. *J. Comput. Chem.* **2010**, *31*, 224−247.

(63) Roos, B. O.; Lindh, R.; Malmqvist, P.-A.; Veryazov, V.; Widmark, P.-O. *J. Phys. Chem. A* **2005**, *109*, 6575−6579.

(64) Finley, J.; Malmqvist, P. A.; Roos, B. O.; Serrano-Andrés, L. *Chem. Phys. Lett.* **1998**, *288*, 299−306.

(65) Roos, B. O.; Andersson, K. *Chem. Phys. Lett.* **1995**, *245*, 215−223.

(66) Cossi, M.; Rega, N.; Scalmani, G.; Barone, V. *J. Comput. Chem.* **2003**, *24*, 669−681.

(67) Malmqvist, P. A.; Roos, B. O.; Schimmelpfennig, B. *Chem. Phys. Lett.* **2002**, *357*, 230−240.

(68) Barbatti, M.; Aquino, A. J. A.; Lischka, H. *Phys. Chem. Chem. Phys.* **2010**, *12*, 4959.

(69) Verlet, L. *Phys. Rev.* **1967**, *159*, 98−103.

(70) Richter, M.; Marquetand, P.; González-Vázquez, J.; Sola, I.; González, L. *J. Chem. Theory Comput.* **2011**, *7*, 1253−1258.

(71) (a) Richter, M.; Marquetand, P.; González-Vázquez, J.; Sola, I.; González, L. *J. Phys. Chem. Lett.* **2012**, *3*, 3090−3095. (b) Mai, S.; Marquetand, P.; Richter, M.; González- Vázquez, J.; González, L. *ChemPhysChem* **2013**, *14*, 2920−2931. (c) Mai, S.; Marquetand, P.; González, L. *J. Chem. Phys.* **2014**, accepted.

(72) Tapavicza, E.; Tavernelli, I.; Rothlisberger, U. *Phys. Rev. Lett.* **2007**, *98*, 023001.

(73) Tavernelli, I.; Curchod, B. F. E.; Rothlisberger, U. *J. Chem. Phys.* **2009**, *131*, 196101.

(74) Tavernelli, I.; Curchod, B. F. E.; Laktionov, A.; Rothlisberger, U. *J. Chem. Phys.* **2010**, *133*, 194104.

(75) (a) Casida, M. E.; Natarajan, B.; Deutsch, T. In *Fundamentals of Time-Dependent Density Functional Theory*; Marques, M. A. L.; Maitra, N. T.; Nogueira, F. M. S.; Gross, E. K. U.; Rubio, A., Eds.; Lecture Notes in Physics 837; Springer: Berlin, 2012; pp 279−299. (b) Huix-Rotllant, M.; Filatov, M.; Gozem, S.; Schapiro, I.; Olivucci, M.; Ferré, N. *J. Chem. Theory Comput.* **2013**, *9*, 3917−3932. (c) Cordova, F.; Doriol, L. J.; Ipatov, A.; Casida, M. E.; Filippi, C.; Vela, A. *J. Chem. Phys.* **2007**, *127*, 164111.

(76) (a) Tapavicza, E.; Tavernelli, I.; Rothlisberger, U.; Filippi, C.; Casida, M. E. *J. Chem. Phys.* **2008**, *129*, 124108. (b) Tapavicza, E.; Meyer, A. M.; Furche, F. *Phys. Chem. Chem. Phys.* **2011**, *13*, 20986−20998. (c) Tapavicza, E.; Bellchambers, G. D.; Vincent, J. C.; Furche, F. *Phys. Chem. Chem. Phys.* **2013**, *15*, 18336−18348. (d) Curchod, B. F. E.; Rothlisberger, U.; Tavernelli, I. *ChemPhysChem* **2013**, *14*, 1314−1340.

(77) Lower, S. K.; El-Sayed, M. A. *Chem. Rev.* **1966**, *66*, 199−241.

(78) Manaa, M. R.; Yarkony, D. R. *J. Chem. Phys.* **1991**, *95*, 1808−1816.

(79) Merchán, M.; Serrano-Andrés, L.; Robb, M. A.; Blancafort, L. *J. Am. Chem. Soc.* **2005**, *127*, 1820−1825.

(80) Escudero, D.; Happ, B.; Winter, A.; Hager, M. D.; Schubert, U. S.; González, L. *Chem. Asian J.* **2012**, *7*, 667−671.

(81) Hammes-Schiffer, S.; Tully, J. C. *J. Chem. Phys.* **1994**, *101*, 4657.

(82) Pittner, J.; Lischka, H.; Barbatti, M. *Chem. Phys.* **2009**, *356*, 147−152.

(83) Barbatti, M.; Ruckenbauer, M.; Plasser, F.; Pittner, J.; Granucci, G.; Persico, M.; Lischka, H. *WIREs Comput. Mol. Sci.* **2014**, *4*, 26−33.

(84) Enemark, J. H.; Feltham, R. D. *J. Am. Chem. Soc.* **1974**, *96*, 5002−5004.

(85) (a) Tong, G. S. M.; Wong, E. L.-M.; Che, C.-M. *Chem.—Eur. J.* **2008**, *14*, 5495−5506. (b) Carreón-Macedo, J.-L.; Harvey, J. N. *J. Am. Chem. Soc.* **2004**, *126*, 5789−5797. (c) Kuta, J.; Patchkovskii, S.; Zgierski, M. Z.; Kozlowski, P. M. *J. Comput. Chem.* **2006**, *27*, 1429−1437. (d) Lodowski, P.; Jaworska, M.; Andruniów, T.; Kumar, M.; Kozlowski, P. M. *J. Phys. Chem. B* **2009**, *113*, 6898−6909. (e) Jaworska, M.; Lodowski, P.; Andruniów, T.; Kozlowski, P. M. *J. Phys. Chem. B* **2007**, *111*, 2419−2422. (f) DeBeer George, S.; Petrenko, T.; Neese, F. *J. Phys. Chem. A* **2008**, *112*, 12936−12943. (g) Goossen, L. J.; Koley, D.; Hermann, H. L.; Thiel, W. *J. Am. Chem. Soc.* **2005**, *127*, 11102−11114.

(86) Ziegler, T.; Seth, M.; Krykunov, M.; Autschbach, J.; Wang, F. *THEOCHEM* **2009**, *914*, 106−109.

(87) Casida, M. E.; Gutierrez, F.; Guan, J.; Gadea, F.-X.; Salahub, D.; Daudey, J.-P. *J. Chem. Phys.* **2000**, *113*, 7062−7071.

(88) Giesbertz, K.; Baerends, E. *Chem. Phys. Lett.* **2008**, *461*, 338−342.

4

RUTHENIUM POLYPYRIDYL COMPLEXES

This chapter contains the results of the studies on ruthenium polypyridyl complexes. Section 4.1 covers a methodological aspect of this thesis: the tris(2,2-bipyridine)ruthenium (II) ($[Ru(bpy)_3]^{2+}$), the prototype Ru polypyridyl complex is used as a testbed for the applicability of ab-initio multiconfigurational calculations to obtain its low-lying excited states at the equilibrium geometry. Besides providing benchmark-grade excitation energies and a comparison with experiment and previous DFT calculations, this section deals with a fundamental issue of multiconfigurational methods, namely the selection of the active orbitals. To rationalise the selection of the active orbitals, we use the novel orbital entanglement analysis developed in the group of Markus Reiher (ETH Zurich).

Section 4.2 switches the focus to the application of ruthenium polypyridyl complexes, namely the improvement of their properties in DSSCs. A study on a series of substituted Ru 2,6-di(quinolin-8-yl)pyridyl ($[Ru(dqp)_2]^{2+}$) complexes, exemplifying how DFT and TD-DFT calculations can rationalise and supplement the properties obtained experimentally and rationalise the changes in photophysics upon ligand substitution, thus paving the road to rational design of a photosensitiser. Although multiconfigurational calculations yield accurate results, in large-scale routine calculations on transition metal complexes DFT is still preferred due to its computational efficiency. In particular, TD-DFT calculations show how the substitution of the dqp ligand may improve the directionality of charge transfer upon photoexcitation and help eliminating the unwanted photodeactivation pathways, allowing for a longer lifetime of the ^{3}MLCT charge-separated state. This work has been performed in a close collaboration with Dr. Michael Jäger (Institute of Organic and Macromolecular Chemistry, University of Jena). The final section 4.3 again addresses the changes in photophysics of a complex upon ligand substitution, this time in a Ru polypyridyl based hydrogen-producing photocatalyst, $[Ru(bpy)_2(tpy)PtI(CH_3CN)]^{2+}$ (tpy = 2,2’:5’,2”-terpyridine) where tpy is bridged to a platinum catalytic hydrogen-producing site. In a joint theoretical and experimental study led by Prof. Dr. Annemarie Huijser (University of Twente), who performed spectroscopic measurements on this photocatalyst, its modification by substituting the bpy ligands with ethyl ($-COOC_2H_5$) groups is shown to increase the catalytic turnover number.

Sections 4.2 and 4.3 will be presented as summaries of the corresponding publications, which will be attached at the end of this chapter.

4.1 MULTICONFIGURATIONAL CALCULATIONS ON TRIS(2,2-BIPYRIDINE)-RUTHENIUM

In this work, $[Ru(bpy)_3]^{2+}$ is used as a testbed for ab-initio multiconfigurational methods, namely CASSCF, RASSCF and the newly-developed DMRG. As it has been already pointed out in Section 3.2.1, until recently ab-initio multiconfigurational calculations on transition metal complexes of the size of $[Ru(bpy)_3]^{2+}$ were computationally not feasible. However the increase of computational power and the recent implementation of the Cholesky decomposition-based density fitting[105] allow such calculations to be performed. In the next section, the results of CASSCF/CASPT2, RASSCF/RASPT2 and DMRG calculations on $[Ru(bpy)_3]^{2+}$ will be presented. Additionally, orbital entanglement calculations with the DMRG wavefunction will be presented, emphasising how orbital entanglement analysis indicates orbitals that should be included in the active space, paving the road to automatic active-space selection in multiconfigurational calculations.

4.1.1 *Computational Details*

Geometry optimisation on $[\mathrm{Ru(bpy)_3}]^{2+}$ has been performed with the RI-MP2 method[145] and def2-TZVP basis set[139] for all atoms, including a relativistic ECP for Ru, using D_3 symmetry. These calculations have been performed with the TURBOMOLE 6.5[146] program package. The optimised structure shows very good agreement with the crystal structure.[147]

Subsequently, single-point CASSCF/CASPT2 and RASSCF/RASPT2 calculations have been performed with the MOLCAS 8.0[140] program package. The ANO-RCC all-electron basis set[141] has been employed with two different contraction schemes, leading to two different basis set sizes: the smaller basis set (to be referred as DZ-*d* in the following) involves the VDZP contraction scheme for all atoms, with *d* functions removed from C and N atoms; while the larger set (to be referred as TZ-DZ) involves a VTZP basis set for the Ru atom instead. The Cholesky-decomposition based density fitting[105] has been employed, and the second-order DKH Hamiltonian[108] has been used for treating the relativistic effects. The spin-orbit coupled states have been calculated with the spin-orbit RAS State Interaction (SO-RASSI) method.[110]

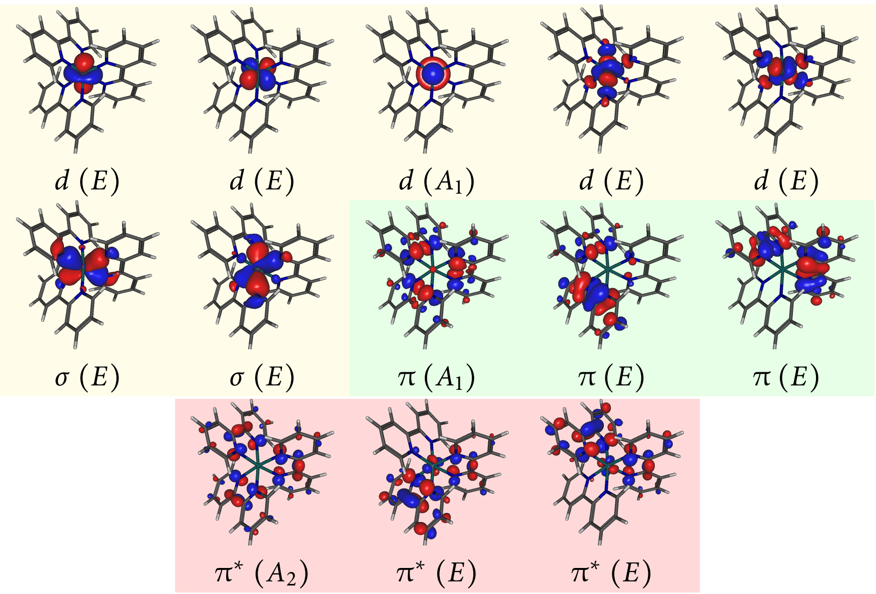

Figure 21: Active orbitals in CASSCF and RASSCF calculations of $[\mathrm{Ru(bpy)_3}]^{2+}$. Red, yellow and green background indicates the orbital in RAS 1, 2 and 3 subspaces in the RASSCF calculations, respectively, and orbitals are labelled according to their symmetry.

The active space for the multiconfigurational calculations should provide a good description of the coordination environment of the metal and the π system of the ligands in the ground and excited states and at the same time be computationally feasible. The calculations described here aim at describing a subset of the lowest MLCT states and $d \rightarrow d$ excitations, therefore the active space must include at least the five Ru 4*d* orbitals, two correlating orbitals for the $d_{x^2-y^2}$ and d_{z^2} orbitals and the bipyridyl π^* orbitals of interest. For the description of the π system and excitations to the π^* orbitals three pairs of π and π^* orbitals have been included: two $\pi\pi^*$ pairs of degenerate orbitals of E symmetry and another pair of A_1 and A_2 symmetry – previous DFT calculations[53] have indicated the importance of transitions involving these orbitals. The resulting active space therefore comprises 16 electrons in 13 orbitals (see Fig. 21). Calculations have been performed without symmetry, however orbital rotations between orbitals of different symmetries were disabled in the orbital optimisation procedure to avoid symmetry-broken solutions. Eleven singlet (ground and 10 excited) and eleven triplet states were calculated in two state-averaged calculations. RASSCF calculations employed the same active orbitals as the CASSCF calculations, but included the d and d correlating orbitals in RAS2, and bipyridyl $\pi\pi^*$ pairs in RAS 1 and 3 respectively: up to three or four excitations were allowed from RAS 1 and to RAS 3 in two different RASSCF calculations. For CASPT2 and RASPT2 calculations, an IPEA shift[142] of 0.25 a. u. and a level shift[143] of 0.3 a. u. has been employed.

Finally, DMRG-CI calculations (i. e. without orbital optimisation) and orbital entanglement analyses were performed with several active spaces. The smallest active space was identical to the CASSCF active space, thus comprising 16 electrons in 13 orbitals and employed the CASSCF orbitals. The larger active space augmented the CASSCF space by additional 9 bipyridyl $\pi\pi^*$ pairs, taken from Hartree-Fock calculations, comprising in total 34 electrons in 31 orbitals. Finally, to investigate the effect of the orbital optimisation on the orbital entanglement, another active space was constructed entirely from Hartree-Fock orbitals, comprising 40 electrons in 37 orbitals, i. e. 15 $\pi\pi^*$ pairs in addition to the d and d correlating orbitals. Different values of m (cf. Section 2.2.4) of up to 2048 have been used. All DMRG calculations and orbital entanglement analyses were performed with the MAQUIS[148] program interfaced to the development version of the MOLCAS program package. In excited state calculations up to 25 states were calculated: here, no distinction is performed between singlet and triplet states, as the employed MAQUIS code currently does not implement spin-symmetry: the spin of the states was tracked a-posteriori via the expectation value of the $\hat{S}^2$ operator.

4.1.2 *Results*

CASSCF AND RASSCF CALCULATIONS. Table 2 characterises the lowest singlet excited states in $[Ru(bpy)_3]^{2+}$.* Eight out of nine lowest excited states are metal-to-ligand charge transfer (MLCT) excitations from Ru d orbitals to ligand π^* orbitals, while the highest one is a Ru-centered $d \rightarrow d$ excitation. Excitations both to π^* orbitals delocalised over all bipyridyl ligands ($\pi^*(A_2)$ orbital) and localised predominantly on one ligand ($\pi^*(E)$) are present. The lower bright excitations (S_4, S_5 or 2^1E) are excitations to the $\pi^*(A_2)$ orbital, thus delocalising the excited electron over all ligands. The higher pair of bright excitations (S_7, S_8 or 3^1E) are excitations to $\pi^*(E)$ orbitals, which are more localised, but due to their degeneracy can be populated only both at the same time, which does not delocalise the excited state electron. Thus, in both cases the electron is delocalised over the bipyridyl ligands immediately after the excitation – a conclusion which is expected due to the overall symmetry of the molecule and largely accepted by the community,[44] yet has been questioned by some solvatochromic and Stark effect absorption spectra studies.[149] A newer electron localisation dynamics study[150] suggests that the electron localisation is solvent-driven and the electron is delocalised in gas-phase, which agrees with the result obtained here.

The last excited state pair (S_9, S_{10} or 4^1E) obtained in our calculations are metal-centered (^{1}MC) $d \rightarrow d$ excitations. A larger energy gap is present between the S_8 and S_9, indicating the lack of description of some states in between.

---

* The influence of spin-orbit coupling is omitted for now and will be discussed later.

St.	Sym.	$\Delta E_{\text{TZ-DZ}}$	$\Delta E_{\text{DZ-}d}$	Character	f
S_1	1^1A_2	2.58	2.47	$d(A_1) \to \pi^*(A_2)$	0.006
S_2	1^1E	2.75	2.60	$d(A_1) \to \pi^*(E)$	0.010
S_3		2.76	2.64	$d(A_1) \to \pi^*(E)$	0.002
S_4	2^1E	2.83	2.69	$d(E) \to \pi^*(A_2)$	0.205
S_5		2.86	2.72	$d(E) \to \pi^*(A_2)$	0.213
S_6	1^1A_1	3.04	2.86	$d(E) \to \pi^*(E)$	0.088
S_7	3^1E	3.13	3.01	$d(E) \to \pi^*(E)$	0.200
S_8		3.14	3.05	$d(E) \to \pi^*(E)$	0.171
S_9	4^1E	3.96	3.90	$d(A_1) \to d(E)$	0.001
S_{10}		3.96	3.90	$d(A_1) \to d(E)$	0.001
T_1	1^3A_2	2.64	2.49	$d(A_1) \to \pi^*(A_2)$	–
T_2	1^3E	2.71	2.55	$d(A_1) \to \pi^*(E)$	–
T_3		2.72	2.55	$d(A_1) \to \pi^*(E)$	–
T_4	2^3E	2.82	2.67	$d(E) \to \pi^*(A_2)$	–
T_5		2.85	2.75	$d(E) \to \pi^*(A_2)$	–
T_6	1^3A_1	2.92	2.80	$d(E) \to \pi^*(E)$	–
T_7	2^3A_2	3.05	2.81	$d(E) \to \pi^*(E)$	–
T_8	3^3E	3.13	2.86	$d(E) \to \pi^*(E)$	–
T_9		3.18	3.07	$d(E) \to \pi^*(E)$	–
T_{10}	4^3E	3.39	3.28	$d(A_1) \to d(E)$	–
T_{11}		3.39	3.29	$d(A_1) \to d(E)$	–

Table 2: Symmetries, characters, spin-free CASPT2 excitation energies (in eV) and oscillator strengths of the lowest 9 singlet and 10 triplet excited states in $[\text{Ru(bpy)}_3]^{2+}$. Bright excitations are highlighted in green.

Indeed, previous DFT calculations[53,54] and our DMRG calculations with more states (see below) indicate a presence of a MLCT state manifold, which is higher in energy than the S_8, the highest MLCT state present in our calculations. The lack of additional MLCT states between the calculated MLCT and the $d \to d$ state is a consequence of the inclusion of only three ligand π^* orbitals in the active space. On the other hand, this active space restriction allows us to describe the $d \to d$ excitation without calculating the missing MLCT manifold (which would be likely computationally infeasible due to a large number of states). Thus, in this work we present the characterisation of the $d \to d$ excitations at the equilibrium geometry for the first time.

The triplet states show a similar excitation pattern as the singlet states – the highest triplet states calculated are also triplet metal-centered (^{3}MC) $d \to d$ excitations. Although the $d \to d$ states lie quite high in energy (3.96 eV for 4^1E or 3.39 eV for 4^3E) and therefore are unlikely to be important for the photochemistry at the moment of photoexcitation, they (especially the ^{3}MC state) become important at later stages of the photodeactivation mechanism (cf. Section 1.3). Since both MLCT and MC $d \to d$ excitations are known to play a major role in the deactivation pathway of Ru polypyridyl complexes, the ability to describe all of these states at different geometries, including the equilibrium geometry, is crucial for future excited state dynamics simulations.

The TZ-DZ basis set blue-shifts all MLCT excitations by 0.14 eV on average compared to the DZ-d set, while the $d \to d$ state is blue-shifted only by 0.06 eV; the TZ-DZ basis set also provides better agreement with the experiment (see below). RASPT2 energies are very similar to the CASPT2 energies: RASSCF/RASPT2 with up to quadruple excitations allowed into the restricted spaces yields energies deviating up to only 0.07 eV from their CASPT2 counterparts. Restricting the excitations to up to triples only increases the maximum deviation up to 0.15 eV. However the RASSCF calculations require more iterations and are in general more difficult to converge, and therefore do not provide any computational saving compared to the CASSCF calculation.

Due to the D_3 symmetry of the molecule, the E excitations are expected to be perfectly degenerate. However, energies in Table 2 indicate a slight deviation from degeneracy, and also the orbitals (Fig. 21) show very small deviations from symmetry. This is due to the fact that the symmetry constraints (imposed with disabling orbital rotations between orbitals of different symmetries) could not be perfectly enforced in the calculations: yet given the artificial splitting of the E states of less than 0.05 eV, the overall effect of this symmetry breaking is very small.

State	Expt.[151]	CAS[a]	CAS(SO)[b]	TD-DFT[54]	DFT[53]
MLCT (2^1E)	2.88[c]	2.83/2.86	2.90	2.98	2.74
MLCT (3^1E)	2.95[d]	3.13/3.14	3.14	–	3.06
$d \rightarrow d$ (4^1E)	4.00[c]	3.96	3.98	–	–

[a] spin-free MS-CASPT2
[b] spin-orbit MS-CASPT2
[c] Gas-phase experimental value
[d] Experimental value in CH_3CN

Table 3: Comparison of CASPT2/TZ-DZ $[Ru(bpy)_3]^{2+}$ excitation energies (in eV) with experimental results and previous theoretical studies.

Despite the symmetry breaking, the agreement with the experimental spectrum[151] is excellent (cf. Table 3). Spin-orbit coupling (see column titled CAS(SO) in Table 3) has a very small effect on the energies, but improves the agreement with the experiment even more. The resulting deviation from the experiment for the MLCT 2^1E and $d \rightarrow d$ 4^1E states does not exceed 0.05 eV. The deviation is slightly larger for the (3^1E) states than for the other states, since the CASPT2 calculations do not account for any solvent effects. Interestingly enough, this excitation energy is better reproduced with the DZ-d basis set: however, most likely this agreement is due to error compensation given the lack of solvent effects in the calculations. Notably, the previous DFT studies[53,54] also show a decent agreement with experiment (errors below 0.15 eV), although not as close as the CASPT2 calculations presented here.

DMRG CALCULATIONS AND ENTANGLEMENT ANALYSIS. DMRG calculations and entanglement analyses were performed to assess the active space employed in the CASSCF calculations. Fig. 22 shows the single-orbital entropy S_i and mutual information I_{ij} for orbitals from the (16,13) and (34,31) active spaces, averaged over 17 lowest states.† Unlike in Section 3.1.2, the main focus of the entanglement analysis is not on identifying static or dynamic correlation, but rather on assessing the importance of orbitals in the active space for state-averaged calculations: therefore we will analyse the state-averaged entanglement here. In the smaller active space (Fig. 22a) we see large values of single-orbital entropy and strong entanglement of all d and π^* orbitals, as one would expect from an average for MLCT states. Additionally, the entanglement between $d_{x^2-y^2}$ and d_{z^2} and the corresponding correlating orbitals (pairs 13–1 and 12–2) is also strong, although their single-orbital entropy is smaller: this indicates the need for correlating orbitals 1 and 2 for the inclusion of the d orbitals. Note that $d_{x^2-y^2}$ and d_{z^2} orbitals show much weaker entanglement with the rest of the active space (the only significant interaction being that with the other d orbitals (6, 7 and 8)) and thus probably may be omitted together with the corresponding correlating orbitals if the description of $d \rightarrow d$ excitations would not be required (which is not the case here, and therefore the presence of the $d_{x^2-y^2}$ and d_{z^2} orbitals is required). The π orbitals 3, 4 and 5 seem to be similarly disentangled from the rest of the active space: also their presence seems to be unjustified at a first glance. We shall demonstrate their importance at a later point.

---

† To ensure the correspondence between the states between the two active spaces, only 17 states, including singlet and triplet MLCT states, but not the $d \rightarrow d$ excitation, have been employed.

The extension of the active space by Hartree-Fock orbitals (Fig: 22b) does not change the entanglement picture significantly: the strong entanglement remains among the d and π^* orbitals (15–20), and the $d_{x^2-y^2}$ and d_{z^2} orbitals are entangled only with their correlating counterparts. Additionally, there is no strong entanglement with any of the new orbitals. This shows that the small (16,13) active space is self-sufficient and does not require any additional orbitals from the larger (40,37) active space, therefore justifying its use in the CASSCF/CASPT2 calculations. Naturally, the states which the small active space can describe are limited by its active orbitals: if e. g. other MLCT excitations in additional π^* orbitals have to be described, the active space should be augmented accordingly.

Fig. 22 allows us to characterise the active spaces only *a posteriori*, only after the CASSCF or DMRG calculation has been performed and the orbitals have been optimised. An entanglement analysis of the guess orbitals before the actual CASSCF calculation would be more useful, since it would allow selection of active space orbitals based on entropy and mutual information, which could potentially be made automatic, unlike the experience and chemical intuition-based traditional CASSCF approach. In an attempt to investigate such active space selection, another entanglement analysis was performed with an (40,37) active space consisting entirely of Hartree-Fock orbitals, a subset of which has been also used as guess orbitals for previous CASSCF and DMRG calculations on $[\mathrm{Ru(bpy)_3}]^{2+}$. The resulting orbital entanglement plot is shown in Fig. 23. Despite the differences in the orbitals, the overall entanglement still resembles Fig. 22, namely the entanglement of $d_{x^2-y^2}$ and d_{z^2} with the prototypes of d correlating orbitals (pairs 4–34 and 5–33) and a strongly-entangled core of nine orbitals (15–23) representing a mixture of d, π and π^* orbitals. These orbitals together with the pairs 4–34 and 5–33 again lead us to the (16,13) active space, whose selection can now be justified with the entanglement analysis of Hartree-Fock orbitals. However, the inclusion of d orbitals into this active space cannot be based on entanglement arguments alone, but also on the *a priori* requirement of the active space to describe $d \rightarrow d$ excitations, thus tailoring the active space to a certain chemical problem.

Note how orbitals 15–17, being predominantly π orbitals (and therefore likely predecessors of the orbitals 3–5 in Fig. 22a), show a major d orbital participation, large values of single-orbital entropy and entanglement with other orbitals. It is therefore mandatory to include these orbitals into the active space, although in the orbital optimisation procedure they may get stripped of their orbital entanglement. It is also noteworthy that more π orbitals with partial d character (e. g. orbitals 6–8) with larger s_i, although lesser entanglement, are present, and that all orbitals from 6 to 32 have larger single-orbital entropies than the remaining orbitals. A very large active space, thus, could potentially include all of these orbitals – however routine calculations with active spaces of such size are still computationally expensive, even with DMRG.

In summary, DMRG calculations with three different active spaces have justified the use of the (16,13) active space in CASSCF/CASPT2 calculations showing its balanced character and self-sufficiency. It has also been shown how this active space can be derived from an entanglement analysis of Hartree-Fock orbitals, which may be undertaken prior to the CASSCF calculation. This

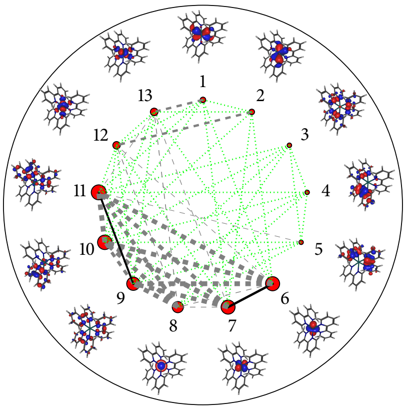

(a) 16 electrons in 13 orbitals

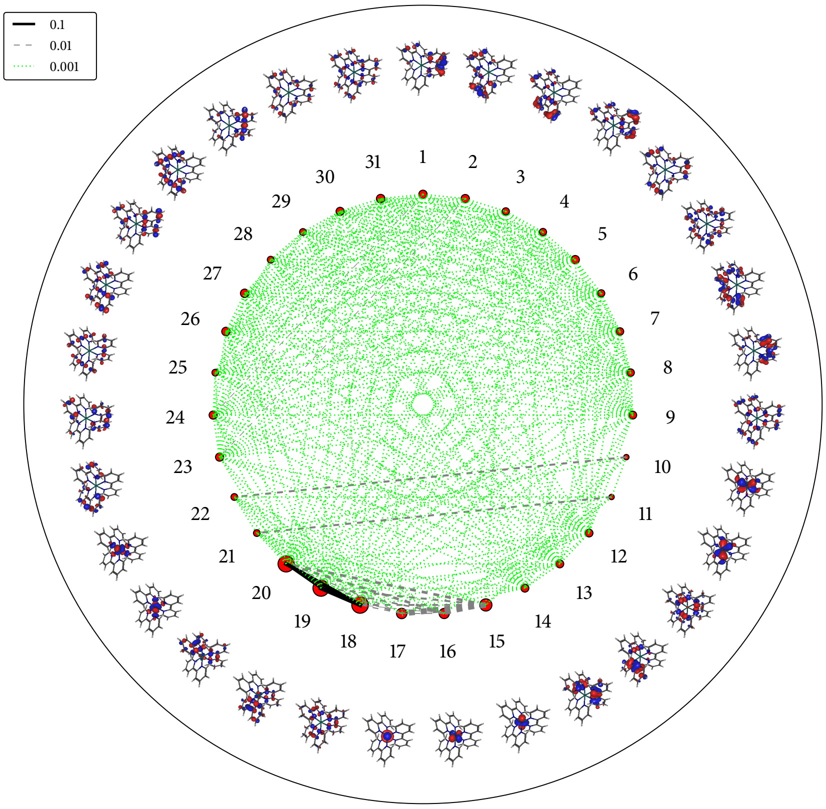

(b) 34 electrons in 31 orbitals. Active space from (a) corresponds to orbitals 10–22 in the same order.

Figure 22: Single-orbital entropy S_i and mutual orbital information I_{ij} for (a) the smaller (16,13) active space and (b) the larger (34,31) active space. The absolute value of S_i for each orbital is indicated by the size of the red point next to it. Mutual information I_{ij} is represented by lines connecting the points between orbitals i and j. Black, dashed grey and dotted green lines indicate strong ($I_{ij} > 0.1$), middle ($0.01 > I_{ij} > 0.1$) and weak entanglement ($0.001 > I_{ij} > 0.01$) respectively. The line width is also proportional to the absolute value of I_{ij}.

opens the road to automatic active space selection methods, although a robust entanglement-based automatic active space selector would require rigorous testing and careful tuning of thresholds for orbital entropies and mutual information, and still would be unable to tailor the active space for certain chemical problems (such as describing $d \rightarrow d$ excitations in our example).

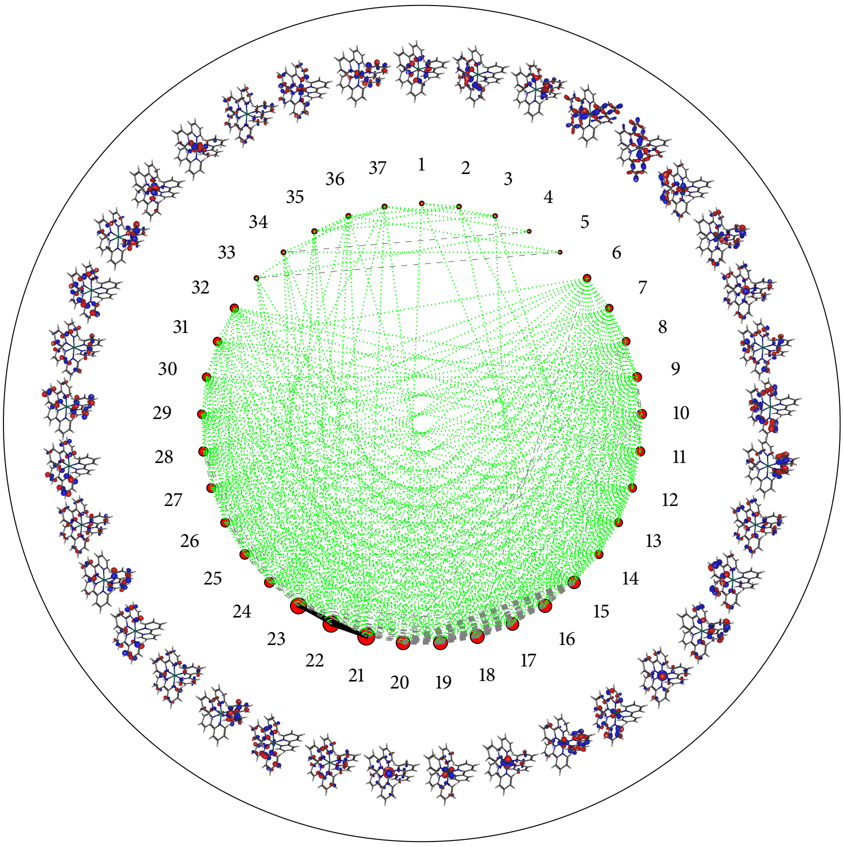

Figure 23: Single-orbital entropy and mutual information for the (40,37) active space consisting of Hartree-Fock orbitals. Legend as in Fig. 22.

4.2 COMPUTATIONAL STUDY ON RU DQP COMPLEXES: EN ROUTE TO PHOTOSENSITISER RATIONAL DESIGN

Although $[Ru(bpy)_3]^{2+}$ and derivatives have been used in solar energy conversion devices,[45,46] its high symmetry poses problems for charge-transfer directionality. $[Ru(dqp)_2]^{2+}$ (Complex **1** in Fig. 24), proposed by Abrahamsson et al.[55] is expected to overcome these problems. To further enhance the charge transfer directionality in **1**, a series of substitutions of one dqp ligand have been proposed by Dr. Michael Jäger (University of Jena): an attachment of a pyridine either directly to the dqp unit, leading to complex **2**, or via a phenylene spacer, leading to complex **3** (Fig. 24). The influence of the substituents on the photophysics of the complexes is studied here with DFT and TD-DFT. This original work has been published in an article titled *"Using computational chemistry to design Ru photosensitizers with directional charge transfer"* in *Coordination Chemistry Reviews*, which will be summarised here and reprinted at the end of this chapter.

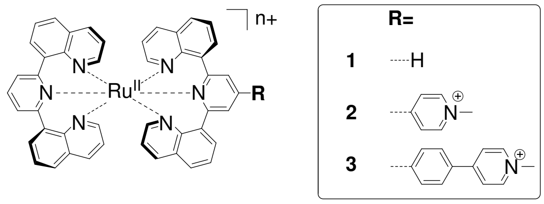

Figure 24: Series of $[Ru(dqp)_2]^{2+}$ complexes with directional charge transfer studied in this work. Reprinted with permission from Appendix 4.A.1.

The published article employs the study of Ru dqp complexes as an example in a tutorial review to illustrate the abilities of computational chemistry to assist the rational design of Ru photosensitisers. It summarises the methods in computational chemistry which can be used in photosensitiser studies with an emphasis on DFT and TD-DFT as the "work horse" of computational coordination chemistry, and shows how calculated properties may be related to experimental observables.

Problematic areas for (TD-)DFT relevant for the properties of Ru polypyridyl photosensitisers, such as London dispersion interactions and charge-transfer excitations are pointed out and shown how they may be addressed: the empirical dispersion corrections for DFT (either as of Grimme's D3 dispersion correction or dispersion-corrected functionals such as ωB97xD[94]) are shown to greatly improve the calculated structure of complex **1**. Not only the calculated structure agrees better with the X-ray structure, but also computed ^{1}H NMR shifts show better agreement with the experiment. This improvement is attributed to the π stacking of the dqp ligands present in the complex: the dispersion effect on the structure is negligible in $[Ru(2,6\text{-}tpy)_2]^{2+}$, a similar bis-tridentate complex chelated with two 2,2':6',2"-terpyridine (2,6-tpy) ligands[‡] which lacks intramolecular π stacking. The problems of charge-transfer excitations are addressed with a comparison of the excited state energies of **1** with CAM-B3LYP,[152] a popular long-range corrected functional with the conventional B3LYP functional. Quite surprisingly, CAM-B3LYP overestimates the excitation energies and presents a larger overall error than the standard B3LYP functional; hence, the usage of the B3LYP functional is advocated throughout the whole study.

Next, the effects of the dqp substitution on the UV-vis absorption spectrum of **1** is analysed. Unsubstituted complex **1** shows several bright ^{1}MLCT states in the visible light range, where the charge is delocalised over the whole ligand system, in particular over the quinoline moieties. The substitution leading to complexes **2** and **3** introduces a low-lying bright ^{1}MLCT excitation to the π^* orbital localised on the substituent, thus enabling directional charge transfer on the substituent immediately upon photoexcitation, in both complexes **2** and **3** to a similar degree. Such directional charge transfer towards the substituent is very favourable since in a photovoltaic device one would attach the Ru complex to the electron acceptor precisely at the substituent.

Finally, the photodeactivation pathways (Fig. 25) of all three complexes have been investigated by characterising the minima of the lowest ^{3}MLCT and ^{3}MC state. Here the picture differs from the absorption picture: complexes **1** and **3** show similar behaviour (Fig. 25a): the lowest-lying ^{3}MLCT state localises the charge on the quinoline moiety (unsubstituted in **3**) and lies closely to the ^{3}MC state, potentially allowing for thermal population of the ^{3}MC state, leading to unwanted charge recombination. Complex **2** (Fig. 25b) behaves differently: its lowest ^{3}MLCT state retains the charge on the substituent, is lying lower than in complexes **1** and **3** and further away from the ^{3}MC state, making the unwanted deactivation via the ^{3}MC less likely. Although photoexcitation initiates directional charge separation for complexes **2** and **3** in the same manner by populating the substituent π^* orbital, only **2** is able to retain the electron on the substituent π^* orbital in the long-living triplet state, whereas **3** deactivates to a different ^{3}MLCT state similar to that in **1**. Additionally, **2** is less prone to the deactivation via the ^{3}MC state.

[‡] Not to be confused with 2,2′:5′,2″-terpyridine (tpy), which is employed in complexes discussed in Section 4.3.

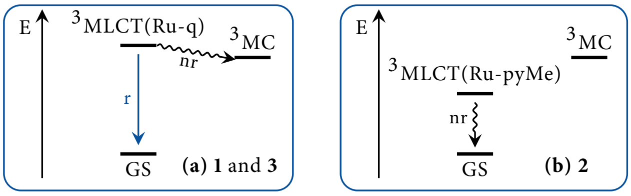

Figure 25: A scheme of photodeactivation pathways for complexes **1**–**3**. The radiative pathway is marked as *r* and nonradiative pathways as *nr*. Adapted from from Appendix 4.A.1.

4.3 SUBSTITUTION EFFECTS IN A RU POLYPYRIDYL-BASED PHOTOCATALYST

One possible electron acceptor, which can be attached to a Ru polypyridyl complex is a Pt^{II} or Pd^{II} coordination sphere, which may act as a hydrogen-evolving catalyst. A series of Ru polypyridyl complexes coupled with Pt and Pd catalytic sites have shown high photocatalytic activity[153] (Fig. 26), which is also influenced by the ligand substituents. Introduction of the ethyl ester groups to the bpy peripheral ligands has shown a remarkable increase of catalytic efficiency for a Ru/Pd complex with substituted (2,2)-bipyridine as peripheral ligands and di(pyridin-2-yl)pyrazine (2,5-dpp) as a bridging ligand (Fig. 26a), with the substituted complex (**EtOOCRuPd**) yielding a TON of 400, while its unsubstituted counterpart (**RuPd**) showed no catalytic activity.[154] A similar pair of complexes, but with a tpy bridging ligand and Pt as the catalytic site centre (**RuPt** and **EtOOCRuPt**, Fig. 26b) has been recently prepared and characterised in the group of Prof. Johannes G. Vos (Dublin City University): unlike **RuPd** and **EtOOCRuPd**, both substituted and unsubstituted species are catalytically active, but the substitution increases the TON from 99 to 720.[155] The mechanism of this catalytic effect enhancement provided by the EtOOC substitution of the bpy peripheral ligand is investigated in this chapter exemplarily on **RuPt** and **EtOOCRuPt**.

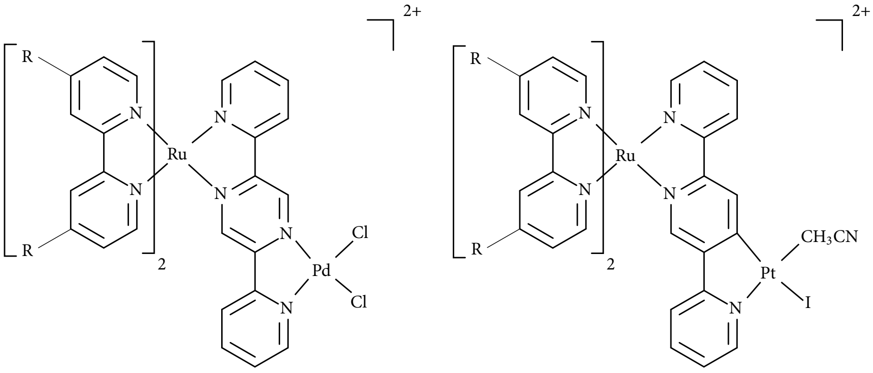

(a) RuPd (R=H), **EtOOCRuPd** (R=EtOOC)

(b) RuPt (R=H), **EtOOCRuPt** (R=EtOOC)

Figure 26: Hydrogen producing photocatalysts from Ref. 154 (a) and in this work (b).

DFT and TD-DFT calculations show that the EtOOC substituent lowers the energy of the MLCT excitations to the peripheral ligands (Ru $d \rightarrow$ bpy π^* excited states). In the unsubstituted complex (**RuPt**), the MLCT excitation to the bridging ligand ($d \rightarrow$ tpy π^*) lies lower than the $d \rightarrow$ bpy π^* excitation to the peripheral ligand, but the states exchange their order upon EtOOC substitution. This change of state ordering is found in the singlet states at the equilibrium geometry (i. e. absorption spectrum) and, more importantly, in the relaxed geometries of triplet states. The lowest triplet state in the **RuPt** complex has the Ru $d \rightarrow$ tpy π^* character, and the Ru $d \rightarrow$ bpy π^* character in the substituted **EtOOCRuPt** complex. In absence of other deactivation pathways, in the long term one would expect to populate the lowest-lying triplet excited state in each complex, although the calculated energy gaps between the two triplet minima in both complexes are less than 0.2 eV and geometry changes between the two minima are small, suggesting easy population redistribution between the states.

From the point of view of the directional charge transfer paradigm, a $d \rightarrow$ tpy π^* lowest triplet state, as found in the unsubstituted **RuPt** complex, is more favourable for the further energy transfer, since the charge is located closer to the acceptor. So how can the presence of a lower-lying $d \rightarrow$ bpy π^* triplet state, which violates the directional charge transfer paradigm, increase the catalytic efficiency? The answer is given by our collaborators' transient absorption experiments led by Prof. Annemarie Huijser, which show a slow (> 3 ps) charge transfer from the bpy to the tpy ligand. The bpy triplet thus can act as a "charge reservoir", slowly releasing the charge towards the tpy bridging ligand and the catalytic core and possibly avoiding charge-recombination pathways.

This study titled *"Peripheral ligands as electron storage reservoirs for photocatalytic hydrogen generation"* and is submitted for publication in Angew. Chem. Int. Ed. The submitted manuscript is reprinted at the end of this chapter.

APPENDIX 4.A ATTACHED PAPERS

APPENDIX 4.A.1

Using computational chemistry to design Ru photosensitizers with directional charge transfer

Michael Jäger§, Leon Freitag§ and Leticia González

Coord. Chem. Rev., in press.
`https://doi.org/10.1016/j.ccr.2015.03.019`

Contributions:

Michael Jäger performed the experimental work, ground state and some excited state calculations and wrote parts of the manuscript draft.

Leon Freitag performed the excited state calculations, provided guidance for the quantum chemical calculations by Michael Jäger and wrote parts of the manuscript draft.

Leticia González conceived the idea together with Michael Jäger, supervised the quantum chemical calculations, helped in the evaluation of the data and was involved in the preparation of the final manuscript.

Reprinted from Coord. Chem. Rev., DOI: 10.1016/j.ccr.2015.03.019, Michael Jäger, Leon Freitag and Leticia González, “Using computational chemistry to design Ru photosensitizers with directional charge transfer”. Copyright 2015, with permission from Elsevier.

---

§ These authors contributed equally to this work

G Model
CCR-112052; No. of Pages 20
ARTICLE IN PRESS

Coordination Chemistry Reviews xxx (2015) xxx–xxx

Contents lists available at ScienceDirect

Coordination Chemistry Reviews

journal homepage: www.elsevier.com/locate/ccr

Review

Using computational chemistry to design Ru photosensitizers with directional charge transfer

Michael Jäger[a,1], Leon Freitag[b,1], Leticia González[b,*]

[a] Laboratory of Organic and Macromolecular Chemistry (IOMC), Friedrich Schiller University Jena, Humboldtstr. 10, 07743 Jena, Germany
[b] Institute of Theoretical Chemistry, University of Vienna, Währinger Straße 17, 1090 Vienna, Austria

Contents

1. Introduction 00
2. Computational methods 00
  2.1. Density functional theory 00
  2.2. Quantum chemical descriptors 00
    2.2.1. Geometries 00
    2.2.2. Energies 00
    2.2.3. Populations and densities 00
    2.2.4. Electronic transitions 00
  2.3. Connection between experimental observables and theory 00
    2.3.1. Thermo- and electrochemistry 00
    2.3.2. Spectroscopic properties 00
    2.3.3. Reaction mechanisms 00
3. A case study: $[Ru(dqp)_2]^{2+}$ photosensitizers with directional charge-transfer character 00
  3.1. Molecular geometry 00
  3.2. Molecular orbitals 00
  3.3. Thermochemistry 00
  3.4. Photochemistry 00
    3.4.1. Characterization of singlet states 00
    3.4.2. Characterization of triplet states 00
4. Concluding remarks 00
5. Computational details and experimental 00
Acknowledgements 00
References 00

ARTICLE INFO

Article history:
Received 19 December 2014
Received in revised form 23 March 2015
Accepted 25 March 2015
Available online xxx

Keywords:
Ru complexes
Photosensitizers
DFT
TD-DFT
Photophysics

ABSTRACT

Recent developments in computational chemistry offer an attractive opportunity to design new photosensitizers with suitable properties. A number of theoretical techniques can be exercised to tune the optical and electrochemical properties required to optimize the efficiency of solar energy conversion schemes. In this contribution, it is illustrated how computational chemistry hand-in-hand with experimental results can aid the design of photosensitizers. To this aim, computational methods with emphasis on recent developments in density functional theory (DFT), as the "work horse" of computational coordination chemistry, are reviewed in the light of explaining how ground and excited properties can be related to different physical observables relevant to design photosensitizers with particular properties. A case study based on a family of $[Ru(dqp)_2]^{2+}$ complexes is used in a tutorial fashion to exemplify the different properties that can be obtained from theory, including nuclear geometries, electronic transitions and mechanistic aspects of photodeactivation, in order to optimize directional charge transfer in photosensitizers.

© 2015 Elsevier B.V. All rights reserved.

---

[*] Corresponding author. Tel.: +43 1427752750.
E-mail address: leticia.gonzalez@univie.ac.at (L. González).
[1] These authors contributed equally to this work.

http://dx.doi.org/10.1016/j.ccr.2015.03.019
0010-8545/© 2015 Elsevier B.V. All rights reserved.

Please cite this article in press as: M. Jäger, et al., Coord. Chem. Rev. (2015), http://dx.doi.org/10.1016/j.ccr.2015.03.019

1. Introduction

One major societal challenge is the generation of sufficient amounts of energy, which is to date primarily provided by the combustion of fossil fuels. Irrespective of the projected abundance of such fuels, i.e. oil, gas and coal resources, severe environmental concerns arise from their extensive use, particularly from the production process itself and from the release of green-house gases that contribute to climate change. In this respect, sunlight provides an abundant and cheap energy source, although this energy is dispersive and therefore requires affordable materials to process it. The process of converting photon energy has been mastered by nature [1], ultimately creating organic matter that also forms the basis of the fossil fuels consumed today. During the last decades, a number of technologies have matured to efficiently generate electricity (photovoltaics) and/or to generate fuels by coupled catalytic processes (photo-electrochemical or photosynthetic devices) [2–4]. Given their importance for our future society, different strategies are pursued to qualitatively fulfill this task, and lead to diverse discussions that concern their current and anticipated application potential, creating a vibrant interdisciplinary field ranging from chemical synthesis and catalysis to material science.

Photovoltaic devices follow a common working principle, which resembles also the primary steps of natural photosynthesis: Photon absorption and exciton migration, primary charge separation, charge transport. Hence, current work is devoted to maximize the overall power conversion efficiency (PCE; power = voltage × current) by minimizing the losses, either in form of excessively spent driving forces, which lowers the open-circuit voltage, or by recombination of charge carriers, reducing the short-circuit current. For example, research in material science focuses on the advancement of processing techniques and engineering of the devices, particularly in silicon-based solar cells, perovskite-based solar cells, quantum dots cells, while the advances in synthetic chemistry allow preparation of molecular components and materials with improved optical and electrochemical properties, e.g. in dye-sensitized solar cells (DSSCs) or organic solar cells. In the latter cases, systematic improvement of PCEs relies on a modular strategy to assemble the functional components (light absorber, conductive domain etc.) and thereby precisely control their interaction. For example, the photophysical and electrochemical properties of a photosensitizer determine its efficiency for charge separation, while its interaction with charge-transporting components, including inorganic semiconductors [5], controls the rates of forward charge transfer vs. undesired processes, e.g. charge trapping and ultimately recombination.

Polypyridyl-based ruthenium complexes, e.g. archetypal $[Ru(bpy)_3]^{2+}$ (bpy is 2,2′-bipyridine), constitute an attractive class of photosensitizers not only for solar energy conversion schemes [6–10], but also for use in optoelectronic/photonic devices [11–14], as optomechanical actuators [15], molecular sensors [16] and switches [17,18], in photoredox catalysis [19–22], and with particular interest in medical and biochemical applications, such as diagnostics and photo-therapy [23–25]. Their broad practical application originates from the widely adjustable photophysical and electrochemical properties, both in the ground and excited states [26–29]. The photophysical processes of Ru-polypyridyl complexes have been studied experimentally in great depth during the last decades [28]. The most important states and associated processes are depicted in the simplified Scheme 1. They will serve as the starting point for the discussion of design strategies to tailor specific properties of photosensitizers (vide infra). After photon absorption in the ground state (GS) of a Ru polypyridyl complex (Scheme 1a), the initially populated singlet metal-to-ligand charge transfer (^{1}MLCT) state undergoes ultrafast intersystem crossing (ISC), typically in or very close to the Franck–Condon region, then populating a triplet MLCT (^{3}MLCT) state or a triplet manifold. The ^{3}MLCT excited state can decay to the ground state via radiative decay – so-called emission – and non-radiative pathways, whereby the excited state lifetime and the emission quantum yields are determined by the individual rate constants.

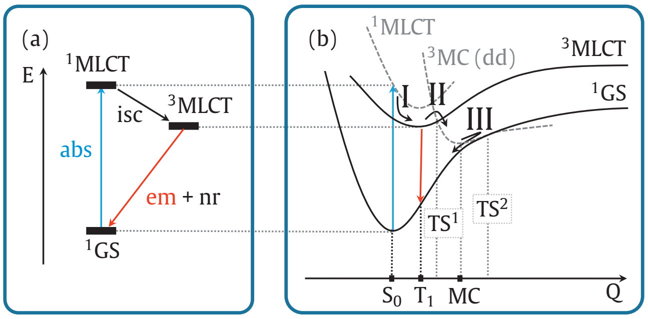

Scheme 1. (a) Simplified Jablonski diagram illustrating the most relevant states (GS = ground state, MLCT = metal-to-ligand-charge transfer) and principle photophysical processes (abs = photon absorption (blue), isc = intersystem crossing, em = emission (red), nr = non-radiative decay) of Ru polypyridyl complexes. (b) Schematic associated potential energy curves illustrating the population and deactivation pathways of the ^{3}MLCT states as a function of the nuclear coordinates (Q): (I) intersystem crossing and relaxation from ^{1}MLCT to ^{3}MLCT state, (II) thermally activated surface crossing from ^{3}MLCT to ^{3}MC (metal-centered or dd transition) state, and (III) surface crossing with intersystem crossing to ^{1}GS.

A typical scenario is depicted in Scheme 1b, where the dominant non-radiative deactivation occurs via thermally activated population of a triplet metal-centered (^{3}MC) state. This state can populate the ground state efficiently, as usually dictated by the energy gap law [28]. The activation barrier to the transition state (TS^1), that ultimately determines the ^{3}MLCT lifetime, can be as low as 1500 cm^{-1} (0.19 eV) for $[Ru(tpy)_2]^{2+}$ (tpy = 2,2′:6′,2″-terpyridine), leading to very short ^{3}MLCT lifetime of 0.2 ns and low quantum yield [30], while this barrier is significantly higher for $[Ru(bpy)_3]^{2+}$ and leads to long excited state lifetimes (~800 ns) and moderate quantum yields (0.06) [27]. Long excited state lifetimes are crucial for an efficient energy transfer to an acceptor. For example, in homogenous photocatalysis, the excited state lifetimes should be as long as possible to enable efficient diffusional encounter with a suitable electron donor or acceptor; whereas in DSSCs lifetimes of several nanoseconds are considered sufficient for charge injection into TiO$_2$, where panchromatic absorption and energy level alignment with respect to the semiconductor valence band are of high current interest [31]. In addition to the excited state lifetime, the versatility of a photosensitizer for charge transfer depends further on the redox properties, which are commonly derived from the emission energy and the ground state redox potentials [28].

The photophysical properties of ruthenium complexes can be widely tailored by the choice of the ligand sphere. Generally, undesired photodissociation and photodegradation is effectively diminished by chelating ligands, for example, by tridentate cyclometalating ligands vs. monodentate isocyanates in DSSC applications [31,32] or by the significantly enhanced photostability of *tris*-bidentate vs. *bis*-tridentate coordination, i.e. $[Ru(bpy)_3]^{2+}$ vs. $[Ru(dqp)_2]^{2+}$ [33]. Historically, the ligand modifications by functional groups allowed to fine-tune the electron transfer properties [27], and/or to prolong the excited state lifetime in case of tpy-based complexes (Scheme 2) [34]. Alternatively, replacement of the pyridine-rings by alternative (hetero)cycles, including (carb)anionic [35–37] and/or carbene [38–42] donors, has stimulated intensive research in the last years. The use of strong σ-donating ligands causes an increased ligand-field splitting, e.g. by carbenes, which raises the relative energy of the ^{3}MC state vs. the ^{3}MLCT and thereby increasing the thermal activation barrier for

Please cite this article in press as: M. Jäger, et al., Coord. Chem. Rev. (2015), http://dx.doi.org/10.1016/j.ccr.2015.03.019

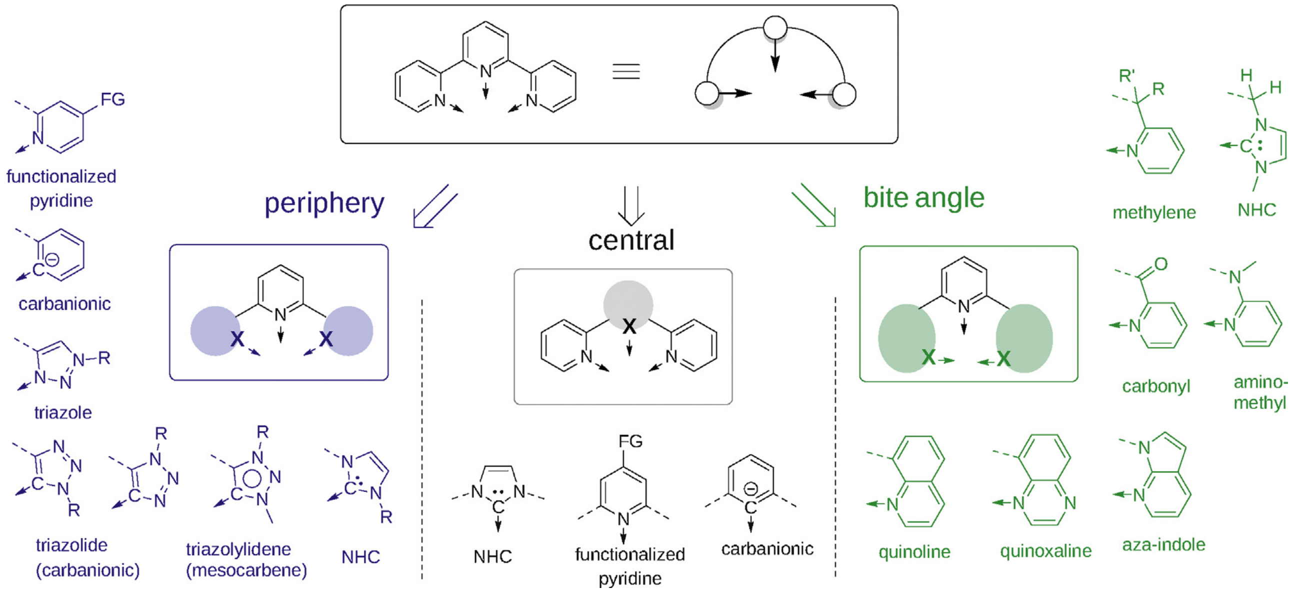

Scheme 2. Design strategy to tune photoredox properties of tridentate tpy (black box) [31–50]: Substitution of the peripheral (left panel, blue) and central heterocycle (central panel, black), and enlargement of bite angle (right panel, green) employing N-heterocyclic carbenes (NHC), cyclometallation, functional groups and five-membered and/or annellated ring systems.

non-radiative deactivation. Alternatively, the gap can be lowered by stabilization of the ^{3}MLCT state, which also leads to red-shifted emission accompanied with shortened lifetimes, e.g. by cyclometalation. Such complexes have been recently proven to be excellent sensitizer platforms for DSSCs [32] – reaching PCE comparable with that of the N3 and N749 reference dyes [43], but without suffering from undesired photo-substitution reactions [31]. In addition, the precise alignment of the donors around the Ru^{II} center influences the photophysical properties [44]. In the case of [Ru(tpy)$_2$]$^{2+}$, the small bite angle of tpy leads to significant distortion of the octahedral ligand field, which enables the efficient deactivation via ^{3}MC states (Scheme 1b). Hence, one approach to increase the excited lifetimes is to increase the bite angle or the tridentate ligand [44] by insertion of methylene [45], carbonyl [46] or aminomethyl [47] groups into the tpy skeleton. Alternatively, annellated ring systems, such as substituted quinolines [33,48,49], quinoxalines or azaindoles [50], have proven to yield significantly prolonged lifetimes by up to 4 orders of magnitude vs. [Ru(tpy)$_2$]$^{2+}$. As a result of such a large spectrum of potential modifications, the manifold of possible ruthenium photosensitizer structures is very large, and calls for an a priori investigation of their resulting photophysical and electrochemical properties. In this regard, computational methods have become an indispensable tool (Section 2) [47,51–53], particularly to estimate photoredox properties and thus driving forces in subsequent charge transfer reactions.

In this contribution we illustrate how to use computational methods to aid the design of an efficient molecular photosensitizer using as an example a series of Ru polypyridyl complexes. We first provide a short theoretical background of modern computational methods and their recent developments, with emphasis on the electronic structure of molecular photosensitizers. Then we explain how the photosensitizers' relevant photophysical and electrochemical properties are derived from the ground state, excited state and singly oxidized/reduced states. This also includes the calculation and visualization of important photophysical and electrochemical properties of the photosensitizer, e.g. vertical transitions and thermochemical analysis. Finally, we present a detailed case study to illustrate how these methods can rationalize the experimentally observed different photochemical behavior in the series of complexes, including different photodeactivation pathways, and thus how joint experimental and theoretical studies can promote rational photosensitizer design.

2. Computational methods

Any quantum chemical method relies on obtaining a computational solution of the time-independent Schrödinger equation, providing electronic energies, electron densities and other properties associated to the wavefunction of the system for a given molecular geometry and an electronic configuration. Since this equation is a many-body problem and cannot be solved exactly, many different approximations or "models" have been developed in the last decades, each with different accuracy and applicability to different molecular systems. The majority of these approximations can be classified into two large classes, depending on whether they are based on the electronic wavefunction or on the electron density. This choice leads to the well-known *ab-initio* wavefunction or density-functional theory (DFT) methods, respectively. Since in this paper all the calculations will be done in the framework of DFT, this method is explained in more detail in Section 2.1. Regarding wavefunction methods, the interested reader is referred to general textbooks, such as Refs. [54,55]. Here only a very brief overview of the *ab-initio* methods that can be currently used to model photosensitizers, with emphasis on the most recent developments, is given.

In the Hartree–Fock (HF) approximation the underlying wavefunction is a single electron configuration described by a Slater determinant, ignoring electron correlation. HF provides a starting point for other methods that aim at including electron correlation, and thus are often named post-HF methods. There is a multitude of post-HF methods available, based e.g. on perturbation theory (Møller–Plesset perturbation theory, MP), on the variational approach (configuration interaction, CI), or on the coupled-cluster (CC) ansatz. Although the CC methods are initially based on a ground-state HF calculation, they also allow calculating properties of electronic excited states, such as transition energies and oscillator strengths. To this aim, a number of flavors have been developed, including equation-of-motion-(EOM-) CC methods [56,57], linear response (LR), LR-CC [56,58,59] and the symmetry-adapted cluster configuration interaction (SAC-CI)

Please cite this article in press as: M. Jäger, et al., Coord. Chem. Rev. (2015), http://dx.doi.org/10.1016/j.ccr.2015.03.019

approach [60,61]. The accuracy of CC methods usually improves with increasing computational cost and scaling, as more and more expensive higher-order terms contributing to electron correlation are included, becoming prohibitively expensive for molecules consisting of more than a dozen of atoms. Polarization propagator methods [62] are another class of methods, closely related to LR methods. Here, the algebraic-diagrammatic construction (ADC) method [63,64] is becoming increasingly popular to obtain excited state properties [65–67]. Currently, the second-order (ADC(2)) [63,67] and third-order (ADC(3)) [68,69] approaches are implemented; these methods include the treatment of single (S) and double (D) excitations, thus being of the size of the CCSD treatment, and in ADC(3) triple (T) excitations are accounted perturbationally. Noteworthy, the ADC(2) method is less computationally expensive than comparable CI or CC methods and can be already applied for medium-sized (especially, organic) molecules, however, until very recently, it has remained mostly overseen [70].

In cases where more than one electronic configuration is present, as it is e.g. the case in some transition metal systems [71], single Slater determinant methods are not suitable and multiconfigurational SCF (MCSCF) methods become mandatory. A popular choice is the complete active space self-consistent field (CASSCF) [72] method. Used in combination with second order perturbation theory (CASPT2) [73], it can usually provide very accurate excited state energies (up to 0.1–0.2 eV accuracy) and reliable photochemical properties [74,75]. A clear disadvantage of these methods though is their computational demand, making them prohibitively expensive for very large systems, as it is the case of many photosensitizers. Modified versions, such as the restricted active space SCF (RASSCF/RASPT2), allow a larger number of active orbitals [76], and have found some applications in metal-containing systems [71,75,77–80]. A further development in this direction is density matrix renormalization group (DMRG) [81,82], which can also consider extensive active spaces [83,84]. Very promisingly, approximations based on density fitting or Cholesky decomposition can dramatically improve the performance of these methods for larger systems [85,86].

The following three subsections provide (i) a general introduction into DFT, (ii) a description of how to obtain and analyze characteristic properties of photosensitizers, and (iii) their connection to experimental observables.

2.1. Density functional theory

DFT [53,87,88,89,90,91,92] is conceptually different from wavefunction theory in the sense that it uses electron density as a basic variable. All ground state properties of the molecule are determined by the ground state density while the time-dependent DFT (TDDFT) approach allows for the calculation of excited state properties [90,93,94]. Kohn–Sham DFT, the most widely used DFT variant for molecules, uses a molecular orbital formalism similar to the wavefunction theory and Kohn–Sham equations, which are similar to HF equations but feature exchange-correlation functionals – analytical expressions dependent on the electron density that describe electron exchange and correlation. This allows calculations at a computational cost comparable to HF, but including electron correlation. On the down side, the functional that describes the electron exchange and correlation exactly is unknown. Instead, there is a large number of approximate exchange-correlation functionals, which employ different approximations, resulting in different suitability for different applications and chemical problems. Perdew and Schmidt have classified the different exchange-correlation functionals according to a “Jacob's ladder of density functional approximations” (Scheme 3) [95], depending on the different terms that contribute to the expression of the exchange-correlation energy E_{xc}.

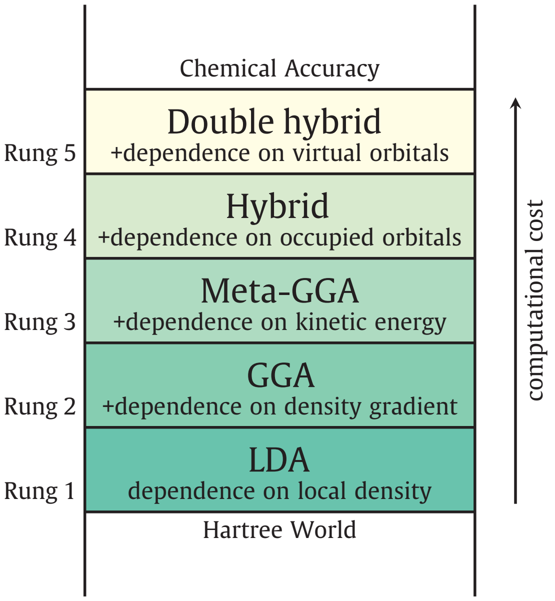
Chemical Accuracy
Rung 5
Double hybrid
+dependence on virtual orbitals
Rung 4
Hybrid
+dependence on occupied orbitals
Rung 3
Meta-GGA
+dependence on kinetic energy
Rung 2
GGA
+dependence on density gradient
Rung 1
LDA
dependence on local density
Hartree World
computational cost

Scheme 3. Jacob's ladder of functionals.
Adapted from Ref. [95].

The lowest rung of the ladder corresponds to the *local density approximation (LDA)*, where the expression for the calculation of E_{xc} employs only the local density at each point. A better approximation employs not only the local density, but also its gradient; this is named the *generalized gradient approximation (GGA)* and is presented at the second rung of the ladder. Several GGA functionals such as BP86 [96,97] and PBE [98] seem to perform generally well to obtain geometries, vibrational frequencies, in particular for transition metal complexes [99]. In the functionals of the third rung (meta-GGA) E_{xc} depends on the second derivatives of the density, or the local kinetic energy. The fourth rung involves an explicit E_{xc} dependence on the occupied orbitals: to this rung belong *hybrid functionals*, which involve an admixture of the exact Hartree–Fock exchange. The hybrid B3LYP [96,100,101] functional is so widely used that it has been named the “gold standard”, but PBE0 [102] and the Minnesota functional family [103] (hybrid and meta-GGA functionals) are also very popular. Functionals of the fifth, final rung have an E_{xc} dependence on the unoccupied orbitals. Among those, the most popular are the *double-hybrid* functionals [104–106], where not only a fraction of the exchange, but also a fraction of the correlation energy is obtained from *ab-initio* calculations. These functionals are computationally much more expensive than other functionals since they involve an *ab-initio* correlated calculation (most commonly MP2). Although there is a tendency to find more accurate functionals on higher rungs of the ladder [94], one should note that in general the advancement on the ladder does not automatically mean a systematically better approximation of the exact exchange-correlation functional; rather, the performance of each specific functional depends on the chemical problem [107].

Some of the known deficiencies of DFT common to functionals on all ladder rungs are the poor description of weak interactions such as London dispersion interactions [108,109] and charge separation. Improper treatment of dispersion interactions may lead to errors in modeling geometries and other ground state properties especially in spatially extended molecules featuring long-range weak interactions such as π-stacking. To address this problem, a variety of dispersion corrections [110] have been developed. Grimme's DFT-D empirical correction in its latest version (DFT-D3) [111] is one of the most successful since it can be applied to the

Please cite this article in press as: M. Jäger, et al., Coord. Chem. Rev. (2015), http://dx.doi.org/10.1016/j.ccr.2015.03.019

majority of popular functionals at almost no extra computational cost.

In systems with charge separation, such as dissociated systems and charge transfer, DFT shows the so-called “delocalization error” [112], which, among others, leads to the underestimation of excitation energies [113,114] and oscillator strengths [115], and produces faulty dipole moments and hyperpolarizabilities [116]. In order to deal with these problems, long-range corrected (LC) functionals which involve a different expression for exchange for long-range electron interactions [117] such as CAM-B3LYP [118] have been developed. Long-range corrected functionals can address the deficiencies caused by the delocalization error [115,119] and especially the tuning of the range-separation parameter ω, as in Refs. [120–122] can lead to a very good agreement with the experiment.

An additional important ingredient to model excited state properties of photosensitizers is the environment. Experiments are usually carried out in solution and therefore calculations should include the solvent. The simplest way to model solvation is using *implicit* models, i.e. representing the solvent as a continuum with a certain bulk dielectric constant. The polarizable continuum model (PCM) family [123] and the conductor-like screening model (COSMO) [124] belong to this sort of methods. When speaking about solvent interactions one should distinguish short and long-range effects, arising due to interactions with the first (few) and subsequent solvent shells, respectively. The implicit solvation methods account for long-range effects and they are probably the most frequently used methods because they are easy to use, computationally inexpensive, and are able to reproduce most of the solvent effects, as long as the solvent does not interact explicitly with the solute. In the latter case, the solvent is best modeled by introducing solvent molecules into the system explicitly, i.e. with an *explicit* solvent model. Here again it is possible to distinguish two levels of complexity. The most straightforward approach to model explicit solvent and recover short-range effects is to consider one or a few solvent molecules attached to the solute, typically by hydrogen bonds (but halogen bonds or other electrostatic interactions are also possible) and perform a cluster calculation with the complete system (solute plus solvent molecules) at the chosen level of theory. If the number of solvent molecules is too large or the level of theory at which the solute is calculated is computationally too expensive, it is also possible to separate the system into two parts and calculate the solvation shell at a more economic level of theory than the solute. Here, a combined approach is also possible. While the short-range effects are recovered by considering few explicit solvent molecules, long-range effects can also be added by placing the combined system inside an implicit solvent model. In the limit, when a large number of solvent molecules need to be considered, a mixed quantum mechanics/molecular mechanics (QM/MM) [125,126] approach, where the solute is treated quantum mechanically and the bulk of the solvent is modeled with classical molecular mechanics, is appropriate. QM/MM models have been recently successfully employed in modeling of solvent broadening of the excitation spectrum and solvent effects on the photorelaxation dynamics of some Ru photosensitizers [127–129]. QM/MM methods are also widely employed to consider other environments beyond solvents; in principle, some of the molecular environments or different building blocks contained in solar energy conversion devices could be modeled simultaneously within multilayer QM/MM approaches [130]. It is noteworthy that the inclusion of the solvent effects can decrease the DFT localization error [131], thus achieving a pleasant side-effect on the overall accuracy of the method.

Besides the choice of the method, another important issue to consider in any quantum chemical calculation is the basis set [132–134]. A basis set consists of functions centered at the atomic nuclei: atomic orbitals are constructed from linear combination of basis functions. In molecular calculations, mostly Gaussian basis sets are employed, although some studies use Slater basis sets, as those developed by the Amsterdam group [135], these are, however, computationally more expensive than comparable Gaussian basis sets. Plane wave basis sets, unlike their Gaussian and Slater counterparts are not centered on atomic nuclei, but they are popular for DFT calculations of extended systems employing periodic boundary conditions. The quality of a basis set depends on the number of basis functions that describe the orbitals. In good-quality basis sets, several basis functions correspond to a single valence shell: basis sets with two, three and so on basis functions per valence shell are called *double-zeta*, *triple-zeta* etc. Multiple shells have different spatial extent and therefore can adapt better to different electronic distributions in different molecular environments, and often basis sets are augmented with additional functions to ensure even greater flexibility: polarization functions are added to improve the description of chemical bonds and influence of external electric field, and diffuse functions are added if the description of very diffuse states, e.g. certain types of excited or anionic states are required [134]. Larger basis sets are generally more accurate, but require significantly more computational time; therefore, for large systems such as photosensitizers, presently only calculations with at most *triple-zeta* basis sets are feasible.

Among Gaussian basis sets, the Pople basis sets (e.g. the *double-zeta* 6-31G or *triple-zeta* 6-311G) [136] and the Ahlrichs basis sets [137] such as the double-zeta def2-SVP (split-valence polarized) or def2-TZVP (triple-zeta valence polarized), are very popular for both DFT and *ab-initio* calculations. Accurate *ab-initio* calculations may often employ atomic natural orbital (ANO) [138–142] or Dunning’s correlation consistent basis sets [143–146], which are generally larger, but give more accurate results and a smoother convergence of results with increasing basis set size. Accurate calculations on systems with heavy elements (such as transition metals) should include relativistic effects. The simplest and the most popular way to account for the majority of relativistic effects excluding spin–orbit couplings, called the scalar relativistic effects [147], are the effective core potentials (ECPs) [148]. ECPs replace the core electrons of a heavy atom with an effective potential simulating the influence of relativistically contracted core electrons on the valence electrons: as a side effect, core electrons in the heavy atom no longer need to be calculated, which constitutes a reduction in computational cost. Some of the most employed ECPs are those from Los Alamos National Laboratory (usually abbreviated by LANL2 with a *double-* or *triple-zeta* complementary basis set for valence electrons, LANL2DZ and LANL2TZ) [149,150], and the Stuttgart-Dresden (SDD) ECPs [151] abbreviated as MWB and MDF (where M stands for neutral atom and WB and DF for the Wood-Boring approximation [152] or Dirac–Fock equations which have been employed to construct the ECP). An alternative to ECPs are methods which involve a different Hamiltonian such as the zeroth order regular approximation (ZORA) [153] or the Douglas–Kroll–Hess Hamiltonian (DKH) [154–157].

In summary, an adequate description of a photosensitizer calculated at the DFT level of theory is the result of a wise combination of a functional and a basis set, as well as the inclusion of other corrections, such as the description of the environment or relativistic effects (see Scheme 4).

2.2. Quantum chemical descriptors

In the following, we discuss some relevant quantum chemical descriptors and properties that can be predicted theoretically.

2.2.1. Geometries

The first step of every quantum chemical calculation is a geometry optimization in the electronic ground state; this provides the

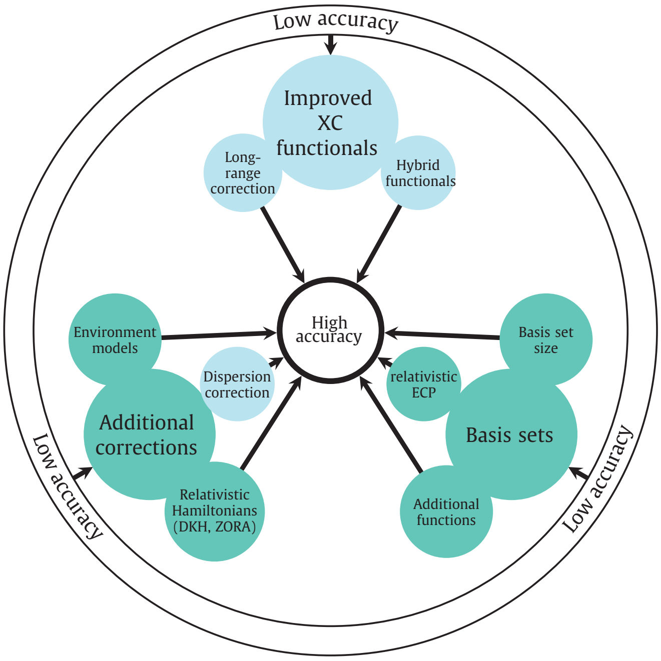

Scheme 4. Summary of the factors that contribute to DFT accuracy in the calculation of photosensitizer properties. Factors that are unique for DFT are presented in light blue, those not unique for DFT are shown in dark green.

equilibrium molecular geometry corresponding to the ground state minimum. This geometry can be compared with the experimental X-ray structure when available and constitutes the starting point of a subsequent molecular characterization: most of the other calculations describing properties of the ground state are based on this geometry. Typically, single-molecule gas-phase or PCM calculations are good enough to reproduce the X-ray structure; however, if the deviations from the crystal structure due to intermolecular packing effects are large and call for investigation, a molecular crystal calculation with periodic boundary conditions may be performed: among other methods, dispersion-corrected DFT [158,159] and QM/MM [160] have been successfully employed to predict the structures of molecular crystals.

After the molecular geometry has been optimized, further calculations can be performed to compute various chemical descriptors, as described below. Beyond the ground state equilibrium geometry, other structures can be optimized: e.g. minima of the potential energy surface (PES) corresponding to possible intermediate species, minima of higher-lying electronic excited states, or minima of the associated ionic species. Unlike the minima, the optimization of the transition states is not straightforward: a good initial guess is usually required, that is often based on a priori knowledge of a suitable reaction coordinate. However, one can perform interpolation between reactant and product structure to obtain a transition state guess, such as in the Quadratic Synchronous (QST2) method [161], especially if the geometrical changes between the reactant and the product are not too significant.

2.2.2. *Energies*

The simplest calculation (which is already implicitly performed when performing a geometry optimization) is a single-point energy calculation. This yields the ground state energy (or, if a different state has been requested, the energy of that state), as well as canonical molecular orbitals (MO) (for HF-based methods) or Kohn–Sham orbitals (for DFT) and their associated electron density. The MOs are one of the simplest descriptors commonly used for interpretation in photovoltaics. One should note that orbitals by themselves are not physical descriptors but rather mathematical entities – they can undergo transformations without changing the wavefunction, allowing for interpretation of the wavefunction from different points of view. Frontier molecular orbitals are used to characterize the nature of the state, which is especially interesting for open-shell states of higher multiplicity, such as triplet states. The energy of frontier orbitals is often used to estimate ionization potentials (IP) and electron affinities (EA), and their combination is related to redox chemical band gaps. This approximation is very crude since the correspondence of the energy of the HOMO and LUMO orbitals with to IP and EA within the Koopmans' theorem is rigorously valid only for the HF theory and it constitutes a further approximation in the context of DFT [162]. But even with HF, discrepancies in the redox potentials are expected because (i) in HF the orbitals are not optimized, (ii) HF theory lacks correlation, and (iii) the unoccupied orbitals are especially very poorly described. A better approach to the calculation of IPs and EAs is to compute the actual difference between the absolute energies of neutral and ionic species (called the ΔSCF method). Zero-point vibrational correction and thermal corrections to the electronic energy, which can be obtained from a vibrational frequency calculation, can further improve the result. The ΔSCF energy is conveniently compared vs. a second redox couple (so-called "reference"), thus the calculated difference resembles the electrochemical potential. Since both neutral and ionic species are calculated at the same level of theory, subtraction of the energies provides additional error cancellation, improving the reliability of the calculated potentials. An additional aspect to take into account when comparing theory with experiment is that one should distinguish between the *adiabatic* and the *vertical* IP/EA values, i.e. depending whether an optimized geometry is employed or not, respectively, for the ionic species.

2.2.3. *Populations and densities*

Population analyses [163] assign electron populations to atoms based on the atomic orbitals centered at the nuclei. They allow estimating basic chemical properties of atoms in the molecule such as formal charge or bond orders between the atoms. The problem with the population analyses is that there is no rigorous definition of what is an atom within a molecule and hence, all partition schemes of molecules into atoms are inevitably arbitrary. Atomic orbital-based methods such as Mulliken [164] or Löwdin [165] population analyses assign electronic population to atoms based on atomic orbital centers. Natural population analysis (NPA) [166] defines atom-centered natural atomic orbitals (NAOs) [166] and bond-centered natural bond orbitals (NBOs) [167] and derives atomic and bond populations from these. The quantum theory of atoms in molecules (QTAIM) model devised by Bader [168] uses the electron density to divide the space into volumes that define the spatial boundaries of atoms, chemical bonds, etc. The electron density, which can be calculated from the molecular orbitals, is, unlike the orbitals themselves, a physical observable. With the QTAIM approach, one can also quantify concepts such as delocalization and π-delocalization in aromatic systems, essential for Ru-based photosensitizers [169]. On itself, however, the total electron density is usually dominated by the core electrons and gives little chemical information about the molecule. Instead, it is the density redistribution that governs the (photo)chemistry and photophysics of the molecule, and thus density differences are much more useful. Several observables are based on density differences. One example is the spin density, or more precisely, the difference between total density of electrons with α spin and β spin. The spin density is useful in open-shell molecules since it shows the distribution of the unpaired electrons. For ionized molecules, this is equivalent to the charge distribution.

Please cite this article in press as: M. Jäger, et al., Coord. Chem. Rev. (2015), http://dx.doi.org/10.1016/j.ccr.2015.03.019

Table 1
Quantum chemical descriptors associated with experimental observables.

	QC descriptor	Observable
Ground state energy-based	Optimized geometry	Crystal structure
	ΔSCF	Band gaps, redox potentials
	IR frequencies and intensities	IR spectrum
Molecular orbitals-based	HOMO/LUMO energies	Band gaps, redox potentials
	Charge distribution from population analyses	Charge distribution
	NTOs	Excited state character
Electron density-based	Spin density	Spin distribution
	Charge distribution from population analyses (Bader)	Charge distribution
	EDDM	Excited state character
Spectroscopic properties	Electronic excitation energies, oscillator strengths	UV/Vis absorption spectrum
	Emission wavelengths	Emission spectrum
	Resonance Raman intensities	RR spectrum
	(Hyper)polarizabilities	
	NMR shielding constants	NMR spectrum

2.2.4. *Electronic transitions*

After the characterization of an equilibrium geometry (typically in the electronic ground state), one can calculate excited states. The first step to characterize an excited state is usually the inspection of molecular orbitals. In a simplified picture, an excited state might be viewed as a transition from an occupied orbital to a virtual one (e.g. an HOMO–LUMO transition). However, in most cases, an excited state is represented by a mix of several electronic transitions – as calculated when using canonical orbitals (orbitals which are directly obtained from a SCF or DFT calculation) – and the appealing simplicity of a one-to-one assignment of an excited state with a single electronic excitation is lost. One possibility to overcome this predicament is to employ natural transition orbitals (NTOs) [170]. In this case the canonical orbitals are transformed such that the transition is described with the fewest orbital pairs possible, thus minimizing the mixing among the orbitals while still allowing one to characterize the transition as an orbital transition (e.g. $\pi^*_{\text{py-pyMe}}$ or $\pi^*_{\text{py-Ph-pyMe}}$). Alternatively, the electron density can be employed to characterize excited states. The electron density difference map (EDDM), i.e. the redistribution of electron density between ground and excited state, is an alternative to NTOs. Since EDDM is derived from electron densities, it encompasses the full electron density redistribution as a result of an excitation, unlike the characterization in terms of canonical orbitals and NTOs, which stick to the orbital representation, but do not provide the description of the excitation in terms of orbitals as the orbital-based methods do. Alternatively, electron density changes can be separated into attachment (in the excited state) and detachment (from the ground state) densities [90,171,172]. This approach facilitates the interpretation in cases of substantial spatial overlap and electron density cancellation in EDDM plots (e.g. Ref. [173]).

2.3. *Connection between experimental observables and theory*

Here we explain how experimental observables relevant in photosensitizers can be connected with the quantum chemical descriptors provided by theory. Table 1 summarizes the quantum chemical descriptors mentioned in the previous section and the corresponding experimentally accessible physical observables.

2.3.1. *Thermo- and electrochemistry*

A vibrational analysis of optimized structures is essential to validate the nature of critical points of the PES but also provide access to calculate a variety of thermochemical properties. In addition to electronic energies, it is possible to calculate enthalpies, entropies, heat capacities, zero-point vibrational energies etc., which serve to construct thermodynamic cycles, including the correction of zero-point vibration and even solvation (Scheme 5). In

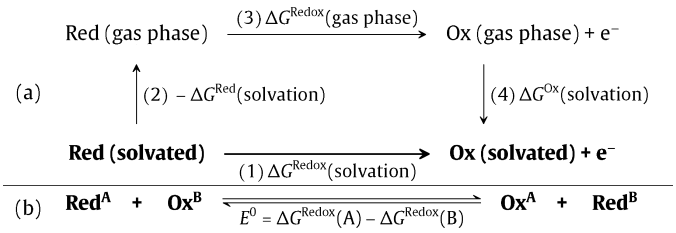
(a)
Red (gas phase)
(3) ΔG^{Redox}(gas phase)
Ox (gas phase) + e^-
(2) $-\Delta G^{\text{Red}}$(solvation)
(4) ΔG^{Ox}(solvation)
Red (solvated)
(1) ΔG^{Redox}(solvation)
Ox (solvated) + e^-
(b)
Red^A + Ox^B
$E^0 = \Delta G^{\text{Redox}}(A) - \Delta G^{\text{Redox}}(B)$
Ox^A + Red^B

Scheme 5. (Panel a) Thermodynamic cycle of a redox couple (Red → Ox + e^-). The reduction process in solution (1) can be modeled by de-solvation of the reduced species (2), formal reduction of the gas phase specimen (3), and re-solvation of the oxidized species (4). The free reaction energy (ΔG^{Redox}) is derived from the absolute energy difference between both species (Red and Ox), and the solvation free energy (ΔG(solvation)). (Panel b) Redox process between two molecules (A and B), where E^0 denotes electrochemical potential of species A vs. B ("reference").

a recent comprehensive review the advances of computational electrochemistry [174] have been highlighted, so here we only summarize the main aspects briefly. The conventional procedure to calculate the redox potential for a redox couple consists of a series of steps. First, an optimization in the gas-phase is performed for each state, followed by the calculation of the contribution of solvation based on an implicit solvent model [175,176]. This approach allows accounting easily for different solvents without the necessity of re-optimizing the geometry – a process which typically only leads to minor changes in the geometry. A more thorough but costly approach is to include explicit models [177] (vide supra). The energy difference between both states including zero-point vibration correction and solvation represents the energy required to remove or add an electron from/to the continuum. However, it is useful to reference this energy value to an experimentally known redox process, e.g. the proton/hydrogen [178,179] or ferrocene/ferrocenium [175] couple. Noteworthy, this strategy benefits from systematic error cancelation from the computational method, particularly if a similar reference couple is chosen. Hence, the effect of substitution in a series of complexes can be estimated with very good precision employing e.g. DFT [175], which is a powerful tool to estimate the redox properties of new compounds (see an example in Section 3).

2.3.2. *Spectroscopic properties*

The wavefunction of a particular state can be employed to calculate physical observables, determined either by expectation values of certain quantum chemical operators (e.g. the dipole moment) or by their derivatives with respect to an applied perturbation, such as geometry changes or applied magnetic or electric field (polarizabilities, hyperpolarizabilities etc.) [87,180]. In this review we are particularly interested in spectroscopic properties of

Please cite this article in press as: M. Jäger, et al., Coord. Chem. Rev. (2015), http://dx.doi.org/10.1016/j.ccr.2015.03.019

photosensitizers. Vibrational frequencies and normal modes can be conveniently calculated from second derivatives of the electronic energy with respect to the nuclear coordinates. IR intensities can be obtained from dipole moment derivatives, thus yielding a complete vibrational spectrum. Usually vibrational properties are computed using the harmonic approximation and anharmonicity is approximated by scaling the vibrational frequencies with an empirical factor [181]. True anharmonic calculations are also possible but computationally much more expensive and often not worth the additional expense [182]. Unlike IR calculations, the simulation of resonance Raman (RR) spectra is less commonplace. However, the interpretation of RR spectra can greatly help to unravel the early steps of excited-state dynamics of a molecule and a number of techniques are available to compute RR intensities, see e.g. Ref. [183].

One of the most important spectral regions to characterize photosensitizers is the UV/vis region, where electronic transitions take place. From excited state calculations one can obtain electronic excitation energies, intensities (oscillator strengths) and excited state characters. These properties are sufficient to reproduce an UV/vis absorption spectrum and assign each band to a particular transition or collection of them, but also allow characterizing dark states and forbidden transitions – which are not visible in experimental spectra. While in most cases it is sufficient to calculate electronic excitations only to describe excited state properties and broaden the resulting stick spectrum artificially to achieve a rough agreement with the shape of the experimental spectrum, accurate reproduction of the band shapes of absorption and emission spectra require the calculation of the vibronic bands. Several approaches have been devised for this, which can be classified as time-dependent [184], which yield the spectra from dynamics on the potential energy surface of the excited state of interest, and time-independent, which require the calculation of the Franck–Condon integrals [185] or the normal mode sampling using the Wigner distribution [186]. In each case, the computational cost increases exponentially with the number of vibrational normal modes in the molecule. Hence, calculation of larger molecules requires either an a priori choice of normal modes [187,188] or a selection of Franck–Condon integrals based on sophisticated prescreening algorithms [187,189,190] – but despite these additional measures vibronic calculations remain much more expensive than calculations of electronic excitations only. Therefore, the former are performed only if simulation of specific vibronic features of the experimental spectrum is required [191], such as vibronically induced absorption maximum shift [187,192,193] or solvent and thermal broadening effects [190,194]. Examples of such calculations include a recent study [195], where the calculated spectra served to reproduce the band shape of the low-temperature emission data, or an accurate prediction of the emission color of phosphorescent Ir(III) complexes [196].

Vertical excitation energies combined with excited state geometry optimizations allow the calculation of luminescence wavelengths. In this case, several computational scenarios are possible [53,75], depending on which geometries are used, see Scheme 6. The fluorescence wavelength can be calculated as (a) the difference between the energies of the ground state and S_1 geometry (provided fluorescence occurs from S_1) or (b) as the vertical energy from the S_1 geometry. Similarly, the phosphorescence wavelength can be calculated as the difference between the S_0 and T_1 geometries (a), or *adiabatically* using the T_1 geometry (b). Ideally, it is the case (b) that should be compared with the experiment, although in some cases, especially for phosphorescence, errors e.g. by neglecting zero point energies, could make the so-called *diabatic* energy (a) closer to the experiment.

Nuclear magnetic resonance (NMR) is a very powerful and ubiquitous analytical tool for the structural elucidation of molecules in solution. In the last years, the calculations of NMR parameters by DFT became available for organic molecules [197], including the calculation of chemical shifts [198] and coupling constants [199], which is further complemented by Boltzmann-weighted sampling of conformations to reproduce the experimental spectrum [200]. Only a few reports exist on ^{1}H NMR of ruthenium complexes, which all originate from catalytic studies of metal hydrides [201,202]. Although the ^{15}N and ^{99}Ru chemical shifts are not a common analytical tool, their NMR parameters can be computed [203]. Interestingly, the assignment of ^{1}H chemical shifts in polypyridyl-type complexes is rarely employed [204,205]. However, as will be shown below, it is a very versatile tool to probe the effect of π-stacking, which causes larger chemical shift differences.

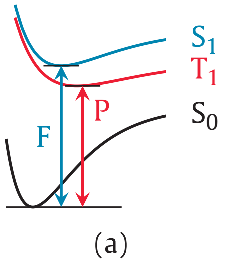

Scheme 6. *Diabatic* (a) and *adiabatic* or vertical (b) calculation of luminescence wavelengths: fluorescence (F) and phosphorescence (P), from the lowest singlet (S_1) and triplet (T_1) excited states, respectively.

2.3.3. Reaction mechanisms

The calculation of stationary properties at particular geometries of the PES is very useful in the interpretation of experimental data, e.g. the origin of luminescent states or redox properties. Very often, however, a deeper understanding of the photophysical and/or photochemical mechanism taking place in the system after irradiation, i.e. the evolution of the nuclear deformations in the active state and the relevant excited states involved, is often required to interpret experimental data. To extract such information from quantum chemical calculations in the case of photosensitizers is, not least due to the size of the molecular complexes and the difficulties implied by the presence of metal atoms, an upward challenge since years. Besides the electronic ground state equilibrium geometry, DFT is typically used to search for the lowest triplet state near the equilibrium and TD-DFT for optimizing other excited state minima. Unfortunately, the characterization of a full PES (which has 3N-6 dimensions for a molecule with N atoms) for molecules of the size of a photosensitizer is beyond reach for computational chemistry and a number of simplifications and assumptions need to be made to facilitate the interpretation of experiments. One major simplification is to choose and study the potential along a *suitable* reaction coordinate, which can be composed of several nuclear coordinates (a collective coordinate), thus reducing the complexity of the studied PES to one or few important coordinates. The optimization of transition states is a good example. It requires a suitable educated guess, which is often generated by distorting a priori known (or at least expected) reaction coordinate. In other cases it is helpful to interpolate the geometric changes between the optimized ground and excited state geometries to obtain a relaxation pathway. The so-obtained energy profiles provide a good foundation to obtain minimum energy pathways and to locate other excited transition state and minima, which may or may not lie on the arbitrarily chosen reaction coordinate(s). In addition, the relaxation from higher-lying states can yield insights into surface crossings. Surface crossings among the singlet manifold are of particular importance to describe the non-radiative decay of the excited state (assuming the initial photosensitizer is in a singlet ground state). Intersections between states of different

Please cite this article in press as: M. Jäger, et al., Coord. Chem. Rev. (2015), http://dx.doi.org/10.1016/j.ccr.2015.03.019

multiplicity can contribute to the deactivation pathway. Spin–orbit coupling (SOC) of the heavy atom (e.g. ruthenium) can initiate intersystem crossing (ISC) [75,206–208], and accordingly, the calculation of ISC rates based on static calculations has gained considerable interest in the last years [209–212]. The calculation of SOCs is possible in the ab initio frame with methods such as CASSCF/CASPT2 [213], see e.g. applications on Re [208,214], Pt [215] and Ru complexes [216,217]. Noteworthy, SOC calculations have also become possible within DFT [218,219,220], and have been applied e.g. to Ru(II) and Os(II) complexes [221], cyclometallated Ir(III) complexes [222], and Re compounds [208,214].

A more direct way to obtain an accurate description of the relevant excited state processes in a photosensitizer is to perform dynamical simulations. This is particularly needed to rationalize dynamical processes, e.g. photo-induced ligand dissociation [204,223,224], rearrangements [225], and relaxation pathways via higher-lying excited states [47,226–228]. Unlike static calculations, dynamics allows directly following the evolution of a nuclear geometry after photoexcitation. One advantage of such simulations is that they can provide not only the actual deactivation pathway, but also quantum yields and time scales. Surface-hopping ab initio molecular dynamics [229–233] is particularly well suited for the study of excited state processes in systems with many degrees of freedom. In surface-hopping dynamics simulations, the nuclei move classically in the field created by electrons in the ground or excited electronic state: this field is calculated quantum mechanically at every time step. Additionally, at each time step the system may hop from one electronic state to the other, with a probability that depends on the coupling between the initial and the final state. So far, surface-hopping dynamics has been extensively employed to explain ultrafast processes in organic molecules [231,234,235], but its usage for transition metal complexes, e.g. [Ru(bpy)$_3$]$^{2+}$ [236,237], has been limited so far, mainly due to the high computational cost of the underlying quantum chemical calculations for large molecules and the inability to incorporate spin–orbit couplings, necessary to describe ISC. Recently, Richter and coworkers [238] have implemented a general surface-hopping method which allows internal conversion and intersystem crossing. Therefore, it is expected that the number of dynamical studies, especially those involving transition metal complexes, will increase in the following years.

3. A case study: [Ru(dqp)$_2$]$^{2+}$ photosensitizers with directional charge-transfer character

In this section, we analyze the peripheral modification of the ligand framework by strong electron-accepting groups employing computational methods, illustrating in a *tutorial* manner most of the concepts introduced in Section 2. Specifically, we focus on the family of [Ru(dqp)$_2$]$^{2+}$ complexes. Based on detailed experimental and theoretical studies of [Ru(dqp)$_2$]$^{2+}$ by Hammarström and Persson [33,48,226,227,239], two modified structures will be proposed and then subsequently investigated by DFT and TD-DFT calculations. Special attention will be paid to the role of dispersion to obtain adequate geometries. Subsequently, the key properties for the hypothesized charge-transfer enhanced complexes are derived. The aim of this section is to illustrate how modern computational chemistry can be used in conjunction with experimental data to promote rational design of photosensitizers.

We selected the family of [Ru^{II}(dqp)$_2$] complexes (Fig. 1) because they fulfill many of the general requirements for an ideal photosensitizer, in particular a pronounced (photo)-stability, long excited state lifetimes, and synthetic versatility. Due to the symmetry of the complex, functionalization at the central pyridine rings is particular attractive to maximize the spatial separation of redox-active units. Previous theoretical explorations by Persson and coworkers [226,227,239] revealed that the relaxed triplet excited state is best described as ^{3}MLCT where the spin density mainly resides on the d-Ruthenium (hole) and a quinoline unit (electron). TD-DFT calculations showed that the optical transitions in the visible light region are primarily of ^{1}MLCT character involving the entire ligand orbitals. In molecular electron transfer assemblies (dyads, triads, etc.), the electron donor and acceptor units are attached in the *para*-position of the heterocycle, mainly due to the strong electronic (mesomeric) effect and the established synthetic routes. In case of the [Ru(dqp)$_2$]$^{2+}$ family, the modification in the 4-position of the central pyridine is particularly attractive, because it breaks the degeneracy of the lowest ^{3}MLCT state (note the four equivalent quinoline units) and thereby localizes the (new) ^{3}MLCT state on *one* subunit. In order to utilize the ^{3}MLCT localization effectively in secondary electron transfer steps, any electron-accepting unit should be attached to the same ligand. Thereby, the electron transfer distance is ensured to be minimal, which results commonly in fast electron transfer rates and consequently to enhanced quantum efficiency. The desired *directional charge transfer character* involves the localization of both the (low energy) absorptions and the relaxed triplet excited state toward the acceptor attached at the pyridine. Hence, the pyridine's π* orbital energy of **1** (the parent system) must be lowered by substitution, e.g. by a strongly withdrawing methyl pyridinium group. In doing so, a formal viologen subunit is formed (**2**) – a widely employed electron acceptor. The degree of conjugation can be modulated by a phenylene spacer (**3**). The compounds **2** and **3** are readily prepared by methylation using methyl iodide from of the pyridine-equipped complexes, followed by anion exchange. The NMR and MS analysis confirmed the purity and identity (see Section 5).

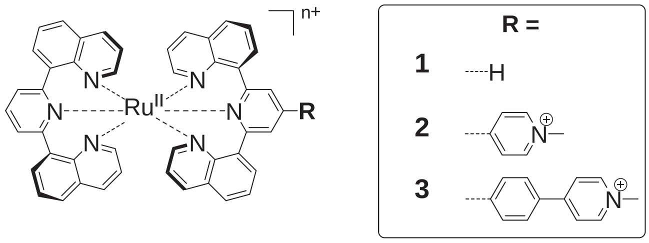

Fig. 1. Family of [Ru^{II}(dqp)$_2$] complexes considered in this work.

3.1. Molecular geometry

The detailed studies of complex **1** by Persson and coworkers focused on the structural features of the coordination site, i.e. Ru—N bond distances and N—Ru—N bond angles [48,226,227,239]. Table 2 shows comparison of these relevant parameters obtained for the parent complex **1** with standard B3LYP, with Grimme's dispersion (D3) correction for B3LYP and the range-separated CAM-B3LYP functional, and with the also dispersion corrected ωB97xD functional, all in the presence of acetonitrile (see Section 5). In general and regardless of the functional employed, the calculated Ru—N distances and N—Ru—N angles are in reasonably good agreement with the experimental data from X-ray analysis, except for a well-known overestimation [240] of the Ru—N bond by approx. 0.04–0.05 Å. A closer look at the geometries reveals that the inclusion of dispersion is critical to adequately describe the spatial stacking and therefore properties of the quinoline π-systems. Despite the known difficulties to unambiguously define "π-stacking", the atomic C5—C5′ distance serves as a measure of the spatial stacking between two quinoline units (Table 2). Nevertheless this value serves as an upper bound: large deviations of the B3LYP values from the experimental value by up to 1 Å can be observed. The basis set and/or implicit

Please cite this article in press as: M. Jäger, et al., Coord. Chem. Rev. (2015), http://dx.doi.org/10.1016/j.ccr.2015.03.019

Table 2
Structural data of **1** from X-ray crystal analysis, previous reports and this work (see Fig. 2 for labeling).

	X-ray (Ref. [48])	Ref. [48] [a]	Refs. [227,239] [b]	B3LYP* [c]	B3LYP[d]	B3LYP-D3[e]	CAM-B3LYP-D3[f]	ωB97xD[g]
Ru—N^B	2.025	2.081	2.085	2.091	2.080	2.060	2.061	2.063
Ru—N^A	2.077	2.114	2.120	2.131	2.117	2.101	2.101	2.108
N^A—Ru—N^B	88.9	89.8	89.5	89.3	89.5	89.4	89.3	90.8
N^A—Ru—$N^{A'}$	92.1	92.7	93.0	92.6	92.6	91.7	91.9	88.1
N^A—Ru—N^C	177.6	179.6	179.0	178.5	178.9	178.9	178.7	178.4
N^B—Ru—$N^{B'}$	176.3	180.0	180.0	180.0	180.0	180.0	180.0	180.0
C5—C5′ [h]	3.462	4.589	4.620	4.443	4.442	3.728	3.755	3.674
RMSD to X-ray[i]	–	0.351	0.356	0.305	0.306	0.192	0.188	0.191

[a] B3LYP/LANL2DZ/6-31g(d,p) EtOH from Ref. [48].
[b] B3LYP/SDD/6-31G(d,p) EtOH from Refs. [227,239].
[c] B3LYP/LANL2DZ/6-31G(d) MeCN.
[d] B3LYP/SDD/6-31g(d) MeCN.
[e] B3LYP-D3/SDD/6-31G(d) MeCN.
[f] CAM-B3LYP-D3/SDD/6-31G(d) MeCN.
[g] ωB97xD/SDD/6-31G(d) MeCN.
[h] As a representative of the π–π distance of the stacked quinoline units, see Fig. 2a.
[i] RMSD to the X-ray structure.

solvent show only a marginal influence on all the different B3LYP-calculated structures, but a dramatic change upon inclusion of dispersion corrections. Indeed, the B3LYP functional is known to insufficiently account for dispersion (e.g. in DNA) [110]. The dispersion correction significantly improves the errors in the energy and consequently the associated geometry at low computational cost [110], as it can be seen from the values obtained from ωB97xD, B3LYP-D3 and CAM-B3LYP-D3. In all cases, the C5—C5′ distance is decreased by 0.7 Å. This dramatic difference can also be seen in Fig. 2, where the X-ray structure of complex **1** and the structures calculated with B3LYP and B3LYP-D3 are shown: the B3LYP structure (panel b) shows the adjacent quinolines stacked at a significant angle, while in the dispersion-corrected structure (panel c) the quinoline arrangement is more flat and closer to the X-ray structure (panel d). Additionally, the inclusion of dispersion also shortens the Ru—N bonds slightly [240], thereby decreasing the deviation to the experimental values by 0.03 Å, whereas the N—Ru—N angles are unaffected.

Another way to compare the geometries optimized with different functionals is to calculate the root mean square deviation (RMSD). In order to minimize the RMSD, it should be calculated after superimposing two geometries in the same orientation, e.g. according to the Kabsch algorithm [241]. The obtained RMSDs with respect to the X-ray structure are provided in Table 2. All dispersion-corrected functionals (B3LYP-D3, CAM-B3LYP-D3 and ωB97xD) show RMSDs smaller than 0.20 Å, whereas non-dispersion corrected functionals show a much larger RMSD. Therefore, dispersion-corrected functionals yield structures which are much closer to the X-ray structure than those without dispersion correction. Note that as long as the dispersion correction is present, the differences in geometries between different functionals are negligible. However, the dispersion correction is only important when π-stacking is present. For instance, if one considers $Ru[(tpy)_2]^{2+}$, a complex which does not show intramolecular π-stacking, the RMSD between the B3LYP-D3 and the B3LYP structure is only 0.036 Å, in contrast to 0.235 Å for **1**. Therefore, based on our experience one would expect the complexes with π-stacking to profit the most from employing dispersion correction for the geometry optimization.

Nuclear magnetic resonance (NMR) is a powerful analytical tool to study molecular arrangements in solution, particularly proton chemical shifts are very sensitive to π-stacking, because the π-electrons cause an up-field shift of the protons above and below the plane. Accordingly, proton chemical shifts have been calculated from the optimized structures of **1** with B3LYP and with the dispersion corrected B3LYP-D3 structure and a sufficiently large basis set [197,198] and contrasted with the experiment. The plot of the calculated vs. the assigned experimental values follows a linear dependence (Fig. 3, left). In the non-dispersion-corrected structure H^4 and H^7 shifts (cf. Fig. 3a for numbering) are two distinct outliers, whereas in the dispersion corrected structure, after a strong up-field shift of −0.35 ppm and −0.32 ppm respectively, they agree better with experimental values.

The up-field shift of the H^4 and H^7 protons in the dispersion-corrected structure agrees with the shorter distance between the quinoline units in the dispersion-corrected structure (Fig. 3, panel b vs. c). Concomitantly, these protons are positioned above the complimentary ring system (Fig. 3, panel d), and thus experience a stronger shielding effect by the π-electron clouds. As described above, the nearest-neighbor atomic distance between the ring system describes the stacking (vide supra). Indeed, the distance of H^4 and H^7 to the nearest carbon atoms (C^3 and C^7, respectively) decrease considerably.

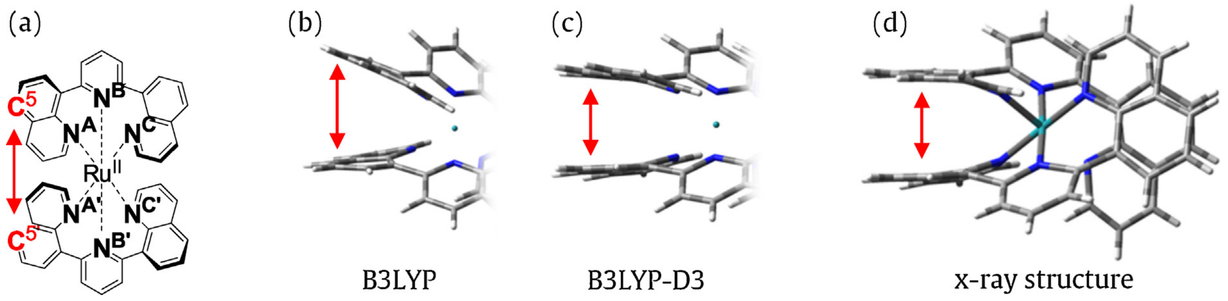

Fig. 2. Chemical structure of **1** (panel a) and optimized ground state geometries (partial representation) using B3LYP (panel b) and B3LYP-D3 (panel c). Solid state structure from X-ray analysis (panel d). Arrows indicate C5—C5′ distance as a measure for π–π stacking.

Please cite this article in press as: M. Jäger, et al., Coord. Chem. Rev. (2015), http://dx.doi.org/10.1016/j.ccr.2015.03.019

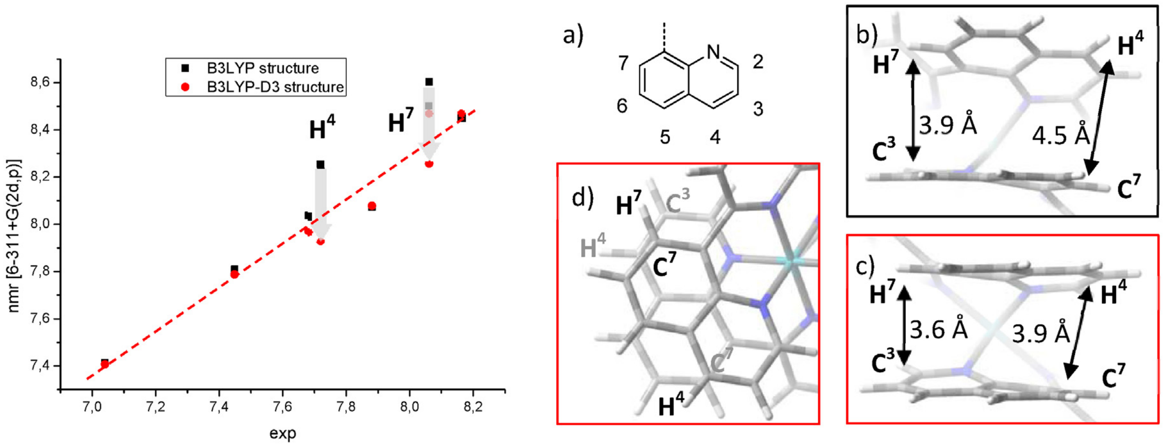

Fig. 3. (Left) Plot of calculated vs. experimental chemical shifts of **1** using the non-corrected (black) and dispersion-corrected (red) structure. Vertical arrows indicate substantial chemical shift differences. (Right side) Numbering scheme of quinolines (a), side-view of two stacked quinolines for B3LYP and B3LYP-D3 structures (b and c, respectively) and top-view of the dispersion-corrected structure (d).

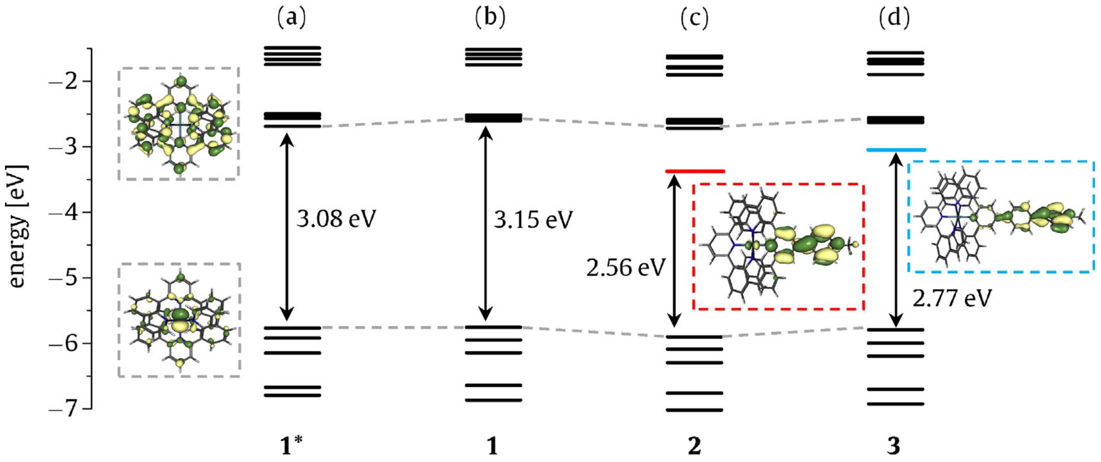

Fig. 4. Kohn–Sham orbital energies of **1** in the B3LYP (a) and B3LYP-D3 structure (b), and B3LYP-D3 structures of **2** (c) and **3** (d).

In summary, DFT can predict molecular structures of photosensitizers which agree well with the experimental data – both crystal structures and NMR spectra. Employment of Grimme's D3 dispersion also significantly improves the quality of the calculated structures, especially in those where π stacking is involved.

3.2. Molecular orbitals

Molecular orbitals (MOs), in particular the frontier orbitals – the highest occupied MO (HOMO) and the lowest unoccupied MO (LUMO) – constitute the simplest basis to elucidate the electronic structure. The vast majority of literature reports use the DFT-derived canonical MOs to assign the nature of the orbital, i.e. as metal-centered, ligand-based, and/or mixtures thereof. The frontier MO orbitals of the complexes **1**, **2**, and **3** are depicted in Fig. 4. In case of complex **1**, similar frontier molecular orbital are found for the non-corrected (a) and the dispersion-corrected geometry (b). The first three HOMOs are metal-based (d_{xy}, d_{yz}, and d_{xz}), while the LUMOs are ligand based (π^*_{dqp}). The HOMOs are virtually identical in energy, while the three LUMOs display a slightly smaller energetic splitting in case of the dispersion-corrected structure. The substituted complexes **2** and **3** exhibit comparable frontier orbitals of the $[Ru^{II}(dqp)_2]$-core with respect to energy and nature of the MO, but the new LUMO is composed of the central pyridine and attached withdrawing group, i.e. $\pi^*_{py-pyMe}$ (c) and $\pi^*_{py-Ph-pyMe}$ (d). Interestingly, the HOMO–LUMO gap is decreased to 2.56 eV (**2**) and 2.77 eV (**3**), respectively, with respect to 3.15 eV (**1**).

The spin density for the oxidized ($\mathbf{1}^+$) and reduced state ($\mathbf{1}^-$) qualitatively resembles the depopulation of the HOMO and population of the LUMO, respectively (cf. Fig. 5).

3.3. Thermochemistry

The influence of the dispersion correction on the thermochemical properties of the functionalized complexes (**2** and **3**) was investigated (Table 3). The formal electrochemical potential of a redox process was calculated from the energetic difference between both states, and referenced vs. the parental complex

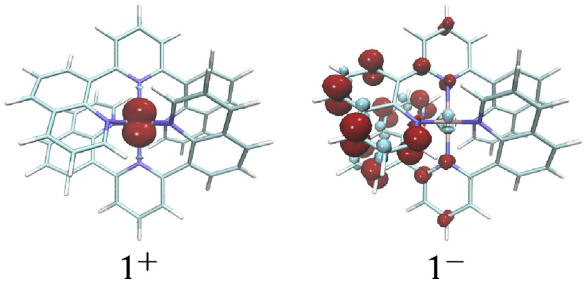

Fig. 5. Spin densities for the oxidized (1^+) and reduced (1^-) state of **1**.

Table 3
Redox properties of complexes **1**–**3**: experimental redox potential (entry 1) and effect of substituent by relative shifts of the oxidation[b] and reduction[c] potentials (entries 2–4).

Entry		Complex **1**		Complex **2**		Complex **3**	
		Ox	Red	Ox	Red	Ox	Red
1	E_exp[a]	0.71	−1.73	0.75	−1.15	+0.69	−1.42[c]
2	ΔE_exp (vs. **1**)	±0[b]	±0[c]	+0.04[b]	+0.58[c]	−0.02[b]	+0.31[c]
3	ΔE_B3LYP (vs. **1**)	±0[b]	±0[c]	+0.13[b]	+0.90[c]	+0.03[b]	+0.58[c]
4	ΔE_B3LYP-D3 (vs. **1**)	±0[b]	±0[c]	+0.13[b]	+0.74[c]	+0.03[b]	+0.42[c]

[a] In MeCN vs $Fc^{0/+}$.
[b] Referenced vs. **1**(ox).
[c] Referenced vs. **1**(red).

1 for systematic error cancelation (vide supra). Hence, the calculated/observed shifts reveal the effect of the substituent on the electrochemical potential. For example, the experimentally observed reduction of **2** is shifted by +0.58 V against the absolute value of **1** (−1.73 V). In general, the calculated values agree qualitatively with the experimental data (Table 3), however, the influence of the substituent is significantly overestimated. The reduction process calculated for the B3LYP structure, which involves the formal occupation of quinoline-centered MOs, shows the largest overestimation (+0.90 V). In the case of the B3LYP-D3 structures, this effect decreases considerably and is directly related to the improved geometry. The remaining difference for the reduction process is attributed to an artificial stabilization of delocalized states, which causes a milder formal potential required to add the electron.

3.4. Photochemistry

3.4.1. Characterization of singlet states

Table 4a lists excitation energies, oscillator strengths and state characters of the 15 lowest singlet excited states of **1** computed at the TD-B3LYP level of theory using both the B3LYP and B3LYP-D3 optimized geometries. The associated orbitals are listed in Fig. 6. The resulting states are MLCT transitions from Ru d orbitals to the π^* orbitals of the dqp ligand. In order to distinguish the different π^* orbitals, subscripts are used to label the localization of the orbital. Accordingly, the lower excited states (S_1 to S_{12}) are mainly transitions to π^* orbitals delocalized over the quinoline moieties ($d \rightarrow \pi^*_q$), occasionally with pyridine contribution ($d \rightarrow \pi^*_{q,py}$), while the higher ones (S_{13} to S_{15}) involve π^* orbitals localized almost exclusively on the pyridine part of the ligand, without quinoline contributions ($d \rightarrow \pi^*_{py}$). Since the inclusion of dispersion affects the quinoline moieties, one would expect subtle differences in the performance of B3LYP on both geometries. Indeed, the order of the lowest nine states is markedly different for B3LYP, as compared with B3LYP-D3. This is because the states up to S_{12} show strong deviations of 0.02–0.14 eV, while the higher-lying excited states have a maximum deviation of 0.01 eV in the excitation energies. As a consequence, the S_6 state, for example, predicted bright on the B3LYP-D3 geometry, becomes dark with B3LYP. Instead, the S_2 state is bright when the non-dispersion-corrected B3LYP geometry is used. This dramatic effect directly correlates with the π stacking of quinolines and emphasizes how important is to describe the geometries correctly, in this case employing dispersion corrections.

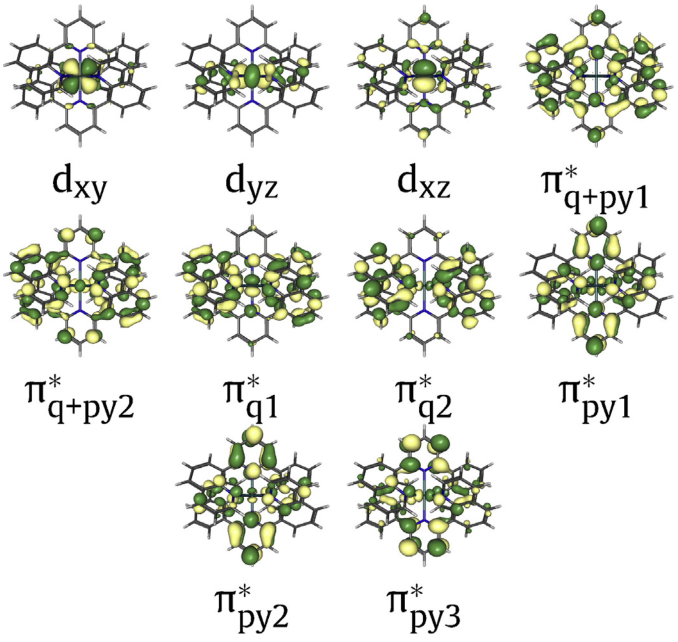

Fig. 6. Canonical orbitals of complex **1**, obtained with TD-B3LYP//B3LYP-D3.

CAM-B3LYP//B3LYP-D3 has been also employed for comparison. As Table 4a shows, CAM-B3LYP retains the characters of the first 15 excited states, but blue-shifts them by 0.81 eV on average. Despite the prominent charge-transfer character of the excited states, B3LYP excitation energies do not show a pronounced underestimation of the excitation energies and agree well with the experimental absorption spectrum of **1** (cf. Fig. 8). In contrast, CAM-B3LYP overestimates the excitation energies significantly, as reported for other polypyridyl complexes [242,243]. In view of these results, the B3LYP functional together with the dispersion-corrected geometry will be used to compute the spectra of complexes **2** and **3**.

The states of Table 4a have been briefly discussed in terms of canonical MOs. This is certainly the most common way to characterize an excited state. However, in cases like the present one, with mixing of transitions, the interpretation of the character of a particular state can be complicated. As explained in the previous section, the nature of the electronic transitions can be visualized using different excited state orbital representations, namely, using canonical MOs, NTOs and EDDMs, as mentioned in Section 2.2.4. Fig. 7 shows, exemplarily the S_1 excited state of the photosensitizer **1** in the three different ways. The canonical orbitals are displayed in panel (a). In this particular case, the state is described by two main contributions with coefficients 0.67 (90%) and −0.21 (10%). Although in both a metal d → ligand π^* character can be immediately recognized, the state is a mixture of two different d to different π^* orbital transitions. NTOs (Fig. 7b) employ an orbital transformation that maximizes the coefficient of the dominant transition pair: unlike in the basis of canonical orbitals, the coefficients of other orbital pairs contributing to the transition are much less than that of the dominant one. This way the transition description is compacted into predominantly one orbital pair, while still preserving the MO information of a transition. This is advantageous in case of strong mixing in the canonical MO basis, since NTOs provide then a familiar concept for a chemist. Here this is exactly the case and with the help of NTOs it is possible to clearly identify the

Table 4a
Excited states of **1** at calculated with TD-B3LYP using the B3LYP and B3LYP-D3 geometries, denoted as TD-B3LYP//B3LYP and TD-B3LYP//B3LYP-D3, respectively. Excitation energies ΔE, oscillator strength f, and character of the electronic transition is provided. $\Delta\Delta E$ is the difference between TD-B3LYP excitation energies calculated with and without dispersion correction.

State[b]	TD-B3LYP//B3LYP-D3			TD-B3LYP//B3LYP			$\Delta\Delta E$/eV	Character EDDM
	ΔE/eV	f	Character (canonical orb.)	ΔE/eV	f	Character (canonical orb.)		
S_1 (S_3)	2.43(3.20)[a]	0.0342	0.44 $d_{xz} \rightarrow \pi^*_{q+py2}$ 0.04 $d_{yz} \rightarrow \pi^*_{q+py2}$	2.51	0.0254	0.43 $d_{xz} \rightarrow \pi^*_{q+py2}$	0.07	$d \rightarrow \pi^*_{q+py}$
S_2 (S_1)	2.48(3.26)	0.0398	0.48 $d_{xz} \rightarrow \pi^*_{q+py1}$	2.41	0.0380	0.49 $d_{xz} \rightarrow \pi^*_{q+py1}$	−0.07	$d \rightarrow \pi^*_{q+py}$
S_3 (S_5)	2.52(3.29)	0	0.17 $d_{yz} \rightarrow \pi^*_{q+py2}$ 0.31 $d_{xz} \rightarrow \pi^*_{q1}$	2.58	0	0.30 $d_{yz} \rightarrow \pi^*_{q+py2}$ 0.17 $d_{xz} \rightarrow \pi^*_{q1}$	0.05	$d \rightarrow \pi^*_{q+py}$
S_4	2.53(3.21)	0.0184	0.44 $d_{xz} \rightarrow \pi^*_{q2}$	2.55	0.0768	0.22 $d_{yz} \rightarrow \pi^*_{q+py1}$ 0.27 $d_{xz} \rightarrow \pi^*_{q2}$	0.02	$d \rightarrow \pi^*_{q}$
S_5 (S_6)	2.59(3.32)	0.0762	0.41 $d_{yz} \rightarrow \pi^*_{q1}$	2.62	0.0801	0.38 $d_{yz} \rightarrow \pi^*_{q1}$	0.03	$d \rightarrow \pi^*_{q}$
S_6 (S_2)	2.64(3.47)	0.0474	0.44 $d_{yz} \rightarrow \pi^*_{q+py1}$	2.50	0.0005	0.22 $d_{yz} \rightarrow \pi^*_{q+py1}$ 0.27 $d_{xz} \rightarrow \pi^*_{q2}$	0.14	$d \rightarrow \pi^*_{q+py}$
S_7	2.66(4.07)	0.0072	0.42 $d_{yz} \rightarrow \pi^*_{q2}$	2.63	0.0060	0.46 $d_{yz} \rightarrow \pi^*_{q2}$	0.03	$d \rightarrow \pi^*_{q}$
S_8 (S_9)	2.73(3.53)	0.0001	0.45 $d_{xy} \rightarrow \pi^*_{q1}$	2.78	0.0006	0.48 $d_{xy} \rightarrow \pi^*_{q1}$	0.05	$d \rightarrow \pi^*_{q}$
S_9 (S_8)	2.74(3.69)	0	0.34 $d_{xy} \rightarrow \pi^*_{q+py1}$ 0.13 $d_{yz} \rightarrow \pi^*_{q+py2}$	2.69	0	0.43 $d_{xy} \rightarrow \pi^*_{q+py1}$ 0.06 $d_{yz} \rightarrow \pi^*_{q+py2}$	−0.05	$d \rightarrow \pi^*_{q+py}$
S_{10}	2.78	0.0103	0.47 $d_{xy} \rightarrow \pi^*_{q+py2}$	2.84	0.0097	0.48 $d_{xy} \rightarrow \pi^*_{q+py2}$	0.06	$d \rightarrow \pi^*_{q+py}$
S_{11}	2.89(3.59)	0.1051	0.44 $d_{xy} \rightarrow \pi^*_{q2}$	2.86	0.0928	0.44 $d_{xy} \rightarrow \pi^*_{q2}$ 0.04 $d_{yz} \rightarrow \pi^*_{q1}$	−0.03	$d \rightarrow \pi^*_{q}$
S_{12}	2.90(3.61)	0	0.15 $d_{xy} \rightarrow \pi^*_{q+py1}$ 0.18 $d_{yz} \rightarrow \pi^*_{q+py2}$ 0.12 $d_{xz} \rightarrow \pi^*_{q1}$	2.89	0	0.05 $d_{xy} \rightarrow \pi^*_{q+py1}$ 0.24 $d_{yz} \rightarrow \pi^*_{q+py2}$ 0.16 $d_{xz} \rightarrow \pi^*_{q1}$	−0.01	$d \rightarrow \pi^*_{q+py}$
S_{13}	3.22(4.00)	0.0241	0.47 $d_{xz} \rightarrow \pi^*_{py1}$	3.23	0.0228	0.47 $d_{xz} \rightarrow \pi^*_{py1}$	0.01	$d \rightarrow \pi^*_{py}$
S_{14}	3.32	0	0.45 $d_{xz} \rightarrow \pi^*_{py2}$	3.32	0	0.46 $d_{xz} \rightarrow \pi^*_{py2}$	0.00	$d \rightarrow \pi^*_{py}$
S_{15}	3.33(4.00)	0.0012	0.20 $d_{yz} \rightarrow \pi^*_{py1}$ 0.26 $d_{xz} \rightarrow \pi^*_{py3}$	3.32	0.0033	0.29 $d_{yz} \rightarrow \pi^*_{py1}$ 0.17 $d_{xz} \rightarrow \pi^*_{py3}$	0.01	$d \rightarrow \pi^*_{py}$

[a] Values obtained at the TD-CAM-B3LYP//B3LYP-D3 level of theory.
[b] The state numbering in parentheses corresponds to TD-B3LYP//B3LYP level of theory.

transition as predominantly $d_{xz} \rightarrow \pi^*{}_{q+py2}$. The EDDM (Fig. 7c), where electron densities are obtained by summing over the squares of all respective orbitals contributing to the particular state (weighed by the transition coefficients), is the most compacted representation of an excited state. The price to pay is that EDDMs do not allow characterizing the transition in terms of orbitals anymore and deriving an orbital picture from density difference could be somewhat difficult – as it involves an arbitrary approximation by visually inspecting the density in terms of similarity to typical orbital shapes. In our example, we may approximately assign the S_1 as a $d \rightarrow \pi^*_{q+py}$ transition by inspecting the EDDM; we cannot, however, distinguish the different d and π^* orbitals anymore, as they are mixed in the EDDM. Although chemists are more used to the concept orbitals than to electron densities, we would argue that the use of EDDMs is very convenient for visualization and from now on, all the relevant states will be represented by EDDMs.

The experimental absorption spectra of complexes **1**, **2**, and **3** are shown in Fig. 8, together with transitions calculated with B3LYP (plotted as bars) and the EDDMs of some representative electronic transitions. Table 4b lists all the electronic transitions, with corresponding oscillator strengths and assignment in terms of EDDMs (Fig. 9). Clearly, the introduction of a substituent at one of the pyridine rings in complexes **2** and **3** affects the absorption spectra, in comparison to **1**: the lowest excited states become MLCT transitions to the substituent π^* orbitals ($d \rightarrow \pi^*_{py-pyMe}$ in **2** and $d \rightarrow \pi^*_{pyMe}$

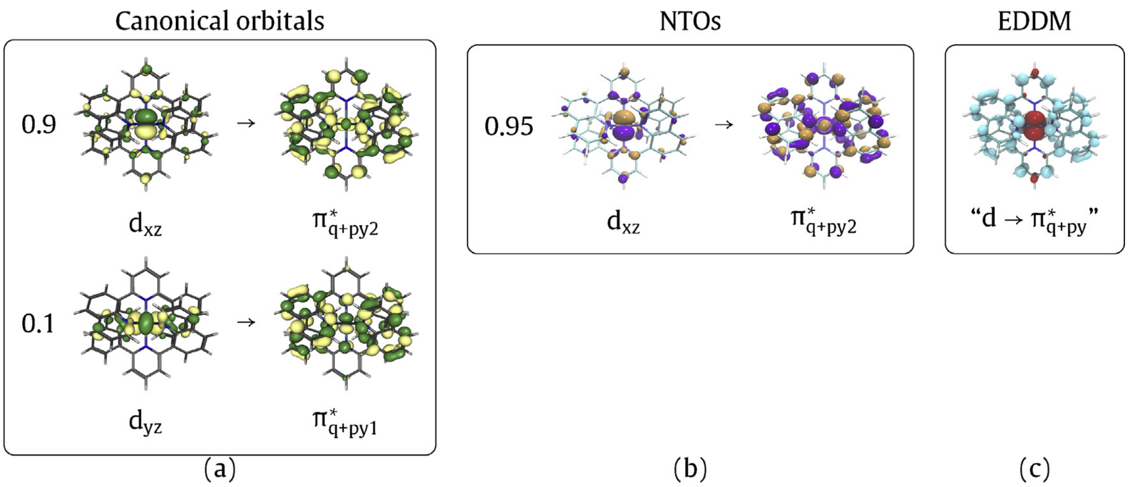

Fig. 7. Orbital representations of the character of the first excited S_1 state of complex **1**. (a) Canonical orbitals, (b) natural transition orbitals (NTOs), and (c) electron density difference map (EDDM).

Please cite this article in press as: M. Jäger, et al., Coord. Chem. Rev. (2015), http://dx.doi.org/10.1016/j.ccr.2015.03.019

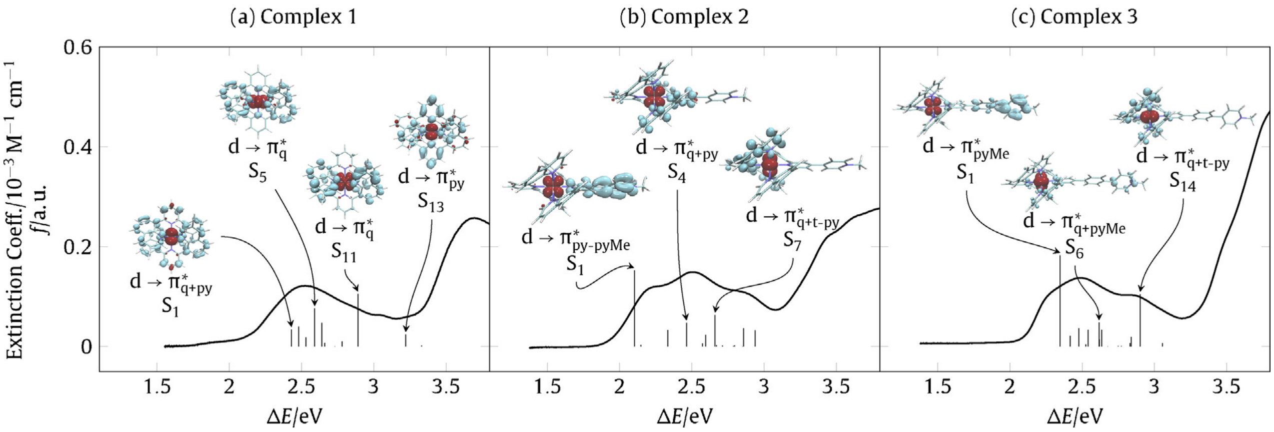

Fig. 8. Experimental absorption spectra for complexes **1**–**3** superimposed with the calculated transitions (TD-B3LYP//B3LYP-D3). The EDDMs of the most important transitions are given.

Table 4b
Excitation energies, oscillator strengths and characters of the lowest excited states of complexes **2** and **3** calculated at the TD-B3LYP level of theory.

State	Complex **2**			Complex **3**		
	ΔE/eV	f	Character (EDDM)[a]	ΔE/eV	f	Character (EDDM)[a]
S_1	2.10	0.1524	$d \rightarrow \pi^*_{py-pyMe}$	2.35	0.1827	$d \rightarrow \pi^*_{pyMe}$
S_2	2.14	0.0033	$d \rightarrow \pi^*_{py-pyMe}$	2.42	0.0209	$d \rightarrow \pi^*_{q+pyMe}$
S_3	2.33	0.0327	$d \rightarrow \pi^*_{py-pyMe}$	2.48	0.0362	$d \rightarrow \pi^*_{py-pyMe}$
S_4	2.46	0.0474	$d \rightarrow \pi^*_{q+py}$	2.53	0.0044	$d \rightarrow \pi^*_{q+py}$
S_5	2.57	0.0059	$d \rightarrow \pi^*_{q+t-py}$	2.54	0.0333	$d \rightarrow \pi^*_{q+t-py}$
S_6	2.59	0.0232	$d \rightarrow \pi^*_{q+t-py}$	2.62	0.0478	$d \rightarrow \pi^*_{q+pyMe}$
S_7	2.65	0.0631	$d \rightarrow \pi^*_{q+t-py}$	2.62	0.0143	$d \rightarrow \pi^*_{q+pyMe}$
S_8	2.66	0.0028	$d \rightarrow \pi^*_{q+py}$	2.64	0.0335	$d \rightarrow \pi^*_{q+pyMe}$
S_9	2.71	0.0014	$d \rightarrow \pi^*_{q+py+q+t-py}$	2.68	0.0003	$d \rightarrow \pi^*_{q+py+q+t-py}$
S_{10}	2.78	0.0008	$d \rightarrow \pi^*_{q+t-py}$	2.75	0.0011	$d \rightarrow \pi^*_{q+py+q+t-py+pyMe}$
S_{11}	2.79	0.0020	$d \rightarrow \pi^*_{q+t-py}$	2.77	0.0007	$d \rightarrow \pi^*_{q+py+q+t-py+pyMe}$
S_{12}	2.85	0.0002	$d \rightarrow \pi^*_{q+py+q+t-py}$	2.83	0.0067	$d \rightarrow \pi^*_{q+py+q+t-py+pyMe}$
S_{13}	2.85	0.0365	$d \rightarrow \pi^*_{q+t-py}$	2.84	0.0197	$d \rightarrow \pi^*_{q+py+q+t-py+pyMe}$
S_{14}	2.93	0.0323	$d \rightarrow \pi^*_{q+t-py}$	2.91	0.1047	$d \rightarrow \pi^*_{q+t-py}$
S_{15}	3.01	0.1577	$\pi_{t-py} \rightarrow \pi^*_{py-pyMe}$(LLCT)	3.05	0.0066	$d \rightarrow \pi^*_{q+t-py+pyMe}$

in **3**) followed by transitions delocalized on one of the quinoline moieties and either the substituted or the unsubstituted pyridine ring ($d \rightarrow \pi^*_{q+py}$ and $d \rightarrow \pi^*_{q+t-py}$, where the π^* subscript indicates whether additionally to the quinolines, the π^* orbital is delocalized onto the substituted pyridine (q + py) or the pyridine coordinated trans to the substituted one (t-py)). While lower-lying excitations to quinoline rings involve largely one of the quinolines, some of the higher-lying excitations (e.g. S_9 and S_{12} in **2** and S_{10} to S_{13} in **3**) are delocalized over both quinoline moieties (denoted with the q + py + q + t-py subscript).

Calculations involving higher excited states of complex **2** show that LLCT excitations ultimately follow the MLCT excitations mentioned above: S_{15} is the first LLCT state of this series. However, as these states absorb in the UV region which is of little importance for the photosensing activity, we will not focus on them further. Instead, one should note that the most prominent change from **1** to **2** and **3** is the appearance of the MLCT transition from Ru to the substituent – denoted as ^{3}MLCT(Ru-pyMe) – as the first excited state. This state is very bright (high oscillator strength), i.e. it will be strongly populated upon photoexcitation with visible light, and

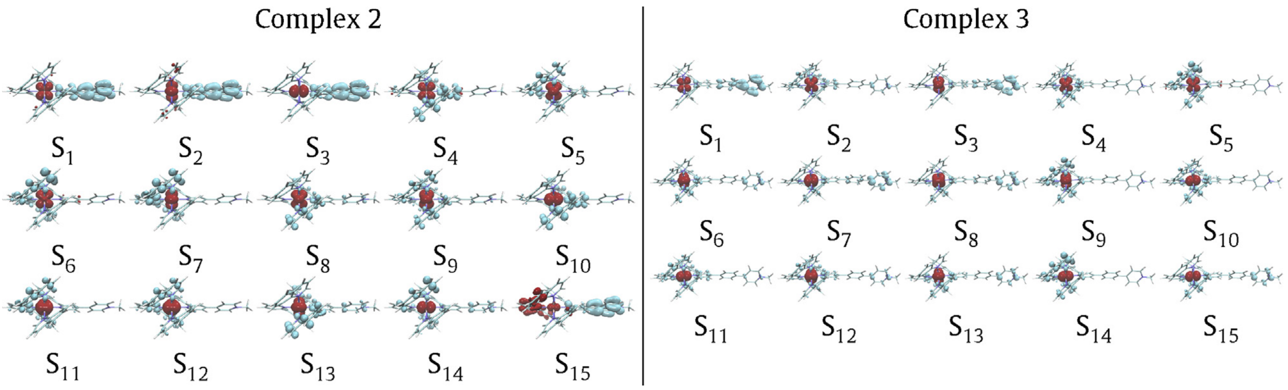

Fig. 9. EDDMs of lowest excited states in complexes **2** and **3**.

Please cite this article in press as: M. Jäger, et al., Coord. Chem. Rev. (2015), http://dx.doi.org/10.1016/j.ccr.2015.03.019

Table 5
Vertical S_0–T_n energy gaps at S_0 equilibrium geometry calculated at the TD-B3LYP level of theory. All triplets are MLCT transitions and no MC states are seen below 2.8 eV. Orbital nomenclature in **1** is as in Fig. 6, in complexes **2** and **3** as mentioned in text above and Tables 4a and 4b.

St.	Complex **1**		Complex **2**		Complex **3**	
	Character (EDDM)	Δ*E*/eV	Character (EDDM)	Δ*E*/eV	Character (EDDM)	Δ*E*/eV
T_1	$d \rightarrow \pi^*_{q1}$	2.00	$d \rightarrow \pi^*_{py-pyMe}$	1.75	$d \rightarrow \pi^*_{q+pyMe}$	1.94
T_2	$d \rightarrow \pi^*_{q+py1}$	2.11	$d \rightarrow \pi^*_{py-pyMe}$	2.04	$d \rightarrow \pi^*_{q+pyMe}$	2.09
T_3	$d \rightarrow \pi^*_{q+py2}$	2.11	$d \rightarrow \pi^*_{q}$	2.11	$d \rightarrow \pi^*_{q+pyMe}$	2.10
T_4	$d \rightarrow \pi^*_{q2}$	2.16	$d \rightarrow \pi^*_{q+pyMe}$	2.18	$d \rightarrow \pi^*_{q}$	2.16
T_5	$d \rightarrow \pi^*_{q+py2}$	2.44	$d \rightarrow \pi^*_{py-pyMe}$	2.19	$d \rightarrow \pi^*_{pyMe}$	2.32
T_6	$d \rightarrow \pi^*_{dq2}$	2.45	$d \rightarrow \pi^*_{q+pyMe}$	2.22	$d \rightarrow \pi^*_{dqp+pyMe}$	2.40
T_7	$d \rightarrow \pi^*_{q1}$	2.53	$d \rightarrow \pi^*_{py-pyMe}$	2.30	$d \rightarrow \pi^*_{q+t-py}$	2.42

features directional charge transfer from the metal to the substituent, unlike the more delocalized lowest excited states of **1**. Thus calculations show that the introduction of substituents in complex **1** leading to **2** and **3** enables directional charge transfer already at the photoexcitation.

The changes from complex **2** to **3**, on the other hand, are less significant. The excitation energies are similar (e.g. the S_1 excitation energy is 2.10 eV in **2** and 2.35 eV in **3**), the relative order of excitations (MLCT excitations to the PyMe substituent followed by excitations to the quinoline moiety) are the same, and the relative oscillator strengths as well as the overall shape of experimental absorption spectra in the visible region are fairly similar. Interestingly enough, the bright S_1 MLCT excitation to the substituent in **3** involves a π^* orbital localized primarily on the PyMe substituent and not on the phenylene spacer, so that although the spacer increases the charge separation upon excitation, it does not directly participate in important electronic transitions: also higher excited states in **3**, which show some transition density on the PyMe substituent, do not involve the spacer. This is precisely why the spectra of **2** and **3** are fairly similar.

In summary, the calculation of the absorption spectra of complexes **1**, **2** and **3** is a beautiful example of how computational chemistry can successfully explain substitution effects on photophysical properties (in this case, the absorption spectrum): Upon introduction of the PyMe substituent on one pyridine ring, the absorption spectrum gets a bright band with a pronounced directional charge transfer character that lies below other excitations, becoming the S_1 state in complexes **2** and **3**. The localization of the absorption on the PyMe substituent is nicely demonstrated using EDDMs. Interestingly, the extension of π-conjugation by the phenylene spacer (complex **3**) does not cause a further bathochromic shift but displays enhanced oscillator strength, in excellent agreement with the pronounced red-edge shoulder of the experimental MLCT band. As seen from the EDDM plots, the spacer in **3** contributes only marginally to the transition and leads to a larger spatial charge separation.

3.4.2. *Characterization of triplet states*

The utility of Ru photosensitizers for photo-induced charge transfer ultimately depends on the energy and lifetime of the lowest (relaxed) ^{3}MLCT. Therefore, one important task for the molecular design is to prevent efficient competing deactivation pathways, commonly assigned to non-radiative decay pathways involving the ^{3}MC states, which facilitate charge recombination and thus compete with the desired charge separation [28,30]. To this aim, the theoretical characterization of triplet states, which can be accessed by structural distortions occurring after excitation and/or by thermal activation, is of key importance.

Table 5 lists the electronic triplet states of complexes **1**–**3** calculated on the S_0 geometry. As one can see, the character of the lowest triplets is, in general, similar to those of the singlet excited states. Also just as the singlet states, the lowest-lying triplet states are MLCT transitions from Ru 4d orbitals into various ligand π^* orbitals; in complexes **2** and **3** the lowest-lying triplets also feature excitation to the pyMe substituent. In none of the complexes the ^{3}MC state appears among the 15 lowest calculated triplets.

Persson and coworkers explored the triplet states of several *bis*-tridentate ruthenium complexes, including **1**, by TD-DFT [226,227,239]. Their work has shown that the PES of the ^{3}MLCT state is relatively flat over an extended region of the coordinate space, allowing for large geometrical changes by thermal population. The analysis of the triplet geometries and the calculation of the transition state between the ^{3}MLCT and ^{3}MC states showed that a significant Ru—N bond elongation is required to overcome the ^{3}MLCT–^{3}MC transition. Despite the large geometrical changes required for this transition, its energy barrier is rather small (only 0.25 eV from calculations by Persson and coworkers [226,227] at the B3LYP/6-31G(d,p)/SDD level of theory without dispersion correction, which compares well to the experimental value of 0.31 eV from an Arrhenius-type analysis of kinetic data [226]), suggesting the possibility of a thermal population of the ^{3}MC state.

To gain insight into the deactivation mechanism of complexes **1**–**3**, following the spirit of Persson's work, we optimized the geometries of the ^{3}MLCT and ^{3}MC states and compared their relative energies with respect to the S_0 state at the equilibrium geometry. The ^{3}MLCT states of all complexes were first located by performing a geometry optimization starting from the optimized S_0 geometry. The character of the so-obtained states in complexes **2** and **3** differ from that of **1**: the latter has the spin density localized on the quinoline ligand (denoted as ^{3}MLCT(Ru-q) in Table 6), while states in complexes **2** and **3** have the spin density localized on the substituent (^{3}MLCT(Ru-pyMe)). An attempt to locate the minima of the ^{3}MLCT (Ru-q) states in **2** and **3** was done by starting TD-DFT optimizations from higher-lying triplets at S_0 geometry. For this aim, the lowest $d \rightarrow \pi^*_q$ states (T_3 in **2** and T_4 in **3**) were chosen (Table 5). While the TD-DFT optimization of T_3 in **2** did not yield a suitable minimum, a minimum was found for T_4 in **3**, and thus it was subjected to a subsequent B3LYP-D3 triplet geometry optimization, in order to be consistent with respect to all other located triplet minima. The latter optimization provided a ^{3}MLCT(Ru-q) minimum for **3**, which shows a similar spin density distribution as in **1** (cf. Fig. 10), and more importantly, is lower in energy than the initially obtained ^{3}MLCT(Ru-pyMe) triplet minimum (see Table 6). Additionally, ^{3}MC minima were located in all complexes by performing a triplet geometry optimization starting from the modified S_0 geometry, where Ru—N1 and Ru—N2 bonds (cf. Table 6) were extended to the reported values obtained from ^{3}MLCT(Ru-q) minimum for **1** [239]. Noteworthy, our calculations on **1** qualitatively agree well with previous work of Persson [239], while quantitative discrepancies in bond lengths in Table 6 should be attributed to the inclusion of dispersion correction.

The obtained triplet energies and geometries allow us to compare deactivation pathways for the complexes **1**–**3**. Table 6 lists

Table 6
Selected Ru—N bond lengths in optimized triplet states of complexes **1**–**3**. N1 and N2 indicate the nitrogens of the quinoline moieties of the unsubstituted dqp ligand. $\Delta E_{diab,S_0}$ is the diabatic energy difference to the S_0 state, including zero-point energy correction.

	^{3}MLCT(Ru-q)[c]			^{3}MC			^{3}MLCT (Ru-pyMe)[c]		
	Ru-N1	Ru-N2	$\Delta E_{diab,S_0}$/eV	Ru-N1	Ru-N2	$\Delta E_{diab,S_0}$/eV	Ru-N1	Ru-N2	$\Delta E_{diab,S_0}$/eV
1[a,d]	2.170[a]	2.077[a]	1.99[d]	2.505[a]	2.166[a]	1.96[d]	–	–	–
1	2.151	2.080	1.80	2.535	2.152	1.85	–	–	–
2	–[b]	–[b]	–[b]	2.535	2.129	1.89	2.104	2.033	1.47
3	2.152	2.078	1.80	2.535	2.150	1.85	2.104	2.083	2.02

[a] Taken from Ref. [239] (Supporting information).
[b] Not found.
[c] Spin localization of triplet state given in parenthesis.
[d] From Ref. [226], no zero-point energy correction.

Ru—N1 and Ru—N2 bond lengths and relative energies to the equilibrium S_0 geometry ($\Delta E_{diab,S_0}$) in all the obtained triplet minima. All ^{3}MC states show similar Ru—N1 and Ru—N2 bond lengths, which are significantly elongated compared to ^{3}MLCT minima in the respective complexes. Furthermore, all ^{3}MC states show almost identical energies, which can be rationalized by the presence of similar Ru—N1 and Ru—N2 bond lengths yielding similar ligand field splitting of Ru d orbitals. Additionally, the ^{3}MLCT(Ru-q) state in complexes **1** and **3** shows also similar Ru—N1 and Ru—N2 bond lengths and energies (both to the corresponding ^{3}MC state and to each other): this suggests a likely thermal population of the ^{3}MC state in **3** just as in **1**. On the other hand, in **2** the ^{3}MLCT(Ru-pyMe) state is located 0.42 eV lower than the ^{3}MC state, rendering the deactivation pathway via the ^{3}MC state less likely. This suggests that **1** and **3** have similar deactivation pathways, while in **2** the presence of the low-lying ^{3}MLCT(Ru-pyMe) state changes the mechanistic picture.

This difference in the photodeactivation pathways is also confirmed experimentally: while **1** and **3** show considerable phosphorescence, **2** shows none. This difference in the phosphorescence in **1** and **3** vs. **2** can also be rationalized by theory. The deactivation mechanism of these complexes is a subtle interplay of the radiative and nonradiative relaxation pathways, which have different time constants: k_r and k_{nr}, respectively. The ratio of these time constants determines the phosphorescence quantum yield: $\Phi = k_r/(k_r + k_{nr})$. The non-radiative k_{nr} can be estimated from the adiabatic energy gap between the ground and the triplet excited state, $\Delta E_{T_1 \to S_0}$ (not to be confused with the diabatic gap $\Delta E_{diab,S_0}$ from Table 6) as [217,244] $k_{nr(T1 \to S0)} \sim \exp(\beta \Delta E_{T_1 \to S_0})$, where β is a parameter that describes structural distortions between the S_0 equilibrium and the T_1 relaxed geometry. According to this expression, a smaller S_0 and T_1 energy gap means a larger non-radiative decay rate and thus a lower phosphorescence quantum yield. Additionally, k_{nr} increases with larger structural distortions [217]. The adiabatic S_0–T_1 energy gap were obtained from TD-DFT calculations at optimized geometries of the T_1 state (^{3}MLCT(Ru-q) in **1** and **3**, ^{3}MLCT(Ru-pyMe) in **2**), and the β parameter can be estimated from comparing RMSD of the S_0 and T_1 geometries of each complex.

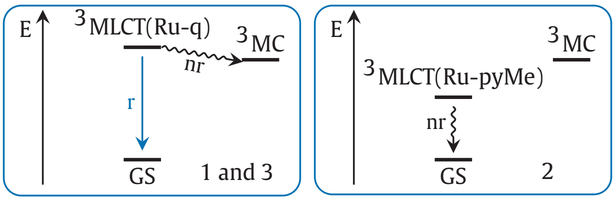

Scheme 7. Deactivation mechanism for the complexes **1**, **2** and **3**. The labels r and nr stand for radiative and non-radiative processes, respectively.

The results of these calculations are indicated in Fig. 10. The calculated S_0–T_1 gaps in complexes **1** and **3** are very similar (1.48 and 1.49 eV, respectively), in line with their similar (^{3}MLCT(Ru-q)) character but different from that in complex **2** (1.30 eV, ^{3}MLCT(Ru-pyMe)). The ^{3}MLCT(Ru-pyMe) state in **3** also shows a higher S_0–T_1 gaps of 1.61 eV. Complex **2** also shows a larger RMSD of S_0 and T_1 structures: 0.25 Å, compared to a smaller RMSD of 0.12 and 0.09 Å in complexes **1** and **3**. As a result, in complex **2** we calculated both a smaller S_0–T_1 energy gap and larger geometrical differences, which results in a larger non-radiative decay rate, and in turn leads to phosphorescence quenching, in accord with the phosphorescence observed experimentally.

Scheme 7 summarizes the suggested deactivation mechanism of the three complexes. Based on the triplet states discussion above, we can postulate that **1** and **3** show similar triplet deactivation mechanisms, including a non-radiative pathway from ^{3}MLCT(Ru-q) via the ^{3}MC state, due to the small energy difference between the ^{3}MLCT(Ru-q) and ^{3}MC minima and the low energy barrier between these states found for complex **1** in Ref. [239], as well as the radiative deactivation from the ^{3}MLCT(Ru-q) directly to the S_0 state, suggested by phosphorescence observed experimentally. Complex **2**, in contrast, is expected to exhibit the radiationless deactivation

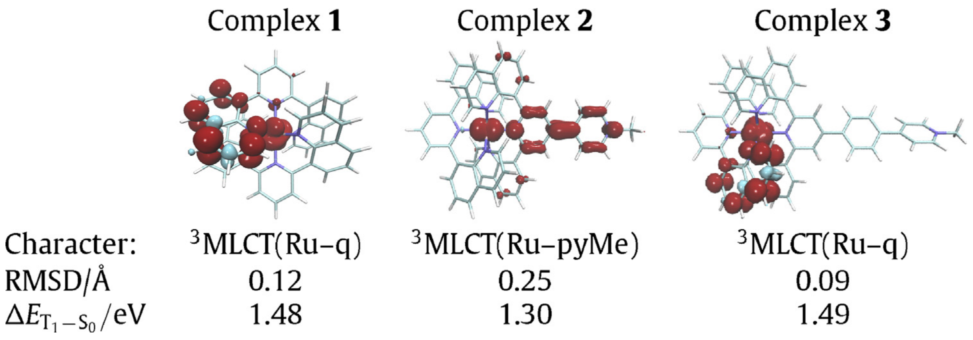

Fig. 10. Spin densities of lowest triplet state characters and S_0–T_1 energy gaps at triplet geometries for complexes **1**–**3**.

Please cite this article in press as: M. Jäger, et al., Coord. Chem. Rev. (2015), http://dx.doi.org/10.1016/j.ccr.2015.03.019

from the ^{3}MLCT(Ru-pyMe) state, but rather unlikely via the ^{3}MC state.

4. Concluding remarks

During the past years, the rapid advances in computational chemistry have led to an increasingly accurate description of Ru photosensitizers. Post-Hartree–Fock methods allow for systematic improvement, but their computational cost is quite large, which still prevents its use in large-scale applications of Ru photosensitizers. Alternatively, the availability of DFT and its TD formalism has made this technique an invaluable tool also to non-experts to describe and interpret key experimental properties of photosensitizers. Numerous functionals, basis sets and corrections thereof have been suggested, which are often optimized to reproduce a specific property with high accuracy. As such, nuclear geometries are generally reproduced satisfyingly, while the calculation of NMR chemical shifts requires larger basis sets for good accuracy. The role of additional corrections, such as solvation models and particularly proper treatment of dispersion, is also undeniable and should be taken into account to achieve accuracy comparable with experiment.

Although the quest of finding a universal functional is a prevailing challenge, DFT is still the method of choice for a large number of theoretical investigations on photosensitizers because it can provide a number of useful descriptors that aid rational design. Central to derive useful properties and calculate observables comparable with the experiment is the wavefunction, consisting of Kohn–Sham MOs. Noteworthy, MOs on their own are devoid of physical meaning and can be transformed without changing the nature of the wavefunction. Particularly useful is a transformation to natural transition orbitals (NTOs) because it aids the interpretation of an electronic transition, especially in the case of cohabitation of many canonical MOs within different electronic transitions belonging to one particular state. In contrast to MOs, the corresponding charge/spin *densities* represent physically meaningful entities, e.g., the re-distribution of an electron in an optical transition or localization of electrons (holes) after reduction (oxidation). The MO energy can also be used as a starting guess to obtain redox properties, although a thermochemical analysis from frequency calculations is more adequate to yield reliable values for redox potentials.

In this contribution, we have analyzed the geometry, electrochemical properties, and excited states of a family of $[Ru(dqp)_2]^{2+}$ photosensitizers (complexes **1**–**3**) to illustrate how theory may complement experimental data. Calculations have been used to enlighten, compare, and interpret results from NMR, X-ray diffraction, and UV–vis spectra.

Regarding structural elucidation, it was shown that dispersion effects are significant and methods that treat these correctly are necessary to obtain suitable equilibrium structures. Geometries and NMR spectra calculated with the dispersion correction yield much better agreement with their experimental counterparts.

The calculation of excited states aided at the rationalization of the different photochemical behaviors observed in these complexes experimentally. In the first place, the characterization of excited singlet states showed how the introduction of a substituent in complex **1** (complexes **2** and **3**) creates a new bright S_1 state, which is beneficial for absorption. The lowest excited singlet states of **2** and **3** are localized on the substituted pyridine unit, facilitating directional charge transfer upon photoexcitation, and remain localized upon intersystem crossing and relaxation to the triplet state. Noteworthy, such localization by *strong withdrawing* substituents also reduces the distance in subsequent electron transfer steps (if an electron acceptor is installed at the methyl group), which would allow for lower driving forces or faster transfer rates. Secondly, the different emissive behavior of the three complexes was explained using singlet-triplet energy gaps and structural distortions of the excited states. Then, exploring different triplet deactivation pathways helped to shed some light into important photosensitizer properties, such as excited state lifetimes. The exploration of potential energy surfaces (PES) with scans along several (often collective) nuclear coordinates can give a deeper insight into the actual triplet deactivation pathways, although it is computationally expensive. Here, deactivation of the ^{3}MLCT has been modeled by elongation of specific Ru—N bonds toward a structurally distorted geometry, leading to a ^{3}MC state and surface crossing with the S_0 PES. An alternative and systematic exploration of the PES is based on TD-DFT geometry optimizations, which allow locating triplet and excited singlet minima further away from the S_0 geometry. The obtained excited state minima can be employed to calculate further photochemical properties. In the present paper this is illustrated by the calculation of emission energies and rationalization of phosphorescence times.

In addition to initial charge separation, the photosensitizer efficiency is also dependent on the lifetime of the excited state. The energy levels and character of the relevant triplet states of the complexes give some insights into possible deactivation pathways of the populated lowest triplet state. Complex **2**, in addition to the lowest singlet charge-separated excited state, shows a low-lying ^{3}MLCT state of the same character which is less likely to deactivate via the ^{3}MC state than the reference complex **1**. Consequently, the excited state lifetime should be increased, whereas the lower energy gap and the resulting faster decay rate to the ground state may over-compensate the previous effect. Complex **3** with the additional phenylene spacer enables larger spatial charge-separation upon photoexcitation, and is expected to follow a similar ^{3}MC deactivation pathway as **1**.

Although extensive, the calculations presented here illustrate only a small subset of theoretical methods and property assessments that can be performed on photosensitizers to assist their design. An obvious extension to provide further insight into the photodeactivation mechanisms of photosensitizers is to perform dynamical simulations. Such calculations are still very demanding for molecules including metals and have not found wide application so far, but future advancement to decrease the computational cost will allow for a deeper exploration of photophysics and photochemistry of photosensitisers, which inarguably benefits their design.

5. Computational details and experimental

Experimental characterization. Complexes **2** and **3** were prepared quantitatively from the non-methylated analogs [245] using an excess of methyl iodide according to literature protocols [246]. Evaporation of all volatile reagents and solvent gave analytically pure compounds according to NMR, MS and UV/vis data, which will be reported elsewhere.

Computational details. Energetics of the ground, lowest triplet and ionized states and the respective geometry optimizations of complexes **1**–**3** were performed with B3LYP, both with and without Grimme's DFT-D3 dispersion correction [111] (the latter designated B3LYP-D3) and ωB97xD functionals, employing 6-31G* basis set for all atoms except Ru, for which the Stuttgart–Dresden 28-electron quasi-relativistic effective core potential (MWB28) [151] and the corresponding basis set has been employed. NMR calculations have been performed with B3LYP and B3LYP-D3 functionals and the larger 6-311G+(2d,p) basis set for non-Ru atoms; for Ru, MWB28 was employed. Energies and properties for all excited states (i.e. higher-lying singlet and triplet states) have been computed with TD-DFT with the B3LYP functional without the D3 correction, as

Please cite this article in press as: M. Jäger, et al., Coord. Chem. Rev. (2015), http://dx.doi.org/10.1016/j.ccr.2015.03.019

it does not influence the excited state energies and gradients; the 6-31G*/MWB28 basis set/ECP combination was employed. Excited state geometry optimizations (referred to as TD-DFT based optimizations) have been performed at the same level of theory. Additionally, the PCM [123] continuum model has been used to simulate acetonitrile as a solvent in all calculations. All calculations have been performed with the Gaussian 09 D.01 program package [247]. EDDM for excited states have been generated with the help of GaussSum 3.0 program package [248,249].

Acknowledgements

M.J. gratefully acknowledges the Carl Zeiss Foundation for financial support. The authors thank the COST Action CM1202, PERSPECT-H2O for collaboratory support via STSM 14852.

References

[1] J. Barber, Chem. Soc. Rev. 38 (2009) 185–196.
[2] M. Graetzel, R.A.J. Janssen, D.B. Mitzi, E.H. Sargent, Nature 488 (2012) 304–312.
[3] O. Khaselev, J.A. Turner, Science 280 (1998) 425–427.
[4] M.G. Walter, E.L. Warren, J.R. McKone, S.W. Boettcher, Q. Mi, E.A. Santori, N.S. Lewis, Chem. Rev. 110 (2010) 6446–6473.
[5] S. Ardo, G.J. Meyer, Chem. Soc. Rev. 38 (2009) 115–164.
[6] J.H. Alstrum-Acevedo, M.K. Brennaman, T.J. Meyer, Inorg. Chem. 44 (2005) 6802–6827.
[7] S. Berardi, S. Drouet, L. Francas, C. Gimbert-Surinach, M. Guttentag, C. Richmond, T. Stoll, A. Llobet, Chem. Soc. Rev. 43 (2014) 7501–7519.
[8] T. Faunce, S. Styring, M.R. Wasielewski, G.W. Brudvig, A.W. Rutherford, J. Messinger, A.F. Lee, C.L. Hill, H. deGroot, M. Fontecave, D.R. MacFarlane, B. Hankamer, D.G. Nocera, D.M. Tiede, H. Dau, W. Hillier, L. Wang, R. Amal, Energy Environ. Sci. 6 (2013) 1074–1076.
[9] D. Gust, T.A. Moore, A.L. Moore, Faraday Discuss. 155 (2012) 9–26.
[10] L.C. Sun, L. Hammarström, B. Akermark, S. Styring, Chem. Soc. Rev. 30 (2001) 36–49.
[11] C. Joachim, J.K. Gimzewski, A. Aviram, Nature 408 (2000) 541–548.
[12] K. Kalyanasundaram, M. Grätzel, Coord. Chem. Rev. 177 (1998) 347–414.
[13] L.Z. Hu, G.B. Xu, Chem. Soc. Rev. 39 (2010) 3275–3304.
[14] B.J. Coe, Coord. Chem. Rev. 257 (2013) 1438–1458.
[15] S. Bonnet, J.P. Collin, Chem. Soc. Rev. 37 (2008) 1207–1217.
[16] S. Tamba, S. Mitsuda, F. Tanaka, A. Sugie, A. Mori, Organometallics 31 (2012) 2263–2267.
[17] J. Otsuki, T. Akasaka, K. Araki, Coord. Chem. Rev. 252 (2008) 32–56.
[18] P.P. Laine, S. Campagna, F. Loiseau, Coord. Chem. Rev. 252 (2008) 2552–2571.
[19] C.K. Prier, D.A. Rankic, D.W.C. MacMillan, Chem. Rev. 113 (2013) 5322–5363.
[20] J.M.R. Narayanam, C.R.J. Stephenson, Chem. Soc. Rev. 40 (2011) 102–113.
[21] J.W. Tucker, C.R.J. Stephenson, J. Org. Chem. 77 (2012) 1617–1622.
[22] K. Zeitler, Angew. Chem. Int. Ed. 48 (2009) 9785–9789.
[23] M.R. Gill, J. Garcia-Lara, S.J. Foster, C. Smythe, G. Battaglia, J.A. Thomas, Nat. Chem. 1 (2009) 662–667.
[24] M.R. Gill, J.A. Thomas, Chem. Soc. Rev. 41 (2012) 3179–3192.
[25] N.A. Smith, P.J. Sadler, Philos. Trans. R. Soc. A: Math. Phys. Eng. Sci. 371 (2013) 20120519.
[26] S. Campagna, F. Puntoriero, F. Nastasi, G. Bergamini, V. Balzani, in: V. Balzani, S. Campagna (Eds.), Photochemistry and Photophysics of Coordination Compounds I, Springer-Verlag, Berlin, 2007, pp. 117–214.
[27] A. Juris, V. Balzani, F. Barigelletti, S. Campagna, P. Belser, A. Vonzelewsky, Coord. Chem. Rev. 84 (1988) 85–277.
[28] D.W. Thompson, A. Ito, T.J. Meyer, Pure Appl. Chem. 85 (2013) 1257–1305.
[29] J.P. Sauvage, J.P. Collin, J.C. Chambron, S. Guillerez, C. Coudret, V. Balzani, F. Barigelletti, L. Decola, L. Flamigni, Chem. Rev. 94 (1994) 993–1019.
[30] E.A. Medlycott, G.S. Hanan, Chem. Soc. Rev. 34 (2005) 133–142.
[31] P.G. Bomben, K.C.D. Robson, B.D. Koivisto, C.P. Berlinguette, Coord. Chem. Rev. 256 (2012) 1438–1450.
[32] K.C.D. Robson, B.D. Koivisto, A. Yella, B. Sporinova, M.K. Nazeeruddin, T. Baumgartner, M. Grätzel, C.P. Berlinguette, Inorg. Chem. 50 (2011) 5494–5508.
[33] M. Abrahamsson, M. Jäger, R.J. Kumar, T. Österman, P. Persson, H.-C. Becker, O. Johansson, L. Hammarström, J. Am. Chem. Soc. 130 (2008) 15533–15542.
[34] M. Maestri, N. Armaroli, V. Balzani, E.C. Constable, A.M.W.C. Thompson, Inorg. Chem. 34 (1995) 2759–2767.
[35] S. Sinn, B. Schulze, C. Friebe, D.G. Brown, M. Jaeger, J. Kuebel, B. Dietzek, C.P. Berlinguette, U.S. Schubert, Inorg. Chem. 53 (2014) 1637–1645.
[36] W.-W. Yang, L. Wang, Y.-W. Zhong, J. Yao, Organometallics 30 (2011) 2236–2240.
[37] J.A.G. Williams, Chem. Soc. Rev. 38 (2009) 1783–1801.
[38] D.G. Brown, N. Sanguantrakun, B. Schulze, U.S. Schubert, C.P. Berlinguette, J. Am. Chem. Soc. 134 (2012) 12354–12357.
[39] J. Dinda, S. Liatard, J. Chauvin, D. Jouvenot, F. Loiseau, Dalton Trans. 40 (2011) 3683–3688.
[40] V. Friese, S. Nag, J. Wang, M.-P. Santoni, A. Rodrigue-Witchel, G.S. Hanan, F. Schaper, Eur. J. Inorg. Chem. (2011) 39–44.
[41] A.R. Naziruddin, C.-L. Kuo, W.-J. Lin, W.-H. Lo, C.-S. Lee, B.-J. Sun, A.H.H. Chang, W.-S. Hwang, Organometallics 33 (2014) 2575–2582.
[42] S. Sinn, B. Schulze, C. Friebe, D.G. Brown, M. Jaeger, E. Altuntas, J. Kuebel, O. Guntner, C.P. Berlinguette, B. Dietzek, U.S. Schubert, Inorg. Chem. 53 (2014) 2083–2095.
[43] B. Schulze, D.G. Brown, K.C.D. Robson, C. Friebe, M. Jaeger, E. Birckner, C.P. Berlinguette, U.S. Schubert, Chem. Eur. J. 19 (2013) 14171–14180.
[44] L. Hammarström, O. Johansson, Coord. Chem. Rev. 254 (2010) 2546–2559.
[45] M. Abrahamsson, M.J. Lundqvist, H. Wolpher, O. Johansson, L. Eriksson, J. Bergquist, T. Rasmussen, H.-C. Becker, L. Hammarström, P.-O. Norrby, B. Åkermark, P. Persson, Inorg. Chem. 47 (2008) 3540–3548.
[46] F. Schramm, V. Meded, H. Fliegl, K. Fink, O. Fuhr, Z. Qu, W. Klopper, S. Finn, T.E. Keyes, M. Ruben, Inorg. Chem. 48 (2009) 5677–5684.
[47] A. Breivogel, M. Meister, C. Förster, F. Laquai, K. Heinze, Chem. Eur. J. 19 (2013) 13745–13760.
[48] M. Abrahamsson, M. Jäger, T. Österman, L. Eriksson, P. Persson, H.-C. Becker, O. Johansson, L. Hammarström, J. Am. Chem. Soc. 128 (2006) 12616–12617.
[49] M. Jäger, R.J. Kumar, H. Görls, J. Bergquist, O. Johansson, Inorg. Chem. 48 (2009) 3228–3238.
[50] G.A. Parada, L.A. Fredin, M.-P. Santoni, M. Jäger, R. Lomoth, L. Hammarström, O. Johansson, P. Persson, S. Ott, Inorg. Chem. 52 (2013) 5128–5137.
[51] W.R. Browne, N.M. O'Boyle, J.J. McGarvey, J.G. Vos, Chem. Soc. Rev. 34 (2005) 641–663.
[52] S. Fantacci, F. De Angelis, Coord. Chem. Rev. 255 (2011) 2704–2726.
[53] A. Vlček Jr., S. Záliš, Coord. Chem. Rev. 251 (2007) 258–287.
[54] F. Jensen, Introduction to Computational Chemistry, 2nd ed., Wiley-VCH, 2006.
[55] C.J. Cramer, Essentials of Computational Chemistry: Theories and Models, 2nd ed., Wiley-VCH, 2004.
[56] J.D. Watts, Radiat. Induc. Mol. Phenom. Nucleic Acids (2008) 65–92.
[57] J.F. Stanton, R.J. Bartlett, J. Chem. Phys. 98 (1993) 7029–7039.
[58] H.J. Monkhorst, Int. J. Quantum Chem. 12 (1977) 421–432.
[59] H. Sekino, R.J. Bartlett, Int. J. Quantum Chem. 26 (1984) 255–265.
[60] H. Nakatsuji, Chem. Phys. Lett. 67 (1979) 334–342.
[61] M. Ehara, M. Ishida, K. Toyota, H. Nakatsuji, Rev. Modern Quantum Chem. (2002) 293–319.
[62] J. Oddershede, Methods in Computational Molecular Physics, Springer, Netherlands, 1983, pp. 249–270.
[63] J. Schirmer, Phys. Rev. A 26 (1982) 2395–2416.
[64] M. Wormit, D.R. Rehn, P.H.P. Harbach, J. Wenzel, C.M. Krauter, E. Epifanovsky, A. Dreuw, Mol. Phys. 112 (2014) 774–784.
[65] A.B. Trofimov, J. Schirmer, J. Phys. B: At. Mol. Opt. Phys. 28 (1995) 2299.
[66] A.B. Trofimov, J. Schirmer, Chem. Phys. 224 (1997) 175–190.
[67] A.B. Trofimov, J. Schirmer, Chem. Phys. 214 (1997) 153–170.
[68] A.B. Trofimov, G. Stelter, J. Schirmer, J. Chem. Phys. 111 (1999) 9982–9999.
[69] A.B. Trofimov, G. Stelter, J. Schirmer, J. Chem. Phys. 117 (2002) 6402–6410.
[70] S. Knippenberg, J.H. Starcke, M. Wormit, A. Dreuw, Mol. Phys. 108 (2010) 2801–2813.
[71] L. Gagliardi, Rev. Comput. Chem. 25 (2007) 249–284.
[72] B.O. Roos, Radiat. Induc. Mol. Phenom. Nucleic Acids 5 (2008) 125–156.
[73] D. Roca-Sanjuán, F. Aquilante, R. Lindh, WIREs Comput. Mol. Sci. 2 (2012) 585–603.
[74] K. Pierloot, Theor. Comput. Chem. 16 (2005) 279–315.
[75] L. González, D. Escudero, L. Serrano-Andrés, ChemPhysChem 13 (2012) 28–51.
[76] P.A. Malmqvist, K. Pierloot, A.R.M. Shahi, C.J. Cramer, L. Gagliardi, J. Chem. Phys. 128 (2008) 204109.
[77] D. Escudero, L. González, J. Chem. Theory Comput. 8 (2012) 203–213.
[78] X. Sala, M.Z. Ertem, L. Vigara, T.K. Todorova, W. Chen, R.C. Rocha, F. Aquilante, C.J. Cramer, L. Gagliardi, A. Llobet, Angew. Chem. Int. Ed. 49 (2010) 7745–7747.
[79] N. Planas, L. Vigara, C. Cady, P. Miró, P. Huang, L. Hammarström, S. Styring, N. Leidel, H. Dau, M. Haumann, L. Gagliardi, C.J. Cramer, A. Llobet, Inorg. Chem. 50 (2011) 11134–11142.
[80] K. Pierloot, Int. J. Quantum Chem. 111 (2011) 3291–3301.
[81] K.H. Marti, M. Reiher, Z. Phys. Chem. 224 (2010) 583–599.
[82] G.K.-L. Chan, S. Sharma, in: S.R. Leone, P.S. Cremer, J.T. Groves, M.A. Johnson (Eds.), Annual Review of Physical Chemistry, vol. 62, 2011, pp. 465–481.
[83] J. Chalupsky, T.A. Rokob, Y. Kurashige, T. Yanai, E.I. Soomon, L. Rulisek, M. Srnec, J. Am. Chem. Soc. 136 (2014) 15977–15991.
[84] L. Freitag, S. Knecht, S.F. Keller, M.G. Delcey, F. Aquilante, T.B. Pedersen, R. Lindh, M. Reiher, L. González, Phys. Chem. Chem. Phys. (2015), http://dx.doi.org/10.1039/C4CP05278A
[85] T.B. Pedersen, F. Aquilante, R. Lindh, Theor. Chem. Acc. 124 (2009) 1–10.
[86] M.G. Delcey, L. Freitag, T.B. Pedersen, F. Aquilante, R. Lindh, L. González, J. Chem. Phys. 140 (2014) 174103.
[87] F. Neese, Coord. Chem. Rev. 253 (2009) 526–563.
[88] W. Koch, M.C. Holthausen, A Chemist's Guide to Density Functional Theory, Wiley-VCH, 2000.
[89] H. Chermette, Coord. Chem. Rev. 178–180 (Part 1) (1998) 699–721.
[90] A. Dreuw, M. Head-Gordon, Chem. Rev. 105 (2005) 4009–4037.
[91] A.C. Tsipis, Coord. Chem. Rev. 272 (2014) 1–29.
[92] J. Kohanoff, N.I. Gidopoulos, in: R. McWeeny (Ed.), Handbook of Molecular Physics and Quantum Chemistry, vol. 2, Part 5, Wiley-Blackwell, 2003, pp. 532–568.
[93] M.E. Casida, J. Mol. Struct. Theochem. 914 (2009) 3–18.

[94] M.E. Casida, M. Huix-Rotllant, Annu. Rev. Phys. Chem. 63 (2012) 287–323.
[95] J.P. Perdew, K. Schmidt, AIP Conf. Proc. 577 (2001) 1–20.
[96] J.P. Perdew, Phys. Rev. B 33 (1986) 8822–8824.
[97] A.D. Becke, J. Chem. Phys. 98 (1993) 5648–5652.
[98] J.P. Perdew, K. Burke, M. Ernzerhof, Phys. Rev. Lett. 77 (1996) 3865–3868.
[99] C.J. Cramer, D.G. Truhlar, Phys. Chem. Chem. Phys. 11 (2009) 10757–10816.
[100] A.D. Becke, Phys. Rev. A 38 (1988) 3098–3100.
[101] C. Lee, W. Yang, R.G. Parr, Phys. Rev. B 37 (1988) 785–789.
[102] C. Adamo, V. Barone, J. Chem. Phys. 110 (1999) 6158–6170.
[103] R. Peverati, D.G. Truhlar, Philos. Trans. R. Soc. A 372 (2014) 20120476.
[104] Y. Zhao, B.J. Lynch, D.G. Truhlar, J. Phys. Chem. A 108 (2004) 4786–4791.
[105] S. Grimme, J. Chem. Phys. 124 (2006).
[106] L. Goerigk, S. Grimme, WIREs Comput. Mol. Sci. 4 (2014) 576–600.
[107] S.F. Sousa, P.A. Fernandes, M.J. Ramos, J. Phys. Chem. A 111 (2007) 10439–10452.
[108] A.J. Stone, The Theory of Intermolecular Forces, Clarendon Press, 1997.
[109] I.G. Kaplan, Intermolecular Interactions: Physical Picture, Computational Methods and Model Potentials, John Wiley & Sons, 2006.
[110] S. Grimme, WIREs Comput. Mol. Sci. 1 (2011) 211–228.
[111] S. Grimme, J. Antony, S. Ehrlich, H. Krieg, J. Chem. Phys. 132 (2010) 154104.
[112] A.J. Cohen, P. Mori-Sanchez, W. Yang, Science 321 (2008) 792–794.
[113] A. Dreuw, J.L. Weisman, M. Head-Gordon, J. Chem. Phys. 119 (2003) 2943–2946.
[114] A. Dreuw, M. Head-Gordon, J. Am. Chem. Soc. 126 (2004) 4007–4016.
[115] Y. Tawada, T. Tsuneda, S. Yanagisawa, T. Yanai, K. Hirao, J. Chem. Phys. 120 (2004) 8425–8433.
[116] B. Champagne, E.A. Perpète, D. Jacquemin, S.J.A. van Gisbergen, E.-J. Baerends, C. Soubra-Ghaoui, K.A. Robins, B. Kirtman, J. Phys. Chem. A 104 (2000) 4755–4763.
[117] T. Tsuneda, K. Hirao, WIREs Comput. Mol. Sci. 4 (2014) 375–390.
[118] T. Yanai, D.P. Tew, N.C. Handy, Chem. Phys. Lett. 393 (2004) 51–57.
[119] M. Kamiya, H. Sekino, T. Tsuneda, K. Hirao, J. Chem. Phys. 122 (2005) 234111.
[120] S.I. Bokarev, D. Hollmann, A. Pazidis, A. Neubauer, J. Radnik, O. Kühn, S. Lochbrunner, H. Junge, M. Beller, A. Brückner, Phys. Chem. Chem. Phys. 16 (2014) 4789–4796.
[121] J. Autschbach, M. Srebro, Acc. Chem. Res. 47 (2014) 2592–2602.
[122] S.I. Bokarev, O.S. Bokareva, O. Kühn, Coord. Chem. Rev., http://dx.doi.org/10.1016/j.ccr.2014.12.016
[123] B. Mennucci, WIREs Comput. Mol. Sci. 2 (2012) 386–404.
[124] A. Klamt, WIREs Comput. Mol. Sci. 1 (2011) 699–709.
[125] R.A. Friesner, Proc. Natl. Acad. Sci. U.S.A. 102 (2005) 6648–6653.
[126] H.M. Senn, W. Thiel, Angew. Chem. Int. Ed. 48 (2009) 1198–1229.
[127] A. Chantzis, T. Very, A. Monari, X. Assfeld, J. Chem. Theory Comput. 8 (2012) 1536–1541.
[128] D.A. Hoff, R. Silva, L.G.C. Rego, J. Phys. Chem. C 115 (2011) 15617–15626.
[129] J.J. Szymczak, F.D. Hofmann, M. Meuwly, Phys. Chem. Chem. Phys. 15 (2013) 6268–6277.
[130] S. Gozem, F. Melaccio, H.L. Luk, S. Rinaldi, M. Olivucci, Chem. Soc. Rev. 43 (2014) 4019–4036.
[131] M. Lundberg, P.E.M. Siegbahn, J. Chem. Phys. 122 (2005).
[132] D. Feller, E.R. Davidson, Rev. Comput. Chem. (1990) 1–43.
[133] E.R. Davidson, D. Feller, Chem. Rev. 86 (1986) 681–696.
[134] F. Jensen, WIREs Comput. Mol. Sci. 3 (2013) 273–295.
[135] E. van Lenthe, E.J. Baerends, J. Comput. Chem. 24 (2003) 1142–1156.
[136] W.J. Hehre, L. Radom, P.V.R. Schleyer, J.A. Pople, Ab Initio Molecular Orbital Theory, Wiley, 1986.
[137] F. Weigend, R. Ahlrichs, Phys. Chem. Chem. Phys. 7 (2005) 3297–3305.
[138] P.-O. Widmark, P.-A. Malmqvist, B.O.O. Roos, Theor. Chim. Acta 77 (1990) 291–306.
[139] P.-O. Widmark, B.J. Persson, B.O.O. Roos, Theor. Chim. Acta 79 (1991) 419–432.
[140] R. Pou-Amérigo, M. Merchán, I. Nebot-Gil, P.-O. Widmark, B.O. Roos, Theor. Chim. Acta 92 (1995) 149–181.
[141] K. Pierloot, B. Dumez, P.-O. Widmark, B.O. Roos, Theor. Chim. Acta 90 (1995) 87–114.
[142] B.O. Roos, R. Lindh, P.-A. Malmqvist, V. Veryazov, P.-O. Widmark, J. Phys. Chem. A 108 (2004) 2851–2858.
[143] T.H. Dunning, J. Chem. Phys. 90 (1989) 1007–1023.
[144] T.H. Dunning, K.A. Peterson, A.K. Wilson, J. Chem. Phys. 114 (2001) 9244–9253.
[145] A.K. Wilson, D.E. Woon, K.A. Peterson, T.H. Dunning, J. Chem. Phys. 110 (1999) 7667–7676.
[146] N.B. Balabanov, K.A. Peterson, J. Chem. Phys. 123 (2005) 064107.
[147] T. Takeda, Z. Phys. B 32 (1978) 43–48.
[148] M. Dolg, Modern Methods and Algorithms in Quantum Chemistry, John v. Neumann Institute for Computing (NIC), Jülich, 2000, pp. 479–508.
[149] P.J. Hay, W.R. Wadt, J. Chem. Phys. 82 (1985) 299–310.
[150] W.R. Wadt, P.J. Hay, J. Chem. Phys. 82 (1985) 284–298.
[151] D. Andrae, U. Häußermann, M. Dolg, H. Stoll, H. Preuß, Theor. Chim. Acta 77 (1990) 123–141.
[152] J.H. Wood, A.M. Boring, Phys. Rev. B 18 (1978) 2701–2711.
[153] E.v. Lenthe, E.J. Baerends, J.G. Snijders, J. Chem. Phys. 99 (1993) 4597–4610.
[154] M. Douglas, N.M. Kroll, Ann. Phys. 82 (1974) 89–155.
[155] B.A. Hess, Phys. Rev. A 32 (1985) 756–763.
[156] B.A. Hess, Phys. Rev. A 33 (1986) 3742–3748.
[157] G. Jansen, B.A. Hess, Phys. Rev. A 39 (1989) 6016–6017.
[158] J. Moellmann, S. Grimme, J. Phys. Chem. C 118 (2014) 7615–7621.
[159] L. Kronik, A. Tkatchenko, Acc. Chem. Res. 47 (2014) 3208–3216.
[160] R. Bjornsson, M. Buehl, J. Chem. Theory Comput. 8 (2012) 498–508.
[161] C.Y. Peng, H.B. Schlegel, Isr. J. Chem. 33 (1993) 449–454.
[162] R. Stowasser, R. Hoffmann, J. Am. Chem. Soc. 121 (1999) 3414–3420.
[163] S.M. Bachrach, Rev. Comput. Chem. 5 (1994) 171–228.
[164] R.S. Mulliken, J. Chem. Phys. 23 (1955) 1841–1846.
[165] L.C. Cusachs, P. Politzer, Chem. Phys. Lett. 1 (1968) 529–531.
[166] A.E. Reed, R.B. Weinstock, F. Weinhold, J. Chem. Phys. 83 (1985) 735–746.
[167] A.E. Reed, L.A. Curtiss, F. Weinhold, Chem. Rev. 88 (1988) 899–926.
[168] R.F.W. Bader, Atoms in Molecules: A Quantum Theory, Clarendon Press, 1994.
[169] M. Presselt, B. Dietzek, M. Schmitt, S. Rau, A. Winter, M. Jäger, U.S. Schubert, J.R. Popp, J. Phys. Chem. A 114 (2010) 13163–13174.
[170] R.L. Martin, J. Chem. Phys. 118 (2003) 4775–4777.
[171] M. Head-Gordon, A.M. Grana, D. Maurice, C.A. White, J. Phys. Chem. 99 (1995) 14261–14270.
[172] F. Plasser, M. Wormit, A. Dreuw, J. Chem. Phys. 141 (2014) 024106.
[173] A. Monari, X. Assfeld, M. Beley, P.C. Gros, J. Phys. Chem. A 115 (2011) 3596–3603.
[174] A.V. Marenich, J. Ho, M.L. Coote, C.J. Cramer, D.G. Truhlar, Phys. Chem. Chem. Phys. 16 (2014) 15068–15106.
[175] S.J. Konezny, M.D. Doherty, O.R. Luca, R.H. Crabtree, G.L. Soloveichik, V.S. Batista, J. Phys. Chem. C 116 (2012) 6349–6356.
[176] L.E. Roy, E. Jakubikova, M.G. Guthrie, E.R. Batista, J. Phys. Chem. A 113 (2009) 6745–6750.
[177] P. Diamantis, J.F. Gonthier, I. Tavernelli, U. Rothlisberger, J. Phys. Chem. B 118 (2014) 3950–3959.
[178] A.A. Isse, A. Gennaro, J. Phys. Chem. B 114 (2010) 7894–7899.
[179] C.P. Kelly, C.J. Cramer, D.G. Truhlar, J. Phys. Chem. B 110 (2006) 16066–16081.
[180] C.E. Dykstra, J.D. Augspurger, B. Kirtman, D.J. Malik, Rev. Comput. Chem. (1990) 83–118.
[181] A.P. Scott, L. Radom, J. Phys. Chem. 100 (1996) 16502–16513.
[182] R.L. Jacobsen, R.D. Johnson, K.K. Irikura, R.N. Kacker, J. Chem. Theory Comput. 9 (2013) 951–954.
[183] M. Wächtler, J. Guthmuller, L. González, B. Dietzek, Coord. Chem. Rev. 256 (2012) 1479–1508.
[184] A. Lami, F. Santoro, Computational Strategies for Spectroscopy, John Wiley & Sons, Inc., 2011, pp. 475–516.
[185] M. Biczysko, J. Bloino, F. Santoro, V. Barone, Computational Strategies for Spectroscopy, John Wiley & Sons, Inc., 2011, pp. 361–443.
[186] R. Crespo-Otero, M. Barbatti, Theor. Chem. Acc. 131 (2012).
[187] R. Improta, A. Lami, V. Barone, F. Santoro, Int. J. Quantum Chem. 110 (2010) 624–636.
[188] J. Eng, C. Gourlaouen, E. Gindensperger, C. Daniel, Acc. Chem. Res. 48 (2015) 809–817.
[189] M. Dierksen, S. Grimme, J. Chem. Phys. 122 (2005).
[190] F. Santoro, R. Improta, A. Lami, J. Bloino, V. Barone, J. Chem. Phys. 126 (2007).
[191] H. Yersin, W. Humbs, J. Strasser, Coord. Chem. Rev. 159 (1997) 325–358.
[192] E. Epifanovsky, K. Kowalski, P.-D. Fan, M. Valiev, S. Matsika, A.I. Krylov, J. Phys. Chem. A 112 (2008) 9983–9992.
[193] J. Guthmuller, F. Zutterman, B. Champagne, J. Chem. Theory Comput. 4 (2008) 2094–2100.
[194] F. Santoro, A. Lami, R. Improta, V. Barone, J. Chem. Phys. 126 (2007).
[195] R.L. Lord, M.M. Allard, R.A. Thomas, O.S. Odongo, H.B. Schlegel, Y.-J. Chen, J.F. Endicott, Inorg. Chem. 52 (2013) 1185–1198.
[196] F. De Angelis, F. Santoro, M.K. Nazeruddin, V. Barone, J. Phys. Chem. B 112 (2008) 13181–13183.
[197] M.W. Lodewyk, M.R. Siebert, D.J. Tantillo, Chem. Rev. 112 (2011) 1839–1862.
[198] R. Jain, T. Bally, P.R. Rablen, J. Org. Chem. 74 (2009) 4017–4023.
[199] T. Bally, P.R. Rablen, J. Org. Chem. 76 (2011) 4818–4830.
[200] K.W. Wiitala, C.J. Cramer, T.R. Hoye, Magn. Reson. Chem. 45 (2007) 819–829.
[201] M.A.M. Al-Ibadi, S.B. Duckett, J.E. McGrady, Dalton Trans. 41 (2012) 4618–4625.
[202] P. Hrobárik, V. Hrobáriková, F. Meier, M. Repiský, S. Komorovský, M. Kaupp, J. Phys. Chem. A 115 (2011) 5654–5659.
[203] J. Autschbach, Coord. Chem. Rev. 251 (2007) 1796–1821.
[204] L. Salassa, C. Garino, G. Salassa, C. Nervi, R. Gobetto, C. Lamberti, D. Gianolio, R. Bizzarri, P.J. Sadler, Inorg. Chem. 48 (2009) 1469–1481.
[205] R. Gobetto, C. Nervi, B. Romanin, L. Salassa, M. Milanesio, G. Croce, Organometallics 22 (2003) 4012–4019.
[206] A. Cannizzo, F. van Mourik, W. Gawelda, G. Zgrablic, C. Bressler, M. Chergui, Angew. Chem. 118 (2006) 3246–3248.
[207] H. Yersin, A.F. Rausch, R. Czerwieniec, T. Hofbeck, T. Fischer, Coord. Chem. Rev. 255 (2011) 2622–2652.
[208] R. Baková, M. Chergui, C. Daniel, A. Vlcek Jr., S. Zális, Coord. Chem. Rev. 255 (2011) 975–989.
[209] C.M. Marian, WIREs Comput. Mol. Sci. 2 (2012) 187–203.
[210] M. Etinski, J. Tatchen, C.M. Marian, J. Chem. Phys. 134 (2011) 154105.
[211] M.C. Daza, M. Doerr, S. Salzmann, C.M. Marian, W. Thiel, Phys. Chem. Chem. Phys. 11 (2009) 1688–1696.
[212] J. Tatchen, N. Gilka, C.M. Marian, Phys. Chem. Chem. Phys. 9 (2007) 5209–5221.
[213] P.-Å. Malmqvist, B.O. Roos, B. Schimmelpfennig, Chem. Phys. Lett. 357 (2002) 230–240.
[214] R. Heydova, E. Gindensperger, R. Romano, J. Sykora, A. Vlcek Jr., S. Zalis, C. Daniel, J. Phys. Chem. A 116 (2012) 11319–11329.

Please cite this article in press as: M. Jäger, et al., Coord. Chem. Rev. (2015), http://dx.doi.org/10.1016/j.ccr.2015.03.019

[215] C. Gourlaouen, C. Daniel, Dalton Trans. 43 (2014) 17806–17819.
[216] L. Freitag, L. González, Inorg. Chem. 53 (2014) 6415–6426.
[217] D. Escudero, B. Happ, A. Winter, M.D. Hager, U.S. Schubert, L. González, Chem. Asian J. 7 (2012) 667–671.
[218] F. Wang, T. Ziegler, E. van Lenthe, S. van Gisbergen, E.J. Baerends, J. Chem. Phys. 122 (2005) 204103.
[219] H. Ågren, O. Vahtras, B. Minaev, Adv. Quantum Chem. 27 (1996) 71–162.
[220] M. Kleinschmidt, J. Tatchen, C.M. Marian, J. Comput. Chem. 23 (2002) 824–833.
[221] E. Ronca, F. De Angelis, S. Fantacci, J. Phys. Chem. C 118 (2014) 17067–17078.
[222] E. Baranoff, B.F.E. Curchod, J. Frey, R. Scopelliti, F. Kessler, I. Tavernelli, U. Rothlisberger, M. Grätzel, M.K. Nazeeruddin, Inorg. Chem. 51 (2012) 215–224.
[223] M.R. Camilo, C.R. Cardoso, R.M. Carlos, A.B.P. Lever, Inorg. Chem. 53 (2014) 3694–3708.
[224] L. Salassa, C. Garino, G. Salassa, R. Gobetto, C. Nervi, J. Am. Chem. Soc. 130 (2008) 9590–9597.
[225] O.P.J. Vieuxmaire, R.E. Piau, F. Alary, J.-L. Heully, P. Sutra, A. Igau, M. Boggio-Pasqua, J. Phys. Chem. A 117 (2013) 12821–12830.
[226] T. Österman, M. Abrahamsson, H.-C. Becker, L. Hammarström, P. Persson, J. Phys. Chem. A 116 (2012) 1041–1050.
[227] T. Österman, P. Persson, Chem. Phys. 407 (2012) 76–82.
[228] T. Guillon, M. Boggio-Pasqua, F. Alary, J.-L. Heully, E. Lebon, P. Sutra, A. Igau, Inorg. Chem. 49 (2010) 8862–8872.
[229] J.C. Tully, J. Chem. Phys. 93 (1990) 1061–1071.
[230] N.L. Doltsinis, D. Marx, J. Theor. Comput. Chem. 1 (2002) 319–349.
[231] M. Barbatti, WIREs Comput. Mol. Sci. 1 (2011) 620–633.
[232] D. Marx, J. Hutter, Ab Initio Molecular Dynamics: Basic Theory and Advanced Methods, Cambridge University Press, 2012.
[233] D. Marx, A. Muramatsu, J. Grotendorst, Quantum Simulations of Complex Many-body Systems: From Theory to Algorithms: Lecture Notes, NIC-Directors, 2002.
[234] L. González, P. Marquetand, M. Richter, J. González-Vázquez, I. Sola, Ultrafast Phenomena in Molecular Sciences, Springer International Publishing, 2014, pp. 145–170.
[235] S. Mai, M. Richter, P. Marquetand, L. González, Excitation of Nucleobases from a Computational Perspective II: Dynamics, Springer, Berlin/Heidelberg, 2014, pp. 1–55.
[236] I. Tavernelli, B.F.E. Curchod, U. Rothlisberger, Chem. Phys. 391 (2011) 101–109.
[237] M.-E. Moret, I. Tavernelli, M. Chergui, U. Rothlisberger, Chem. Eur. J. 16 (2010) 5889–5894.
[238] M. Richter, P. Marquetand, J. González-Vázquez, I. Sola, L. González, J. Chem. Theory Comput. 7 (2011) 1253–1258.
[239] O.A. Borg, S.S.M.C. Godinho, M.J. Lundqvist, S. Lunell, P. Persson, J. Phys. Chem. A 112 (2008) 4470–4476.
[240] Y. Minenkov, A. Singstad, G. Occhipinti, V.R. Jensen, Dalton Trans. 41 (2012) 5526–5541.
[241] W. Kabsch, Acta. Cryst. Sec. A 32 (1976) 922–923.
[242] M.G. Fraser, A.G. Blackman, G.I.S. Irwin, C.P. Easton, K.C. Gordon, Inorg. Chem. 49 (2010) 5180–5189.
[243] J. Guthmuller, L. González, Phys. Chem. Chem. Phys. 12 (2010) 14812–14821.
[244] J.S. Wilson, N. Chawdhury, M.R.A. Al-Mandhary, M. Younus, M.S. Khan, P.R. Raithby, A. Köhler, R.H. Friend, J. Am. Chem. Soc. 123 (2001) 9412–9417.
[245] M. Jäger, Beyond Classical Ruthenium(II) Polypyridyl Complexes, Uppsala Universitet, 2009.
[246] M.I.J. Polson, N.J. Taylor, G.S. Hanan, Chem. Commun. (2002) 1356–1357.
[247] M.J. Frisch, G.W. Trucks, H.B. Schlegel, G. Scuseria, M.A.E. Robb, J.R. Cheeseman, G. Scalmani, V. Barone, B. Mennucci, G.A. Petersson, H. Nakatsuji, M. Caricato, X. Li, H.P. Hratchian, A.F. Izmaylov, J. Bloino, G. Zheng, J.L. Sonnenberg, M. Hada, M. Ehara, K. Toyota, R. Fukuda, J. Hasegawa, M. Ishida, T. Nakajima, Y. Honda, O. Kitao, H. Nakai, T. Vreven, J. Montgomery, J.A.J. Peralta, F.E. Ogliaro, M. Bearpark, J.J. Heyd, E. Brothers, K.N. Kudin, V.N. Staroverov, R. Kobayashi, J. Normand, K. Raghavachari, A. Rendell, J.C. Burant, S.S. Iyengar, J. Tomasi, M. Cossi, N. Rega, N.J. Millam, M. Klene, J.E. Knox, J.B. Cross, V. Bakken, C. Adamo, J. Jaramillo, R. Gomperts, R.E. Stratmann, O. Yazyev, A.J. Austin, R. Cammi, C. Pomelli, J.W. Ochterski, R.L. Martin, K. Morokuma, V.G. Zakrzewski, G.A. Voth, P. Salvador, J.J. Dannenberg, S. Dapprich, A.D. Daniels, Ö. Farkas, J.B. Foresman, J.V. Ortiz, J. Cioslowski, D.J. Fox, Gaussian, Inc., Wallingford, CT, 2013.
[248] N.M. O'Boyle, J.G. Vos, GaussSum 3. 0, Dublin City University, Dublin, Ireland, 2009, Available at http://gausssum.sourceforge.net
[249] N.M. O'Boyle, A.L. Tenderholt, K.M. Langner, J. Comput. Chem. 29 (2008) 839–845.

Please cite this article in press as: M. Jäger, et al., Coord. Chem. Rev. (2015), http://dx.doi.org/10.1016/j.ccr.2015.03.019

APPENDIX 4.A.2

Peripheral ligands as electron storage reservoirs for photocatalytic hydrogen generation

Qing Pan, Leon Freitag, Tanja Kowacs, Jane C. Falgenhauer, Jeroen P. Korterik,
Derck Schlettwein, Wesley R. Browne, Mary T. Pryce, Sven Rau, Leticia
González, Johannes G. Vos and Annemarie Huijser

Manuscript submitted to Angew. Chem.

Contributions:

Qing Pan, Tanja Kowacs, Jane C. Falgenhauer, Jeroen P. Korterik, Derck Schlettwein, Wesley R. Browne, Mary T. Pryce, Sven Rau, Johannes G. Vos and Annemarie Huijser conceived the idea, performed the synthesis, characterisation, transient absorption spectroscopy and electrochemical studies and wrote the draft of the manuscript.

Leon Freitag performed the quantum chemical calculations and helped with the preparation of the final version of the manuscript.

Leticia González supervised the quantum chemical calculations and was involved in the preparation of the final version of the manuscript.

Peripheral ligands as electron storage reservoirs for photocatalytic hydrogen generation

Qing Pan, Leon Freitag, Tanja Kowacs, Jane C. Falgenhauer, Jeroen P. Korterik, Derck Schlettwein, Wesley R. Browne, Mary T. Pryce, Sven Rau, Leticia González*, Johannes G. Vos* and Annemarie Huijser*

Abstract: The contrasting excited state properties of two related Ru/Pt catalysts with very different photocatalytic H_2 generation capabilities are reported. The photophysics of the bipyridyl-based complex **RuPt** and its ethyl ester-modified analogue **EtOOCRuPt**, are investigated by density functional theory and ultrafast transient absorption. For **RuPt**, internal conversion (IC) from the peripheral ligand based ^{3}MLCT states to those on the bridging ligand is observed on a ps time scale. In contrast, for **EtOOCRuPt** excited state equilibration is ultrafast (535±17 fs) in the direction of the peripheral ligands. The reverse IC occurs on a slower (>3 ps) time scale. These photodynamics create an electron reservoir on the peripheral ligands. This switch in the balance of population of bridging and peripheral ligand based ^{3}MLCT states is responsible for the improvement in turn-over numbers for **EtOOCRuPt**, and provides an unexpected novel design feature for H_2 generating molecular photocatalysts.

The impact of increasing atmospheric concentrations of CO_2 on life is driving the urgent development of carbon neutral energy sources. The enormous potential of solar energy places solar-driven energy generation high on the agenda [1] and this has resulted in the development of photovoltaic devices such as dye-sensitized solar cells.[2] A key disadvantage of photovoltaic cells and indeed of wind and wave energy lies in the storage of energy generated. This has brought the design of new photocatalytic systems that can produce chemical energy directly with light-driven generation of H_2 from water to the forefront. Molecular photocatalysts that seek to mimic natural photosynthesis have been studied intensively in recent years.[3] In these assemblies a photosensitizer is bound covalently to a catalytic center via a bridging ligand, which offers key advantages over the intermolecular approach[4] in which the photosensitizers and catalytic centers are mixed in solution relying on diffusion limited processes for energy and electron transfer. However, it has been shown that eliminating these diffusional processes does not necessarily improve performance, a priori and the importance of the photocatalyst design cannot be overstated.

The efficiency of catalytic H_2 generation by molecular photocatalytic assemblies has shown to be dependent on parameters such as the nature of the photosensitizer, the bridging ligand, and the catalytic center both in terms of turn-over numbers (TON) and turn-over frequency (TOF).[5] Despite the intricate involvement of these components, relatively few photophysical studies of such assemblies have been reported to date.[6] Recently the tuning of catalytic activity of very stable platinum(II) catalytic centers was reported.[7] Furthermore, it was shown that the additional charge localized on the bridging ligand of the electrochemically mono reduced ruthenium-platinum catalyst prevents directional transfer of the second electron. Utilization of ^{3}MLCT excited states localized on the peripheral ligands was postulated as a pathway to increasing the efficiency of the essential second electron transfer process.[8] To the best of our knowledge no other investigations on the photodynamics of supramolecular assemblies as a function of the peripheral ligands have been reported. Two examples showing a dependence of TON values on the nature of the peripheral ligands have recently been reported by our groups. [9, 10]

In this contribution we show, through time resolved spectroscopy of **EtOOCRuPt** and **RuPt** (See Figure 1), that the introduction of ester moieties greatly affects the balance towards population of ^{3}MLCT states localized on peripheral ligands. It is proposed that this rebalancing results in the creation of an electron reservoir on these ligands, which results in an increase in TON (18 h) from 100 for **RuPt** to 720 for **EtOOCRuPt**[10] and more generally opens new pathways towards the design of improved photocatalysts.

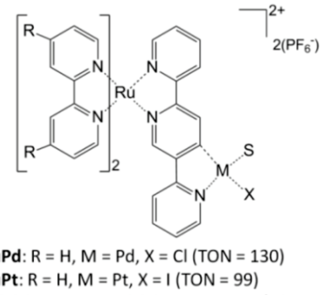

RuPd: R = H, M = Pd, X = Cl (TON = 130)
RuPt: R = H, M = Pt, X = I (TON = 99)
EtOOCRuPt: R = EtOOC, M = Pt, X= I (TON = 720)

Figure 1. Structure of the photocatalysts and their H_2 generation TONs. **RuPd** = $[(bpy)_2Ru(2,5\text{-}tpy)PdClS]^{2+}$; **RuPt** = $[(bpy)_2Ru(2,5\text{-}tpy)PtIS]^{2+}$. The precursor is denoted as **Ru**. **EtOOCRuPt** = $[(EtOOC\text{-}bpy)_2Ru(2,5\text{-}tpy)PtIS]^{2+}$. The Ru precursor is denoted as **EtOOCRu** (EtOOC-bpy = 4,4'-di(carboxyethyl)bipyridine, S = solvent).[10, 11] bpy = 2,2'-bipyridine, 2,5-tpy = 2,5-terpyridine

---

[a] Q. Pan, J. P. Korterik, Dr. J. M. Huijser
MESA+ Institute for Nanotechnology, University of Twente
P.O. Box 217, 7500 AE, Enschede, The Netherlands
E-mail: j.m.huijser@utwente.nl
[b] L. Freitag, Prof. dr. L. González
Institute of Theoretical Chemistry, University of Vienna
Währinger Str. 17, 1090 Vienna, Austria
E-mail: leticia.gonzalez@univie.ac.at
[c] T. Kowacs, Prof. dr. S. Rau
Institute of Inorganic Chemistry Materials and Catalysis, University of Ulm, Albert-Einstein-Allee 11, 89081 Ulm, Germany
[d] Dr. M.T. Pryce, Prof. dr. J. G. Vos
SRC for Solar Energy Conversion, School of Chemical Sciences, Dublin City University, Glasnevin, Dublin 9, Ireland, E-mail: han.vos@dcu.ie
[e] J. C. Falgenhauer, Prof. dr. D. Schlettwein
Institute of Applied Physics, Justus-Liebig-University
Ludwigstraße 23, 35390 Gießen, Germany
[f] Prof. dr. W. R. Browne
Stratingh Institute for Chemistry, University of Groningen
9747 AG, Groningen, The Netherlands

Supporting information for this article is available on the WWW under ....

Intersystem crossing (ISC) to the triplet manifold in Ru(II)-polypyridyl complexes occurs within ~100 fs of photoexcitation [12] and hence it is the energetics of the triplet states that determines photocatalytic reactivity. The geometries at the minima and the energy gaps between the lowest tpy and bpy-based ^{3}MLCT states calculated by density functional theory methods, indicate that the order of the ^{3}MLCT states changes upon ethyl ester modification of the peripheral ligands (see Supporting Information). For **RuPt** and **Ru**, a tpy-based ^{3}MLCT state is the lowest in energy, whereas for **EtOOCRuPt**, an EtOOC-bpy based state is lowest, see Figure 2. Stabilization of the peripheral ligand based ^{3}MLCT states is more pronounced in the precursors: in **EtOOCRu** the bpy ^{3}MLCT states are stabilized by 0.43 eV relative to **Ru**, resulting in a gap of 0.30 eV between the two lowest ^{3}MLCT states. The same trend is observed for the dinuclear complexes, although with a smaller energy gap (0.10 eV). In all cases the gap exceeds kT at 298 K, suggesting that the excited state equilibrium is shifted to the tpy ^{3}MLCT state in **Ru** and **RuPt**, and to the EtOOC-bpy ^{3}MLCT state in **EtOOCRu** and **EtOOCRuPt**.

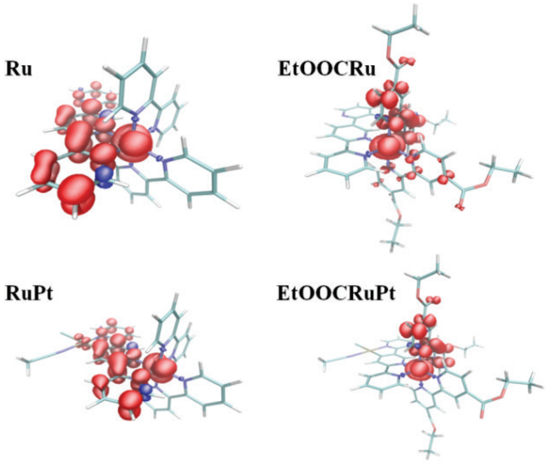

Figure 2. Spin densities of the lowest triplet states of **Ru**, **EtOOCRu**, **RuPt** and **EtOOCRuPt**.

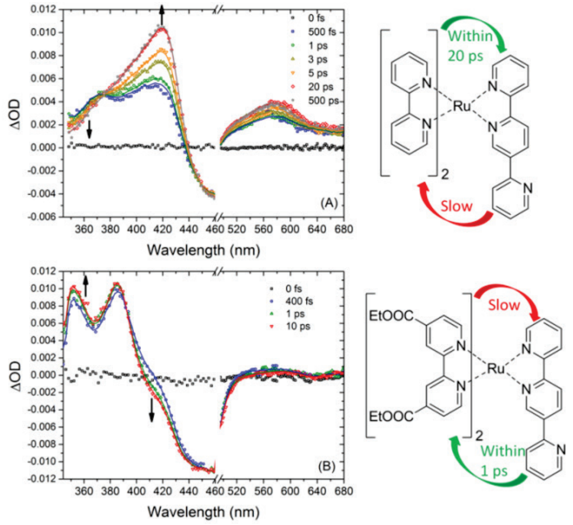

Figure 3. Transient absorption spectra of **Ru** (A) and **EtOOCRu** (B), including fits presented as solid curves. The right panel illustrates the excited state equilibrium inversion realized by esterification of the bpy ligands.

The time evolution of the population of the (EtOOC-)bpy and tpy-localized excited states for **Ru** and **EtOOCRu** (Figure 3 and Supporting Information) indicates that ISC occurs within ~100 fs as expected [12] with the dynamics of ^{3}MLCT states observed after 100 fs. The transient absorption (TA) spectrum of **Ru** shows two bands around 370 nm and 420 nm, with the first due to excited state absorption (ESA) of the bpy radical anion and the second tpy radical anion. The ESA increase around 420 nm concomitant with a decrease at ca. 370 nm, which manifests IC from a bpy based ^{3}MLCT to the tpy bridge based ^{3}MLCT within ca. 20 ps. This latter process competes with vibrational cooling.[13] The temporal evolution of the TA spectrum for **EtOOCRu** is the reverse of **Ru**, with an increase in population of the peripheral ligand based ^{3}MLCT states (Figure 3, lower right panel), however, the absence of spectral changes at times beyond a few ps (up to at least 6 ns) indicates that the excited state equilibration of **EtOOCRu** is ultrafast (see Supporting Information).

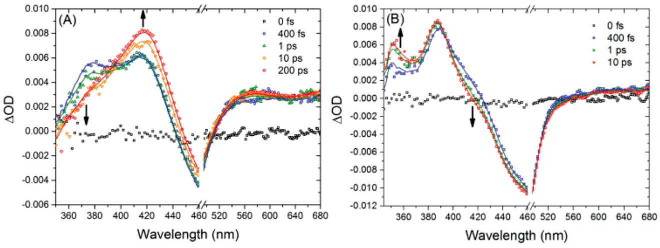

Figure 4. TA spectra of **RuPt** (A) and **EtOOCRuPt** (B), fits are presented as solid curves.

The TA spectra of **RuPt** and **EtOOCRuPt** (Figure 4) are similar to those of their mononuclear precursors. For **RuPt**, an ESA band at ca. 370 nm becomes less intense in time concomitant with a grow-in of a feature at ca. 420 nm, which indicates IC from the bpy based ^{3}MLCT states to tpy ^{3}MLCT states (see the Supporting Information for details regarding photophysical modeling). Again, as observed for the two monometallic precursors discussed above, the direction of IC observed for **EtOOCRuPt** is opposite to that of **RuPt** indicating that cyclometallation by Pt does not change the ultrafast photophysics of the chromophore significantly.

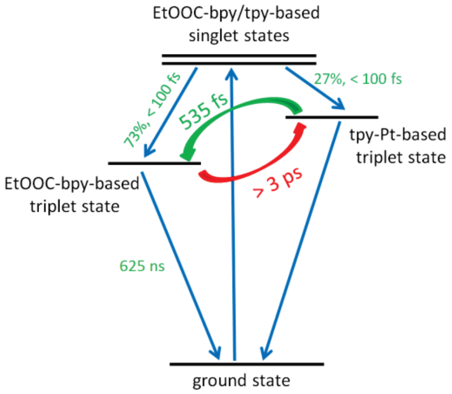
EtOOC-bpy/tpy-based singlet states
73%, < 100 fs
535 fs
27%, < 100 fs
tpy-Pt-based triplet state
EtOOC-bpy-based triplet state
> 3 ps
625 ns
ground state

Figure 5. Simplified photophysical model of light-induced processes in **EtOOCRuPt**.

A photophysical model of **EtOOCRuPt** established by target analysis of the TA data is shown in Figure 5. Details for an analogous model for **EtOOCRu** are provided in the Supporting Information. Photoexcitation leads to EtOOC-bpy and tpy-based singlet excited states, which undergo ultrafast ISC[12] into EtOOC-bpy and tpy-Pt localized triplet states. The electron density at the tpy ligand moves on an ultrafast timescale to the EtOOC-bpy ligands (535±17 fs). IC from the EtOOC-bpy based ^{3}MLCT states to the bridging tpy based ^{3}MLCT states occurs at >3 ps. This equilibration results in only a minor population of the bridge based states.

The TA data discussed above allow for the interpretation of the time-resolved photoluminescence data obtained before.[10] They show that the excited state decay of **Ru** is mono-exponential (τ = 796±6 ns), indicating that the various peripheral and bridging ligand based low lying ^{3}MLCT states are thermally equilibrated.[14] For **EtOOCRu** (τ = 1.05±0.01 μs) and **EtOOCRuPt** (τ = 625±31 ns), ultrafast equilibration results in a minor population of the tpy based ^{3}MLCT states, yielding a mono-exponential emission decay. However, for **RuPt** a bi-exponential decay (τ_1 = 124±58 ns, 15 %; τ_2 = 658±19 ns, 85 %) is observed. **RuPd** shows analogous features with the fast component more pronounced. [13] As in the case of **RuPd** the fast component observed for **RuPt** is assigned to an increased rigidity of the bridging ligand upon coordination of the Pt center, resulting in a lowering of the energy of the deactivation ^{3}MC level at the Ru moiety. The increased rigidity may also reduce the vibrational freedom of the ligand thereby increasing the difficulty of population transfer between tpy- and bpy-based ^{3}MLCT states. This hypothesis is in agreement with calculations which show that the difference between the bpy and tpy structures is larger after binding of the Pt center (see Supporting Information). As a result, both ^{3}MLCT states contribute to the photoluminescence, resulting in a bi-exponential decay. Addition of the ethyl ester groups to the peripheral ligands lowers the energy of the MLCT based on those ligands, manifested in a red shift in the lowest energy ^{1}MLCT transitions.[10] This inverts the equilibrium between bridging and peripheral ligand based ^{3}MLCT states and hence electron density in the excited state is based on the peripheral ligands and not the bridging ligand.

The active involvement of the peripheral ligands in the photodynamics of **EtOOCRuPt** is quite unexpected and has major consequences for the future design of photosensitizer-bridge-catalyst assemblies. A priori, one would anticipate that the movement of electron density from the photosensitiser to the catalytic center by population of a bridging ligand based ^{3}MLCT state would be beneficial for photocatalytic H^+ reduction. However, for **EtOOCRuPt** the electron density is the opposite, and is based on peripheral ligand based ^{3}MLCT states, while at the same time much higher TONs are achieved with **EtOOCRuPt** compared to **RuPt**. It is generally accepted that proton reduction at the catalytic site and the absorption of a second photon are the two rate-limiting steps for hydrogen generation, since typical time constants for hydrogen generation are more than a microsecond.[15] As outlined above it was shown[8] that when the electron density accumulated on the bridging ligand is high, directional transfer of the second electron to the hydrogen generating center is inefficient and it was postulated that electron storage on the peripheral ligands could lead to increased hydrogen generation. In this contribution we present the first detailed photophysical evidence of such behavior. In the excited state electron density is almost totally located on the ^{3}MLCT states of the peripheral ligands, while internal conversion from the peripheral to the bridging ligand is taking place at a >3 ps timescale. Under catalytic conditions this process is likely to be further promoted by protonation of the Pt catalytic center since this will lower the energy of the bridge based ^{3}MLCT states. As a results a more efficient photocatalytic assembly is expected and the increased TON of 720 (18 h) observed for **EtOOCRuPt** compared to 100 (18 h) for **RuPt** clearly indicate that this approach is very promising.

In conclusion, this photophysical study shows that it is feasible to design new photocatalysts where in the excited state the electron density is based at the peripheral ligands rather than on the bridge. It is shown that 'storing' electron density at the peripheral ligands correlates with a dramatic increase in activity towards H_2 generation activity. These results allow for the development of new design futures for the optimization of molecular photocatalysts.

Acknowledgements

This work is supported by the Dutch Organization for Scientific Research (NWO) and the EU COST Action CM-1202 (PERSPECT-H_2O, short-term scientific mission 16737). Prof. Huib J. Bakker of the AMOLF Institute in Amsterdam is acknowledged for scientific discussions

Keywords: photocatalysis, excited state equilibrium, transient absorption, internal conversion, density functional theory

---

[1] N. S. Lewis, D. G. Nocera, *Proc. Natl. Acad. Sci. USA* **2006**, *103*, 15729-15735.

[2] A. Hagfeldt, M. Gratzel, *Acc. Chem. Res.* **2000**, *33*, 269-277.

[3] a) L. C. Sun, L. Hammarström, B. Akermark, S. Styring, *Chem. Soc. Rev.* **2001**, *30*, 36-49; b) A. Magnuson, M. Anderlund, O. Johansson, P. Lindblad, R. Lomoth, T. Polivka, S. Ott, K. Stensjo, S. Styring, V. Sundstrom, L. Hammarström, *Acc. Chem. Res.* **2009**, *42*, 1899-1909; c) L. Hammarström, *Acc. Chem. Res.* **2015**, *48*, 840-850.

[4] a) W. T. Eckenhoff, R. Eisenberg, *Dalton Trans.* **2012**, *41*, 13004-13021; b) S. Losse, J. G. Vos, S. Rau, *Coord. Chem. Rev.* **2010**, *254*, 2492-2504.

[5] a) V. Artero, M. Chavarot-Kerlidou, M. Fontecave, *Angew. Chem. Int. Ed.* **2011**, *50*, 7238-7266; b) S. Rau, D. Walther, J. G. Vos, *Dalton T* **2007**, 915-919; c) M. Schulz, M. Karnahl, M. Schwalbe, J. G. Vos, *Coord. Chem. Rev.* **2012**, *256*, 1682-1705

[6] a) S. Rau, B. Schafer, D. Gleich, E. Anders, M. Rudolph, M. Friedrich, H. Gorls, W. Henry, J. G. Vos, *Angew. Chem. Int. Ed.* **2006**, *45*, 6215-6218; b) S. Tschierlei, M. Karnahl, M. Presselt, B. Dietzek, J. Guthmuller, L. Gonzalez, M. Schmitt, S. Rau, J. Popp, *Angew. Chem. Int. Ed.* **2010**, *49*, 3981-3984; c) S. Tschierlei, M. Presselt, C. Kuhnt, A. Yartsev, T. Pascher, V. Sundstrom, M. Karnahl, M. Schwalbe, B. Schafer, S. Rau, M. Schmitt, B. Dietzek, J. Popp, *Chem. Eur. J.* **2009**, *15*, 7678-7688.

[7] .M. G. Pfeffer, T. Kowacs, M. Wachtler, J. Guthmuller, B. Dietzek, J. G. Vos, S. Rau, *Angew. Chem. Int. Ed.* **2015**, *54*, 6627-6631

[8] M. Wächtler, J. Guthmuller, S. Kupfer, M. Maiuri, D. Brida, J. Popp, S. Rau, G. Cerullo, B. Dietzek, *Chemistry - A European Journal*, **2015**, 7668-7674

[9] G. S. Bindra, M. Schulz, A. Paul, S. Soman, R. Groarke, J. Inglis, M. T. Pryce, W. R. Browne, S. Rau, B. J. Maclean, J. G. Vos, *Dalton Trans.* **2011**, *40*, 10812-10814.

[10] T. Kowacs, Q. Pan, A. Huijser, S. Rau, P. Lang, W. R. Browne, M. T. Pryce, J. G. Vos, *Inorg.Chem.* **2015**, *submitted*.

[11] G. S. Bindra, M. Schulz, A. Paul, R. Groarke, S. Soman, J. L. Inglis, W. R. Browne, M. G. Pfeffer, S. Rau, B. J. MacLean, M. T. Pryce, J. G. Vos, *Dalton Trans.* **2012**, *41*, 13050-13059

[12] a) N. H. Damrauer, G. Cerullo, A. Yeh, T. R. Boussie, C. V. Shank, J. K. McCusker, *Science* **1997**, *275*, 54-57; b) A. T. Yeh, C. V. Shank, J. K. McCusker, *Science* **2000**, *289*, 935-938.

[13] Q. Pan, F. Mecozzi, J. P. Korterik, D. Sharma, J. L. Herek, J. G. Vos, W. R. Browne, A. Huijser, *J. Phys. Chem. C* **2014**, *118*, 20799-20806.

[14] D. Magde, M. D. Magde Jr., E. C. Glazer, *Coord. Chem. Rev.* **2015**

[15] a) M. Frey, *Chembiochem* **2002**, *3*, 153-160; b) M. Guttentag, A. Rodenberg, R. Kopelent, B. Probst, C. Buchwalder, M. Brandstatter, P. Hamm, R. Alberto, *Eur J Inorg Chem* **2012**, 59-64; c) M. L. Helm, M. P. Stewart, R. M. Bullock, M. R. DuBois, D. L. DuBois, *Science* **2011**, *333*, 863-866.

5

SUMMARY AND CONCLUSION

This thesis encompasses a series of theoretical studies describing the reactivity, photodynamics and the electronic structure of ground and excited states of several ruthenium nitrosyl and polypyridyl complexes. Theoretical and computational chemistry can offer valuable tools for investigating the chemistry of coordination compounds, being able to predict their electronic structure and reaction mechanisms. In particular, ruthenium nitrosyl complexes have been studied in this thesis because of their potential application in PDT as NO photoreleasers, the intermediate role in the metabolism of ruthenium anticancer drugs and the non-innocence of the NO ligand, leading to an intricate electronic structure. A *cis*↔*trans* isomerisation reaction mechanism for RuHIndNO, a nitrosyl derivate of a promising anti-cancer drug candidate, has been investigated with DFT. Calculations have shown that the dissociative mechanism is preferred over two other mechanisms, associative and twist, due to its lower activation barrier. Although dissociative mechanisms are also common in non-nitrosyl transition metal chemistry, the non-innocent behaviour of the NO ligand may contribute to the stabilisation of the transition state of the dissociative mechanism.

A further study has been conducted on the electronic structure of RuHIndNO with multiconfigurational methods, which has been able to characterise the electron correlation in the ruthenium coordination sphere, in particular in the Ru–NO bond. More insight on the coordination mode of the NO and oxidation states of the NO and the metal has been provided, resulting in an electronic structure description which goes beyond the Enemark-Feltham notation for ruthenium nitrosyls.

Computational studies of excited states can help rationalising the photodynamical processes occurring after photoexcitation and how these processes are influenced by different ligands. Quantum chemical calculations along with surface-hopping dynamics have been used to unravel the NO photodissociation mechanism in ruthenium nitrosyl complexes. At this point, surface-hopping dynamics deserve special attention, since it allowed insights which would have been hardly possible with static quantum chemical calculations, such as the influence of different states after the photoexcitation and the timescales of the photoprocesses.

Further DFT and TD-DFT calculations were used to explain the improvement of directional charge transfer upon ligand substitution in a series of ruthenium polypyridyl-based photosensitisers. The calculations could rationalise the changes in the absorption spectra and photodeactivation pathways observed in the experiments. Finally, in a joint theoretical and experimental study, DFT calculations were employed to undermine a new design principle of a hydrogen-producing photocatalyst. These studies provide examples on how theoretical and computational chemistry can aid the rational design of functional molecules for solar light conversion, photocatalysis and photodynamic therapy.

DFT and TD-DFT are nowadays usually the methods of choice for the quantum chemical calculations on large systems, as they offer good accuracy at a modest computational cost in many cases. However, certain situations, quite common in transition metal complexes, such as charge-transfer states or significant static correlation, may act as pitfalls for DFT and TD-DFT. In those cases DFT and TD-DFT may show poor accuracy or simply fail. The poor performance of DFT can be forgiven in a less accurate study or improved with targeted tuning of the functional, such as altering the amount of exact exchange[129] and/or tuning the range separation parameter in the long-range corrected functionals.[156] However, functional tuning in general lacks systematicity and transferability to other systems,[129,130] and does not help against DFT failures due to strong static correlation. Regarding static correlation, performance of DFT ranging from good to complete failure was witnessed in the course of this thesis. On the other side, a vast arsenal of new developments in the field of multiconfigurational methods such as density matrix renormalisation group (DMRG) or Cholesky decomposition-based density fitting emerged in the recent years, allowing the treatment of increasingly larger systems. This thesis presents several multiconfigurational calculations on ruthenium complexes, all of which show excellent agreement with the experiment. Additionally, DMRG calculations with orbital entanglement analysis provide us with better understanding of the electron correlation in ground and excited state of transition metal complexes.

The question whether multiconfigurational methods are going to take away the predominance of DFT and TD-DFT in transition metal chemistry in the near future is open. The ruthenium complexes studied in this thesis are currently close to the size limit for multiconfigurational methods, and the computational cost and scaling of multiconfigurational methods in large systems cannot compete with that of DFT and TD-DFT. However, the accuracy offered by multiconfigurational methods is attractive, leading to a steady increase of the number of multiconfigurational studies on TM complexes. At the very least, multiconfigurational methods may be used for the calibration of DFT and TD-DFT methodology to be employed in more demanding computational studies.

Surface-hopping dynamics is another promising computational technique for photodynamics studies, allowing insights into excited state processes beyond the standard static quantum chemical picture. Although dynamics is significantly more computationally demanding than quantum chemical calculations, the development of more computationally efficient quantum chemical methods also enables surface-hopping studies on larger systems. Together with the development of surface-hopping formalisms such as SHARC[121] which allow a proper treatment of spin-orbit couplings, these advances will allow for more surface-hopping dynamics with TM complexes in the near future.

BIBLIOGRAPHY

1 Emsley, J. *Nature's Building Blocks: An A-Z Guide to the Elements*; OUP Oxford, 2011.

2 Cotton, A. F.; Wilkinson, G. *Advanced Inorganic Chemistry: a Comprehensive Text*; Wiley Eastern Limited, 1996.

3 Grubbs, R. H.; Trnka, T. M. In *Ruthenium in Organic Synthesis*; Murahashi, S.-I., Ed.; Wiley-VCH Verlag GmbH & Co. KGaA, 2004; pp 153–177.

4 Rademaker-Lakhai, J. M.; van den Bongard, D.; Pluim, D.; Beijnen, J. H.; Schellens, J. H. M. *Clin. Cancer Res.* **2004**, *10*, 3717–3727.

5 (a) Hartinger, C. G.; Zorbas-Seifried, S.; Jakupec, M. A.; Kynast, B.; Zorbas, H.; Keppler, B. K. *J. Inorg. Biochem.* **2006**, *100*, 891–904; (b) Hartinger, C. G.; Jakupec, M. A.; Zorbas-Seifried, S.; Groessl, M.; Egger, A.; Berger, W.; Zorbas, H.; Dyson, P. J.; Keppler, B. K. *Chem. Biodivers.* **2008**, *5*, 2140–2155.

6 Bacher, F.; Arion, V. B. *Reference Module in Chemistry, Molecular Sciences and Chemical Engineering*; Elsevier, 2014.

7 Ackroyd, R.; Kelty, C.; Brown, N.; Reed, M. *Curr. Opin. Chem. Biol.* **2001**, *74*, 656–669.

8 (a) Culotta, E.; Koshland, D. E. *Science* **1992**, *258*, 1862–1865; (b) Fang, F. C. *Nitric Oxide and Infection*; Springer, 1999; (c) Ignarro, L. J. *Nitric Oxide: Biology and Pathobiology*; Academic Press, 2000.

9 Bonavida, B.; Khineche, S.; Huerta-Yepez, S.; Garbán, H. *Drug Resist. Updat.* **2006**, *9*, 157–173.

10 (a) Pandey, R. K. *J. Porphyr. Phtalocyanines* **2000**, *04*, 368–373; (b) Dolmans, D. E. J. G. J.; Fukumura, D.; Jain, R. K. *Nat. Rev. Cancer* **2003**, *3*, 380–387; (c) Detty, M. R.; Gibson, S. L.; Wagner, S. J. *J. Med. Chem.* **2004**, *47*, 3897–3915; (d) Zhao, B.; He, Y.-Y. *Expert Rev. Anticancer Ther.* **2010**, *10*, 1797–1809.

11 Frei, A.; Rubbiani, R.; Tubafard, S.; Blacque, O.; Anstaett, P.; Felgenträger, A.; Maisch, T.; Spiccia, L.; Gasser, G. *J. Med. Chem.* **2014**, *57*, 7280–7292.

12 Brown, J. M. In *Methods in Enzymology*; Brüne, H. S., Bernhard,, Eds.; Oxygen Biology and Hypoxia; Academic Press, 2007; Vol. 435; pp 295–321.

13 (a) Ford, P. C.; Bourassa, J.; Miranda, K.; Lee, B.; Lorkovic, I.; Boggs, S.; Kudo, S.; Laverman, L. *Coord. Chem. Rev.* **1998**, *171*, 185–202; (b) Bourassa, J.; Lee, B.; Bernard, S.; Schoonover, J.; Ford, P. C. *Inorg. Chem.* **1999**, *38*, 2947–2952; (c) Bourassa, J. L.; Ford, P. C. *Coord. Chem. Rev.* **2000**, *200–202*, 887–900; (d) Conrado, C. L.; Bourassa, J. L.; Egler, C.; Wecksler, S.; Ford, P. C. *Inorg. Chem.* **2003**, *42*, 2288–2293; (e) Jaworska, M.; Stasicka, Z. *J. Mol. Struct.* **2006**, *785*, 68–75.

14 Hoshino, M.; Laverman, L.; Ford, P. C. *Coord. Chem. Rev.* **1999**, *187*, 75–102.

15 (a) Patra, A. K.; Afshar, R.; Olmstead, M. M.; Mascharak, P. K. *Angew. Chem. Int. Ed.* **2002**, *41*, 2512–2515; (b) Patra, A. K.; Rowland, J. M.; Marlin, D. S.; Bill, E.; Olmstead, M. M.; Mascharak, P. K. *Inorg. Chem.* **2003**, *42*, 6812–6823.

16 Eroy-Reveles, A. A.; Leung, Y.; Beavers, C. M.; Olmstead, M. M.; Mascharak, P. K. *J. Am. Chem. Soc.* **2008**, *130*, 4447–4458.

17 (a) Works, C. F.; Ford, P. C. *J. Am. Chem. Soc.* **2000**, *122*, 7592–7593; (b) Works, C. F.; Jocher, C. J.; Bart, G. D.; Bu, X.; Ford, P. C. *Inorg. Chem.* **2002**, *41*, 3728–3739.

18 Patra, A. K.; Mascharak, P. K. *Inorg. Chem.* **2003**, *42*, 7363–7365.

19 (a) Rose, M. J.; Olmstead, M. M.; Mascharak, P. K. *J. Am. Chem. Soc.* **2007**, *129*, 5342–5343; (b) Rose, M. J.; Mascharak, P. K. *Chem. Commun.* **2008**, 3933–3935; (c) Fry, N. L.; Rose, M. J.; Rogow, D. L.; Nyitray, C.; Kaur, M.; Mascharak, P. K. *Inorg. Chem.* **2010**, *49*, 1487–1495; (d) Bohlender, C.; Wolfram, M.; Goerls, H.; Imhof, W.; Menzel, R.; Baumgaertel, A.; Schubert, U. S.; Mueller, U.; Frigge, M.; Schnabelrauch, M.; Wyrwa, R.; Schiller, A. *J. Mater. Chem.* **2012**, *22*, 8785–8792.

20 Fry, N. L.; Mascharak, P. K. *Acc. Chem. Res.* **2011**, *44*, 289–298.

21 Szundi, I.; Rose, M. J.; Sen, I.; Eroy-Reveles, A. A.; Mascharak, P. K.; Einarsdóttir, Ó. *Photochem. Photobiol.* **2006**, *82*, 1377–1384.

22 Rose, M. J.; Patra, A. K.; Alcid, E. A.; Olmstead, M. M.; Mascharak, P. K. *Inorg. Chem.* **2007**, *46*, 2328–2338.

23 Serli, B.; Zangrando, E.; Gianferrara, T.; Yellowlees, L.; Alessio, E. *Coord. Chem. Rev* **2003**, *245*, 73–83.

24 Jørgensen, C. K. *Coord. Chem. Rev.* **1966**, *1*, 164–178.

25 (a) Enemark, J. H.; Feltham, R. D. *J. Am. Chem. Soc.* **1974**, *96*, 5002–5004; (b) Enemark, J. H.; Feltham, R. D. *Coord. Chem. Rev.* **1974**, *13*, 339–406.

26 (a) Li, M.; Bonnet, D.; Bill, E.; Neese, F.; Weyhermüller, T.; Blum, N.; Sellmann, D.; Wieghardt, K. *Inorg. Chem.* **2002**, *41*, 3444–3456; (b) Serres, R. G.; Grapperhaus, C. A.; Bothe, E.; Bill, E.; Weyhermüller, T.; Neese, F.; Wieghardt, K. *J. Am. Chem. Soc.* **2004**, *126*, 5138–5153; (c) Singh, P.; Sarkar, B.; Sieger, M.; Niemeyer, M.; Fiedler, J.; Záliš, S.; Kaim, W. *Inorg. Chem.* **2006**, *45*, 4602–4609; (d) Caramori, G. F.; Frenking, G. *Organometallics* **2007**, *26*, 5815–5825; (e) Caramori, G. F.; Frenking, G. *Croat. Chem. Acta* **2009**, *82*, 219–232; (f) Caramori, G. F.; Kunitz, A. G.; Andriani, K. F.; Doro, F. G.; Frenking, G.; Tfouni, E. *Dalton Trans.* **2012**, *41*, 7327–7339; (g) Aguilar, C. M.; Rocha, W. R. *Inorganica Chim. Acta* **2013**, *408*, 18–26; (h) Cheng, H.-Y.; Chang, S.; Tsai, P.-Y. *J. Phys. Chem. A* **2004**, *108*, 358–361; (i) Conradie, J.; Ghosh, A. *J. Phys. Chem. B* **2007**, *111*, 12621–12624; (j) Sizova, O. V.; Baranovski, V. I.; Ivanova, N. V.; Sizov, V. V. *Mol. Phys.* **2003**, *101*, 715–720; (k) Andriani, K. F.; Caramori, G. F.; Doro, F. G.; Parreira, R. L. T. *Dalton Trans.* **2014**, *43*, 8792–8804.

27 De Candia, A. G.; Marcolongo, J. P.; Etchenique, R.; Slep, L. D. *Inorg. Chem.* **2010**, *49*, 6925–6930.

28 Radoń, M.; Pierloot, K. *J. Phys. Chem. A* **2008**, *112*, 11824–11832.

29 Radoń, M.; Broclawik, E.; Pierloot, K. *J. Phys. Chem. B* **2010**, *114*, 1518–1528.

30 Bučinský, L.; Büchel, G. E.; Ponec, R.; Rapta, P.; Breza, M.; Kožíšek, J.; Gall, M.; Biskupič, S.; Fronc, M.; Schiessl, K.; Cuzan, O.; Prodius, D.; Turta, C.; Shova, S.; Zając, D. A.; Arion, V. B. *Eur. J. Inorg. Chem.* **2013**, *2013*, 2505–2519.

31 Lahiri, G. K.; Kaim, W. *Dalton Trans.* **2010**, *39*, 4471–4478.

32 Ford, P. C.; Pereira, J. C. M.; Miranda, K. M. In *Nitrosyl Complexes in Inorganic Chemistry, Biochemistry and Medicine II*; Mingos, D. M. P., Ed.; Structure and Bonding 154; Springer Berlin Heidelberg, 2013; pp 99–135.

33 Tocheva, E. I.; Rosell, F. I.; Mauk, A. G.; Murphy, M. E. P. *Science* **2004**, *304*, 867–870.

34 Novozhilova, I. V.; Coppens, P.; Lee, J.; Richter-Addo, G. B.; Bagley, K. A. *J. Am. Chem. Soc.* **2006**, *128*, 2093–2104.

35 Kaim, W. In *Advances in Inorganic Chemistry*; Olabe, J. A., van Eldik, R., Eds.; NOx Related Chemistry; Academic Press, 2015; Vol. 67; pp 295–313.

36 Rose, M. J.; Mascharak, P. K. *Coord. Chem. Rev.* **2008**, *252*, 2093–2114.

37 Roncaroli, F.; Videla, M.; Slep, L. D.; Olabe, J. A. *Coord. Chem. Rev* **2007**, *251*, 1903–1930.

38 Merkle, A. C.; Fry, N. L.; Mascharak, P. K.; Lehnert, N. *Inorg. Chem.* **2011**, *50*, 12192–12203.

39 Fry, N. L.; Mascharak, P. K. *Dalton Trans.* **2012**, *41*, 4726–4735.

40 Adamson, A. W.; Demas, J. N. *J. Am. Chem. Soc.* **1971**, *93*, 1800–1801.

41 (a) Zeitler, K. *Angew. Chem. Int. Ed.* **2009**, *48*, 9785–9789; (b) Narayanam, J. M. R.; Stephenson, C. R. J. *Chem. Soc. Rev.* **2010**, *40*, 102–113; (c) Tucker, J. W.; Stephenson, C. R. J. *J. Org. Chem.* **2012**, *77*, 1617–1622; (d) Prier, C. K.; Rankic, D. A.; MacMillan, D. W. C. *Chem. Rev.* **2013**, *113*, 5322–5363; (e) Koike, T.; Akita, M. In *Ruthenium in Catalysis*; Dixneuf, P. H., Bruneau, C., Eds.; Topics in Organometallic Chemistry 48; Springer International Publishing, 2014; pp 371–395; (f) Schultz, D. M.; Yoon, T. P. *Science* **2014**, *343*, 1239176.

42 (a) Joachim, C.; Gimzewski, J. K.; Aviram, A. *Nature* **2000**, *408*, 541–548; (b) Hu, L.; Xu, G. *Chem. Soc. Rev.* **2010**, *39*, 3275–3304.

43 Juris, A.; Balzani, V.; Barigelletti, F.; Campagna, S.; Belser, P.; von Zelewsky, A. *Coord. Chem. Rev.* **1988**, *84*, 85–277.

44 Campagna, S.; Puntoriero, F.; Nastasi, F.; Bergamini, G.; Balzani, V. In *Photochemistry and Photophysics of Coordination Compounds I*; Balzani, V., Campagna, S., Eds.; Topics in Current Chemistry 280; Springer Berlin Heidelberg, 2007; pp 117–214.

45 Kalyanasundaram, K. *Coord. Chem. Rev.* **1982**, *46*, 159–244.

46 (a) Sun, L.; Hammarström, L.; Åkermark, B.; Styring, S. *Chem. Soc. Rev.* **2001**, *30*, 36–49; (b) Berardi, S.; Drouet, S.; Francàs, L.; Gimbert-Suriñach, C.; Guttentag, M.; Richmond, C.; Stoll, T.; Llobet, A. *Chem. Soc. Rev.* **2014**, *43*, 7501–7519.

47 (a) Gill, M. R.; Garcia-Lara, J.; Foster, S. J.; Smythe, C.; Battaglia, G.; Thomas, J. A. *Nat. Chem.* **2009**, *1*, 662–667; (b) Smith, N. A.; Sadler, P. J. *Phil. Trans. R. Soc. A* **2013**, *371*, 20120519; (c) Gill, M. R.; Thomas, J. A. *Chem. Soc. Rev.* **2012**, *41*, 3179–3192.

48 Damrauer, N. H.; Cerullo, G.; Yeh, A.; Boussie, T. R.; Shank, C. V.; McCusker, J. K. *Science* **1997**, *275*, 54–57.

49 Cannizzo, A.; van Mourik, F.; Gawelda, W.; Zgrablic, G.; Bressler, C.; Chergui, M. *Angew. Chem. Int. Ed.* **2006**, *118*, 3246–3248.

50 Bräm, O.; Messina, F.; El-Zohry, A. M.; Cannizzo, A.; Chergui, M. *Chem. Phys.* **2012**, *393*, 51–57.

51 Bhasikuttan, A. C.; Suzuki, M.; Nakashima, S.; Okada, T. *J. Am. Chem. Soc.* **2002**, *124*, 8398–8405.

52 (a) Nozaki, K.; Takamori, K.; Nakatsugawa, Y.; Ohno, T. *Inorg. Chem.* **2006**, *45*, 6161–6178; (b) Alexander, B. D.; Dines, T. J.; Longhurst, R. W. *Chem. Phys.* **2008**, *352*, 19–27; (c) Moret, M.-E.; Tavernelli, I.; Rothlisberger, U. *J. Phys. Chem. B* **2009**, *113*, 7737–7744; (d) Tavernelli, I.; Curchod, B. F.; Rothlisberger, U. *Chem. Phys.* **2011**, *391*, 101–109.

53 Daul, C.; Baerends, E. J.; Vernooijs, P. *Inorg. Chem.* **1994**, *33*, 3538–3543.

54 Xie, Z.-Z.; Fang, W.-H. *J. Mol. Struct.: THEOCHEM* **2005**, *717*, 179–187.

55 (a) Abrahamsson, M.; Jäger, M.; Österman, T.; Eriksson, L.; Persson, P.; Becker, H.-C.; Johansson, O.; Hammarström, L. *J. Am. Chem. Soc.* **2006**, *128*, 12616–12617; (b) Abrahamsson, M.; Jäger, M.; Kumar, R. J.; Österman, T.; Persson, P.; Becker, H.-C.; Johansson, O.; Hammarström, L. *J. Am. Chem. Soc.* **2008**, *130*, 15533–15542.

56 (a) Abrahamsson, M.; Lundqvist, M. J.; Wolpher, H.; Johansson, O.; Eriksson, L.; Bergquist, J.; Rasmussen, T.; Becker, H.-C.; Hammarström, L.; Norrby, P.-O.; Åkermark, B.; Persson, P. *Inorg. Chem.* **2008**, *47*, 3540–3548; (b) Schramm, F.; Meded, V.; Fliegl, H.; Fink, K.; Fuhr, O.; Qu, Z.; Klopper, W.; Finn, S.; Keyes, T. E.; Ruben, M. *Inorg. Chem.* **2009**, *48*, 5677–5684; (c) Breivogel, A.; Meister, M.; Förster, C.; Laquai, F.; Heinze, K. *Chem. Eur. J.* **2013**, *19*, 13745–13760.

57 Robson, K. C. D.; Koivisto, B. D.; Yella, A.; Sporinova, B.; Nazeeruddin, M. K.; Baumgartner, T.; Grätzel, M.; Berlinguette, C. P. *Inorg. Chem.* **2011**, *50*, 5494–5508.

58 Tschierlei, S.; Karnahl, M.; Presselt, M.; Dietzek, B.; Guthmuller, J.; González, L.; Schmitt, M.; Rau, S.; Popp, J. *Angew. Chem. Int. Ed.* **2010**, *49*, 3981–3984.

59 Born, M.; Oppenheimer, R. *Ann. Phys.* **1927**, *84*, 457.

60 Piela, L. *Ideas of Quantum Chemistry*; Elsevier: Amsterdam, 2007.

61 Fock, V. *Z. Phys* **1930**, *61*, 126–148.

62 Bartlett, R. J.; Stanton, J. F. In *Reviews in Computational Chemistry*; Lipkowitz, K. B., Boyd, D. B., Eds.; John Wiley & Sons, Inc., 1994; pp 65–169.

63 Sinanoğlu, O.; Tuan, D. F. *J. Chem. Phys.* **1963**, *38*, 1740–1748.

64 Boguslawski, K.; Tecmer, P.; Legeza, Ö.; Reiher, M. *J. Phys. Chem. Lett.* **2012**, *3*, 3129–3135.

65 Szabo, A.; Ostlund, N. S. *Modern Quantum Chemistry: Introduction to Advanced Electronic Structure Theory*; Dover: Mineola, New York, 1996.

66 Møller, C.; Plesset, M. S. *Phys. Rev.* **1934**, *46*, 618.

67 (a) Janssen, C. L.; Nielsen, I. M. B. *Chem. Phys. Lett.* **1998**, *290*, 423–430; (b) Nielsen, I. M. B.; Janssen, C. L. *Chem. Phys. Lett.* **1999**, *310*, 568–576; (c) Jiang, W.; DeYonker, N. J.; Wilson, A. K. *J. Chem. Theory Comput.* **2012**, *8*, 460–468.

68 (a) Pulay, P.; Hamilton, T. P. *J. Chem. Phys.* **1988**, *88*, 4926–4933; (b) Gordon, M. S.; Schmidt, M. W.; Chaban, G. M.; Glaesemann, K. R.; Stevens, W. J.; Gonzalez, C. *J. Chem. Phys.* **1999**, *110*, 4199–4207.

69 Rissler, J.; Noack, R. M.; White, S. R. *Chemical Physics* **2006**, *323*, 519–531.

70 Boguslawski, K.; Tecmer, P.; Barcza, G.; Legeza, Ö.; Reiher, M. *J. Chem. Theory Comput.* **2013**, *9*, 2959–2973.

71 Roos, B. O. In *Lecture Notes in Quantum Chemistry*; Roos, B. O., Ed.; Lecture Notes in Chemistry 58; Springer Berlin Heidelberg, 1992; pp 177–254.

72 Olsen, J. *Int. J. Quantum Chem.* **2011**, *111*, 3267–3272.

73 Olsen, J.; Roos, B. O.; Jo/rgensen, P.; Jensen, H. J. A. *J. Chem. Phys.* **1988**, *89*, 2185–2192.

74 Ma, D.; Li Manni, G.; Gagliardi, L. *J. Chem. Phys.* **2011**, *135*, 044128.

75 (a) White, S. R. *Phys. Rev. Lett.* **1992**, *69*, 2863–2866; (b) White, S. R. *Phys. Rev. B* **1993**, *48*, 10345–10356.

76 (a) Chan, G. K.-L.; Sharma, S. *Annu. Rev. Phys. Chem.* **2011**, *62*, 465–481; (b) Wouters, S.; van Neck, D. *Eur. Phys. J. D* **2014**, *68*, 272; (c) Yanai, T.; Kurashige, Y.; Mizukami, W.; Chalupský, J.; Lan, T. N.; Saitow, M. *Int. J. Quantum Chem.* **2015**, *115*, 283–299.

77 Boguslawski, K.; Marti, K. H.; Legeza, Ö.; Reiher, M. *J. Chem. Theory Comput.* **2012**, *8*, 1970–1982.

78 (a) Pierloot, K. In *Computational Organometallic Chemistry*; Cundari, T. R., Ed.; Marcel Dekker Inc.: New York, 2001; pp 123–158; (b) Pierloot, K. *Int. J. Quantum Chem.* **2011**, *111*, 3291–3301.

79 Andersson, K.; Malmqvist, P. A.; Roos, B. O.; Sadlej, A. J.; Wolinski, K. *J. Phys. Chem.* **1990**, *94*, 5483–5488.

80 Finley, J.; Malmqvist, P. A.; Roos, B. O.; Serrano-Andrés, L. *Chem. Phys. Lett.* **1998**, *288*, 299–306.

81 Shiozaki, T.; Győrffy, W.; Celani, P.; Werner, H.-J. *J. Chem. Phys.* **2011**, *135*, 081106.

82 Buenker, R. J.; Peyerimhoff, S. D.; Butscher, W. *Mol. Phys.* **1978**, *35*, 771–791.

83 Werner, H.-J. In *Advances in Chemical Physics*; Lawley, K. P., Ed.; John Wiley & Sons, Inc., 1987; pp 1–62.

84 Keller, S. F.; Reiher, M. *CHIMIA* **2014**, *68*, 200–203.

85 Moritz, G.; Reiher, M. *J. Chem. Phys.* **2007**, *126*, 244109.

86 (a) Chan, G. K.-L.; Dorando, J. J.; Ghosh, D.; Hachmann, J.; Neuscamman, E.; Wang, H.; Yanai, T. In *Frontiers in Quantum Systems in Chemistry and Physics*; Wilson, S., Grout, P. J., Maruani, J., Delgado-Barrio, G., Piecuch, P., Eds.; Progress in Theoretical Chemistry and Physics 18; Springer Netherlands, 2008; pp 49–65; (b) Marti, K. H.; Reiher, M. *Z. Phys. Chem.* **2010**, *224*, 583–599; (c) Schollwöck, U. *Ann. Phys.* **2011**, *326*, 96–192.

87 Koch, W.; Holthausen, M. C. *A chemist's guide to density functional theory*; Wiley-VCH, 2000.

88 Kohn, W.; Sham, L. J. *Phys. Rev.* **1965**, *140*, A1133–A1138.

89 Perdew, J. P.; Schmidt, K. Jacob's ladder of density functional approximations for the exchange-correlation energy. AIP Conference Proceedings. 2001; pp 1–20.

90 Cramer, C. J.; Truhlar, D. G. *Phys. Chem. Chem. Phys.* **2009**, *11*, 10757–10816.

91 Lundberg, M.; Siegbahn, P. E. M. *J. Chem. Phys.* **2005**, *122*, 224103.

92 Cohen, A. J.; Mori-Sánchez, P.; Yang, W. *Science* **2008**, *321*, 792–794.

93 (a) Grimme, S.; Antony, J.; Ehrlich, S.; Krieg, H. *J. Chem. Phys.* **2010**, *132*, 154104; (b) Grimme, S. *WIREs Comput. Mol. Sci.* **2011**, *1*, 211–228.

94 Chai, J.-D.; Head-Gordon, M. *Phys. Chem. Chem. Phys.* **2008**, *10*, 6615–6620.

95 González, L.; Escudero, D.; Serrano-Andrés, L. *ChemPhysChem* **2012**, *13*, 28–51.

96 Casida, M. E. *J. Mol. Struct.: THEOCHEM* **2009**, *914*, 3–18.

97 Casida, M.; Huix-Rotllant, M. *Annu. Rev. Phys. Chem.* **2012**, *63*, 287–323.

98 Marques, M.; Gross, E. *Annu. Rev. Phys. Chem.* **2004**, *55*, 427–455.

99 Dreuw, A.; Head-Gordon, M. *Chem. Rev.* **2005**, *105*, 4009–4037.

100 Ziegler, T.; Seth, M.; Krykunov, M.; Autschbach, J.; Wang, F. *J. Mol. Struct.: THEOCHEM* **2009**, *914*, 106–109.

101 Tsuneda, T.; Hirao, K. *WIREs Comput. Mol. Sci.* **2014**, *4*, 375–390.

102 (a) Whitten, J. L. *J. Chem. Phys.* **1973**, *58*, 4496–4501; (b) Baerends, E. J.; Ellis, D. E.; Ros, P. *Chem. Phys.* **1973**, *2*, 41–51.

103 Werner, H.-J.; Manby, F. R.; Knowles, P. J. *J. Chem. Phys.* **2003**, *118*, 8149–8160.

104 Beebe, N. H. F.; Linderberg, J. *Int. J. Quantum Chem.* **1977**, *12*, 683–705.

105 Pedersen, T.; Aquilante, F.; Lindh, R. *Theor. Chem. Acc.* **2009**, *124*, 1–10.

106 Reiher, M.; Wolf, A. *Relativistic Quantum Chemistry: The Fundamental Theory of Molecular Science*; John Wiley & Sons, 2014.

107 Lenthe, E. v.; Baerends, E. J.; Snijders, J. G. *J. Chem. Phys.* **1993**, *99*, 4597–4610.

108 Hess, B. A. *Phys. Rev. A* **1985**, *32*, 756–763.

109 Andrae, D.; Häußermann, U.; Dolg, M.; Stoll, H.; Preuß, H. *Theoret. Chim. Acta* **1990**, *77*, 123–141.

110 Malmqvist, P. A.; Roos, B. O.; Schimmelpfennig, B. *Chem. Phys. Lett.* **2002**, *357*, 230–240.

111 Wang, F.; Ziegler, T. *J. Chem. Phys.* **2005**, *123*, 154102.

112 Mennucci, B. *WIREs Comput. Mol. Sci.* **2012**, *2*, 386–404.

113 Klamt, A. *WIREs Comput. Mol. Sci.* **2011**, *1*, 699–709.

114 (a) Lin, H.; Truhlar, D. G. *Theor. Chem. Acc.* **2006**, *117*, 185–199; (b) Senn, H. M.; Thiel, W. *Angew. Chem. Int. Ed.* **2009**, *48*, 1198–1229.

115 Tannor, D. J. *Introduction to Quantum Mechanics: A Time-dependent Perspective*; University Science Books, 2007.

116 (a) Tully, J. C. *Faraday Disc.* **1998**, *110*, 407–419; (b) Doltsinis, N. L.; Marx, D. *J. Theor. Comput. Chem.* **2002**, *01*, 319–349; (c) Barbatti, M. *WIREs Comput. Mol. Sci.* **2011**, *1*, 620–633.

117 Pittner, J.; Lischka, H.; Barbatti, M. *Chem. Phys.* **2009**, *356*, 147–152.

118 Hammes-Schiffer, S.; Tully, J. C. *J. Chem. Phys.* **1994**, *101*, 4657.

119 Tully, J. C. *J. Chem. Phys.* **1990**, *93*, 1061–1071.

120 Merchán, M.; Serrano-Andrés, L.; Robb, M. A.; Blancafort, L. *J. Am. Chem. Soc.* **2005**, *127*, 1820–1825.

121 (a) Richter, M.; Marquetand, P.; González-Vázquez, J.; Sola, I.; González, L. *J. Chem. Theory Comput.* **2011**, *7*, 1253–1258; (b) Mai, S.; Marquetand, P.; González, L. *Int. J. Quantum Chem.* **2015**, in press.

122 Büchel, G. E.; Gavriluta, A.; Novak, M.; Meier, S. M.; Jakupec, M. A.; Cuzan, O.; Turta, C.; Tommasino, J.-B.; Jeanneau, E.; Novitchi, G.; Luneau, D.; Arion, V. B. *Inorg. Chem.* **2013**, *52*, 6273–6285.

123 Coe, B. J.; Glenwright, S. J. *Coord. Chem. Rev.* **2000**, *203*, 5–80.

124 Karton, A.; Tarnopolsky, A.; Lamère, J.-F.; Schatz, G. C.; Martin, J. M. L. *J. Phys. Chem. A* **2008**, *112*, 12868–12886.

125 Perdew, J. P. *Phys. Rev. B* **1986**, *33*, 8822–8824.

126 Becke, A. D. *J. Chem. Phys.* **1993**, *98*, 5648–5652.

127 Lee, C.; Yang, W.; Parr, R. G. *Phys. Rev. B* **1988**, *37*, 785–789.

128 Zhao, Y.; Truhlar, D. G. *J. Chem. Phys.* **2006**, *125*, 194101.

129 Harvey, J. N. *Principles and Applications of Density Functional Theory in Inorganic Chemistry I*; Structure and Bonding 112; Springer Berlin Heidelberg, 2004; pp 151–184.

130 Harvey, J. N. *Annu. Rep. Prog. Chem., Sect. C: Phys. Chem.* **2006**, *102*, 203–226.

131 Vancoillie, S.; Zhao, H.; Radoń, M.; Pierloot, K. *J. Chem. Theory Comput.* **2010**, *6*, 576–582.

132 Delcey, M. G.; Pierloot, K.; Phung, Q. M.; Vancoillie, S.; Lindh, R.; Ryde, U. *Phys. Chem. Chem. Phys.* **2014**, *16*, 7927–7938.

133 Cremer, D. *Mol. Phys.* **2001**, *99*, 1899–1940.

134 Boguslawski, K.; Jacob, C. R.; Reiher, M. *J. Chem. Theory Comput.* **2011**, *7*, 2740–2752.

135 Cannizzo, A.; Blanco-Rodríguez, A. M.; El Nahhas, A.; Šebera, J.; Záliš, S.; Vlček., A.; Chergui, M. *J. Am. Chem. Soc.* **2008**, *130*, 8967–8974.

136 (a) Bhasikuttan, A. C.; Okada, T. *J. Phys. Chem. B* **2004**, *108*, 12629–12632; (b) McCusker, J. K. *Acc. Chem. Res.* **2003**, *36*, 876–887; (c) Bräm, O.; Messina, F.; Baranoff, E.; Cannizzo, A.; Nazeeruddin, M. K.; Chergui, M. *J. Phys. Chem. C* **2013**, *117*, 15958–15966; (d) Juban, E. A.; McCusker, J. K. *J. Am. Chem. Soc.* **2005**, *127*, 6857–6865; (e) Hedley, G. J.; Ruseckas, A.; Samuel, I. D. W. *J. Phys. Chem. A* **2009**, *113*, 2–4; (f) Iwakura, I.; Kobayashi, T.; Yabushita, A. **2009**, *48*, 3523–3528; (g) Auböck, G.; Chergui, M. *Nat Chem* **2015**, *7*, 629–633.

137 Fry, N. L.; Heilman, B. J.; Mascharak, P. K. *Inorg. Chem.* **2011**, *50*, 317–324.

138 Frisch, M. J.; Trucks, G. W.; Schlegel, H. B.; Scuseria, G. E.; Robb, M. A.; Cheeseman, J. R.; Scalmani, G.; Barone, V.; Mennucci, B.; Petersson, G. A.; Nakatsuji, H.; Caricato, M.; Li, X.; Hratchian, H. P.; Izmaylov, A. F.; Bloino, J.; Zheng, G.; Sonnenberg, J. L.; Hada, M.; Ehara, M.; Toyota, K.; Fukuda, R.; Hasegawa, J.; Ishida, M.; Nakajima, T.; Honda, Y.; Kitao, O.; Nakai, H.; Vreven, T.; Montgomery, J. A., Jr.; Peralta, J. E.; Ogliaro, F.; Bearpark, M.; Heyd, J. J.; Brothers, E.; Kudin, K. N.; Staroverov, V. N.; Kobayashi, R.; Normand, J.; Raghavachari, K.; Rendell, A.; Burant, J. C.; Iyengar, S. S.; Tomasi, J.; Cossi, M.; Rega, N.; Millam, J. M.; Klene, M.; Knox, J. E.; Cross, J. B.; Bakken, V.; Adamo, C.; Jaramillo, J.; Gomperts, R.; Stratmann, R. E.; Yazyev, O.; Austin, A. J.; Cammi, R.; Pomelli, C.; Ochterski, J. W.; Martin, R. L.; Morokuma, K.; Zakrzewski, V. G.; Voth, G. A.; Salvador, P.; Dannenberg, J. J.; Dapprich, S.; Daniels, A. D.; Farkas, Ö.; Foresman, J. B.; Ortiz, J. V.; Cioslowski, J.; Fox, D. J. Gaussian 09 Revision D.01. Gaussian Inc. Wallingford CT 2009.

139 Weigend, F.; Ahlrichs, R. *Phys. Chem. Chem. Phys.* **2005**, *7*, 3297–3305.

140 Aquilante, F.; De Vico, L.; Ferré, N.; Ghigo, G.; Malmqvist, P.; Neogrády, P.; Pedersen, T. B.; Pitoňák, M.; Reiher, M.; Roos, B. O.; Serrano-Andrés, L.; Urban, M.; Veryazov, V.; Lindh, R. *J. Comput. Chem.* **2010**, *31*, 224–247.

141 Roos, B. O.; Lindh, R.; Malmqvist, P.-A.; Veryazov, V.; Widmark, P.-O. *J. Phys. Chem. A* **2005**, *109*, 6575–6579.

142 Ghigo, G.; Roos, B. O.; Malmqvist, P.-Å. *Chem. Phys. Lett.* **2004**, *396*, 142–149.

143 Roos, B. O.; Andersson, K. *Chem. Phys. Lett.* **1995**, *245*, 215–223.

144 Rose, M. J.; Mascharak, P. K. *Inorg. Chem.* **2009**, *48*, 6904–6917.

145 (a) Weigend, F.; Häser, M. *Theoret. Chem. Acta* **1997**, *97*, 331–340; (b) Weigend, F.; Häser, M.; Patzelt, H.; Ahlrichs, R. *Chem. Phys. Lett.* **1998**, *294*, 143–152.

146 TURBOMOLE V6.5 2013, a development of University of Karlsruhe and Forschungszentrum Karlsruhe GmbH, 1989-2007, TURBOMOLE GmbH, since 2007; available from `http://www.turbomole.com`.

147 Rillema, D. P.; Jones, D. S. *J. Chem. Soc., Chem. Commun.* **1979**, 849–851.

148 Dolfi, M.; Bauer, B.; Keller, S.; Kosenkov, A.; Ewart, T.; Kantian, A.; Giamarchi, T.; Troyer, M. *Comp. Phys. Comm.* **2014**, *185*, 3430–3440.

149 (a) Kober, E. M.; Sullivan, B. P.; Meyer, T. J. *Inorg. Chem.* **1984**, *23*, 2098–2104; (b) Oh, D. H.; Boxer, S. G. *J. Am. Chem. Soc.* **1989**, *111*, 1130–1131.

150 Moret, M.-E.; Tavernelli, I.; Chergui, M.; Rothlisberger, U. *Chem. Eur. J.* **2010**, *16*, 5889–5894.

151 Kirketerp, M.-B. S.; Nielsen, S. B. *Int. J. Mass Spectrom.* **2010**, *297*, 63–66.

152 Yanai, T.; Tew, D. P.; Handy, N. C. *Chem. Phys. Lett.* **2004**, *393*, 51–57.

153 (a) Rau, S.; Walther, D.; Vos, J. G. *Dalton Trans.* **2007**, 915–919; (b) Schulz, M.; Karnahl, M.; Schwalbe, M.; Vos, J. G. *Coord. Chem. Rev.* **2012**, *256*, 1682–1705.

154 Bindra, G. S.; Schulz, M.; Paul, A.; Soman, S.; Groarke, R.; Inglis, J.; Pryce, M. T.; Browne, W. R.; Rau, S.; Maclean, B. J.; Vos, J. G. *Dalton Trans.* **2011**, *40*, 10812–10814.

155 Kowacs, T.; Pan, Q.; Huijser, A.; Rau, S.; Lang, P.; Browne, W. R.; Pryce, M. T.; Vos, J. G. *Inorg. Chem.* **2015**, submitted.

156 Bokareva, O. S.; Grell, G.; Bokarev, S. I.; Kühn, O. *J. Chem. Theory Comput.* **2015**, *11*, 1700–1709.

ACKNOWLEDGEMENTS

This work would not have been possible without the support for many people. First, I would like to thank my supervisor Prof. Leticia González for her guidance and scientific support during my scientific endeavours in the last years, and for initiating and supporting all the wonderful collaborations that seemed "way too many projects" at first but turned out to be great scientific adventures in due course and finally found their way into this thesis. Working with other people is one of the best things in science and therefore I would like to thank my collaborators: Dr. Anatolie Gavriluța, Dr. Gabriel Büchel, Dr. Ghenadie Novitchi, Dr. Paul-Steffen Kuhn, Prof. Vladimir Arion and all other members from the French-Austrian project for my very first collaboration in Vienna; Dr. Michael Jäger for his hard work and enthusiasm to learn computational chemistry resulting in a collaboration which ultimately ended up in what is Appendix 4.A.1 now; Dr. Stefan Knecht, Prof. Markus Reiher, Dr. Yingjin Ma, Sebastian Keller and the rest of the Reiher group for welcoming me in Zurich, helping me with DMRG and supporting a collaboration project which is still ongoing; Dr. Mickaël G. Delcey, Dr. Francesco Aquilante, Prof. Thomas Bondo Pedersen and Prof. Roland Lindh for their work on the Cholesky decomposition gradients; Dr. Annemarie Huijser, Qing Pan and Prof. Han Vos for another ("last-minute") collaboration on hydrogen-producing photocatalysts.

I would like to thank all current and former González group members with whom I had a chance to work with in Vienna from our very beginning here for all the scientific and non-scientific discussions and just the nice time in the group: Martin Thomas, Dr. Marianna Assmann, Dr. Martin Richter, Federico Latorre, David Ferro, Dr. Stephan Kupfer, Dr. Rana Obaid, Dr. Daniel Kinzel, Christoph Bauer, Dr. Felix Plasser, Dr. Philipp Marquetand, Dr. Juanjo Nogueira, Dr. Matthias Ruckenbauer, Dr. Andrea Fülöpová, J. Patrick Zobel, Dr. Aurora Muñoz-Losa, Prof. Antonio Mota, Lucy Grosvenor, Dr. Andrew Atkins and Dr. Stefan Ruider, and our numerous bachelor students including my students Elias Leutgeb and Isolde Sandler. Additional thanks go to my office mates Michael Gastegger, Sebastian Mai and Clemens Rauer for all the scientific, leisure, explosive, playful, dangerous, SHARCy, and just funny moments in the office. Special thanks go to Dr. Markus Oppel and our former system administrators Jackie Klaura and Michaela Jirovec for the computer maintenance and support, and the current and former secretaries Kathrine Baumann, Edith Steinwidder and Nicole Irmler for the efficient handling of the paperwork.

I would like to express my gratitude to Lara for her support in these years, my parents for what they did for me and their high expectations of me (which I'm never going to fulfill, I guess) and my friends for being there. Special thanks go to Sarah Theiner for proofreading parts of the manuscript and Hristo Varbanov for all the scientific discussions about ruthenium and platinum complexes and providing me with a link from my theoretical chemistry bubble to the "real chemistry world".

Finally I would like to thank the University of Vienna and the COST for the financial support during the thesis.

> *"It might be a very insignificant breakthrough, but it is hell of a lot better than no breakthrough."*
>
> —Christoph Elschenbroich, Organometallchemie, 5. Auflage, p. 674

SELBSTSTÄNDIGKEITSERKLÄRUNG

Hiermit erkläre ich, dass ich die vorliegende Arbeit selbstständig und ohne Zuhilfenahme weiterer als der aufgeführten Quellen angefertigt habe. Alle wörtlich oder sinngemäß übernommenen Textstellen anderer Verfasser wurden als solche gekennzeichnet.

CURRICULUM VITAE

Leon Freitag

Education

Nov. 2011 – present	Ph. D. at the **University of Vienna** Advisor: Prof. Leticia González
Oct. 2011	M. Sc. *(Diplom)* in Chemistry **Friedrich-Schiller-Universität Jena** | Grade: 1.2 Thesis: “The hydrogen dissociation in dimethylfluoroethylene: a high accuracy quantum chemical study” Advisor: Prof. Leticia González
Aug. 2010	B. Sc. *(Vordiplom)* in Chemistry **Friedrich-Schiller-Universität Jena** | Grade: 1.3
2008–2009	Exchange Year at **Pembroke College, University of Oxford**, Oxford, UK
June 2006	**Carl-Zeiss-Gymnasium Jena**, Abitur | Grade: 1.1

Scholarships

2014	COST STSM grants for short research stays research with Prof. Hans Jørgen Aagaard Jensen (University of Southern Denmark) and Prof. Markus Reiher (ETH Zürich)
2007–2011	*Studienstiftung des deutschen Volkes* (German National Academic Merit Foundation) scholarship
Summer 2009	DAAD IREU (International Research Experience for Undergraduates) scholarship

Research Interests and Expertise

Computational investigation of transition metal complexes, including:

- photochemistry and photodynamics with DFT and ab-initio quantum chemical methods
- photodeactivation mechanisms of ruthenium photosensitizers
- mechanisms of action of ruthenium- and platinum-based anticancer drugs
- computational studies of reaction mechanisms

Publications

- M. Jäger, L. Freitag, and L. González: “Using computational chemistry to design Ru photosensitizers with directional charge transfer”, Coord. Chem. Rev. **2015**, in press.

- L. Freitag, S. Knecht, S. F. Keller, M. G. Delcey, F. Aquilante, T. Bondo Pedersen, R. Lindh, M. Reiher and L. González: “Orbital entanglement and CASSCF analysis of the Ru–NO bond in a Ruthenium nitrosyl complex”, Phys. Chem. Chem. Phys. **2015**, *17*, 14383-14392.

- M. G. Delcey, L. Freitag, T. Bondo Pedersen, F. Aquilante, R. Lindh and L. González: “Analytical gradients of complete active space self-consistent field energies using Cholesky decomposition: Geometry optimization and spin-state energetics of a ruthenium nitrosyl complex”, J. Chem. Phys. **2014**, *140*, 174103.

- L. Freitag and L. González: "Theoretical Spectroscopy and Photodynamics of a Ruthenium Nitrosyl Complex", Inorg. Chem. **2014**, *53*, 6415–6426.

- A. Gavriluta, G. E. Büchel, L. Freitag, G. Novitchi, J. B. Tommasino, E. Jeanneau, P.-S. Kuhn, L. González, V. B. Arion, and D. Luneau: "Mechanism Elucidation of the cis–trans Isomerization of an Azole Ruthenium–Nitrosyl Complex and Its Osmium Counterpart", Inorg. Chem. **2013**, *52*, 6260–6272.

- E. J. F. Dickinson, L. Freitag, and R. G. Compton: "Dynamic Theory of Liquid Junction Potentials", J. Phys. Chem. B **2010**, *114*, 187–197.

Conference Talks

- "Exploring Electronic Structure and Photodynamics of Ruthenium Complexes. A challenge for Theory", ECostBio Scientific Workshop, 12–13. 1. 2015, Marseille, France.

- "Exploring Ground and Excited States of Ruthenium Nitrosyl Complexes", Gordon Research Seminar on Computational Chemistry, 19–20. 7. 2014, Mount Snow Resort, West Dover, VT, USA.

- "Theoretical Insights into Excited States and Photodegradation Pathways in Ruthenium Nitrosyl and Polypyridyl Complexes", Current Challenges in Supramolecular Artificial Photosynthesis, European Symposium & Young Researchers Meeting, 10–13. 3. 2014, Jena, Germany.

- "New insights into electronic structure of ruthenium complexes with ab-initio multiconfigurational methods", TCCM - II. Annual Workshop of the Joint Doctorate Program on Theoretical Chemistry and Computational Modelling, 5.–6. 9. 2013, Sopron, Hungary.

Conference Posters

- L. Freitag and L. González: "Ground and Excited State Studies of Ruthenium Nitrosyl Complexes", 50th Symposium for Theoretical Chemistry, 14–18. 9. 2014, Vienna, Austria.

- L. Freitag and L. González: "Exploring Ground and Excited States of Ruthenium Nitrosyl Complexes", Gordon Research Conference on Computational Chemistry, 20–25. 07. 2014, West Dover, VT, USA.

- L. Freitag and L. González: "Theoretical Insights into Excited States and Photodegradation Pathways in Ruthenium Nitrosyl and Polypyridyl Complexes", Current Challenges in Supramolecular Artificial Photosynthesis, European Symposium & Young Researchers Meeting, 9.–13. 3. 2014, Jena, Germany.

- L. Freitag, L. González: "Ab-initio multiconfigurational calculations on $[Ru(bipy)_3]^{2+}$", 9th European Conference on Computational Chemistry, 1.–5. 9. 2013, Sopron, Hungary.

- L. Freitag, M. Delcey, T.B. Pedersen, F. Aquilante, R. Lindh and L. González: "A new look at the electronic structure of the $\{RuNO\}^6$ moiety using density-fitting CASSCF calculations and localised orbitals", VIII-th International Symposium of Theoretical Chemical Physics, 25–31. 8. 2013, Budapest, Hungary.

- L. Freitag, L. González and R. Lindh: "Effect of electron correlation on the valence-Rydberg mixed states of a fluoroethylene derivative", Electronic Structure Theory for Strongly Correlated Systems, 30. 5.–1. 6. 2012, Palermo, Italy.
- L. Freitag, B. P. Prascher and A. K. Wilson: "The Resolution of the Identity (RI) Approximation Applied to the Correlation Consistent Composite Approach", ACS Fall 2009 National Meeting, 16.–20. 8. 2009 , Washington, DC, USA.

Languages

Russian, Ukrainian, Polish: mother tongue
English, German: fluent
Bulgarian: good command
Serbian, Italian: basic knowledge